

Ispitivanje uređaja za smanjenje aerodinamičkog otpora cestovnih vozila

Puljić, Damjan

Master's thesis / Diplomski rad

2014

Degree Grantor / Ustanova koja je dodijelila akademski / stručni stupanj: **University of Zagreb, Faculty of Mechanical Engineering and Naval Architecture / Sveučilište u Zagrebu, Fakultet strojarstva i brodogradnje**

Permanent link / Trajna poveznica: <https://urn.nsk.hr/urn:nbn:hr:235:406756>

Rights / Prava: [In copyright](#) / [Zaštićeno autorskim pravom.](#)

Download date / Datum preuzimanja: **2025-03-26**

Repository / Repozitorij:

[Repository of Faculty of Mechanical Engineering and Naval Architecture University of Zagreb](#)



UNIVERSITY OF ZAGREB
FACULTY OF MECHANICAL ENGINEERING AND NAVAL
ARCHITECTURE

MASTER'S THESIS

Damjan Puljić

Zagreb, 2014.

UNIVERSITY OF ZAGREB
FACULTY OF MECHANICAL ENGINEERING AND NAVAL
ARCHITECTURE

MASTER'S THESIS

Supervisors:

prof. dr. sc. Zoran Lulić (University of Zagreb)
Dr.-Ing. Ante Šoda (MAGNA Steyr Engineering)

Student:

Damjan Puljić

Zagreb, 2014.

I declare that I made this thesis all by myself, using the best of my knowledge and references listed on the end of the thesis.

Zagreb, November 2014.

Damjan Puljić

ACKNOWLEDGEMENTS

This thesis is a part of the CULT project, which was carried out by the company Magna Steyr, Graz, Austria. From September 2012 to May 2013 all of the simulations in this thesis were carried out at the Magna Steyr Engineering, Thermal & Energy Management department, Graz, Austria, where I did my 9-months internship.

First of all I would like to thank my supervisor Dr.-Ing. Ante Šoda for teaching me basics of automotive aerodynamics and CFD. He selflessly shared his knowledge and he always showed great will to help.

I would like to thank my university supervisor prof. Zoran Lulić and his team at the Chair of IC Engines and Motor Vehicles, Faculty of Mechanical Engineering and Naval Architecture, University of Zagreb. He and his team supported me with everything I needed, especially during my stay in Graz.

I would like to thank all Magna Steyr Thermal & Energy Management department team. They supported me with a wealth of knowledge and experience in the automotive design and development. They were not only my co-workers but also good friends and it was a pleasure to work in such stimulating environment.

I would also like to thank to all professors who gave me their knowledge during my education.

At the end I would like to thank my parents, who have supported me selflessly during my growing up and education.

Zagreb, November 2014.

Damjan Puljić



SVEUČILIŠTE U ZAGREBU
FAKULTET STROJARSTVA I BRODOGRADNJE



Središnje povjerenstvo za završne i diplomske ispite
Povjerenstvo za diplomske ispite studija strojarstva za smjerove:
procesno-energetski, konstrukcijski, brodogradnja i inženjersko modeliranje i računalne simulacije

Sveučilište u Zagrebu Fakultet strojarstva i brodogradnje	
Datum	Prilog
Klasa:	
Ur.broj:	

DIPLOMSKI ZADATAK

Student: **Damjan Puljić**

Mat. br.: 0035173073

Naslov rada na hrvatskom jeziku: **Ispitivanje uređaja za smanjenje aerodinamičkog otpora cestovnih vozila**

Naslov rada na engleskom jeziku: **Investigation of Aerodynamic Drag Reduction Devices in Automotive Engineering**

Opis zadatka:

This thesis should be done as a part of the project CULT (Cars' Ultra Light Technologies), carried out by the company Magna Steyr, Graz, Austria. The CULT vehicle is a small city car, belonging to the A-segment vehicles. The main idea of the project is to develop a realistic, production-ready vehicle with extremely low CO₂ emissions of only 49 g/km. In order to achieve this goal, aerodynamic optimization must be one of the most important development goals, especially the aerodynamic drag should be as low as possible.

The main task within this thesis is to investigate various drag reduction devices for A-segment vehicles. Investigation work need to be carried out with the help of Computational Fluid Dynamics (CFD) and numerical results need to be validated against the results of wind-tunnel measurements.

Contents of this thesis need to cover the following topics:

- Detailed description of the CULT vehicle with a focus on the aerodynamic related parts.
- Description of the complete CFD process in the automotive aerodynamics – from design of CAD surfaces to the analysis of CFD results.
- Analysis of the various drag reduction devices - one example are side mirrors (rear-view mirrors), which are designed with the idea of reducing aerodynamic losses in the wake behind the car.
- Validation of the numerical results against the results of wind-tunnel measurements.
- Standardisation of the post-processing method.

All literature sources and received help have to be cited in the thesis.

Zadatak zadan:

25. rujna 2014.

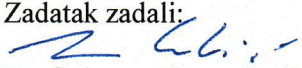
Rok predaje rada:

27. studeni 2014.

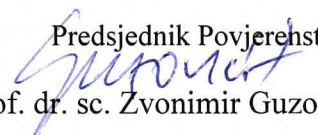
Predviđeni datumi obrane:

3., 4. i 5. prosinac 2014.

Zadatak zadali:


Prof. dr. sc. Zoran Lulić

Dr.-Ing. Ante Sola (MAGNA Steyr Engineering)


Prof. dr. sc. Zvonimir Guzović

CONTENTS

LIST OF FIGURES.....	III
LIST OF TABLES	VIII
ABBREVIATIONS.....	IX
NOMENCLATURE.....	X
SUMMARY	XII
1 Introduction.....	1
1.1 Bluff Body Aerodynamics.....	2
1.2 Aerodynamics of Road Vehicles	5
1.2.1 History of Aerodynamics of Road Vehicles	6
1.2.2 Coordinate System	7
1.2.3 Dimensionless Aerodynamic Coefficients	8
1.2.4 Reference Area.....	9
1.3 Air Pressure Definition.....	10
1.3.1 Aerostatics.....	10
1.3.2 Aerodynamics.....	10
1.4 Driving Resistances	14
1.5 Intelligent Use of Aerodynamics	16
2 Magna Steyr - CULT	18
2.1 About Magna Steyr.....	18
2.2 Transportation in modern urban areas	21
2.3 Aerodynamics of City Cars	23
2.4 CULT – Cars Ultra Light Technologies	25
3 Aerodynamic Optimization of CULT vehicle	27
3.1 Front-End Packaging	29
3.2 Side mirrors (Rear View Cameras)	34
3.3 Front-Wheel Spoilers.....	36
4 CFD (Computational Fluid Dynamics).....	37
4.1 Pre-Processing	39
4.1.1 Altair HyperMesh.....	39
4.1.2 Ansys TGrid	42
4.1.3 Grids	46
4.2 Solver – ANSYS Fluent & Simulation Set-Up	50
4.2.2 Simulation Set-Up.....	51
5 Post-Processing	55

5.1	Simulation results	56
5.2	Geometry overview	58
5.3	Flow visualization.....	59
5.3.1	Cut planes flow visualization	59
5.3.2	3D contours flow visualization	64
5.4	C_p diagrams	66
5.5	F_x and F_z accumulated diagrams	69
6	Wind Tunnel Scaled Model (1:4)	72
6.2	Wind Tunnel Test Set-up.....	75
6.3	Wind Tunnel Test Results	77
6.4	Wind tunnel data post-processing.....	78
7	Analysis AND Validation of the Results	81
7.1	CFD Grid Influence	83
7.1.1	Tetrahedral Elements Refinement Influence	83
7.1.2	Influence of Different Prismatic Layers	87
7.2	Solver Influence – Cell-Based vs. Node-Based Reconstruction of Gradients	91
7.3	Road Roughness Influence	97
7.4	Geometry Discretization - Blunt vs. Sharp Edge	101
7.5	CFD and Wind Tunnel (1:4) Comparison	105
7.6	Reynolds Number Influence	108
7.7	Wheel Geometry Influence.....	111
7.8	Cooling Inlets Influence	119
7.8.1	Cooling Air Shutter (CAS) Mechanism Influence	119
7.8.2	Influence of Other Cooling Air Inlets	123
7.9	Front-Wheel Spoilers Optimization.....	125
7.10	Side Mirrors Influence and Optimization	128
7.10.1	Side Mirrors Influence – Middle 0° vs. Bottom $+15^\circ$	130
7.10.2	Side Mirrors Influence – Without SM-s vs. Bottom $+15^\circ$	138
8	Recommendations for CFD Method Improvements	146
8.1	Averaging of the Results	146
8.2	Dimensionless Wall Distance (y^+)	147
9	Conclusion	149
	REFERENCES	150
	APPENDIX	152

LIST OF FIGURES

Figure 1.1	treamlines around typical streamlined body (right) and typical bluff body (left), $Re \approx 1 \cdot 10^4$; Pictures S. Hucho [1]	2
Figure 1.2	Flow behind streamlined body (a) and bluff body (b), schematics [1]	3
Figure 1.3	Boundary layer definition [1]	3
Figure 1.4	Share of the two types of resistances (ger. <i>Widerstand</i>) on different types of bodies (ger. <i>Körper</i>): pressure (ger. <i>Druck</i>) and friction (ger. <i>Reibung</i>) aerodynamic resistance [1]	4
Figure 1.5	Low drag vehicle during wind tunnel test (VW XL 1, 2012) [14]	5
Figure 1.6	Development of aerodynamic drag in automotive history [2]	6
Figure 1.7	Coordinate system for aerodynamic forces and moments definition in Automotive aerodynamics	7
Figure 1.8	Definition of reference area (projected area) A_{ref} [1]	9
Figure 1.9	Reference area A_{ref} [2]	9
Figure 1.10	Three different pressure definitions: static pressure, dynamic pressure and total pressure [3]	10
Figure 1.11	a) and b) Measurement of the static pressure [3]	11
Figure 1.12	Total pressure measurement [3]	11
Figure 1.13	Dynamic pressure measurement [3]	12
Figure 1.14	Aerodynamic drag (ger. <i>Widerstand</i> - W) and rolling resistance (R) - depending on vehicle speed, an example with BMW 520i ($CD = 0,27$; $A_{ref} = 2,18m^2$; $m = 1570kg$) [1]	14
Figure 1.15	Relation between aerodynamic drag and rolling resistance [14]	15
Figure 1.16	Different approaches to fuel consumption reduction [14]	16
Figure 2.1	History line of Magna Steyr [17]	18
Figure 2.2	Magna Steyr AG & Co KG, Graz [17]	19
Figure 2.3	Johann Puch (Slovene: <i>Janez Puh</i>) [31]	20
Figure 2.4	The Magna Man by Frank Stronach (book front page) [33]	20
Figure 2.5	Modes of transportation in modern urban areas and resulting CO2 emissions [10]	21
Figure 2.6	a) Fiat 500, 1970 [12], b) Steyr Puch 500 [13]	22
Figure 2.8	Separation of flow on cuboids with different length/width (L/W) ratios [2]	23
Figure 2.7	Aerodynamic drag (ger. C_w) on the bodies with different shape and different length/width ratio (l/d); Barth (1966) [2]	23
Figure 2.9	Aerodynamic drag increase for typical European mass produces vehicles from 1996. to 2010. [14]	24
Figure 2.10	MAGNA Steyr CULT prototype [23]	25
Figure 2.11	Ford Model T	26
Figure 2.12	VW Type 1	26
Figure 3.1	CULT – under-body cover removed. CNG tank (green) is placed in the central tunnel, below body in white. Complete exhaust system is in the engine compartment (grey)	27
Figure 3.2	CULT's front-end air inlets	29
Figure 3.3	a) and b) - Front-end packaging	29

Figure 3.4 Cooling air guides on CULT cooling package	30
Figure 3.5 a) Initial CAC channel, b) Aerodynamically optimized CAC channel	31
Figure 3.6 Left – initial CAC channel, right – new, aerodynamically optimized CAC channel	31
Figure 3.7 a) Air flaps at cooling air inlet, b) Parts of the assembly of CAS mechanism	32
Figure 3.8 Closed and opened position of air flaps	33
Figure 3.9 “Side mirrors” on the CULT	34
Figure 3.10 a), b) and c) - Side mirrors different views	35
Figure 3.11 CULT Front-wheel spoiler (blue)	36
Figure 3.12 Front-wheel spoiler - MINI Countryman	36
Figure 4.1 An example of CFD visualization - streamlines around CULT side mirrors	37
Figure 4.2 An example of CFD visualization: velocity coefficient contours in Y0 section of the vehicle	38
Figure 4.3 Altair Hypermesh working environment	39
Figure 4.4 An example of a surface STL – format mesh, which is used to build a CFD model	40
Figure 4.5 a) – Hole in surface mesh, b) – Hole closed	41
Figure 4.6 a) and b) - Patches for different CULT parts in TGrid	42
Figure 4.7 Y0 section of the car geometry with cooler grid	43
Figure 4.8 CULT wrapper surface: refined and separated on the parts	44
Figure 4.9 Fluid domain boundaries – virtual Wind Tunnel	44
Figure 4.10 Wheels cutting and connection with the ground	45
Figure 4.11 Cut through the three dimensional hybrid grid. Red elements are prisms and the blue ones are tetrahedral elements	46
Figure 4.12 An example of refinement zones in T-Grid	48
Figure 4.13 Y0 section of CULT CFD grid – Fluent Post (borders between refinement zones can be clearly seen)	48
Figure 4.14 Y0 section for CULT CFD grid – TGrid	49
Figure 4.15 ANSYS Fluent working environment	50
Figure 4.16 Virtual Wind Tunnel around car– boundary conditions. Purple plane is defined as a ground, grey plane as an air inlet and the blue plane as an air outlet.	53
Figure 5.1 Aerodynamic coefficients diagram, monitored during simulation – CULT simulation 01	57
Figure 5.2 Geometry overview 3D visualization – CULT simulation 01	58
Figure 5.3 Cut planes definition	59
Figure 5.4 Velocity coefficient visualization in Y0 plane – CULT simulation 01	59
Figure 5.5 Velocity-X coefficient visualization in Y0 plane – CULT simulation 01	60
Figure 5.6 Total pressure coefficient visualization in Y0 plane – CULT simulation 01	61
Figure 5.7 Vorticity magnitude visualization in Y0 plane – CULT simulation 01	62
Figure 5.8 Turbulence kinetic energy visualization in Y0 plane – CULT simulation 01	63
Figure 5.9 Pressure coefficient 3D visualization – three standard views: View 1, View 2, and View 3 – CULT simulation 01	64
Figure 5.10 Wall shear stress 3D visualization – three standard views: View 1, View 2, and View 3 – CULT simulation 01	65

Figure 5.11 Three curves of CULT’s outer surface in Y0 plane used for visualization of C_p values.....	66
Figure 5.12 Pressure coefficient distribution on the upper body – CULT simulation 01	67
Figure 5.13 Pressure coefficient distribution on the under body – CULT simulation 01	67
Figure 5.14 Pressure coefficient distribution on the rear base – CULT simulation 01	68
Figure 5.15 An example of diagram of accumulated force in X-direction (drag force - F_x)..	69
Figure 5.16 An example of diagram of accumulated force in Z-direction (lift force - F_z)	70
Figure 5.17 Example of simulation comparison in F_x accumulated diagrams.	70
Figure 5.18 Red line (ΔdF_x) explanation	71
Figure 6.1 Aerodynamics in a design process of a car	72
Figure 6.3 Aero Scaled Model (ASM) parts	73
Figure 6.2 Aero Scaled Model (ASM) Geometry	73
Figure 6.4 Pressure probes position on the ASM.....	74
Figure 6.5 Pressure probes coordinates in Y0 section plane – CAD coordinate system	74
Figure 6.6 CULT ASM in wind tunnel during test	77
Figure 6.7 ASM wind tunnel test - aerodynamic optimization progress	77
Figure 6.8 Example of pressure probe measurement – CULT wind tunnel 01.....	78
Figure 6.9 Pressure coeff. distribution on the upper body – WT measurement.....	79
Figure 6.10 Pressure coeff. distribution on the under body – WT measurement.....	79
Figure 6.11 Pressure coeff. distribution on the rear base – WT measurement.....	80
Figure 7.1 Default and fine grid settings comparison	83
Figure 7.2 Aerodynamic coefficients diagram – Default grid vs. Fine grid	84
Figure 7.3 Velocity-X coefficient visualization in Y0 plane – CULT simulations 51 and 55.	85
Figure 7.4 Pressure coeff. distribution on the upper body – CULT simulation 51 and 55	85
Figure 7.5 Pressure coeff. distribution on the under body – CULT simulation 51 and 55	86
Figure 7.6 Pressure coeff. distribution on the rear base – CULT simulation 51 and 55.....	86
Figure 7.7 Aerodynamic coefficients diagram – 5 prism layers vs. 10 prism layers	88
Figure 7.8 Pressure coeff. distribution on the upper body – CULT simulation 18 and 17	89
Figure 7.9 Pressure coeff. distribution on the under body – CULT simulation 18 and 17	89
Figure 7.10 Pressure coeff. distribution on the rear base – CULT simulation 18 and 17.....	90
Figure 7.11 Aerodynamic coefficients diagram – Node Based vs. Cell Based Solver.....	92
Figure 7.12 Pressure coeff. distribution on the upper body – CULT simulation 46 and 52	93
Figure 7.13 Pressure coeff. distribution on the under body – CULT simulation 46 and 52	93
Figure 7.14 Pressure coeff. distribution on the rear base – CULT simulation 46 and 52.....	94
Figure 7.15 Turbulence kinetic energy in Z276 plane – CULT simulations 46 and 52.....	94
Figure 7.16 Vorticity magnitude in Z470 plane – CULT simulations 46 and 52	95
Figure 7.17 Wall shear stress 3D visualization – CULT simulations 46 and 52	95
Figure 7.18 Aerodynamic coefficients diagram – Road roughness influence	97
Figure 7.19 Pressure coeff. distribution on the upper body – CULT simulation 12 and 15	98
Figure 7.20 Pressure coeff. distribution on the under body – CULT simulation 12 and 15	98
Figure 7.21 Pressure coeff. distribution on the rear base – CULT simulation 12 and 15.....	99
Figure 7.22 Total pressure coefficient in Y0 plane – CULT simulations 12 and 15	99
Figure 7.23 Total pressure coefficient in Z470 plane – CULT simulations 12 and 15.....	100
Figure 7.24 Turbulence kinetic energy in Z276 plane – CULT simulations 12 and 15.....	100

Figure 7.25 Observed edge – trailing edge of the under body (beginning of rear diffuser) ..	101
Figure 7.26 Aerodynamic coefficients diagram – Blunt edge vs. Sharp edge	102
Figure 7.27 Velocity-X coefficient in Y0 plane – CULT simulations 47 and 46	103
Figure 7.28 Total pressure coefficient in Y0 plane – CULT simulations 47 and 46	103
Figure 7.29 Aerodynamic coefficients diagram – CULT basic simulation, CAS open.....	105
Figure 7.30 Pressure coeff. distribution on the upper body – WT and CFD sim. 51.....	106
Figure 7.31 Pressure coeff. distribution on the under body – WT and CFD sim. 51.....	106
Figure 7.32 Pressure coeff. distribution on the rear base – WT and CFD sim. 51	107
Figure 7.33 Aerodynamic coefficients diagram – Different air inlet speeds, MOCK UP	108
Figure 7.34 Pressure coeff. distribution on the upper body – WT and CFD (different air speeds).....	109
Figure 7.35 Pressure coeff. distribution on the under body – WT and CFD (different air speeds).....	109
Figure 7.36 Pressure coeff. distribution on the rear base – WT and CFD (different air speeds)	110
Figure 7.37 CULT type wheels	111
Figure 7.38 ASM type wheels.....	111
Figure 7.39 CULT Aero Scaled Model (ASM) geometry.....	112
Figure 7.40 ASM vs. CULT wheels – position comparison	112
Figure 7.41 Aerodynamic coefficients diagram – ASM wheels vs. CULT wheels	113
Figure 7.42 Pressure coeff. distribution on the upper body – ASM vs. CULT wheels	114
Figure 7.43 Pressure coeff. distribution on the under body – ASM vs. CULT wheels	114
Figure 7.44 Pressure coeff. distribution on the rear base – ASM vs. CULT wheels	115
Figure 7.45 Velocity-X coefficient in Y0 plane – ASM wheels vs. CULT wheels.....	115
Figure 7.46 Total pressure coefficient in Y0 plane – ASM wheels vs. CULT wheels	116
Figure 7.47 Vorticity magnitude in Y0 plane – ASM wheels vs. CULT wheels.....	116
Figure 7.48 Wall shear stress 3D visualization – ASM wheels vs. CULT wheels	117
Figure 7.49 Pressure coefficient 3D visualization – ASM wheels vs. CULT wheels.....	117
Figure 7.50 CAS closed and CAS open definition.....	119
Figure 7.51 Aerodynamic coefficients diagram – CAS closed vs. CAS open.....	120
Figure 7.52 Pressure coeff. distribution on the upper body – CAS closed vs. CAS open	121
Figure 7.53 Pressure coeff. distribution on the under body – CAS closed vs. CAS open	121
Figure 7.54 Pressure coeff. distribution on the rear base – CAS closed vs. CAS open.....	122
Figure 7.55 Position of the CAC air inlet and Cooling inlet upper.....	123
Figure 7.56 Aerodynamic coefficients diagram – CAS closed vs. Full MOCK UP.....	124
Figure 7.57 Front-wheel spoilers – three investigated positions.....	125
Figure 7.58 Aerodynamic coefficients diagram – front-wheel spoilers position influence ...	126
Figure 7.59 Front-wheel spoilers influence - aerodynamic drag	126
Figure 7.60 Front-wheel spoiler wake sketch	127
Figure 7.61 Three different side mirror’s positions	128
Figure 7.62 Three different side mirror’s incidence angles (angles of attack).....	128
Figure 7.64 Aerodynamic coefficients diagram – Side Mirrors Middle 0° vs. Bottom +15°	130
Figure 7.63 a) Basic position – Middle 0°, b) Best case position – Bottom +15°	130
Figure 7.65 Total pressure coefficient in Y0 plane – SM-s Middle 0° vs. Bottom +15°.....	131

Figure 7.66 Vorticity magnitude in Y0 plane – SM-s Middle 0° vs. Bottom +15°	131
Figure 7.67 Vorticity magnitude in Z815 plane – SM-s Middle 0° vs. Bottom +15°	132
Figure 7.68 Turbulence kinetic energy in Z815 plane – SM-s Middle 0° vs. Bottom +15° ..	132
Figure 7.69 Wall shear stress 3D visualization - SM-s Middle 0° vs. Bottom +15°	133
Figure 7.70 Veloc. coeff. streamlines in isometric view – SM-s Middle 0° vs. Bottom +15°	133
Figure 7.71 Veloc. coeff. streamlines in side view – SM-s Middle 0° vs. Bottom +15°	134
Figure 7.72 Pressure coeff. distribution on the upper body – SM-s Middle 0° vs. Bottom +15°	134
Figure 7.73 Pressure coeff. distribution on the under body – SM-s Middle 0° vs. Bottom +15°	135
Figure 7.74 Pressure coeff. distribution on the rear base – SM-s Middle 0° vs. Bottom +15°	135
Figure 7.75 F_x accumulated diagram – SM-s Middle 0° vs. Bottom +15°	136
Figure 7.76 F_z accumulated diagram – SM-s Middle 0° vs. Bottom +15°	136
Figure 7.78 Aerodynamic coefficients diagram – without SM-s vs. Bottom +15°	138
Figure 7.77 a) Geometry case without side mirrors, b) Best case position – Bottom +15° ...	138
Figure 7.79 Total pressure coefficient in Y0 plane – without SM-s vs. Bottom +15°	139
Figure 7.80 Vorticity magnitude in Y0 plane – without SM-s vs. Bottom +15°	139
Figure 7.81 Vorticity magnitude in Z815 plane – without SM-s vs. Bottom +15°	140
Figure 7.82 Turbulence kinetic energy in Z815 plane – without SM-s vs. Bottom +15°	140
Figure 7.83 Wall shear stress 3D visualization – without SM-s vs. Bottom +15°	141
Figure 7.84 Veloc. coeff. streamlines in isometric view – without SM-s vs. Bottom +15° ..	141
Figure 7.85 Veloc. coeff. streamlines in side view – without SM-s vs. Bottom +15°	142
Figure 7.86 Pressure coeff. distribution on the upper body – without SM-s vs. Bottom +15°	142
Figure 7.87 Pressure coeff. distribution on the under body – without SM-s vs. Bottom +15°	143
Figure 7.88 Pressure coeff. distribution on the rear base – without SM-s vs. Bottom +15° ..	143
Figure 7.89 F_x accumulated diagram – without SM-s vs. Bottom +15°	144
Figure 7.90 F_z accumulated diagram – without SM-s vs. Bottom +15°	145
Figure 8.1 Drag coefficient (CD) data from CFD simulation – CULT simulation 01	146
Figure 8.2 Dimensionless velocity (u +) in a function of dimensionless distance (y +) [30]	147
Figure 8.3 Wall y +3D visualization – three standard views: View 1, View 2, and View 3 – CULT simulation 01	148

LIST OF TABLES

Table 4.1 Grid settings overview for CULT simulation 01	54
Table 4.2 Numerical and physical settings overview for CULT simulation 01	54
Table 5.1 An example of simulation data stored in Microsoft Excel.....	56
Table 5.2 An example of simulation results in Microsoft Excel.....	56
Table 7.1 CULT – all simulations overview	82
Table 7.2 Aerodynamic coeff. – simulations 51 and 55 (avg. values for last 200 iter.)	84
Table 7.3 Prism layer settings for 5 and 10 prism layers grid.....	87
Table 7.4 Aerodynamic coeff. – simulations 18 and 17 (avg. values for last 200 iter.)	88
Table 7.5 Aerodynamic coeff. – simulations 46 and 52 (avg. values for last 200 iter.)	92
Table 7.6 Aerodynamic coeff. – simulations 12 and 15 (avg. values for last 200 iter.)	97
Table 7.7 Aerodynamic coeff. – simulations 47 and 46 (avg. values for last 200 iter.)	102
Table 7.8 Aerodynamic coefficients – sim. 51 (avg. values for last 200 iter.)	105
Table 7.9 Aerodynamic coefficients – CFD basic and WT basic (CAS open).....	105
Table 7.10 Aerodynamic coefficients – CULT CFD simulations (MOCK UP).....	108
Table 7.11 Aerodynamic coefficients – ASM WT measurement (MOCK UP)	108
Table 7.12 Aerodynamic coefficients – ASM wheels vs. CULT wheels (avg. val. for last 200 iter.)	113
Table 7.13 Aerodynamic coeff. – simulations 12 and 17 (avg. values for last 200 iter.)	120
Table 7.14 CAS influence – wind tunnel measurement.....	120
Table 7.15 CAS influence – CFD simulation	120
Table 7.16 Aerodynamic coeff. – simulations 12 and 14 (avg. values for last 200 iter.)	124
Table 7.17 Aerodynamic coefficients – FWS-s influence (avg. values for last 200 iter.)	126
Table 7.18 Side mirrors position influence – results.....	129
Table 7.19 Aerodynamic coeff. – simulations 12 and 32 (avg. values for last 200 iter.)	130
Table 7.20 Aerodynamic coeff. – simulations 16 and 32 (avg. values for last 200 iter.)	138

ABBREVIATIONS

2D	Two Dimensional
3D	Three Dimensional
AOA	Angle Of Attack (Incidence Angle)
ASM	Aero Scaled Model
CAC	Charge Air Cooler
CAD	Computer Aided Design
CAS	Cooling Air Shutter
CFD	Computational Fluid Dynamics
CNG	Compressed Natural Gas
CO ₂	Carbon dioxide
COUNT	Thousandth part of aerodynamic coefficient C_D and C_z
CPU	Central Processing Unit
CULT	Cars' Ultra Light Technologies
FWS	Front-Wheel Spoiler
NACA	National Advisory Committee for Aeronautics
OEM	Original Equipment Manufacturer
STL	Surface Tessellation Language
UBC	Under Body Cover (also used German <i>UBV</i>)
WCP	Without Cooling Package
WT	Wind Tunnel

NOMENCLATURE

Symbol:	Unit (SI):	Description:
$ \vec{\omega} $	1/s	Vorticity magnitude
A_{ref}	m ²	Referent area of the vehicle
C_D	-	Drag coefficient
C_{my}	-	Momentum coefficient
C_p	-	Pressure coefficient
C_{ptot}	-	Total pressure coefficient
Cv_x	-	Velocity-X coefficient
C_z	-	Lift coefficient
C_{zf}	-	Lift coefficient on the vehicle's front axis
C_{zr}	-	Lift coefficient on the vehicle's rear axis
F_x	N	Drag force
F_z	N	Lift force
L_{ref}	-	Referent length of the vehicle
M_y	N/m	Momentum around y axis
P_x	W	Aerodynamic drag power
p_∞	Pa	Free stream pressure
p_{abs}	Pa	Absolute pressure
p_{stat}	Pa	Static pressure
p_{tot}	Pa	Total pressure
q_∞	Pa	Free stream dynamic pressure
u^+	-	Dimensionless velocity
u_i'	m/s	Turbulent fluctuations
u_τ	m/s	Shear (friction) velocity
v_∞	m/s	Free stream air speed
y^+	-	Dimensionless wall distance
μ_∞	kg/ms	Dynamic viscosity
ρ_∞	kg/m ³	Free stream air density
τ_w	Pa	Wall shear stress
Cv	-	Velocity coefficient
M	mach	Mach number
Re	-	Reynolds number
d	m	Vehicle's width
k	J/kg	Turbulence kinetic energy
l	m	Vehicle's length
p	Pa	Relative pressure
q	Pa	Dynamic pressure

Symbol:	Unit (SI):	Description:
t	°C	Temperature
v	m/s	Air speed
y	m/s	Velocity
β	°	Yaw angle
δ	m	Boundary layer thickness
ρ	kg/m ³	Air density

SUMMARY

This thesis is a part of the project CULT (Cars' Ultra Light Technologies), carried out by the company Magna Steyr, Graz, Austria. The CULT vehicle is a small city car, belonging to the A-segment vehicles with 4 seats. The main idea of the project is to develop a realistic, production-ready vehicle with CO₂ emissions of only 49g/km. In order to achieve this goal, large efforts in aerodynamics development are inevitable, especially the aerodynamic drag should be as low as possible.

Main objective in this thesis is to investigate various drag reduction devices for A-segment vehicles. One example are side mirrors (rear-view mirrors), which are designed with the idea influencing the flow at the back of the car and reducing aerodynamic losses in the wake behind the car.

Investigation work in this thesis is carried out with the help of Computational Fluid Dynamics (CFD) and numerical results are validated against the results from the wind-tunnel measurements. In the last decades CFD has become very popular engineering tool in automotive industry. In early stages of vehicle development CFD offers clear advantages compared to the classic wind tunnel testing. Smart and parallel usage of these two methods represents a successful formula for good aerodynamic optimization, not only in automotive industry but also in other branches of modern engineering.

Another objective of this thesis is to show the complete CFD process in automotive aerodynamics – from design of CAD surfaces to the analysis of CFD results. Understanding of this process is very important for the correct application of CFD in design and development of new cars, especially for a young engineer starting his/her professional career in automotive industry.

Analysis of numerical and experimental results in this investigation showed that considerable drag reduction can be achieved with only small changes of vehicle geometry. Referring to the example above, it was proved that side mirrors can serve as drag reduction devices.

Key words: aerodynamics, drag reduction, CFD, automotive design, city car, A-segment, wind tunnel, scaled model, side mirrors

PROŠIRENI SAŽETAK (eng. Extended summary - Croatian)

Ovaj diplomski rad je dio projekta CULT (eng. *Cars' Ultra Light Technologies*), kompanije Magna Steyr iz Graza (Austrija). Od rujna 2012. do svibnja 2013. cjelokupnu pripremu, sve simulacije i post-procesiranje podataka odradio sam u razvojnom centru kompanije Magna Steyr u Grazu, gdje sam bio na praksi u trajanju od 9 mjeseci. Budući da je rad u cijelosti napisan na engleskom jeziku, napisan je ovaj prošireni sažetak na hrvatskome jeziku koji nudi pregled cijeloga rada. Sažetak je podijeljen na poglavlja, na isti način kako je pisan sam rad.

Ideja projekta CULT je razviti realističan mali gradski automobil (A-segment cestovnih vozila) spreman za proizvodnju, s emisijom CO₂ od samo 49g/km. Da bi se to postiglo otpor zraka mora biti što je moguće manji, što znači velike napore u razvoju, posebno u području aerodinamike.

Ovaj diplomski rad je dio razvojnog procesa u području aerodinamike u projektu CULT. Glavni zadatak diplomskoga rada su uređaji za smanjenje aerodinamičkog otpora zraka za vozila koja pripadaju A-segmentu. Ti uređaji služe kako bi utjecali na strujanje zraka oko vozila s ciljem smanjenja aerodinamičkog otpora. Na vozilu CULT nalazi se nekoliko takvih uređaja, koje je potrebno optimirati. Jedan primjer su bočna osvrtna zrcala – retrovizori, koji su oblikovani na način da utječu na strujanje zraka iza automobila smanjujući aerodinamičke gubitke u vrtložnom tragu. Konstrukcija retrovizora opisana je u poglavlju 3., a njihova optimizacija u poglavlju 7.

Istraživanje u ovome radu je napravljeno pomoću CFD-a (eng. *Computational Fluid Dynamics* – Računalna dinamika fluida), te su numerički rezultati su uspoređeni i potvrđeni s mjerenjima u zračnom tunelu.

Drugi zadatak rada je prikazati cjelokupni proces aerodinamičke optimizacije pomoću CFD-a u automobilskoj industriji – od CAD površina do analize CFD rezultata.

Analiza numeričkih i eksperimentalnih rezultata u ovom istraživanju je pokazala da se značajno smanjenje aerodinamičkog otpora može postići sa samo malim izmjenama na geometriji automobila. Pozivajući se na primjer iznad, dokazano je da retrovizori mogu služiti kao uređaji za smanjenje aerodinamičkog otpora zraka.

Ključne riječi: aerodinamika, smanjenje otpora zraka, CFD, vozila, automobili, A-segment, gradski automobil, zračni tunel, umanjeni model, retrovizori

1. Uvod (eng. *Introduction*)

Cilj uvoda rada je upoznati čitatelja s aerodinamikom automobila i njenom važnosti u automobilskoj industriji. Svakodnevno povećanje ekološke svijesti u svijetu postavlja automobilskoj industriji do sada najveće izazove u povijesti. Zajedno s razvojem tehnologije otvorene su razne nove mogućnosti u konstruiranju automobila, gdje aerodinamika dobiva sve veće značenje.

Da bi se razumjela kompleksnost aerodinamike automobila treba početi s razumijevanjem aerodinamike tupih tijela (eng. *Bluff Body*). Tupa tijela nisu aerodinamički oblikovana i strujanje zraka oko njih se znatno razlikuje u usporedbi s aerodinamički oblikovanim tijelima (eng. *streamlined bodies*), kao što su npr. avioni. U radu su kratko i jednostavno objašnjene bitne pojave vezane za aerodinamiku tupih tijela – geometrija tijela, strujanje zraka oko tijela, granični sloj i sile koje djeluju na tijelo.

Nakon što su opisane osnove aerodinamike tupih tijela nastavlja se dalje s aerodinamikom automobila, koja je jedno posebno područje aerodinamike. Osim karakterističnog tupog oblika automobila (u većini slučajeva), ono što aerodinamiku automobila čini posebnom je utjecaj tla. Cestovna vozila su preko kotača u stalnoj vezi s tlom, te tlo i kotači značajno utječu na strujanje zraka oko vozila.

Da bi se bolje razumio utjecaj aerodinamike na razvoj komercijalnih automobila dan je kratak povijesni pregled aerodinamike cestovnih vozila. Pitanje implementacije trenutnog stupnja razvoja aerodinamike (a i tehnike općenito) nije samo pitanje raspoloživog znanja i tehnologije, nego je to rezultat kompleksnog utjecaja tržišnih potreba i trenutnih svjetskih trendova.

Kako kasnije ne bi došlo do nesporazuma, u nastavku su pojašnjene sve osnovne fizikalne veličine koje će se kasnije koristiti – sile, momenti, koeficijenti. Budući da postoje razni nazivi i oznake vezane za tlak, odlučeno je ovdje staviti sve nazive i oznake na jedno mjesto, te ih definirati. Na taj način izbjeći će se eventualni nesporazumi, kada se uđe dublje u samu temu.

Da bi se bolje razumjela povezanost aerodinamike i potrošnje goriva dano je kratak objašnjenje i podjela otpora vožnje automobila. Prikazan je udio aerodinamičkog otpora u ukupnim otporima vožnje i objašnjena je posebna važnost aerodinamike prilikom vožnje velikim brzinama.

Nadalje, budući da se razvoj aerodinamike odvija u jednom kompleksnom sustavu cjelokupnog razvoja, proizvodnje i prodaje automobila (tržišta automobila), ideja je predočiti čitatelju koliko suradnje je potrebno između različitih timova u automobilskoj industriji kako bi se u konačnici proizvelo aerodinamički napredno vozilo.

2. Magna Steyr – CULT

Nakon što su u uvodu dane informacije vezane za aerodinamiku automobila, cilj ovog poglavlja je pružiti čitatelju informacije o kompaniji Magna Steyr, specifičnosti aerodinamike malih gradskih automobila (A-segment) i samog projekta CULT.

Kompanija Magna Steyr je najveći nezavisni svjetski OEM (eng. *Original Equipment Manufacturer* – proizvođač originalnih dijelova) proizvođač u automobilskoj industriji. Drugim riječima, tvrtka Magna Steyr razvija i proizvodi automobile za najveće svjetske brendove u automobilskoj industriji.

Iz novih zahtjeva na tržištu pojavio se je i koncept malog gradskog automobila. Osnovna ideja takvog automobila je mobilnost u urbanim sredinama, te vrlo niska emisija ugljikovog dioksida (CO₂). Upravo jedan takav automobil je automobil CULT. Automobil CULT pripada A-segmentu vozila s 4 sjedala. A-segment vozila, definiran od strane europske komisije, je najmanja klasa cestovnih automobila, do duljine 3600mm. Zovu se još i mali gradski automobili ili mini automobili. Cilj projekta CULT je razviti automobil s najmanjom emisijom CO₂ u klasi i 300kg manje mase od konkurencije.

3. Aerodinamička optimizacija vozila CULT (eng. *Aerodynamic Optimization of CULT vehicle*)

U ovome poglavlju su opisane specifičnosti vezane za konstrukciju automobila CULT, s naglaskom na dijelove vezane za aerodinamiku. Budući da se za gorivo pogonskog agregata koristi zemni plin, važan dio u konstrukciji CULT-a je spremnik zemnog plina, koji je pozicioniran ispod vozila u tunelu koji povezuje prednji i stražnji dio automobila. Osim toga, kompletan ispušni sustav se nalazi na prednjoj strani u prostoru motora, što omogućava jednostavniju konstrukciju poklopaca na podvozju. Koristeći poklopce na podvozju dobiva se glatko podvozje što omogućava bolji protok zraka ispod automobila (manje vrtloženja i gubitaka).

Važno dio vezan za aerodinamiku vozila je paket hlađenja – njegovo pozicioniranje i brtvljenje. Sustavu hlađenja je potrebna određena količina protoka zraka kako bi mogao funkcionirati. Ako je količina zraka nedovoljna, postoji opasnost od pregrijavanja. Isto tako, ako je količina zraka prevelika usmjeravaju se nepotrebne količine zraka kroz hladnjake i u prostor oko motora te se tako povećavaju aerodinamički gubici u strujanju zraka. Iz toga je razloga na CULT vozilu sustav dovoda zraka pažljivo optimiran, koristeći uvodnike zraka i aerodinamički optimiziran zračni kanal za hlađenje hladnjaka prednabijanja. Novitet u ovom dijelu je aktivni mehanizam dovoda zraka za hlađenje (eng. *active Cooling Air Shutter mechanism* – CAS). Ideja mehanizma je spriječiti protok zraka kroz hladnjake kada on nije potreban i tako smanjiti aerodinamički otpor. Utjecaj CAS mehanizma na aerodinamiku automobila je istražen u poglavlju 7.

Osim CAS-a, na automobilu su još dva uređaja za smanjenje otpora zraka: retrovizori (bočna osvrtna zrcala) i spojleri prednjih kotača. Retrovizori nisu klasična zrcala, nego se umjesto

zrcala koriste kamere. Iako se radi o kamerama, tijekom rada, zbog jednostavnosti, koristi se konvencionalni termin „bočna zrcala“ (eng. *side mirrors*), a u ovom sažetu se koristi uobičajeni termin u hrvatskoj – retrovizori. Zanimljivost kod CULT-ovih retrovizora je nosač kamere koji je oblikovan poput avionskog krila (korišten je aerodinamički profil NACA 0012). Cilj je bio dobiti oblik retrovizora koji će imati što manji otpor zraka. Na kraju poglavlja opisani su spojleri kotača, koji su u automobilskoj industriji već dobro poznati uređaj za smanjenje aerodinamičkog otpora zraka.

4. CFD (eng. *Computational Fluid Dynamics* – Računalna dinamika fluida)

Ideja ovog poglavlja je opisati način korištenja CFD-a za pripremu i pokretanje aerodinamičke simulacije u automobilskoj industriji. Teoretska pozadina CFD-a ovdje nije tema, nego samo njegova primjena. CFD proces podijeljen je u 3 dijela: pre-procesiranje, procesiranje i post-procesiranje. Pre-procesiranje se odnosi na pripremu simulacije, procesiranje je postavljanje i pokretanje simulacije, a post-procesiranje se odnosi na obradu podataka dobivenih simulacijom.

Za pripremu simulacije korišteni su softveri Altair HyperMesh i Ansys TGrid. HyperMesh je program za pripremu i kreiranje 2-D mreže koja predstavlja geometriju automobila. Nakon pripreme geometrije automobila, ta se geometrija koristi kao početna površina u programu TGrid. U TGrid-u se kreira konačna geometrije automobila kao jedna površina (2-D mreža) koja će biti korištena kao osnova za kreiranje 3-D CFD rešetke. U poglavlju su opisani svi osnovne koraci na koje treba obratiti pažnju prilikom izrade rešetke. Osim toga, cjelokupan tekstu je popraćen savjetima koji mogu biti vrlo korisni, posebno početnicima.

Bitno je naglasiti da postoje dvije vrste elemenata koje su u ovome radu korišteni za izgradnju CFD rešetke – prizmatični elementi i tetraedarski elementi. Prizmatični elementi daju točnije rezultate u blizini površine tijela, gdje viskozne sile igraju važnu ulogu. Međutim, prizmatični elementi tvore strukturiranu rešetku i vrlo je teško napraviti takvu rešetku na složenoj 3-D geometriji. Suprotno od toga, tetraedarski elementi su numerički gledano manje točni, ali tvore nestrukturiranu rešetku koja omogućava puno jednostavniju izgradnju same rešetke.

Nakon što je CFD rešetka dovršena, rešetka se učitava u softver Ansys Fluent. Fluent je softver namijenjen za drugi dio CFD procesa – procesiranje. U ovome dijelu je opisan postupak podešavanja simulacije prije samog pokretanja. Također su dani numerički i fizikalni parametri simulacije. Ti parametri su standardizirani unutar odjela za Aerodinamiku u kompaniji Magni Steyr (dio njih je i općeprihvaćen unutar aerodinamike automobila u cijelom svijetu).

5. Post-procesiranje (eng. *Post-Processing*)

Post-procesiranje podataka dobivenih simulacijom je najzahtjevnija i najizazovnija faza u cijelom procesu i u nju treba uložiti puno vremena, truda i pažnje. Zbog velikog broja simulacija, kako bi se omogućila jednostavnija, brža i kvalitetnija obrada podataka uvedeni su posebni standardi u ovu fazu. Svaka kreirana datoteka, svaki zapis u njoj, svaka vizualizacija, dijagram i tablica su standardizirani.

Što se sve izradi tijekom standardizirane obrade podataka prikazano je u ovome poglavlju na primjeru osnovne (bazne) simulacije – CULT simulation 01. Rezultati se sastoje od tablica s postavkama i osnovnim rezultatima, dijagrama aerodinamičkih veličina i vizualizacija.

Prva vizualizacija je geometrija automobila, koja služi za provjeru geometrije, budući da se prilikom ispitivanja geometrija mijenja od simulacije do simulacije. Daljnje vizualizacije se odnose na vizualizacije strujanja koje se mogu vizualizirati u nekoj ravnini ili na nekoj površini. Za vizualizacije u ravninama odabrane su četiri standardne ravnine. U svakoj od tih ravnina prikazane su vizualizacije koeficijenta brzine strujanja zraka, koeficijenta brzine strujanja zraka u X smjeru, koeficijent totalnog tlaka, veličina vrtloženja i turbulentna kinetička energija. Svaka od tih veličina opisana je u poglavlju uz priloženu sliku, koja je rezultat simulacije broj 1 (CULT simulation 01).

Osim u ravnini, prikazane su i 3D vizualizacije na površini automobila. Prikazan je koeficijent tlaka i smično naprezanje. Koeficijent tlaka prikazuje na kojim dijelovima se stvaraju sile otpora zraka vezane za tlak, a smično naprezanje prikazuje gdje nastaje otpor zraka vezan uz trenje između vozila i struje zraka. Te dvije vizualizacije zajedno obuhvaćaju obje vrste otpora zraka (otpor zraka uzrokovan tlakom i trenjem).

Prilikom mjerenja u zračnom tunelu korišteni su senzori tlaka, koji su raspoređeni po sredini automobila (Y0 ravnina). Kako bi se rezultati dobiveni mjerenjima na tim sensorima mogli usporediti s računalno dobivenim rezultatima, potrebno je prilikom post-procesiranja napraviti dijagrame koji će to omogućiti. Iz tog razloga su uvedeni dijagrami raspodjele koeficijenta tlaka. Ti dijagrami prikazuju raspodjelu koeficijenta tlaka u Y0 ravnini. Postoje tri različita dijagrama, svaki dijagram prikazuje rezultate na određenom području automobila – gornji dio, podvozje, stražnji dio. Definicija područja prikazana je na slici 5.11. Kasnije su se ti dijagrami pokazali korisnima i za međusobnu usporedbu CFD simulacija, iz razloga što je često lakše uspoređivati rezultate prikazane dijagramom, nego uspoređivati dvije vizualizacije (slike).

Na kraju ovog poglavlja prikazani su i objašnjeni dijagrami koji prikazuju akumuliranu aerodinamičku silu na automobil. Postoje dvije vrste dijagrama, jedan prikazuje silu u smjeru osi X (otpor zraka), a drugi u smjeru osi Z (uzgon). Ova vrsta dijagrama je vrlo dobra za usporedbu dvije simulacije s različitom geometrijom, što će se kasnije iskoristiti u poglavlju 7 kada se budu uspoređivali različiti položaji retrovizora.

6. Umanjeni model za zračni tunel (eng. *Wind tunnel scaled model*)

U ranoj fazi projekta ne postoji realno vozilo (prototip) i iz tog razloga jedina mogućnost za aerodinamičko ispitivanje je korištenje CFD-a. Međutim, postoji mogućnost izrade pojednostavljenog umanjenom modela za aerodinamičko ispitivanje u zračnom tunelu. Njegova svrha je provjera rezultata dobivenih CFD-om i stvaranje referentnih točaka u ranoj fazi projekta, potrebnih za daljnji razvoj. Umanjeni model korišten u projektu CULT je u omjeru 1:4 (25% veličine realnog modela).

Ovo poglavlje opisuje prednosti korištenja umanjenog modela, te detaljno opisuje umanjeni model automobila CULT (Cult ASM). Osim toga prikazuje osnovne parametre potrebne za podešavanje mjerenja u zračnom tunelu, te rezultate mjerenja dobivenih mjerenjem na umanjenom modelu automobila CULT. Na kraju poglavlja opisan je način obrade podataka dobivenih mjerenjima pomoću senzora tlaka postavljenima na vozilo. Kako bi se rezultati mjerenja tlaka mogli usporediti s CFD-om, preračunati su u koeficijent tlaka i prikazani pomoću tri različita dijagrama (na isti način kao i prilikom post-procesiranja rezultata simulacija).

7. Analiza i provjera rezultata (eng. *Analysis & Validation of the Results*)

Ukupno je za potrebe ovog rada napravljeno 57 simulacija. 55 simulacija je prikazano u tablici 7.1, a ostale dvije simulacije, sa drugačijom osnovnom geometrijom, obrađene su odvojeno u nastavku poglavlja. Tablica 7.1. je vrlo važna iz razloga što sadrži osnovne podatke i rezultate od 55 simulacija. Pomoću nje je moguća gruba usporedba bilo koje dvije ili više simulacija. Postoje dvije osnovne simulacije, simulacija broj 1 i simulacija broj 12. Simulacija broj 1 je s otvorenim CAS mehanizmom, a simulacija broj 12 je s zatvorenim CAS mehanizmom.

Poglavlje 7 sadrži 10 potpoglavlja – svako potpoglavlje obrađuje jedan problem. Na početku poglavlja je važno uvesti termin eng. „*COUNT*“ (hrv. bod). Count je tisućiti dio aerodinamičkog koeficijenta. Ako se npr. uspoređuju dva aerodinamička koeficijenta – $C_d = 0.322$ i $C_d = 0.318$, može se reći da je razlika između ta dva koeficijenta 4 COUNT-a. Taj termin je u uobičajenoj primjeni u aerodinamici automobila, te olakšava komunikaciju, što je vrlo važno za analizu rezultata.

Utjecaj CFD rešetke

Cilj ovog poglavlja je usporediti postavke vezane za finoću mreže (broja elemenata). Jedan dio poglavlja ispituje utjecaj broja tetraedarskih elemenata na rezultate, a drugi dio poglavlja ispituje utjecaj količine slojeva prizmatičnih elemenata. Cilj ovih ispitivanja je provjeriti da li su standardne postavke za kreiranje CFD rešetke dovoljno dobro definirane. Na kraju je zaključeno da u odnosu na osnovne postavke, simulacije s većim brojem elemenata ne pokazuju zamjetno drugačije rezultate, što navodi na to da su standardne postavke zadovoljavajuće.

Utjecaj Solvera – Cell-Based naprotiv Node-Based rekonstrukcije gradijenata (eng. *Solver Influence – Cell-Based vs. Node-based Reconstruction of Gradients*)

U softveru Fluent postoje dvije metode ocjene (izračuna) gradijenata: Green-Gauss Cell-Based ocjena gradijenata i Green-Gauss Node-Based ocjena gradijenata (eng. *Cell* – ćelija, eng. *Node* – točka). Cell-Based metoda ocjenjuje gradijent pomoću aritmetičke sredine vrijednosti u centru susjednih ćelija. S druge strane, Node-Based metoda ocjenjuje vrijednost gradijenata pomoću aritmetičke sredine vrijednosti susjednih točaka na stranici elementa (eng. *face*). Za Node-based metodu je poznato da je točnija od standarde Cell-based metode, kada su u pitanju nestrukturirane rešetke, posebno tetraedarske. U poglavlju je istraženo da li je ta tvrdnja točna, odnosno da li to vrijedi za tip rešetke korištene u ovome radu. Na kraju je zaključeno da je Node-Based metoda ocjene gradijenata točnija u usporedbi sa Cell-Based metodom, naravno kada se radi o tipu rešetke kakva je korištena u ovome radu.

Utjecaj hrapavosti ceste (eng. *Road Roughness Influence*)

Već je rečeno kako tlo ima veliki utjecaj na aerodinamiku automobila. Iz tog razloga potrebno je točno definirati svojstva ceste (tla) u postavkama simulacije. Standardna postavka je hrapavost ceste u iznosu 0.5 m, što je određeno u prijašnjim projektima i potvrđeno mjerenjima u zračnom tunelu. U ovom poglavlju napravljena je usporedba dvije simulacije, jedna simulacija sa standardnom hrapavosti ceste, a druga simulacija gdje je hrapavost ceste 0.0 m (glatka cesta). Usporedba je pokazala da hrapavost ceste ima velik utjecaj na strujanje zraka, što potvrđuje da vrijednost hrapavosti ceste treba pažljivo odabrati.

Diskretizacija geometrije – Tupi rub naprotiv oštrog ruba (eng. *Geometry Discretization – Blunt vs. Sharp Edge*)

Geometrija automobila korištenjem softvera TGrid se može kreirati na način da se oštri rubovi zadrže (teži i sporiji način) ili da se oštri rubovi zatupe (lakši i brži način). Ovo poglavlje istražuje da li je uloženi trud i vrijeme u kreiranje oštrog ruba opravdano. Za istraživanje je odabran rub koji se nalazi na podvozju automobila u blizini stražnjeg difuzora. Taj rub je zanimljiv iz razloga što na tome području geometrija ima nagli prijelaz, pa je pretpostavljeno da bi utjecaj kvalitete ruba trebao biti izraženiji nego na drugim mjestima.

Zaključeno je da je na određenim mjestima (kao npr. rub promatran u ovom poglavlju) uloženi trud i vrijeme za kreiranje oštrog ruba opravdano jer donosi stabilnost u simulaciju (simulacija ranije konvergira). Iz tog razloga, prilikom kreiranja geometrije automobila potrebno je rubove razvrstati na važne i nevažne, te se važnim rubovima treba pridodati pažnja i pripaziti da ostanu oštri.

Usporedba CFD-a i zračnog tunela (eng. *CFD and Wind Tunnel Comparison*)

U zračnom tunelu se mjere dvije fizikalne veličine: aerodinamička sila i tlak na površini automobila (pomoću senzora tlaka). Te veličine se mogu usporediti s rezultatima CFD simulacije. Rezultati pokazuju da se strujanje zraka razlikuje, odnosno rezultati se ne podudaraju. Najveće razlike su na stražnjem dijelu podvozja i na stražnjem kraju automobila. Raspored tlaka na stražnjem kraju (eng. *Rear base*) je potpuno drugačiji. Budući da se ovdje uspoređuje CFD geometrija koja je u realnoj veličini (omjer 1:1) i geometrija umanjenog modela (omjer 1:4), postoji opravdana sumnja da je ponašanje strujanja zraka različito upravo iz tog razloga. Druga opravdana sumnja je to što su kotači različiti – CFD koristi dizajn kotača s aluminijskim naplaticima, a zračni tunelu koristi dizajn čeličnih naplataka. Osim dizajna postoji i razlika u veličini kotača. Zadatak slijedeća dva poglavlja je istražiti i pronaći pravi uzrok nejednakosti rezultata.

Utjecaj Reynoldsova broja (eng. *Reynolds Number Influence*)

Ponašanje strujanja zraka je usko povezano s Reynoldsovim brojem. Reynoldsov broj ovisi (između ostalog) o brzini strujanja zraka. Ako se mijenja brzina strujanja, mijenja se i vrijednost Reynoldsovog broja. Cilj ovog poglavlja je vidjeti koliko vrijednost Reynoldsovog broja, odnosno brzina strujanja zraka, utječe na konačni rezultat. Uspoređene su CFD simulacije s brzinom strujanja od 70 km/h, 140 km/h i 280 km/h, te mjerenja u zračnom tunelu pri brzini od 140 km/h i 280 km/h.

Zaključak je da Reynoldsov broj ne utječe u velikoj mjeri na rezultate, te ne može biti uzrok toliko velike razlike između rezultata dobivenih CFD simulacijama i mjerenjima u zračnom tunelu.

Utjecaj geometrije kotača (eng. *Wheel Geometry Influence*)

Ovo poglavlje je istražilo koliko različiti kotači mogu utjecati na strujanje zraka. Kao osnovna geometrija automobila uzeta je geometrija umanjenog modela korištena u zračnom tunelu, ali u prirodnoj veličini (omjer 1:1). Napravljene su dvije CFD simulacije (koje se ne nalaze u Tablici 7.1), jedna s kotačima koji su standardni u svim CFD simulacijama i druga simulacija s kotačima koji su korišteni na umanjenom modelu u zračnom tunelu. U poglavlju je jasno prikazana razlika u dizajnu i dimenzijama kotača. Rezultati su pokazali da su upravo različiti kotači ti koji su odgovorni za razlike u strujanju zraka između CFD-a i mjerenja u zračnom tunelu. Kada se na geometriji umanjenog modela koristi dizajn kotača kao i u CFD-u (dizajn aluminijskih naplataka), strujanje zraka, a time i raspodjela tlaka je vrlo slična kao i kod geometrije realnog automobila. Ovdje još valja dodati da vjerojatno nisu oblik i dimenzije kotača jedini razlozi, nego i osjetljiva geometrija podvozja vozila u području u blizini stražnjih kotača (ranije promatrani rub na naglom prijelazu geometrije podvozja).

Utjecaj uvodnika zraka za hlađenje (eng. *Cooling Inlets Influence*)

U ovome dijelu je ispitivano koliko otpora zraka stvara paket hlađenja. Budući da se na prednjem dijelu vozila CULT nalaze tri otvora kroz koje struji zrak za hlađenje, ispitano je koliko aerodinamičkog otpora stvara zrak koji prolazi kroz njih. Takvo ispitivanje se uobičajeno radi na način da se usporede simulacije s otvorenim i zatvorenim otvorima zraka. Međutim, automobil CULT ima mehanizam koji zatvara najveći od tri otvora zraka kada zrak nije potreban (CAS mehanizam). Iz tog razloga, ovo ispitivanje je podijeljeno na dva dijela, prvi dio ispituje aerodinamičku efikasnost CAS mehanizma, a drugi dio otpore zraka koji nastaju prilikom strujanja zraka kroz druga dva manja otvora.

Hladnjak motora i klimatizacijskog uređaja su smješteni na lijevoj strani prednjeg dijela automobila i iz tog razloga je u projektu odlučeno da će polovina (desna strana) CAS mehanizma biti skroz zatvorena. Ispitivanja u ovome radu su pokazala da se zatvaranjem CAS mehanizma, u usporedbi sa djelomično otvorenim, smanjuje otpor zraka za 16 count-a. Može se zaključiti da CAS mehanizam služi kad jako dobar uređaj za smanjenje aerodinamičkog otpora zraka. Ispitivanja u zračnom tunelu su dala vrlo slične rezultate za efikasnost CAS mehanizma – 15 count-a.

Drugi dio, gdje se istražuje utjecaj ostala dva manja otvora zraka je pokazao da su ta dva otvora odgovorna za mali dio otpora zraka - 4 count-a od ukupnog koeficijenta otpora zraka otpada na njih.

Optimizacija prednjih spojlera kotača (eng. *Front Wheel Spoilers Optimization*)

Cilj ovog poglavlja je pronaći najbolju poziciju za spojlere prednjih kotača. Zbog ograničenog vremena za provedbu ovog ispitivanja ispitana su, osim osnovnog, dva dodatna položaja spojlera. Dakle, uspoređena su tri različita položaja – prednji, srednji i stražnji. Srednji položaj je osnovni položaj, a prednji i stražnji položaj su za 25mm udaljeni od osnovnog položaja. Rezultati su pokazali da kako se spojler kotača pomiče prema naprijed, tako se otpor zraka smanjuje. Razlog tome je to što, kako se spojler pomiče naprijed, tako njegov vrtložni trag zaklanja sve veću površinu kotača.

Utjecaj i optimizacija retrovizora (Side Mirrors Influence and Optimization)

Već je spomenuto kako retrovizori na CULT vozilu imaju specifičan oblik. Cilj ovog poglavlja je pronaći optimalan položaj retrovizora. Iz tog razloga uspoređeno je devet različitih položaja. Mijenjane su dvije varijable vezane za položaj – pozicija (gore, sredina i dolje) i napadni kut ($+15^\circ$, 0° i -15°). Kombinacijom svake pozicije sa svaki napadnim kutom dobiva se devet različitih položaja.

Osim toga dodana je i jedna simulaciju bez retrovizora, kako bi se mogla vidjeti sama efikasnost retrovizora u osnovnom položaju i kako bi se moglo istražiti da li retrovizori mogu služiti kao uređaji za smanjenje otpora zraka.

Usporedbom rezultata pronađen je najbolji položaj – položaj „Dolje $+15^\circ$ “ (eng. *Bottom $+15^\circ$*). U nastavku je najbolji položaj detaljno uspoređen s osnovnim položajem, a zatim i s simulacijom bez retrovizora. Analiza je napravljena detaljno i pronađeni su pravi uzroci smanjenja otpora zraka. Kada su retrovizori u položaju „Dolje $+15^\circ$ “ tada utječu na vrtloge koji nastaju na A nosaču, te ih preusmjeravaju. Na taj način ti vrtlozi, umjesto na krov automobila, idu u stranu. Time se utječe na vrtložni trag iza vozila i smanjuju se aerodinamički gubici koji nastaju u njima. To se na automobil odražava porastom tlaka na zadnjem kraju automobila, odnosno smanjenjem otpora zraka.

Kada se najbolji položaj retrovizora uspoređi s simulacijom bez retrovizora, vidi se da simulacija s retrovizorima ima manji otpor zraka (i ukupan otpor i koeficijent otpora zraka). Na osnovu toga, dolazi se do zaključka da se retrovizori mogu koristiti kao uređaji za smanjenje otpora zraka (u pravilu postavljanje retrovizora na automobil povećava otpor zraka).

8. Preporuke za poboljšanje CFD metode (eng. *Recommendations for CFD Method Improvements*)

U CFD metodi se koriste mnoga pojednostavljenja. Cilj ovog poglavlja je ukazati da neka pojednostavljenja korištena u radu možda i nisu opravdana, odnosno da je isplativo uložiti više vremena, te ih izbjeći. Na taj način se u konačnici štedi vrijeme i raspolaze s točnijim rezultatima. Prvi dio poglavlja objašnjava kako su sve vizualizacije korištene u ovom radu zapravo rezultat nakon zadnje iteracije, a bilo bi točnije da se prikazuju kao srednja vrijednost zadnjih nekoliko stotina iteracija (npr. 200 ili 500 iteracija).

U drugom se dijelu poglavlja raspravlja o bez dimenzijskoj udaljenosti od površine (y^+) i veličini prvog sloja prizmatičnih elemenata. Zaključeno je da je visina prvog sloja prizmatičnih elemenata u projektu CULT manja nego što je to preporučeno.

9. **Zaključak** (eng. *Conclusion*)

Ovaj rad je pokazao kako se otpor zraka može smanjiti upotrebom uređaja za smanjenje aerodinamičkog otpora. Sva tri takva uređaja istražena u ovome radu su se pokazala vrlo korisnima. Uspoređujući s prednostima koje takvi uređaji donose, njihova cijena nije velika, te su puno ekonomičniji u usporedbi s drugim načinima smanjenja otpora vožnje kod današnjih vozila.

Još jedna zanimljivost u ovome radu je usporedba CFD rezultata s rezultatima dobivenima u zračnom tunelu. Taj dio rada je pokazao kako na prvi pogled zanemariva razlika u geometriji može dovesti do totalno krivih rezultata i zaključaka.

Aerodinamika ima velik potencijal kod vozila kao što je automobil CULT. Postoji još puno prostora za istraživanja u tom području. Svakodnevno povećanje ekološke svijesti i današnje prometne poteškoće u urbanim sredinama sigurno će donijeti još sredstava za projekte poput projekta CULT, a time i novim istraživanjima u području aerodinamike.

1 INTRODUCTION

In the last decade automotive industry is on the biggest intersection in the history. Growth of environmental awareness, together with new technologies and rising petroleum prices is introducing a vast range of possibilities for the future design of ground vehicles. Also, technology reached high level and production prices of high-tech components are becoming lower and available to the wide range of customers. Consequently, lots of different ideas (old and the new ones) are being tested in the automotive industry.

Until now history showed that great changes in people's everyday life are hard to accomplish in a short time. Therefore these changes need to go step by step. This thesis deals with a new concept of the city car, which can change everyday's life in future urban environments.

City car concept exists on the market for a long time. The idea of the concept investigated in this thesis is to revitalize the concept with a different approach and technologies from 21st century. Magna Steyr started the project CULT (Cars Ultra Light Technologies) with the goal to design commercial city car with lowest emissions on the market. To accomplish lowest emissions, lowest driving resistances need to be achieved – therefore, aerodynamic optimization is unavoidable.

Vehicle aerodynamics plays a very important part in total driving resistances. Aerodynamic engineers are trying different ways to reduce aerodynamic drag, however this must be achieved without big increase of production price of the car. As a result, many moderately priced drag reduction devices and solutions are implemented in modern road vehicles.

Several drag reduction devices will be investigated in this thesis using CFD (Computational Fluid Dynamics) and wind tunnel testing. In addition, some CFD related particularities will be also subject to investigation. The underlying idea of this thesis is to cover all basic things of the entire CFD investigation process in modern automotive industry. Additional value to the CFD results are wind tunnel test results. Wind tunnel test in this investigation was carried out on 1:4 detailed scaled model. This chapter describes basic principles of automotive aerodynamics.

1.1 Bluff Body Aerodynamics

Aerodynamics is a science that investigates air flow around bodies and resulting forces acting on the body. Bluff body aerodynamics investigates flow around bodies that are generally not aerodynamically shaped (“Bluff Bodies” or in German literature “*Stumpfkörper*”), as oppose to the streamlined bodies (aircrafts, etc.). Typical examples of bluff bodies are commercial and heavy-duty vehicles, buildings and bridges. Vast majority of road vehicles also belongs to that group.

To define a bluff body following things need to be known [1]:

- Geometry of the body (relative dimensions of length, width, height and cross-sectional area)
- Air flow around the body
- Forces acting on the body

Figure 1.1 shows typical examples of streamlined (left) and bluff body (right). Streamlined body has much higher aspect ratio (length/height), and body is shaped in the way that flow stays attached to the surface all the way. On the contrary, bluff body has a small aspect ratio and sharp edges where separation of the flow occurs. Consequently, flow, presented in the figure by the streamlines, is totally different for these two types of the bodies. Bluff body produces strong wake, while streamlined body has much lower influence on the environment around it.

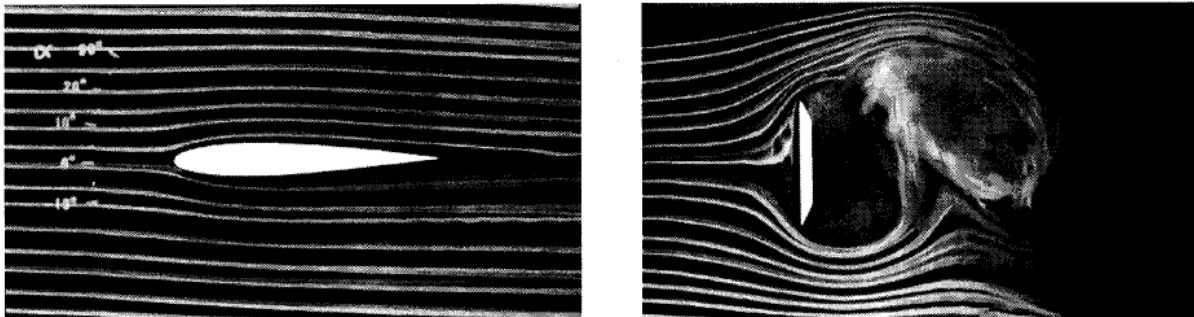


Figure 1.1 treamlines around typical streamlined body (right) and typical bluff body (left), $Re \approx 1 \cdot 10^4$; Pictures S. Hucho [1]

In Figure 1.2 influence of the body on the environment can be easily proved by observing speed downstream of the trailing edge. Figure shows two different types of bodies – one is streamlined (a) and other is bluff body (b). Both of them are reducing air speed because of energy losses in the flow, caused by the body aerodynamic resistance. It is obvious that this effect is much lower on the streamlined body.

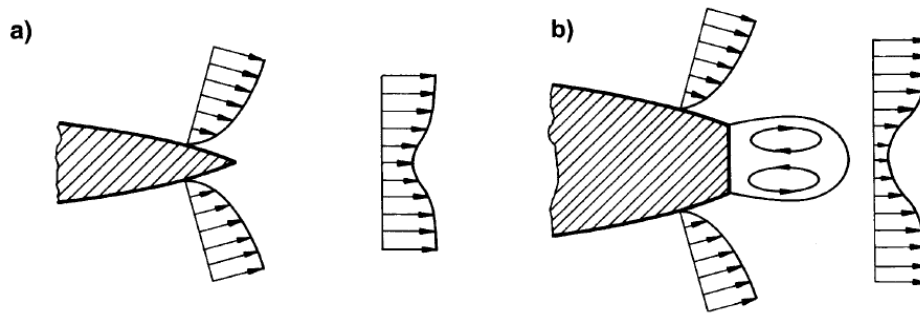


Figure 1.2 Flow behind streamlined body (a) and bluff body (b), schematics [1]

There are two types of aerodynamic forces acting on the body in the flow: friction force and pressure force.

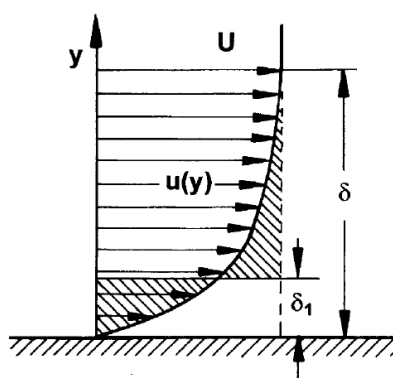


Figure 1.3 Boundary layer definition [1]

Friction forces are present because of the viscosity of the air. Particles along the body surface are connected to the body surface and they are moving together with the body. At particular distance from the surface there is relative motion between surface and the air particles – air is flowing around body. Because of this relative motion and due to viscosity of air, interaction of particles creates friction-related losses (aerodynamic drag). At sufficient distance from the body surface, air flow speed is not affected by the friction caused by the body surface. Flow between this unaffected air flow and the body surface is called boundary layer. Consequently, in the boundary layer friction forces

have very important role.

Other type of aerodynamic forces is pressure force. Pressure forces act on the body in flow because of pressure differences on body surface. For example, on one bluff body there is gauge pressure on the front end, due to stagnation point of the flow. On the back of the body, pressure is lower (vacuum pressure) due to flow separations and recirculation in the wake. Differences between high pressure at the front and low pressure at the back create pressure-related drag force.

Which of these two forces is dominant depends on the body shape and, in general, behavior is opposite between streamlined and bluff bodies. Figure 1.4 shows shares of these two types of aerodynamic forces in cases of different body shapes. Friction forces are more dominating with the streamlined bodies, while pressure forces plays dominant role in the case of bluff bodies.


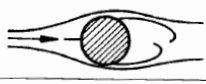
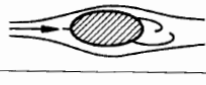

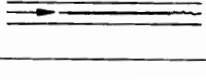
Körper	Widerstand	
	Druck	Reibung
	100%	0%
	90%	10%
	60%	40%
	10%	90%
	0%	100%

Figure 1.4 Share of the two types of resistances (ger. *Widerstand*) on different types of bodies (ger. *Körper*): pressure (ger. *Druck*) and friction (ger. *Reibung*) aerodynamic resistance [1]

Streamlined bodies have small wake and also small frontal area of stagnation point pressure, so pressure differences between front and the back are small. Therefore, share of pressure resistance force is small.

Boundary layer is very important in friction generation. On the streamlined bodies boundary layer is attached to the body most of the time. On the bluff bodies, boundary layer is usually attached to the body only on some areas on the surface. As soon as boundary layer detaches, friction forces drop and detachment of the flow produces wake and increase pressure-related forces. Because pressure forces, created by the separation, are much bigger than friction forces, overall share of pressure forces increases.

Majority of vehicles has all properties that put them into the group of the bluff bodies:

- Low aspect ratio – bluff body shape
- Separation of the flow
- Dominating pressure forces
- Strong wake created by the vehicle

1.2 Aerodynamics of Road Vehicles

Automotive aerodynamics investigates flows around ground vehicles. Ground has a big influence on vehicle’s performances, especially at high driving speeds.

All road vehicles share specific requirements that need to be satisfied, like maximum length, width, height, specific shape to satisfy need for space for passengers, luggage, engine and equipment, wheels, suspension system... These technical requirements cannot be avoided. Due to these requirements aerodynamic optimization of road vehicles is very complicated field of automotive engineering and requires close collaboration with different teams in a typical vehicle design process.



Figure 1.5 Low drag vehicle during wind tunnel test (VW XL 1, 2012) [14]

1.2.1 History of Aerodynamics of Road Vehicles

At the beginning of automotive development driving velocities were relatively low and aerodynamics was not taken into account during design process. But, as vehicles were becoming faster, aerodynamics started to be involved in the design process. With greater speeds aerodynamics influences are becoming more important. During 70s and 80s of the last century a great increase of petroleum price occurred together with the beginning of environmental awareness and these two things changed a typical design process of modern vehicles. Since then fuel consumption and emissions are one of the main topics in car design process and these cannot be solved without valuable aerodynamics input. Together with weight reduction, and engines and transmissions with better efficiency, aerodynamics plays the crucial role in low fuel consumption requirements (see Chapter 1.4).

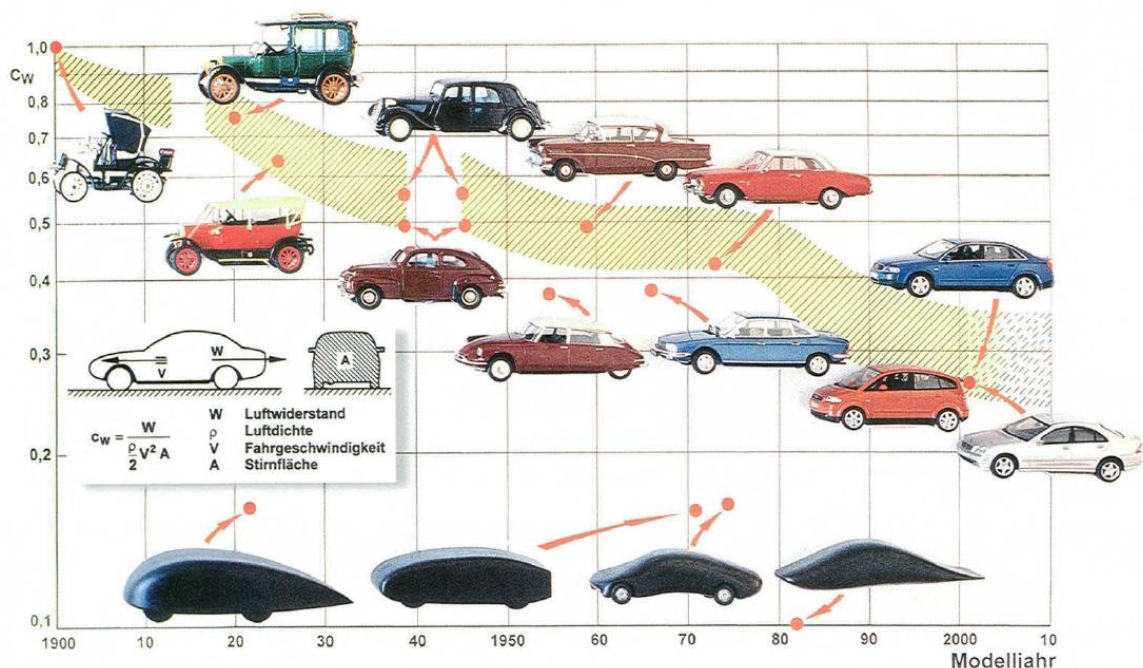


Figure 1.6 Development of aerodynamic drag in automotive history [2]

Figure 1.6 shows reduction of aerodynamic drag throughout the automotive history, for commercial vehicles (top) and also for prototypes (bottom). From the early time in automotive history aerodynamics engineers gave solutions for low drag bodies, but a long time was required for the designers and customers to accept them. Figure 1.6 helps to understand history of aerodynamics. The main point to note is that implementation of aerodynamic benefits into commercial vehicles is not just a question of available knowledge and technology, but a result of complex influence of market needs and current trends in the world.

1.2.2 Coordinate System

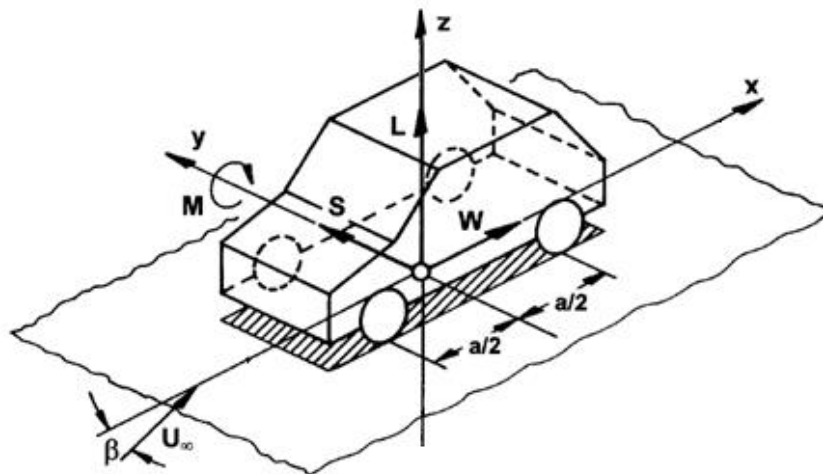


Figure 1.7 Coordinate system for aerodynamic forces and moments definition in Automotive aerodynamics

Figure 1.7 shows basic standards in automotive aerodynamics related to position of coordinate system, direction of forces and moments and calculating drag coefficient.

Zero point (origin) of the coordinate system lies in the middle between vehicle axles (x coordinate), in the middle between the wheels (y coordinate), and on the ground (z coordinate).

In this thesis only flows with zero yaw angle (β) will be investigated (wind direction always parallel to vehicle longitudinal axis), therefore these forces and moments will be used:

- Vector W represents drag force – F_x
- Vector L represents lift force – F_z
- Vector M represents momentum around y axis – M_y

Because flows with yaw angles will not be investigated and assumption that averaged flow is symmetric, other forces and moments acting on the vehicle will not be investigated (average values of these forces and moments are equal to zero).

1.2.3 Dimensionless Aerodynamic Coefficients

Each force which is monitored in the simulation is transferred into a dimensionless coefficient. Dimensionless coefficients are used for a comparison of aerodynamics forces between different vehicles, independent from body size.

Drag coefficient is the most often used parameter related to automotive aerodynamics. It depends on drag force and reference area of the vehicle, as well as properties of the air stream:

$$C_D = \frac{F_x}{q_\infty \cdot A_{ref}}$$

C_D – drag coefficient

F_x – aerodynamic force in x direction (drag force)

A_{ref} – reference area of the vehicle (usually frontal cross – section)

$q_\infty = \frac{1}{2} \cdot \rho_\infty \cdot u_\infty$ – free stream dynamic pressure

ρ_∞ – free stream air density

u_∞ – free stream air speed

Lift coefficient represents force acting in vertical direction (positive lift in case of most road vehicles, negative lift, also called *downforce*, in the case of racing cars):

$$C_z = \frac{F_z}{q_\infty \cdot A_{ref}}$$

C_z – lift coefficient

F_z – aerodynamic force in z direction (lift force)

To calculate components of lift coefficient acting on front and rear axle of the vehicle (C_{zf}, C_{zr}), **Moment coefficient** around y axis (pitching moment) is also required:

$$C_{my} = \frac{M_y}{q_\infty \cdot A_{ref} \cdot L_{ref}}$$

$$C_{zf} = \frac{1}{2} C_z - C_{my} \cdot \frac{L_{ref}}{2}$$

$$C_{zr} = \frac{1}{2} C_z + C_{my} \cdot \frac{L_{ref}}{2}$$

C_{my} – momentum coefficient around y axis

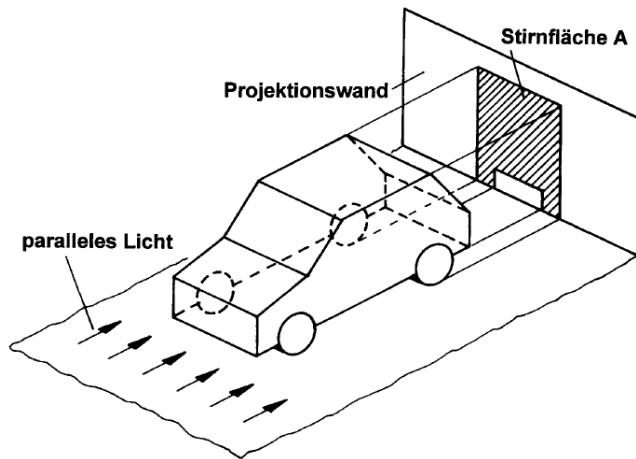
L_{ref} – referent length of the vehicle (usually wheel base of the vehicle)

C_{zf} – lift coefficient on the vehicle's front axis

C_{zr} – lift coefficient on the vehicle's rear axis

1.2.4 Reference Area

Reference area (A_{ref}) represents the projected area of vehicle shape in the direction of air flow (Figure 1.8)



ger. *paralleles Licht* – parallel light
 ger. *Projektionswand* – projection plane (wall)
 ger. *Stirnfläche* – front area (projected area)

Figure 1.8 Definition of reference area (projected area) A_{ref} [1]

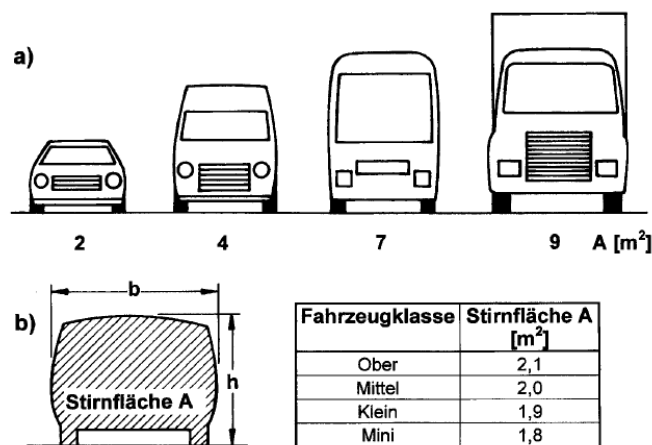


Figure 1.9 Reference area A_{ref} [2]:

a) size compared between different type of vehicles

b) typical values for different classes of cars:

- ger. *mini* – mini class
- ger. *klein* – small class,
- ger. *mittel* – middle class
- ger. *ober* – top class

1.3 Air Pressure Definition

Before starting the analysis of results a precise definition of air pressure and air pressure coefficients is required. To give a more complete overview of pressure definitions also aerostatic pressure definitions are included below (for more detailed definitions see [3]).

1.3.1 Aerostatics

Absolute pressure - p_{abs}

Absolute pressure is a pressure measured at the certain point in the flow. It is zero-referenced against ideal vacuum – it is always positive. It can be used to calculate ambient pressure (e.g. meteorology – determination of atmospheric pressure at certain point).

Relative pressure – p

Relative pressure is zero-referenced against ambient air pressure. It is used to measure pressure difference between specific points and ambient. Relative pressure can be positive or negative. If it is positive then it is called “gauge pressure” and if it is negative it is called “vacuum pressure”.

1.3.2 Aerodynamics

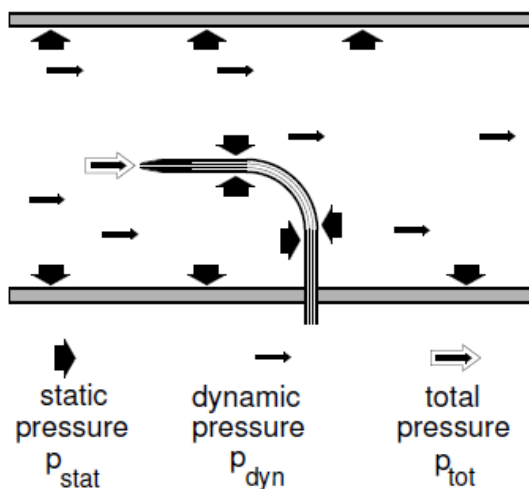


Figure 1.10 Three different pressure definitions: static pressure, dynamic pressure and total pressure [3]

Static pressure - p_{stat}, p

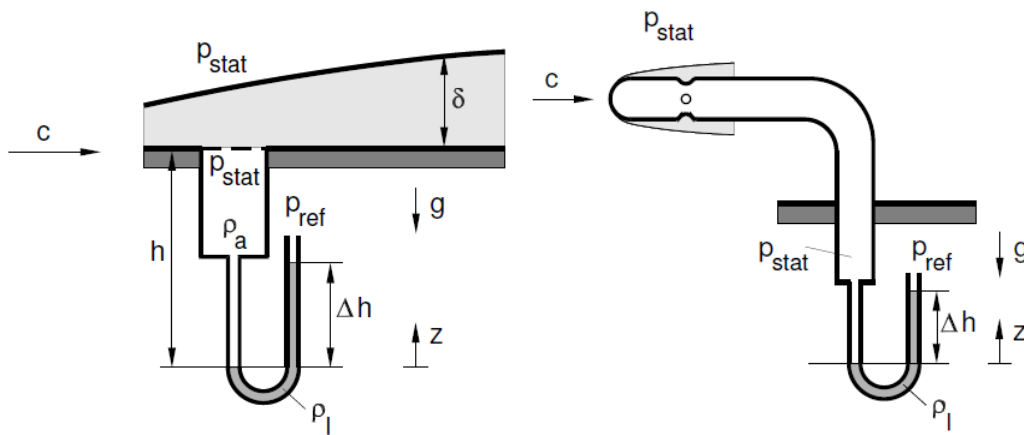


Figure 1.11 a) and b) Measurement of the static pressure [3]

Static pressure is equal to relative pressure in aerostatics - it is used to measure pressure difference between specific point and ambient. In aerodynamics ambient pressure is static pressure of undisturbed flow (usually standard atmosphere).

Later in the text, when word “**pressure**” is used it refers to static pressure.

Total pressure - p_{tot}

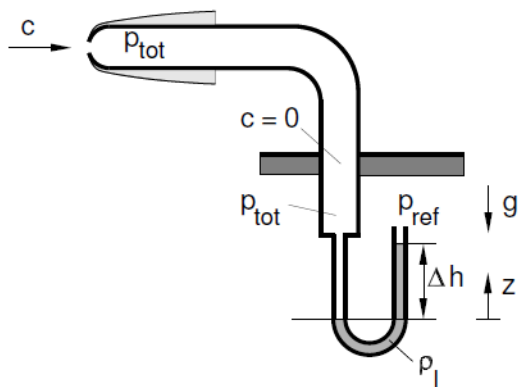


Figure 1.12 Total pressure measurement [3]

Total pressure is pressure measured at stagnation point [3]. In addition to static pressure, total pressure also includes air flow inertia (dynamic pressure):

$$p_{tot} = p + q$$

p – static pressure
 q – dynamic pressure

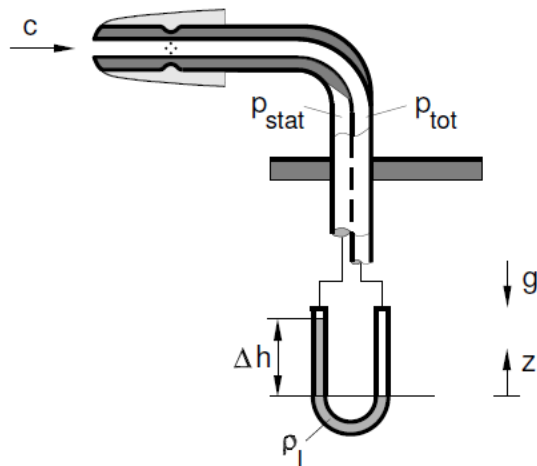
Dynamic pressure - q 

Figure 1.13 Dynamic pressure measurement [3]

Dynamic pressure is a result of kinetic energy of fluid flow:

$$q = \frac{1}{2} \rho u^2$$

ρ – air density

u – air speed

Dynamic pressure can be calculated (or measured) by subtracting static pressure from total pressure [3]:

$$q = p_{tot} - p$$

Free stream pressure - p_∞

Static pressure in the free stream is equal to zero. Therefore, free stream pressure is dynamic pressure measured in the free stream (undisrupted flow). In a case of wind tunnel measurement, it is measured at air inlet. Free stream pressure is used for definition of aerodynamic coefficients and pressure coefficients (Chapter 1.2.3).

$$p_{stat\infty} = 0$$

$p_{stat\infty}$ – free stream static pressure

$$p_\infty = p_{tot\infty} = p_{stat\infty} + q_\infty = q_\infty = \frac{1}{2} \rho_\infty u_\infty^2$$

$p_{tot\infty}$ – free stream total pressure

q_∞ – free stream dynamic pressure

ρ_∞ – free stream air density

u_∞ – free stream air speed

Pressure coefficient - C_p

Pressure coefficient is dimensionless coefficient. It is ratio between local static pressure and free stream total pressure (or free stream dynamic pressure, since free stream static pressure is equal to zero):

$$C_p = \frac{p}{p_{tot\infty}} = \frac{p}{\frac{1}{2}\rho_\infty u_\infty^2}$$

p – static pressure at observed point

$p_{tot\infty}$ – free stream total pressure

Total pressure coefficient - C_{ptot}

Total pressure coefficient is dimensionless coefficient. It is ratio between local total pressure and free stream total pressure (or free stream dynamic pressure, since free stream static pressure is equal to zero):

$$C_{ptot} = \frac{p_{tot}}{p_{tot\infty}} = \frac{p + \frac{1}{2}\rho u^2}{\frac{1}{2}\rho_\infty u_\infty^2}$$

p_{tot} – total pressure at the observed point

$p_{tot\infty}$ – free stream total pressure

1.4 Driving Resistances

To achieve low fuel consumption, the sum of all driving resistances needs to be as low as possible. There are several driving resistances involved in vehicles movement. In the case of constant speed on the straight road three main resistances act: rolling resistance, transmission resistance and aerodynamic drag.

In comparison to other two driving resistances, transmission resistances are very small (efficiency of transmission is around 95%), and there is not lot of space for reduction left in this field [4].

Rolling resistance has a fairly large influence in total driving resistances, especially with heavy vehicles (commercial vehicles) and at low driving speeds. Lower rolling resistance can be achieved with optimized design of pneumatics (tires) [4].

In the case of passenger road vehicles, beyond speed of approximately 70 km/h the aerodynamic resistance starts to dominate (Figure 1.14 and Figure 1.15). Therefore, when analyzing the driving resistances at the higher speeds (e.g. highway), aerodynamics has the main role.

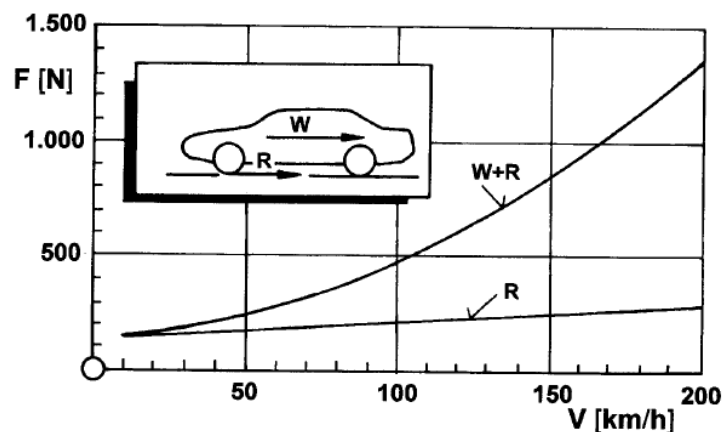


Figure 1.14 Aerodynamic drag (ger. *Widerstand* - W) and rolling resistance (R) - depending on vehicle speed, an example with BMW 520i ($C_D = 0,27$; $A_{ref} = 2,18\text{m}^2$; $m = 1570\text{kg}$) [1]

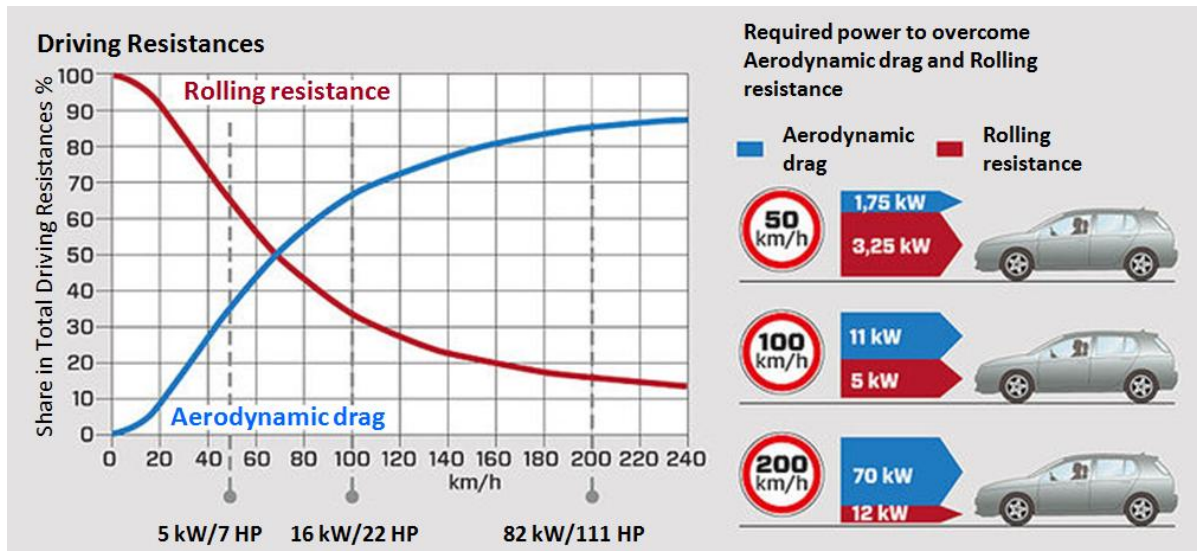


Figure 1.15 Relation between aerodynamic drag and rolling resistance [14]

Aerodynamic drag – vehicle speed influence:

At low speeds, driving resistances are small, and aerodynamics is not crucial, but as speeds increases, aerodynamics starts to have a big role as showed in the following formula [4]:

$$F_x = q_\infty \cdot A_{ref} \cdot C_D = \frac{1}{2} \cdot \rho_\infty \cdot u_\infty^2 \cdot A_{ref} \cdot C_D$$

$$F_x \sim u_\infty^2$$

F_x – Aerodynamic force in x direction

C_D – aerodynamic drag coefficient

A_{ref} – referent area of vehicle (usually frontal cross – section)

$q_\infty = \frac{1}{2} \cdot \rho_\infty \cdot u_\infty$ – free stream dynamic pressure

u_∞ – free stream air speed

ρ_∞ – free stream air density

Aerodynamic drag force required to overcome air drag is proportional to square of air speed, whereas the power required to overcome aerodynamic drag is proportional to the third power of speed [4]:

$$P_x = F_D \cdot u_\infty = q_\infty \cdot A_{ref} \cdot C_D \cdot u_\infty$$

$$P_x = \frac{1}{2} \cdot \rho_\infty \cdot u_\infty^2 \cdot A_{ref} \cdot C_D \cdot u_\infty$$

$$P_x \sim u_\infty^3$$

P_x = aerodynamic drag power

1.5 Intelligent Use of Aerodynamics

In future CO₂ emissions will have to be reduced (see Chapter 2.2) and aerodynamics can be very effective tool for that. If used intelligently, aerodynamics can bring improvements comparable to weight reduction, but at much lower cost. In Figure 1.16 different approaches to fuel consumption are shown (all related to a typical middle-class car). Out of three different approaches (aerodynamic optimization, weight reduction and start-stop system integration), for the same saving in the fuel consumption (0.2 liter), aerodynamic optimization has the potential to be the most economical.

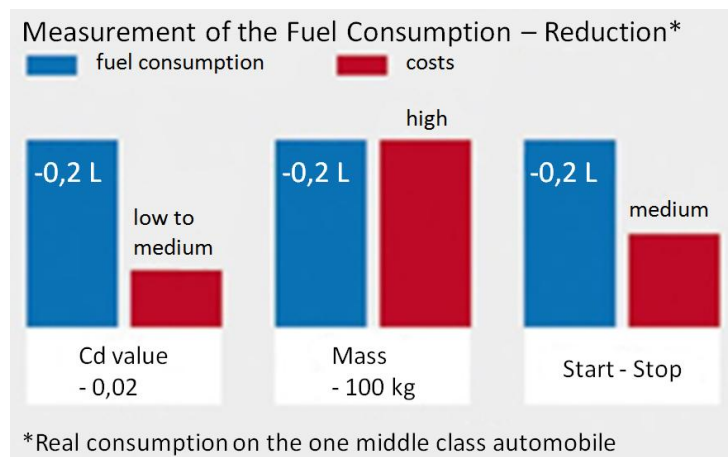


Figure 1.16 Different approaches to fuel consumption reduction [14]

On the other hand intelligent use of aerodynamics needs not only excellent engineering but also advanced social and networking skills. It will require a close collaboration and mutual respect of aerodynamicists, exterior designers, packaging specialists (cooling package) and marketing managers.

Cooling package

Packaging specialists are important because a considerable part of aerodynamic drag is generated by the engine cooling package and other devices (such as air conditioning condenser). Together, aerodynamicist and packaging specialist need to design cooling that will have lowest drag while providing air mass flow needed for cooling.

Exterior design

Exterior designer is a main responsible person for appearance of the car. Exterior design (styling) is very important for sales, because cars have always been sold depending on their appearance as much as their technical characteristics. Of course, aerodynamicist needs to interfere into exterior design and often it is hard to satisfy both, design and aerodynamics requirements.

Problem for aerodynamicists occurs if choosing of the initial shape is left only to exterior designers. After the exterior design is defined, aerodynamicists do not have a lot of freedom left in shaping the car and it can be very difficult to reach low values of aerodynamic drag.

One of the possible ways to design a low drag vehicle is that aerodynamic engineer finds a suitable low drag shape that suits project demands. Next step would be for a designer to modify this shape to get look which corresponds to current trends. At this step designer has a lot of freedom, but it should be very careful not to ruin basic shape chosen by aerodynamicist. After final shape is designed, aerodynamicist needs to find a way to reduce drag with detail optimization working closely with designer. With increasing demands for lower fuel consumption and low emissions, predictions are that this procedure will probably become a standard in automotive industry.

Marketing

When “what people like” is to be defined, then good marketing skills are required. Making big improvements in aerodynamics make sense only if low-drag vehicles will be commercially successful on the market. History shows that such tasks are not impossible for marketing, but they cannot be implemented overnight.

Close cooperation between different development and engineering teams was crucial in Magna Steyr CULT project (see next Chapter).

2 MAGNA STEYR - CULT

2.1 About Magna Steyr

Company name: **Magna Steyr AG & Co KG**

Address: **Liebenauer Hauptstrasse 317, A-8041 Graz, Austria**

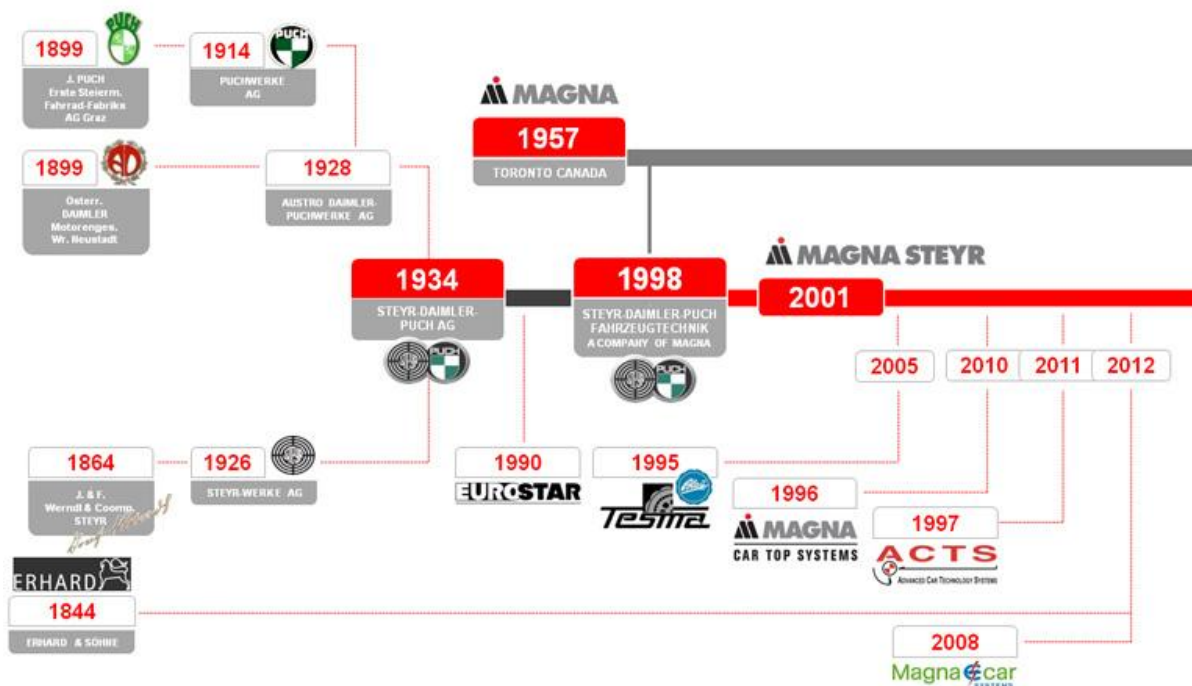


Figure 2.1 History line of Magna Steyr [17]

Magna Steyr is a part of Magna International Inc. since 1998 (Figure 2.1), when Magna International Inc. acquired a majority holding in Steyr-Daimler-Puch AG, which has a history more than one hundred years.

Magna International Inc. is the most diversified automotive supplier in the world. Company designs, develops and manufactures automotive systems, assemblies, modules and components, and engineers and assembles complete vehicles. Primary customers for MAGNA Steyr are original equipment manufacturers (OEMs) of cars and light trucks in three geographic segments - North America, Europe, and Rest of World (primarily Asia, South America and Africa). [17]

Magna International Inc. has 313 manufacturing operations and 88 product development, engineering and sales centers in 29 countries on five continents as of Q4 2012.

Magna Steyr AG & Co KG, with its experience over 100 years in vehicle production and a broad range of services, is the worldwide leading brand-independent engineering and manufacturing partner for OEMs (Original Equipment Manufacturers).



Figure 2.2 Magna Steyr AG & Co KG, Graz [17]

Extensive range of Magna Steyr services covers four product groups:

- Engineering Services: From systems and modules to complete vehicle engineering
- Vehicle Contract Manufacturing: Flexible solutions from niche to volume production
- Fuel & Battery Systems: From conventional energy storage systems (made of steel, plastic and aluminum) to Battery Systems for renewable energies
- Roof Systems: Entire range of roof systems including soft tops, retractable hard tops and modular tops

As a contract manufacturer, MAGNA Steyr has produced more than 2.5 million vehicles - of 21 different models - to date. Future company focus will include offering customized solutions for the aerospace and diversified industries.

Globally 10,500 employees support these services. Based on this global network of 36 locations on three continents, company policy is to stay close to the customers. For Magna Steyr partnership includes strengthening and fostering their customers' market position by integrating unique ideas and new developments.

The history of MAGNA STEYR is inextricably linked to two people, two great pioneers in trade and industry: **Johann Puch** and **Frank Stronach**. Although they lived virtually a century apart, both their ideas and visions played a decisive role in the future of the company. [17]

Johann Puch (Slovene: *Janez Puh*)

Johann Puch was born on 27 June 1862 to Slovene-speaking peasants in Sakušak near Ptuj (Pettau), the part of multi-ethnic Styria which today belongs to Slovenia. He founded his own manufacturing company in 1899, called Johann Puch - *Erste steiermärkische Fahrrad-Fabriks-Actien Gesellschaft* (eng. *First Styrian Bicycle Stock Company*) in Graz. The company started producing motorcycles in 1903 and automobiles in 1904. By 1912 Puch's factory employed 1,100 workers and manufactured 300 cars, 300 motorcycles and 16,000 bicycles per year. He retired in 1912 but remained honorary president of the company.

He died on July 19, 1914 of a stroke while attending a horserace in Zagreb (Agram).

The Puch company manufactured vehicles for the Austro-Hungarian Army during World War I. Puch's motorcycles and cars were successful in races and rallies all over Europe and carried his name among vehicle producers. From 1934 the tradition was continued by the Steyr-Daimler-Puch company in Graz and Vienna [31].



Figure 2.3 Johann Puch (Slovene: *Janez Puh*) [31]

Frank Stronach (born as *Franz Strohsack*)

Frank Stronach was born on 6 September 1932 in Kleinsemmering, Styria, Austria. Stronach's childhood was marked by the Great Depression and the Second World War.

In 1954, he arrived in Montreal, Quebec, and later moved to Ontario. In 1956, Stronach started his first business, Multimatic Investments Ltd. in the old manufacturing district of Toronto. In 1969 his firm acquired its first automotive parts contract and merged with Magna Electronics. In 1973 the name was converted from Multimatic Investments Ltd to **Magna International Ltd.** Over the following decades, after several mergers and acquisitions, his business gradually became the major force it is today. In 1998, Magna took over Steyr Daimler Puch to the newly merged company Magna Steyr [32].

Frank Stronach also wrote a book about his business success – *Tha Magna Man*.

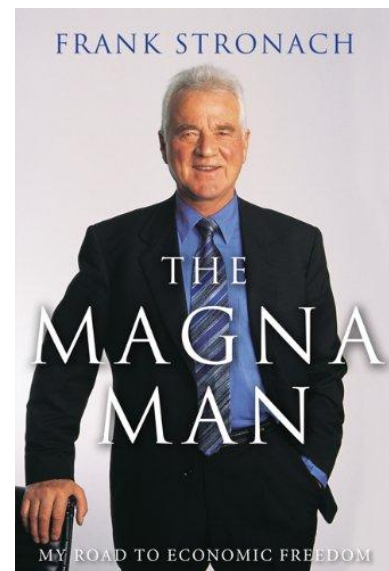


Figure 2.4 The Magna Man by Frank Stronach (book front page) [33]

2.2 Transportation in modern urban areas

Cities all over the World are facing growing environment pollution problems, including significant CO₂ emissions linked to transportation. People need mobility and this mobility can be achieved with different means: public transportation, cycling and walking or with private transportation. All these means together are called urban passenger transportation. Different usage of these transportation methods affects efficiency of transportation in cities and produces different levels of CO₂ emissions. In Figure 2.5 CO₂ emissions are related with usage of public transport, walking and cycling.

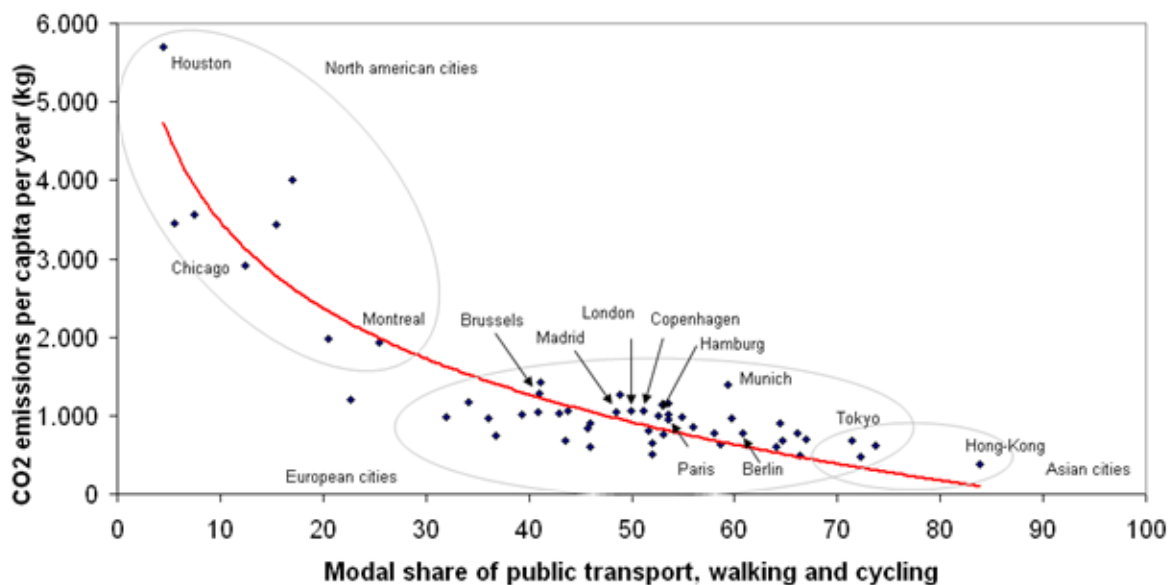


Figure 2.5 Modes of transportation in modern urban areas and resulting CO₂ emissions [10]

It can be seen that in North American cities the largest part of the transportation is made by private vehicles. On the contrary, in Asian cities people do not use private transportation much. Europe is somewhere in the middle between these two extremes. It can be seen that as more people use private transportation there are more emissions per capita, respectively the urban areas are becoming less environmentally friendly.

To reduce CO₂ emissions, but not affecting mobility, both usage of public transportation should be increased and CO₂ emissions emitted by private transportation (cars) have to be reduced. Reducing CO₂ emissions by increasing usage of public transportation is more straightforward, but it affects life of an individual citizen. Cars are still a symbol of freedom, and people have to be motivated to reduce the usage of cars. That does not mean that it is not possible to change the perception of personal freedom and living standard, but these changes will need a long time to be implemented.

Therefore, the fastest way to reduce the urban passenger transportation CO₂ emissions is to introduce low emissions cars.

With the introduction of the small city cars, optimized for low CO₂ emissions, Figure 2.5 would look very different. Nowadays, all big automotive companies are introducing new City Car concepts (also called Urban Cars [11]), and slowly, but steady, market is filled with these cars. Future will show how these cars will be accepted by the customers. Forecasts for city cars are good, because they will bring lot of very important advantages to the life in big cities:

- Better mobility and better parking opportunities
- Lower fuel consumption due to optimization – more value for customers
- Lower price in initial costs and maintenance costs (if simple, but robust technology is in use)

Other thing, which is very important for automotive companies, is constant increase of CO₂ emissions taxes, due to environmental regulations. These government’s regulations should force companies to invest more money in this segment of vehicles.

Based on all these facts prediction is that, in the close future, city cars will take a huge share on the market for private motorized transport in both developed and developing countries.

Actually, City car is nothing new, it exists on the market for a long time. Figure 2.6 a) shows the Fiat 500, produced from 1957. until 1975. This car is one of the first City Cars in the world. [12] Coincidentally, this car was also produced by Steyr-Daimler-Puch in Graz [13].



a)



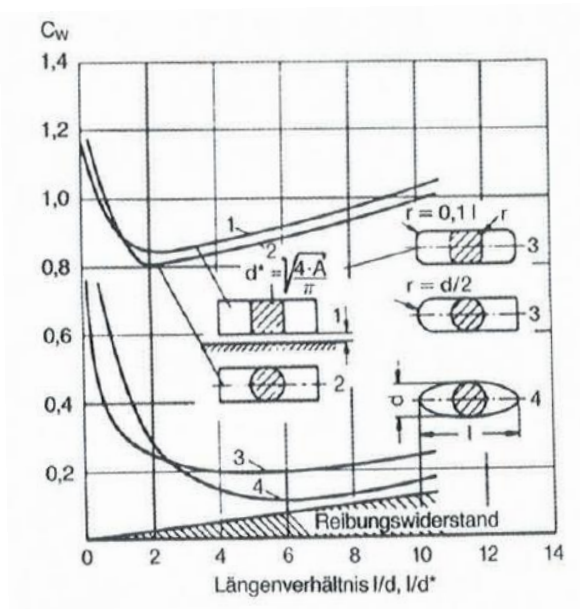
b)

Figure 2.6 a) Fiat 500, 1970 [12], b) Steyr Puch 500 [13]

2.3 Aerodynamics of City Cars

Restricted maximum length and customer demands for comfort and space inside the car lead to the common shape of all city cars. That means short body and blunt rear-end geometry,

which is bad for aero-drag and puts severe limits on aerodynamic optimization of vehicles.



In the past, there have been many investigations of aerodynamics of small cars. It can be seen in Figure 2.7 that up to the length/width ratio L/W of about 2 (for bodies with sharp corners) or about 5 (for bodies with rounded edges), longer the body is (higher L/W ratio), the aerodynamic drag is lower.

Figure 2.7 Aerodynamic drag (ger. C_w) on the bodies with different shape and different length/width ratio (l/d); Barth (1966) [2]

Figure 2.8 shows also bodies with different length/width ratio (L/W), and it can be easily seen that longer body creates smaller wake, which generally (not a rule!) leads to better aerodynamic properties.

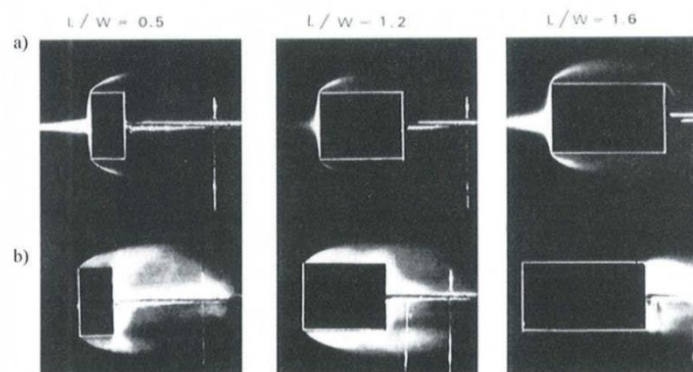


Figure 2.8 Separation of flow on cuboids with different length/width (L/W) ratios [2]

The overall aerodynamic drag force depends on two geometrical characteristics (see Chapter 1.4) - reference area (A_{ref}) and aerodynamic drag coefficient (C_D):

$$F_x = q_\infty \cdot A_{ref} \cdot C_D$$

$$F_x \approx A_{ref} \cdot C_D$$

Figure 2.9 shows that despite constant decreasing Cd-value, aerodynamic drag of typical European cars is actually increasing. This negative trend is the result of constantly increasing vehicle size A_{ref} . It is still hard for the most of customers to sacrifice comfort for better fuel economy and lower emissions. Therefore, there is a really difficult task for today’s engineers to create cars which will satisfy all requirements. This claim is especially true for small cars.

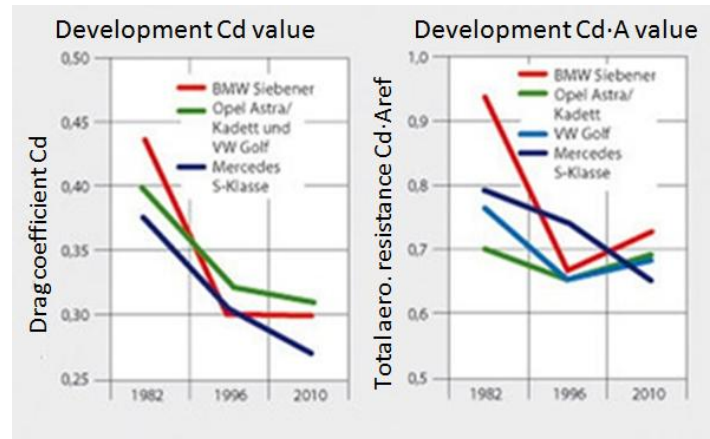


Figure 2.9 Aerodynamic drag increase for typical European mass produces vehicles from 1996. to 2010. [14]

If the term “city car” also implies the purpose of the car (to be used mostly in urban areas), then it can be concluded that aerodynamics is not of crucial importance for this type of cars. If city cars are predominantly used for driving in urban areas, where speed is very limited, aerodynamics does not play important role in complete driving resistances (Chapter 1.4).

In practice even city cars are often used on highways and open roads (e.g. every day trip to the workplace, or small trips between cities). Also, nowadays taxes for CO₂ emissions are constantly increasing (see Chapter 2.2) and as a reference for measuring CO₂ emission equal standard test cycles are used for all type of cars [22]. Because in these tests aerodynamics plays important role it is necessary to improve aerodynamic coefficient in order to pay less taxes.

Consequently, term “city car” is only related to the car’s size, not the purpose and opportunities which that type of the vehicle gives. The wide range of possible applications of city cars applies especially when modern technology is incorporated in such a vehicle.

2.4 CULT – Cars Ultra Light Technologies

CULT (Cars Ultra Light Technologies) is MAGNA Steyr project with the goal to develop a city car, belonging to the A-segment vehicles with 4 seats (mini cars). A-segment is defined by the European Commission as the first segment in the European market car classification, with length limit up to approx. 3600mm.

Compared with the competitors (VW Up, Opel Adam, Fiat 500, Toyota Aygo, Peugeot 107, Citroën C1) the CULT car needs to satisfy following requirements:

- **Best in class fuel consumption (target of CO2 emission 49 g/km)**
- **300 kg less weight than competitors**

In order to achieve given emissions demands and range of 400km, CULT is powered by a CNG engine, with the optimized power train.



Figure 2.10 MAGNA Steyr CULT prototype [23]

As already mentioned in Chapter 2.2, due to current and incoming taxes for CO2 emissions, MAGNA Steyr wants to use this project as a showcase for potential new customers (OEMs), as one possible way to avoid massive fines and save money in the future [24].

Furthermore, CULT needs to be in affordable purchase price segment with low maintenance costs. In the past, in automotive industry, after every recession cars with simple technology and low maintenance costs were very popular. Figure 2.11 and Figure 2.12 show two examples of such car, Ford Model T and VW Type 1 (VW “Beetle”). Common features which the CULT shares with these two successful cars are: great value for money, robust and simple technology (for its time) and main idea of the developer. Henry Ford’s idea for Model T was:

"I will build a car for the great multitude. It will be large enough for the family, but small enough for the individual to run and care for. It will be constructed of the best materials, by the best men to be hired, after the simplest designs that modern engineering can devise. But it will be so low in price that no man making a good salary will be unable to own one – and enjoy with his family the blessing of hours of pleasure in God's great open spaces." [15].



Figure 2.11 Ford Model T



Figure 2.12 VW Type 1

It can be seen that Henry Ford’s idea, with some changes, can fit the idea of CULT project, because the main guiding thought is the same. Of course, CULT is trying to adopt this revolutionary thinking to the needs of the 21st century:

- **Low emission**
- **Traffic safety**
- **Aerodynamics**
- **Lightweight construction**

3 AERODYNAMIC OPTIMIZATION OF CULT VEHICLE

In order to reach project goals (see Chapter 2.4) CULT fosters a modern and innovative approach in many fields. In this chapter (and also in the whole thesis) only fields important for aerodynamics and fuel consumption will be discussed in details.

CULT has a CNG (Compressed Natural Gas) internal combustion engine, with better process efficiency than standard gasoline engines and consequently lower fuel consumption and exhaust emissions. But, using CNG engine brings problems related to fuel storage. As a result, CULT fuel tank is in the unusual place compared with conventional vehicles. It is positioned in the central tunnel below the Body-In-White (Figure 3.1 - green). Other packaging novelty is the exhaust system: whole exhaust system is placed in engine compartment (Figure 3.1- grey).

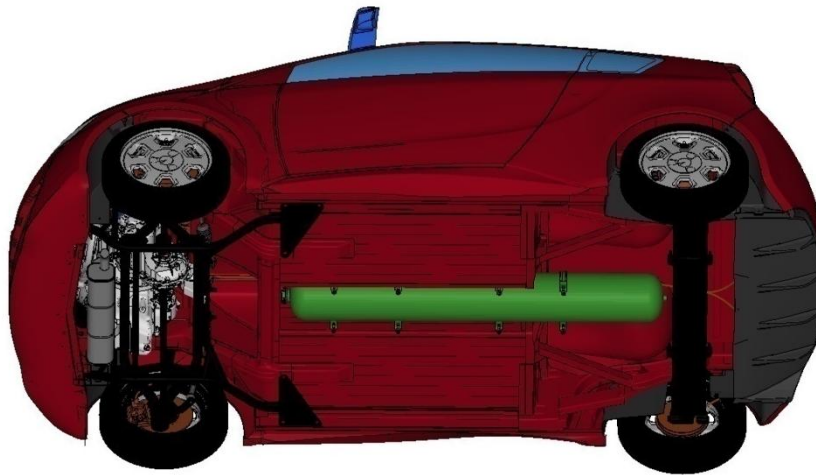


Figure 3.1 CULT – under-body cover removed. CNG tank (green) is placed in the central tunnel, below body in white. Complete exhaust system is in the engine compartment (grey)

This novel positioning of exhaust system and fuel tank position bring clear benefits for the aerodynamic flow. Since there are no obstacles under the car (exhaust pipes, fuel lines), it is easier to make a smooth and aerodynamically optimized under body cover. Second potential benefit is the channel where the CNG tank is placed. This channel connects engine compartment with rear end of the car, so there exists a potential for reducing aerodynamic drag at the rear end by connecting the air flow from the engine compartment to the rear end, therefore increasing pressure in the wake.

Except full under body cover and possible CNG tank tunnel benefit, many other “aerodynamic drag reduction devices” are present. In this chapter all this devices will be shortly introduced.

Overview of parts important for aerodynamics:

- **Full under-body cover**
- **CNG tank tunnel positioning**
- **Cooling-air guides**
- **Charge-Air Cooler (CAC) channel**
- **Active Cooling Air Shutter mechanism (CAS)**
- **Aerodynamically optimized rear view cameras (“side mirrors”)**
- **Front-wheel spoilers**

As it was already mentioned in previous Chapters, basic shape of CULT was determined by customer’s needs and it is similar to many city cars available on the market today. That means short body and blunt rear-end geometry. To reduce aerodynamic drag on such car is not an easy task and all details and possible opportunities for drag reduction need attention.

3.1 Front-End Packaging

An important issue for the overall aerodynamic properties of road vehicles is positioning and sealing of the cooling package. Usually, cooling losses contribute around 10% of aerodynamic drag and optimization of cooling package can significantly contribute to overall aerodynamic performance.

The front-end of CULT vehicle has three air inlets (Figure 3.2): one inlet for the CAC (charge air cooler) and two inlets for main cooling package which consist of radiator (engine cooling) and condenser (air conditioning). Radiator and condenser are placed in a cooling frame vertically and CAC is placed horizontally, above the engine (Figure 3.3, a). All three air coolers have air guides, which are optimized for minimum aerodynamic losses and maximum air flow.

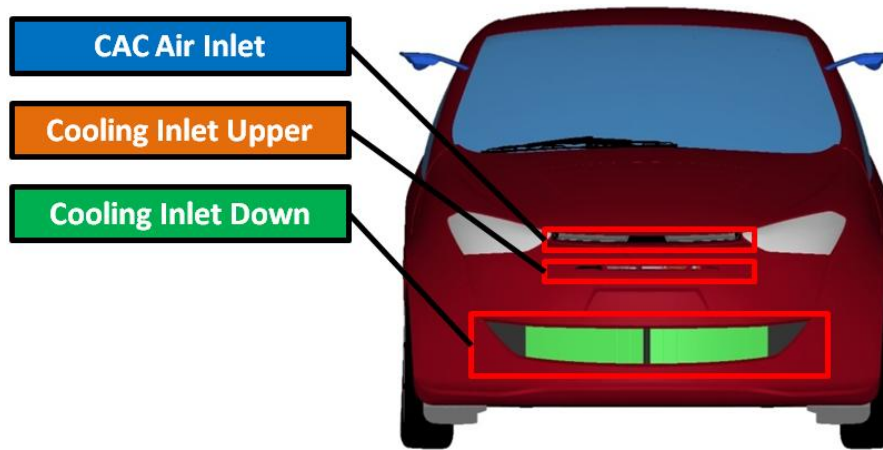


Figure 3.2 CULT's front-end air inlets

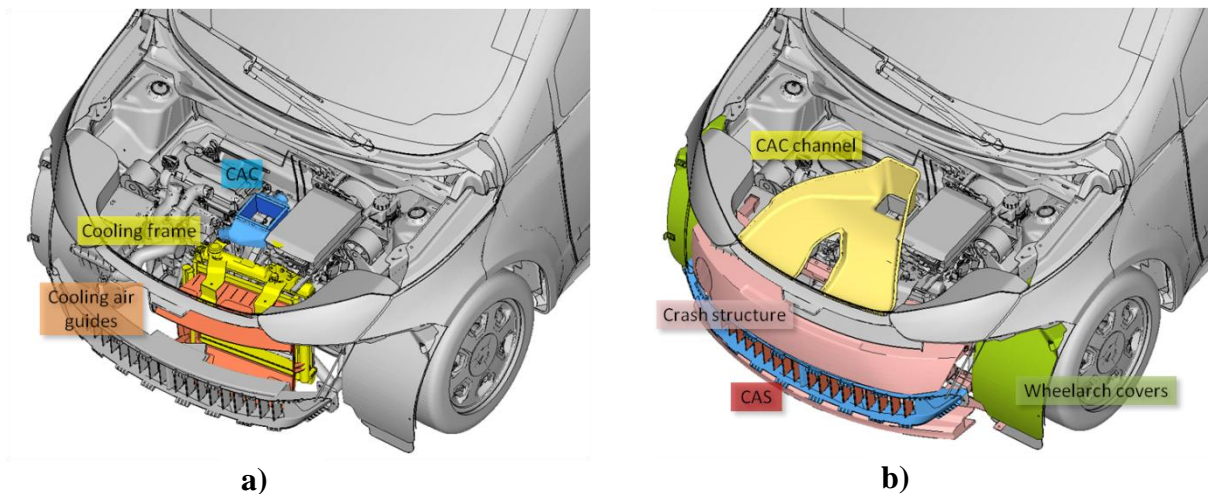


Figure 3.3 a) and b) - Front-end packaging

Engine requires a certain minimum mass flow through the coolers for optimal operation. The same is true for other devices which need cooling (e.g. charge air cooler, engine oil cooler, air conditioning condenser...). Task for engineers is to satisfy all these cooling requirements, with a minimum increase of aerodynamic drag.

Cooling air guides

Important part for the cooling and aerodynamic efficiency are so-called cooling-air guides (Figure 3.4). Coolers are porous bodies and they are creating resistance for air flow, therefore it is easier for the flow to bypass the coolers. Cooling air guides do not allow air to bypass coolers. With properly designed air guides all the air that is going inside air intakes is forced to pass through the coolers.

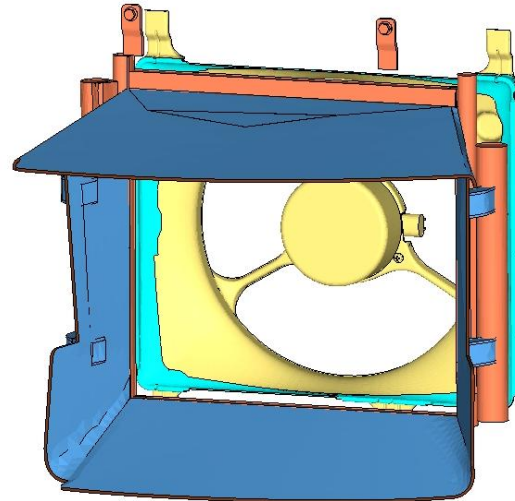


Figure 3.4 Cooling air guides on CULT cooling package

All air that goes inside engine compartment (passing through the coolers or not) interacts with engine and auxiliary devices before it leaves the engine bay. Most of the air usually re-joins the under body flow; part of the air is going out around wheels and through wheel arches, and part through the opening between engine compartment and front windscreen. In that way, lots of aerodynamic losses are generated. Letting the air passing through the engine compartment is necessary to satisfy requirements for minimum mass flow through the engine coolers. But not all the air that goes inside engine compartment participates to cooling. Part of the air that does not participate in cooling is a waste of energy and needs to be minimized. With the introduction of cooling air guides, unnecessary losses created by the air that is going through the engine compartment are minimized.

To see how much losses are generated in engine compartment, engineers use “mock up” geometry (by means of wind-tunnel or CFD simulations), where all inlets are closed, so there is no flow through the car. By comparing results of mock-up (closed inlets) simulation with the simulation of the standard car (with realistic geometry, e.g. open air inlets) cooling package efficiency can easily be determined.

Charge Air Cooler (CAC) channel

Because of limited space in engine compartment of the CULT car, charge air cooler is physically separated from rest of the cooling package and placed horizontally above the engine. Because of this position, special channel is required to provide it with sufficient amount of fresh air. This air channel is a bit more complicated than air guides because it’s purpose is not only to prevent the air to bypass the air cooler, it has to minimize the channel flow losses as well.

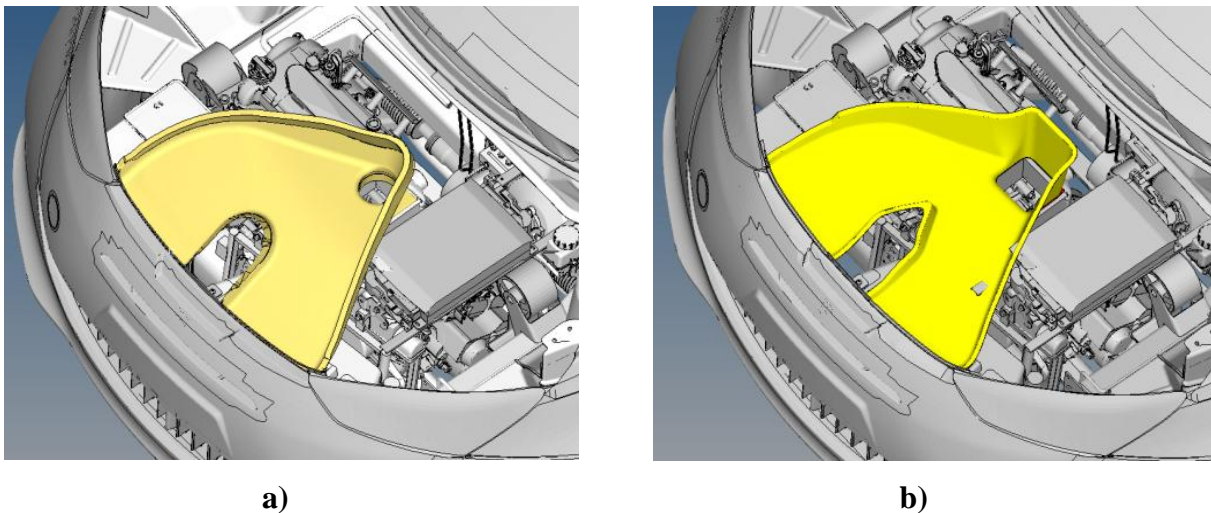


Figure 3.5 a) Initial CAC channel, b) Aerodynamically optimized CAC channel

In Figure 3.5 initial and aerodynamically optimized CAC air channel geometry is shown.

In Figure 3.6 below, streamlines clearly show that the basic channel was creating strong air swirling, which has reducing mass flow through the cooler. With aerodynamically optimized air channel this problem was reduced and the mass flow increased for approx. 25%. The optimization of channel geometry was performed in the Magna Steyr aerodynamics department by the means of software tools Ansys Fluent CFD solver and Tosca Fluid optimization program.

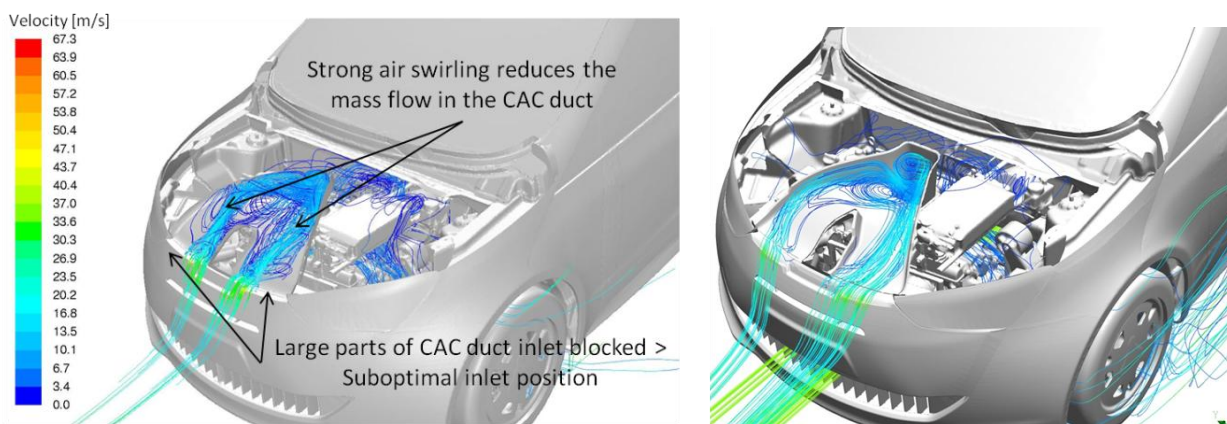


Figure 3.6 Left – initial CAC channel, right – new, aerodynamically optimized CAC channel

Active Cooling Air Shutter Mechanism (CAS)

It has already been mentioned how the air flow that goes inside engine compartment negatively influences the overall aerodynamics of the car. On the other hand, that air flow is necessary for the operation of engine and other devices. In general, when designing an air intake, engineers design it for the maximum mass flow required (“worst-case scenario” for engine cooling, usually an up-hill drive at low velocity with car pulling a trailer and/or driving at maximum speed on the highway with very high ambient temperature). Because engine does not need all the time that huge amount of air it would be a big benefit for aerodynamic drag if air intake can be closed when cooling air requirements are low. The CULT vehicle has such a device, and it is called Active Cooling Air Shutter mechanism (short CAS).

CAS (Figure 3.7) is basically frame in which moveable air flaps are located. There is an actuator in the middle of the frame, which moves air flaps to a desired position. There are two possible positions for air flaps: closed and open. Because of the curvature on the front bumper, which air flaps needs to match at closed position and fact that in the open position air flaps need to be aligned with the on-coming flow, every flap needs to rotate at different angle (Figure 3.8).

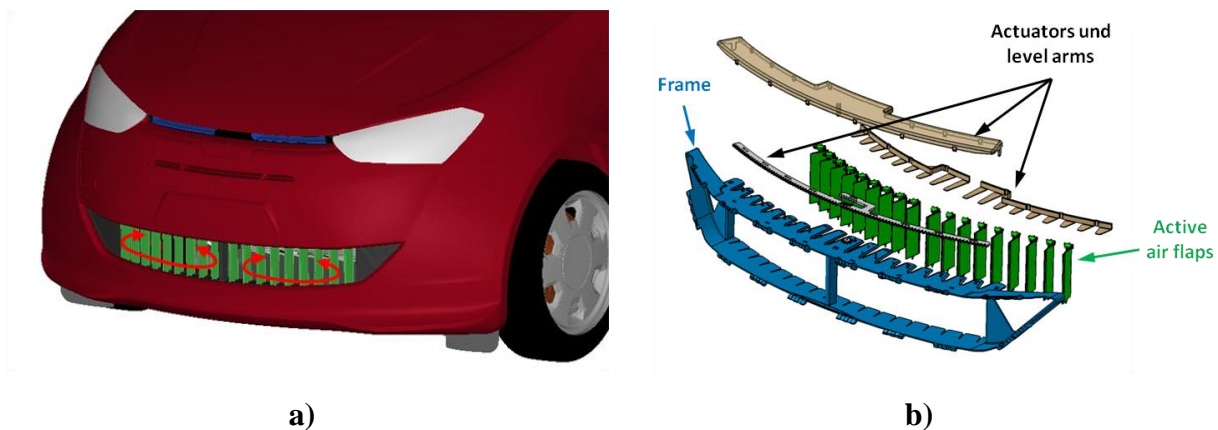


Figure 3.7 a) Air flaps at cooling air inlet, b) Parts of the assembly of CAS mechanism

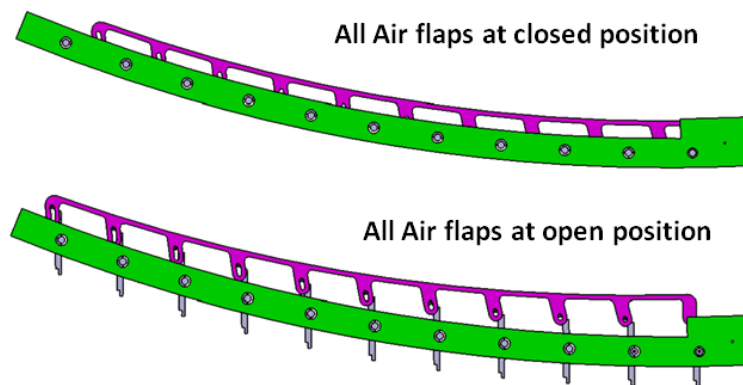


Figure 3.8 Closed and opened position of air flaps

In recent years the similar mechanisms are becoming popular in automotive industry because of increased demands on fuel efficiency and reduction of CO₂ emissions. Several automotive brands are already implementing this feature in their production vehicles, all of them in price range well above the CULT [18].

All this aerodynamics optimizations which involves cooling package need close collaboration between cooling experts, aerodynamicists and packaging specialists. Of course, if some modifications of exterior are required, also designer needs to be involved.

3.2 Side mirrors (Rear View Cameras)

Side view mirrors on the CULT are not classical mirrors, CULT uses rear view cameras instead. Still, in the following text, the term “side mirrors” will be used because it is a common term in automotive engineering.

From both aerodynamic and exterior styling points of view, the idea of cameras brings a lot of freedom in design. These side mirrors can be placed in position independent of driver’s field of vision and shape can be freely chosen (concerning that camera with necessary equipment can be fitted inside). Since side mirrors are very important parts in car’s design, usually a designer has the final word.

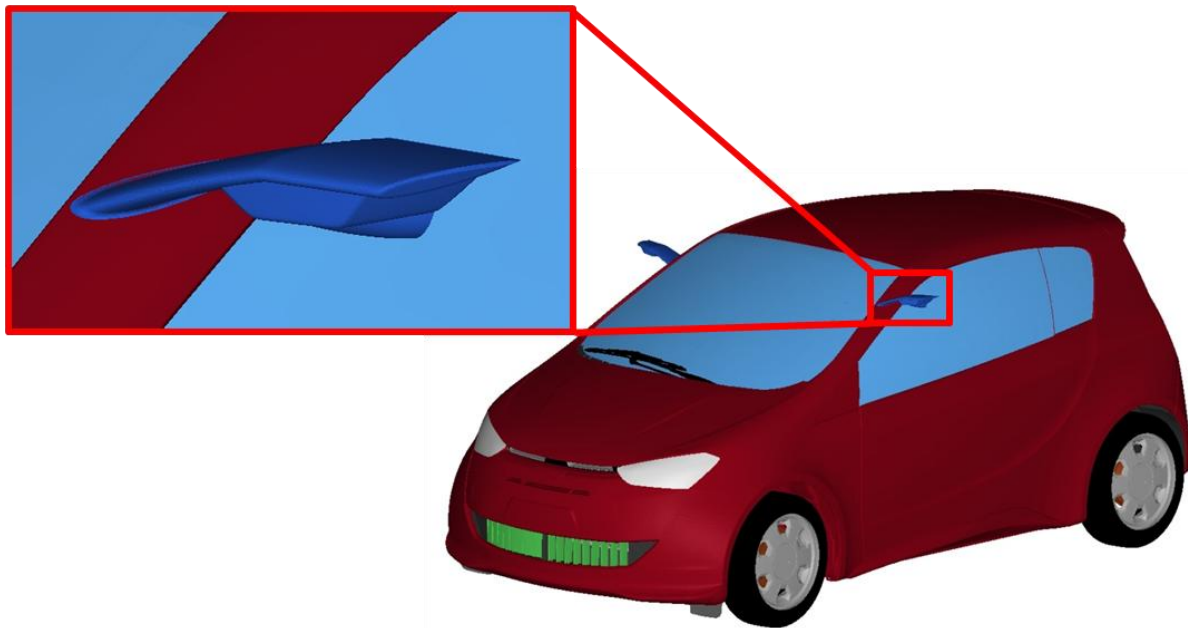


Figure 3.9 “Side mirrors” on the CULT

Figure 3.9 and Figure 3.10 show final shape of side mirrors in their initial position. Side view mirrors were subject of investigation and close collaboration between aerodynamicist and designer. Final product was a set of low-drag side mirrors, with additional potential for aerodynamics optimization (details in Chapter 7.10).

The CULT’s side mirror consists of two parts. One part is a wing-like carrier and another part is camera casing, where camera is mounted. For carrier shape popular NACA 0012 symmetric airfoil is used, because this airfoil was designed for a minimal aerodynamic resistance. Because of interesting position on the A-pillar, where lot of vortices are created, and because of special mirror (wing-like) shape, there is a lot of potential for aerodynamic research. Chapter 7.10 presents different side-view mirrors positions and orientations, which were tested in this research, and their influence on the overall aerodynamic characteristic of the vehicle.

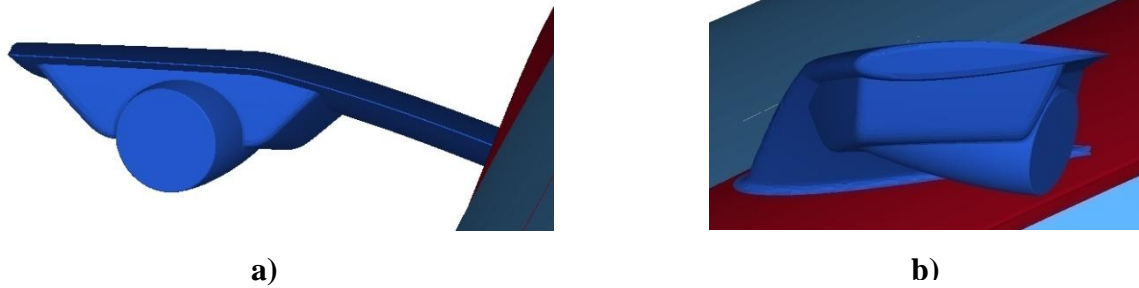
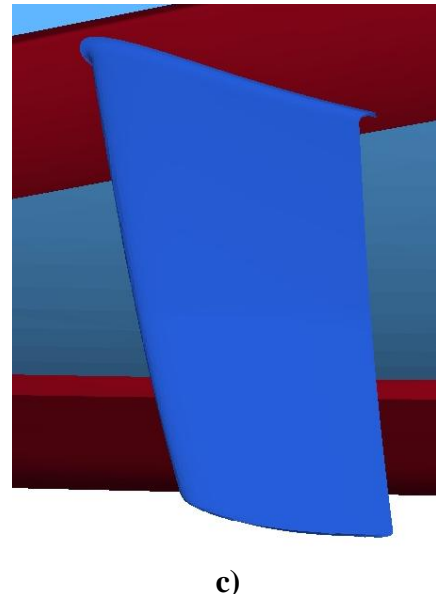


Figure 3.10 a), b) and c) - Side mirrors different views

Finally, the question is why this cameras need to be at the position where classic side mirrors are, when they could be integrated in door pillars or somewhere on the rear end of the car instead? Except potential styling and aerodynamic benefits from this shape and position, one of the main reasons for designing side mirrors in a “classical” way were production costs. In case cameras were placed inside the tailgate doors, the modification to the door structure and long wires to connect cameras with monitors in the cabin would be necessary. If mirrors were integrated in side doors, production cost of doors would increase.



Additional consideration favoring the chosen position of rear-view cameras is the driving safety. Rear-end positioned cameras are not able to cover the side of the vehicle, exposing the driver to potential risks during overtaking and/or changing lanes.

With potential styling, safety and aerodynamics benefits, positioning of side view cameras as a separate parts in the place of “classical” side mirrors seems the best choice.

3.3 Front-Wheel Spoilers

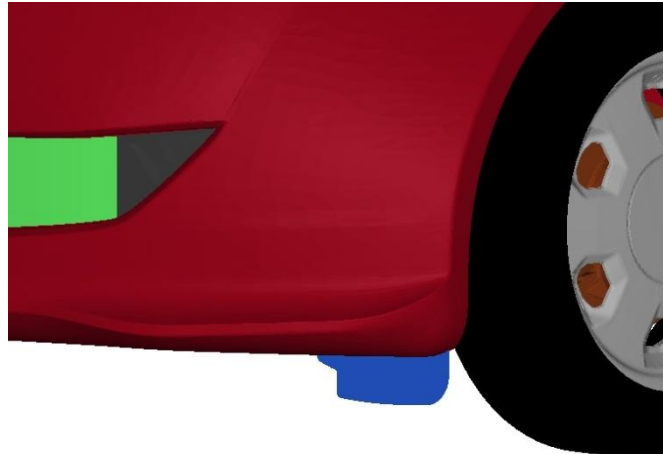


Figure 3.11 CULT Front-wheel spoiler (blue)

Wheel spoilers are very popular aerodynamic devices because of two reasons. First, they can reduce great amount of drag produced by wheels. Second, they can be very useful in aerodynamic optimization because of their aerodynamic interaction with under body and rear-end of the car. In addition, they are not so expensive for production. However, to find a suitable size and position of wheel spoilers is not an easy task and it usually requires lot of trial-and-error testing. With CULT only front-wheel spoilers are present (Figure 3.11). Generally, front-wheel spoilers contribute more to the lower aerodynamic drag than rear-wheel spoiler, so they are more important. In this thesis several different positions of front-wheel spoilers are examined, to show how big influence of wheel spoilers can be (Chapter 7.9)

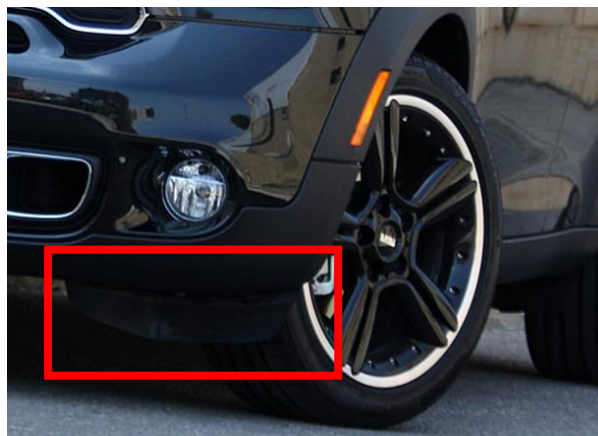


Figure 3.12 Front-wheel spoiler - MINI Countryman

4 CFD (COMPUTATIONAL FLUID DYNAMICS)

Aerodynamic flow around ground vehicles is very complex and it is not possible to fully mathematically describe it and find closed analytical solution. Hence, measurements of the aerodynamic properties in the wind tunnel still give irreplaceable and most correct results. Nevertheless, with advancing knowledge and careful usage of physical modeling and computational methods fluid flow around cars can today be mathematically described and numerically solved to a satisfying accuracy. That was one of the main motives to use Computational Fluid Dynamics (CFD) and ultimately reduce expensive experimental methods in automotive engineering. In general, CFD is a branch of fluid mechanics that uses numerical methods and algorithms to solve and analyze problems that involve fluid flows.

As the theoretical background of CFD methods is outside the scope of this thesis, only practical use of the method will be discussed in more details. For a theoretical background of CFD there is a wealth of literature available.

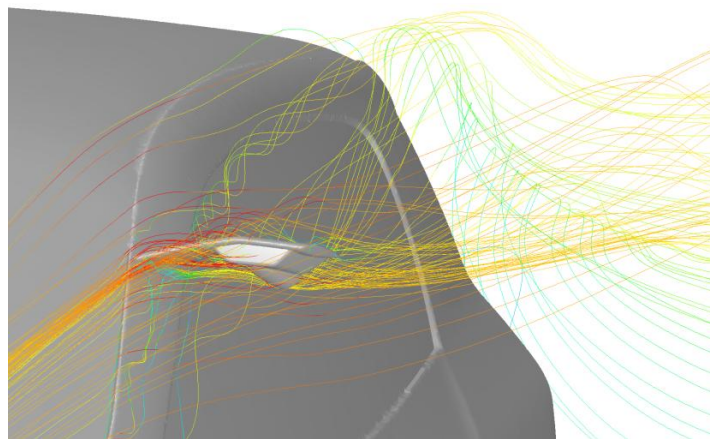


Figure 4.1 An example of CFD visualization - streamlines around CULT side mirrors

With constantly increasing computational power, CFD has become very popular and very practical in aerodynamic investigations in the automotive industry. With greater CPU power it is possible to get satisfying results in acceptable time. CFD solving methods are improving all the time, lots of different software packages are available and results reached sufficient accuracy to be reliably used in vehicle development. However, correct usage of CFD still continues to require a lot of knowledge and experience.

Usage of CFD brings following benefits compared with the wind tunnel measurements:

- There is no need for a real model – investigations are possible in early phase of project
- Analysis of the whole domain and visualization of the flow – better understanding of the flow physics
- Capital investments much lower than wind tunnel

In general, for every CFD test a corresponding validation in the wind tunnel would be required. However, today the CFD methods are so reliable and robust that number of required wind tunnel measurements can be significantly reduced. With CFD aerodynamically bad geometry cases can be easily recognized in the early phase of design, which speeds up the whole development process and reduces costs greatly. Today, both methods are in parallel usage in automotive industry because both have some irreplaceable advantages, and they generally give best results when used in parallel.

In CFD simulation process there are following standardized steps:

1. **Pre-Processing** (Chapter 4.1) - preparing geometry and creating CFD grid, usually the most time-consuming part of the process, lots of manual work required
2. **Solving** (Chapter 4.2) - Simulation Set-up and run
3. **Post-Processing** (Chapter 5) - Analysis of simulation results (usually the most challenging part - lot of engineering skills, knowledge and experience are required).

As already mentioned, after CFD simulation process is done the current “state of art” requires validation - measurements in the wind tunnel. With wind tunnel tests engineers can see how close CFD is to reality. In the validation process engineers need to take into account that even wind tunnel is only a simulation of reality, since the only reality is the actual road usage of a car. However, in automotive industry it is still customary to use the official drag coefficients that results from the wind tunnel tests.

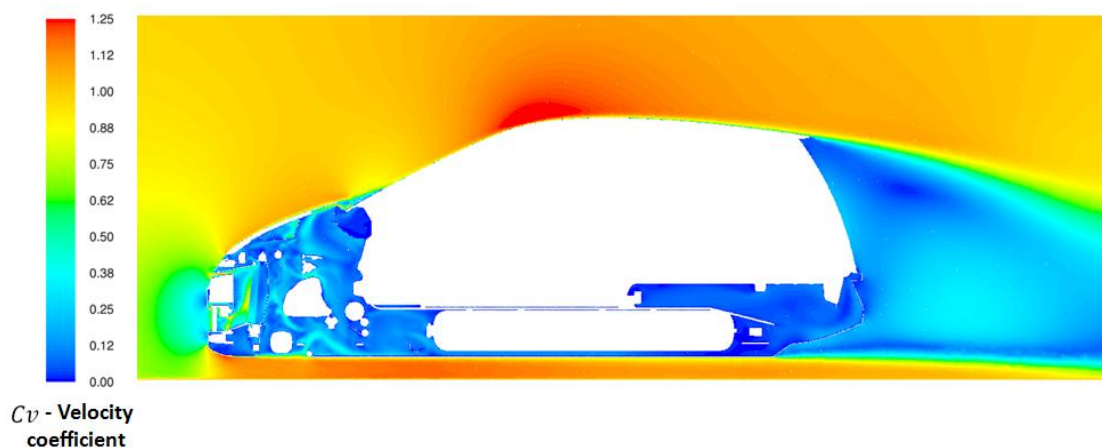


Figure 4.2 An example of CFD visualization: velocity coefficient contours in Y0 section of the vehicle

4.1 Pre-Processing

Task of CFD Pre-Processing is to create CFD grid, a set of discrete points on the vehicle surface and in the flow domain, which will be used in simulation. For this step, at the Magna Steyr Aerodynamic Department, two software packages are used; Altair HyperMesh (for surface preparation) and Ansys TGrid (for surface and volume meshing).

4.1.1 Altair HyperMesh

Choosing the appropriate geometry

In the design process of the vehicle, lots of different teams are working in parallel on different geometrical representations of the vehicle and whole process can be very complicated and difficult to synchronize. So, before starting any work aerodynamic engineer needs to be sure that he is dealing with the appropriate (updated) geometry. Depending on design stage, different geometries are available and current design stage geometry needs to be chosen. Correct geometry also implies correct position of suspension - the same position that will be used in the wind tunnel tests. For aerodynamic measurements, the so-called MAS II position geometry is used as a standard - complete car with suspension position that corresponds to the prescribed (standardized) load.

In the first phase of Pre-Processing the software Altair HyperMesh is used.

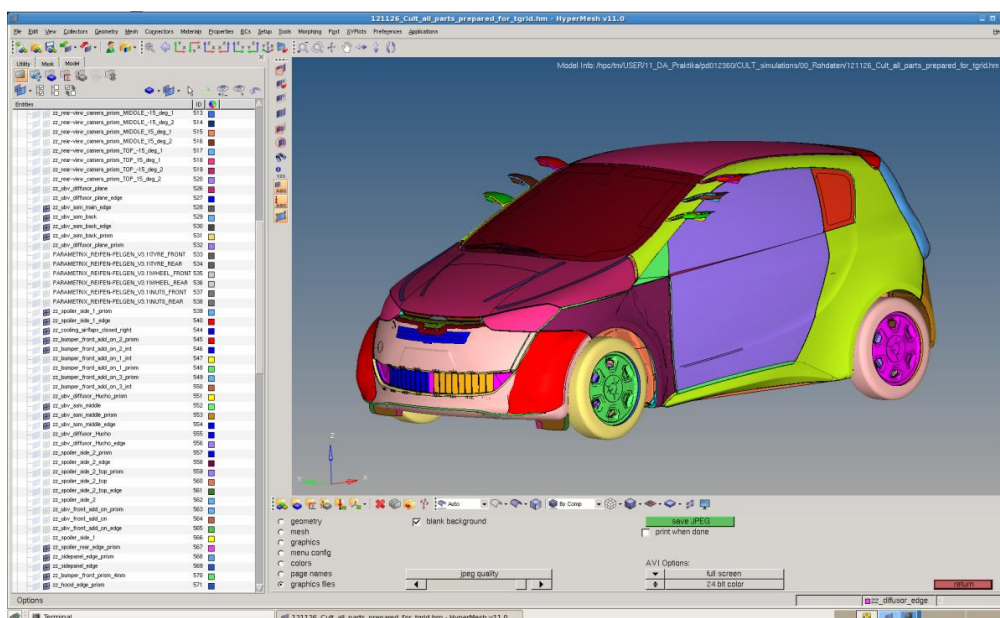


Figure 4.3 Altair Hypermesh working environment

Altair HyperMesh is a high-performance finite element pre-processor capable to prepare even the largest models, starting from import of CAD geometry to exporting an analysis run for various disciplines. HyperMesh enables engineers to prepare high quality meshes with

maximum accuracy. HyperMesh offers the biggest variety of solid meshing capabilities on the market, including domain specific methods such as SPH, NVH or CFD meshing [19].

Geometry preparing

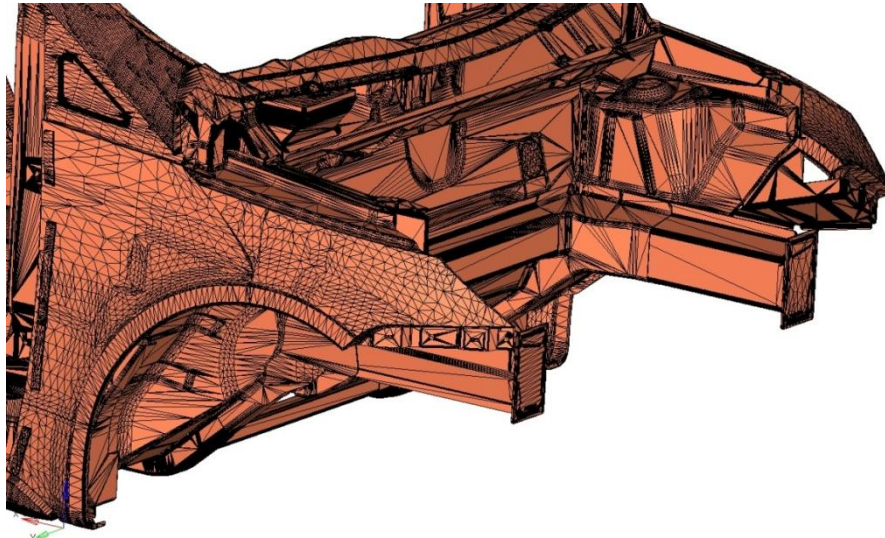
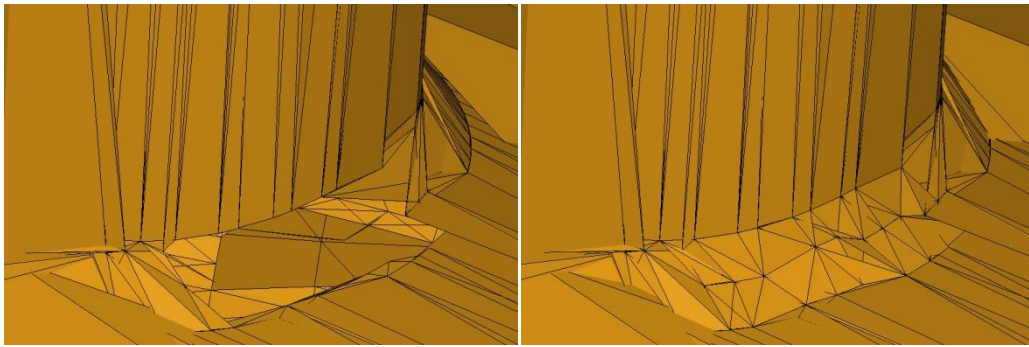


Figure 4.4 An example of a surface STL – format mesh, which is used to build a CFD model

CAD geometry is usually given in the form of unmeshed surfaces, so the first stage is to mesh surfaces. Also, at this point engineers need to prepare and simplify the geometry for better (faster, more reliable) aerodynamics simulation. With HyperMesh the user can create mesh, which is usually a 3D triangular surface mesh in the STL – format (Surface Tessellation Language) consisting of triangular 2D facets. From now on, surface mesh that represents geometry will be also called “geometry” and three-dimensional grid that represents fluid will be simply called “grid”.

Geometry of full CAD vehicle is very complex and, as a result, CFD grid on this complex geometry can be of less-than-perfect quality. That leads to simulation errors and/or very long computing time. Task of CFD engineer is to use his knowledge and experience to simplify the geometry in order to avoid later problems with too complicated grid. Also, simplification reduces final number of grid elements and enables shorter simulation duration.



a)

b)

Figure 4.5 a) – Hole in surface mesh, b) – Hole closed

For successful creation of CFD grid, geometry needs to be closed (“*watertight*”). At this point user needs to close all visible holes and, if necessary, create geometry which is for some reason missing. If some holes are not closed, there is a possibility that grid will be created inside body/geometry (meshing is going through the hole), which should be avoided. Rough closures can be done in Hypermesh, but the complete “*watertighting*” should be completed in another program, Ansys TGrid (see next chapter).

Which part of the geometry is not necessary, what can be deleted and what is necessary to be kept - these are the tasks that engineer is encountering now. Sometimes it is simple to make decision, but often is really hard to choose what can be changed and what not. Mistakes that are made here can adversely impact the whole process, so for this step engineer needs to take enough time. Final result after this step should be a compromise between simplification of the geometry and accuracy of final result - changes made on the geometry should not affect the accuracy of final flow simulation results.

4.1.2 Ansys TGrid

When procedure in HyperMesh is done, surface mesh is transferred into Ansys TGrid.

ANSYS TGrid software is a specialized preprocessor used to create unstructured prismatic/tetrahedral, Hex-Core or native hexahedral (Cull-Cell) grids for complex and very large surface meshes. TGrid offers advanced prism layer creation tools including collision detection and sharp corner handling. TGrid is also equipped with an advanced wrapping procedure that produces a high-quality, size function driven connected triangular surface mesh from a large set of unconnected faceted surfaces. TGrid software's robust, automated algorithms save preprocessing time and generate high-quality meshes for CFD analysis in ANSYS Fluent software.

Extensive tools are included in TGrid for improving imported surface mesh quality and for rapidly assembling meshes from multiple parts.

TGrid's convenient mesh quality diagnostic tools allow easy verification of mesh size and quality [20].

Creating octree patch

As already mentioned in previous chapter, final stage of watertighting should be done in TGrid. TGrid has a special tool for that, the so-called “octree patch”. Purpose of the octree patch is to close rest of the holes and disallow the grid from going inside the body later in the process. Octree patch should be made on all parts where is not sure that the part is completely closed (without any hole). In the case of CULT geometry, octree patches were made on body-in-white, with some additional parts - doors, tires, engine, roof, crash structures, hood, lights, tank, transmission... - Figure 4.6 a) and b). In general, “patches” can be imagined as balloons that are inside every hollow part with the purpose to block CFD grid going inside.

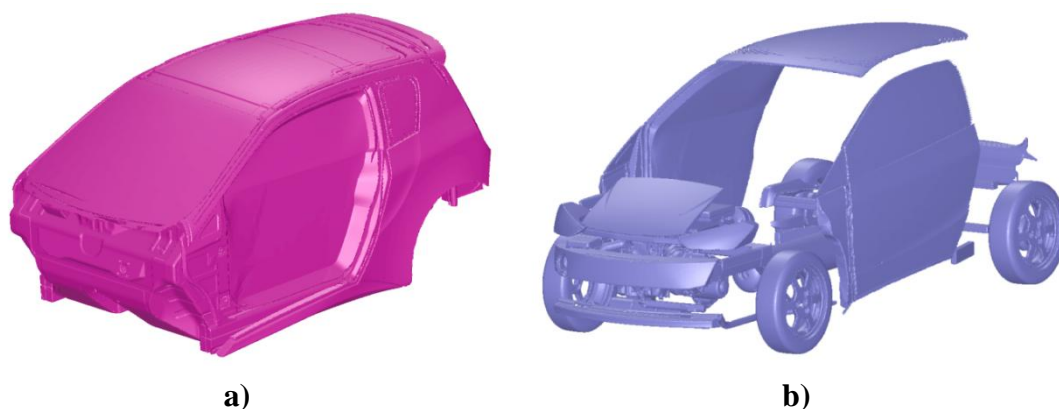


Figure 4.6 a) and b) - Patches for different CULT parts in TGrid

After octree patches are made, rest of the Pre-Processing can be semi-automated with the help of scripts and standards. The scripts are lists of commands that replace input of manual commands by user. Scripts are very useful, saving a lot of time and reducing possibility for mistakes. But, to use scripts, first, valid standards should be determined. To use same scripts on different vehicles, also geometry preparing in Hypermesh and TGrid need to be done with the usage of same standards.

In the following text, process based on scripts will be shortly described.

Coolers tri-dimensional grid

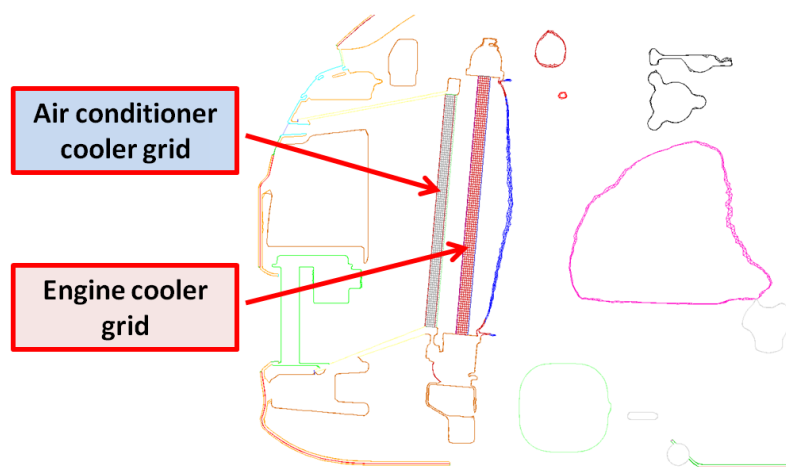


Figure 4.7 Y0 section of the car geometry with cooler grid

Coolers need to be represented as a structured grid (grid made from rectangular elements). In the original CAD geometry only the coolers frames exist (see Figure 3.4). Structured grids need to be integrated inside these frames. Later, in simulation Set-Up, porosity to cooler’s structural grid will be added, therefore CFD coolers will be able to simulate the effect of real coolers on the flow through the engine compartment.

Wrapping

With wrapping all parts are wrapped into one continuous surface – wrapper surface. In that way the complete geometry becomes a single surface, which is a starting point for CFD surface grid. Therefore, in further procedure only the wrapper surface is needed.

Refining wrapper surface

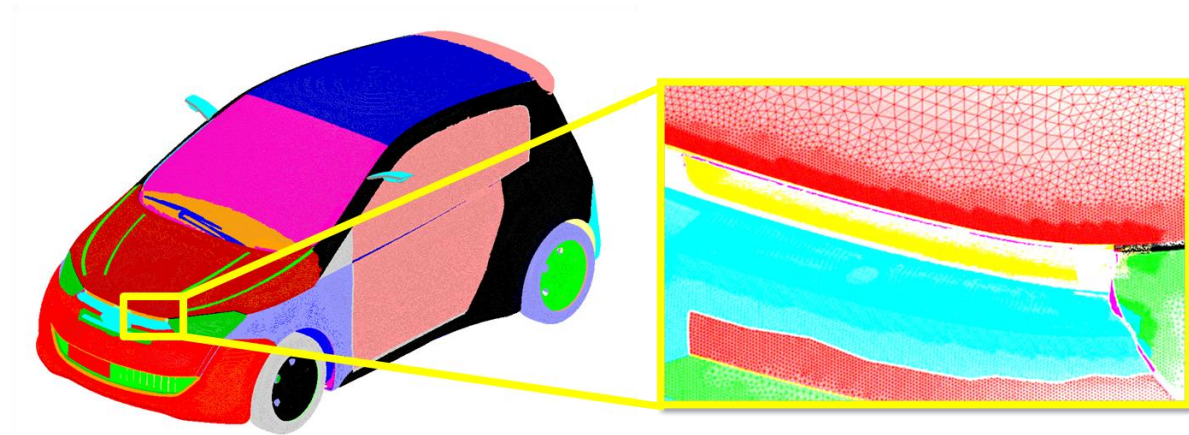


Figure 4.8 CULT wrapper surface: refined and separated on the parts

At this point engineer has a difficult task – to refine the wrapper surface in order to capture the flow features near walls correctly and to enable the automatic generation of a subsequent volume mesh. Generally, the most important phenomena in fluid flow are generated close to the surface. Therefore, quality of wrapper surface has a big influence on the results. Basic guidelines for wrapper surface refining: in places where big gradients of physical quantities are expected, finer surface mesh should be present. Consequently, making good CFD surface mesh is usually an iterative process. With growing experience, good meshes can be made in first attempt, because same types of cars, as well as same areas of the car, usually have similar aerodynamic behavior. That also opens a possibility to make refinement standards for each type of the car and save CFD preprocessing time.

Importing “Wind Tunnel”

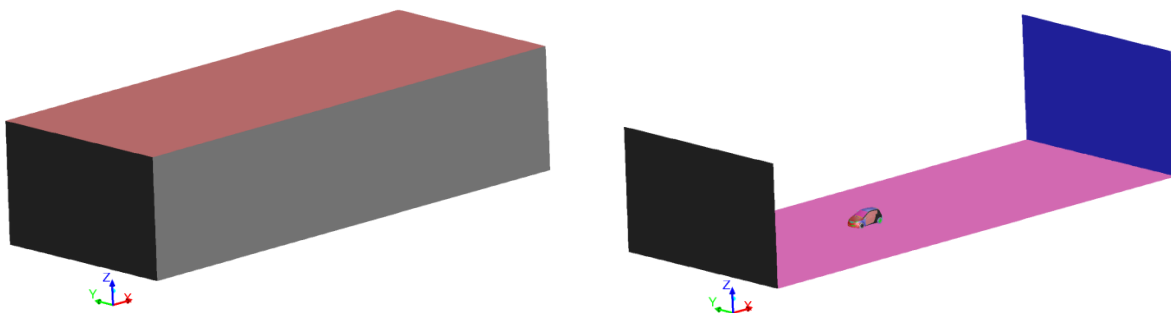


Figure 4.9 Fluid domain boundaries – virtual Wind Tunnel

The outer extent of every CFD open-air simulation needs to be limited by some boundaries and these boundaries should possess valid boundary conditions. In other words, a CFD low domain needs to be bounded. In automotive industry, creating boundaries is also called “Importing Wind Tunnel”, because these boundaries can be observed as a virtual wind tunnel around the vehicle. Virtual wind tunnel is represented by six surfaces, connected into one

rectangle: inlet, outlet, two side borders, top border, and ground. All boundaries should be properly meshed surfaces. Because CFD grid in this particular case will be made out of tetrahedral elements, wind tunnel planes are meshed with triangle elements. Size of these elements depends on the maximum size of the elements that will be used for CFD volume grid generation. Also, it is very important to pay attention to the wind tunnel ground refinement, especially under and close to the vehicle. Later, in the simulation set-up (see Chapter 4.2), boundary conditions for these six surfaces will be defined.

Actually, wind tunnel is also a part of the wrapper surface, because it is connected with the car wrapper surface over tires (connection between tires and ground/road). For easier understanding it can be said that CFD grid will be created inside one big wrapper surface, which connects vehicle surface mesh with the WT surface mesh.

Wheels cutting

Wheels are very important part in aerodynamic simulation. They are the only existing connection between wrapper surface of the car and the wind tunnel. After wind tunnel is imported, valid connection between ground of the wind tunnel and the car’s wheels has to be made. In reality, where wheels are touching the ground, wheels are flattened; therefore, a good approximation of the reality can be made by cutting tires with the wind tunnel ground. Where exactly to slice the tires can be calculated from the dynamic radius of the wheel [4].

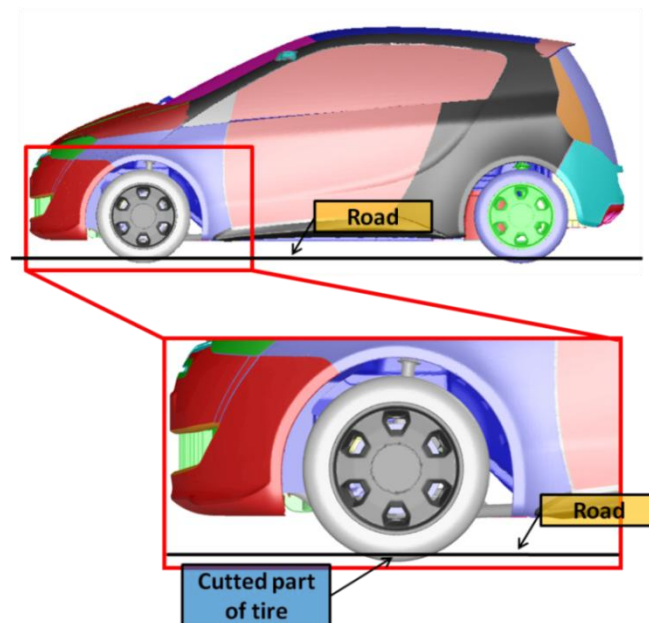


Figure 4.10 Wheels cutting and connection with the ground

Approximate dynamic radius of the wheel can be calculated from the following formula [4]:

$$r_d = 0.97 \cdot r$$

r_d – dynamic radius of the wheel

r – radius of undeformed (unladen) wheel

4.1.3 Grids

In general, for CFD simulations in automotive industry, hybrid grids are in use. Hybrid grid consists of two types of elements: **prismatic elements** along viscous walls and **tetrahedral or hexahedral elements** in the rest of the domain.

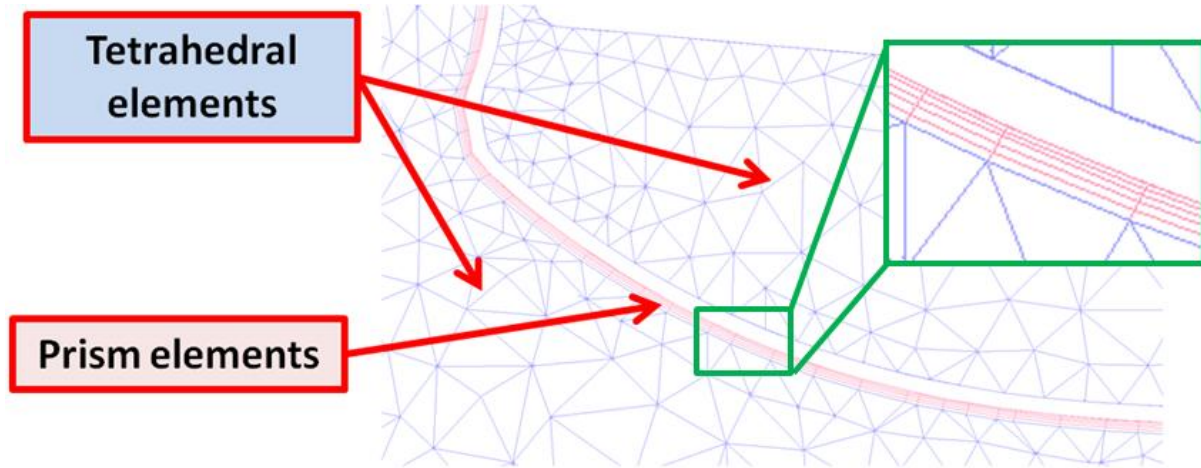


Figure 4.11 Cut through the three dimensional hybrid grid. Red elements are prisms and the blue ones are tetrahedral elements.

Prism elements bring better results close to the body surface, where viscous forces play important role. However, prism grid is structured and it is difficult to create such a grid on a complicated 3-D geometry. On the contrary, tetrahedral elements are numerically less accurate but tetrahedral grid is unstructured and this allows much simpler grid creation.

Boundary layer – Prism layer

On the most of the vehicle “wetted” external design surfaces (in general design surfaces are all surfaces which can be seen from outside the car or inside the passenger cabin) flow is attached and boundary layer in the fluid flow is present. In the boundary layer friction forces are very important and there prism elements should be used. Design surfaces are usually simple and smooth enough for creating prism elements without spending too much time. Of course, the best would be to put the prism elements on all surfaces – e.g. inside engine compartment and under body. Because of very complicated geometry on these surfaces a lot of time would be necessary for such an operation, usually without big influence on the final results of CFD simulation. Therefore, the best compromise is to create prism layers only on design surfaces, where attached boundary layer is expected.

Settings for prism layer are usually standardized. Later, in Chapter 7.1, different setting for prism layer will be investigated.

Total number of prism elements is determined by number of surface elements where prisms will be created and number of prism layers (e.g. if surface has one million of elements, and total five layers of prisms are created, total number of prism elements is five million).

Total accumulated prism layer thickness should be of similar size as the boundary layer thickness. Boundary layer thickness (δ) can approximately be determined from empirical formulas [1]:

- Boundary layer thickness for laminar flow:

$$\delta = \frac{5.0x}{\sqrt{Re}}$$

x – boundary layer length

Re – Reynolds number

- Boundary layer thickness for turbulent flow:

$$\delta = \frac{0.37x}{Re^{\frac{1}{5}}}$$

Tetrahedral grid

After prisms are generated, rest of the domain is filled with tetrahedral grid. To reduce final number of grid elements, without decreasing precision of final results, it is very important to understand where is necessary to put smaller elements and where not. Smaller elements should be used in the regions where higher gradients of physical quantities are expected. In the areas where gradients are not expected it is better to use bigger elements, which will still give correct results without great influence on the total number of grid elements.

During grid generation the engineer needs to carefully determine tetrahedral grid settings. Settings can be divided onto **global settings** and **refinement zones settings**.

Global settings refer to the whole domain. Input values are element growth rate and maximum element size.

Refinement zones are used where special grid settings are required (where global grid settings are not sufficient). Each refinement zone (Figure 4.12) has its own local element growth rate and maximum element size. Actual version of TGrid allows cuboid shapes of refinement zones. Two cuboids (inner and outer) define one refinement zone. Inner cuboid (defined with black lines in the Figure 4.12) defines boundaries where maximum element size will be kept. Outer cuboid (defined with green lines in the Figure 4.12) defines area where elements are able to grow with dedicated growth rate. Purpose of this area is to match element sizes of different zones. Final size of an element at the edge of the “green” area should be close to element size in surrounding area.

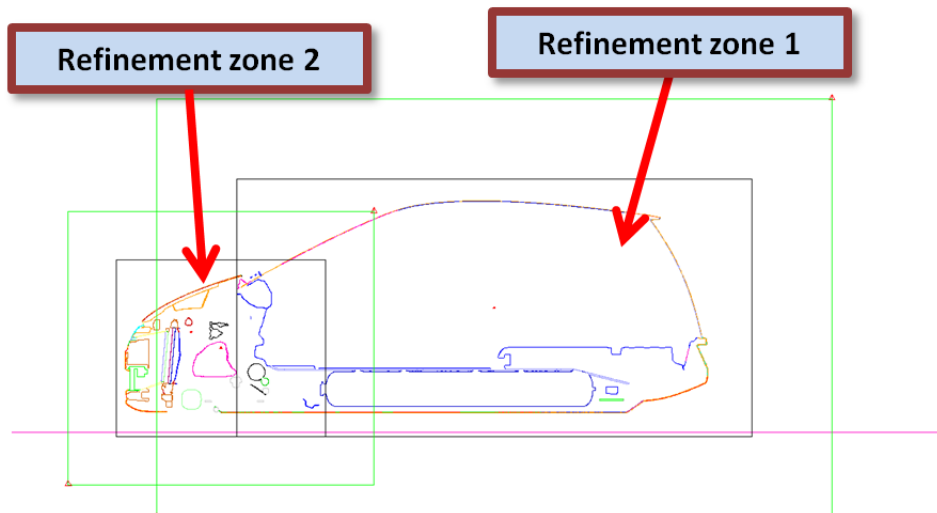


Figure 4.12 An example of refinement zones in T-Grid

Combining more of these refinement zones engineer needs to create grid with satisfying element sizes. There are two guidelines to be followed:

- First from the aerodynamics point of view – put smaller elements in areas where fluid flow features are changing
- Second, from the CFD point of view – transition from small to big elements should be made without large element-size jumps.

An important notice to an inexperienced user at this step is: if there is a need to change element size close to the surface it is necessary to go few steps back to the “Refining wrapper surface” (see previous chapter). It is always good to keep in mind that, as everything else, grid is building from foundations – elements close to surface are largely determined with surface mesh.

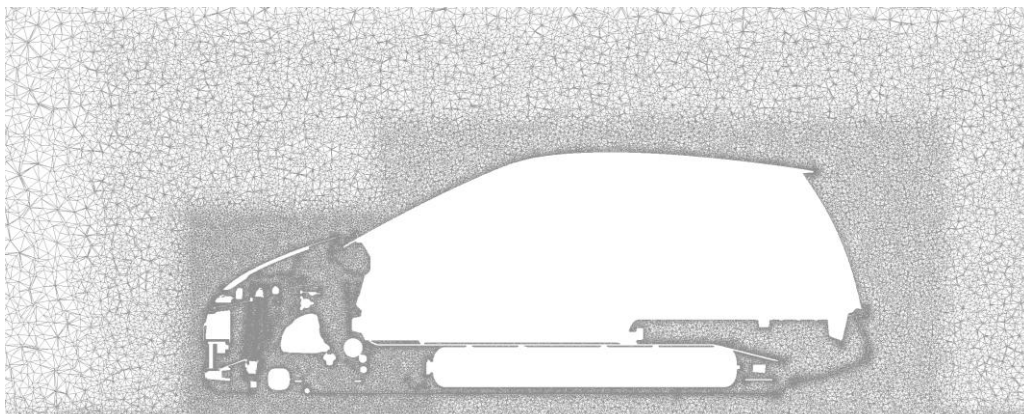


Figure 4.13 Y0 section of CULT CFD grid – Fluent Post (borders between refinement zones can be clearly seen)

To sum up, a CFD grid is growing from the wrapper surface. First prismatic layer is determined directly by the underlying wrapper surface, and each other layer from previous one and the prescribed growth rate. Tetrahedral cells are growing until element size reaches its maximum size. Maximum size is determined by the global settings and refinement zones settings. It is very important to keep in mind that CFD grid is growing inside one wrapper

surface, which is defined with the vehicle wetted surface and wind tunnel. Note: wind tunnel surface mesh should be corresponding size to the maximum element size in the grid (defined in the global grid settings).

As in every project, engineer need to be aware of the deadlines and available resources. Accordingly, total Size of the grid is limited by CPU availability and deadlines. In the CULT project, targets for final number of grid elements have been set to:

- Prism elements: around **5 millions**
- Tetrahedral elements: around **60-70 millions**

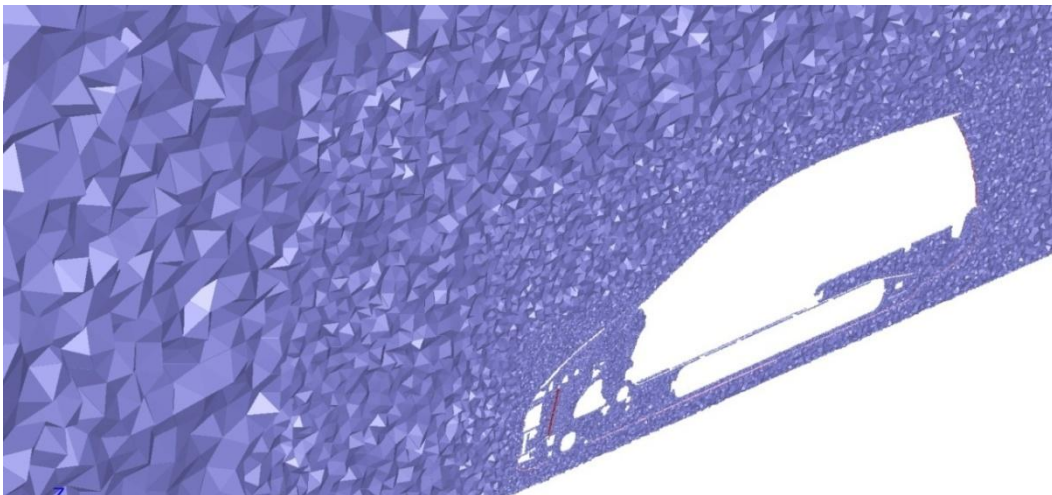


Figure 4.14 Y0 section for CULT CFD grid – TGrid

4.2 Solver – ANSYS Fluent & Simulation Set-Up

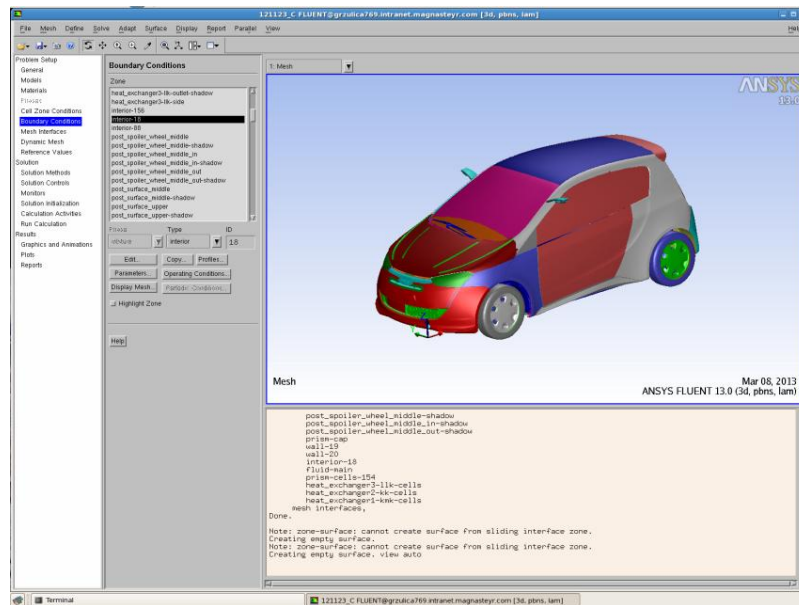


Figure 4.15 ANSYS Fluent working environment

About Fluent

ANSYS Fluent software contains the broad physical modeling capabilities needed to model flow, turbulence, heat transfer, and reactions for industrial applications. Applications range from air flow over an aircraft wing to combustion in a furnace, from bubble columns to oil platforms, from blood flow to semiconductor manufacturing, and from clean room design to wastewater treatment plants. Special models that give the software the ability to model in-cylinder combustion, aero acoustics, turbo machinery, and multiphase systems have served to broaden its reach.

Advanced solver technology provides fast, accurate CFD results, flexible moving and deforming meshes, and superior parallel scalability. The interactive solver setup, solution and post-processing capabilities of ANSYS Fluent make it easy to pause a calculation, examine results with integrated post-processing, change any setting, and then continue the calculation within a single application. Case and data files can be read into ANSYS CFD-Post for further analysis with advanced post-processing tools and side-by-side comparison of different cases.

The combination of these benefits with the extensive range of physical modeling capabilities and the fast, accurate CFD results that ANSYS Fluent software has to offer results in one of the most comprehensive software packages for CFD modeling available in the world today [21].

4.2.2 Simulation Set-Up

Basic numerical settings:

- Time dependency: NO (steady simulation)
- Solver: coupled solver (pressure based)
- Turbulence model: k- ω SST
- Number of iterations: min. 1500

In this thesis only steady simulations are employed. This brings a degree of inaccuracy due to inherently unsteady flow around ground vehicles, but CPU-related limitations (number of cores and RAM available) allowed only that approach. However, in many cases steady simulation is a fast way to get enough correct results to estimate aerodynamic efficiency of the vehicle.

Pressure based solver is used when maximum air speed in the flow is below mach 0.3. In that case air flow can be considered as incompressible and there is no need to take compressibility into account.

Set up of corresponding turbulence model depends on the flow type we are trying to simulate. Every turbulence model available in Fluent was created based on specific fluid flow behavior. In case of a typical car, the k- ω SST turbulence model was used, which is suitable for the bluff-body type of flows. Compared to the wind tunnel measurements, the k- ω SST turbulence model shows good results in most cases.

For a simulation to finish properly, all physical values have to be numerically converged, so minimum number of iterations needs to be carefully chosen. As it will be shown in Chapter 7, sometimes it could happen that simulation ostensibly look like it converged, but in reality it did not. If there is a reasonable doubt that simulation did not converge, simulation needs to be restarted for additional iterations.

Physical settings:

- **Air speed and Mach number**

Generally, in automotive aerodynamics, default air speed used for wind tunnel measurements is 140 km/h (38.89 m/s). Mach number (M) is dimensionless coefficient that represents ratio of the current air speed and local speed of the sound:

$$M = \frac{u}{u_{sound}} = \frac{55}{340} \approx 0.16$$

$u \approx 55$ m/s – greatest air speed in simulation (at the leading edge of the roof)

$u_{sound} \approx 340$ m/s - local speed of sound

When Mach number is below 0.3 flow can be considered as incompressible, which simplifies calculation method. In the case of CULT, the greatest air speed in the simulation is far away below Mach number of 0.3, therefore flow is considered as incompressible. Note: greatest air speed is usually at the leading edge of the roof.

- **Air properties:**

Air properties need to be set up for standard atmosphere. It is very important to set up these parameters correctly to avoid possible errors later, when results will be compared to other simulations/tests.

- Temperature: $t = 20 \text{ }^\circ\text{C}$
- Dynamic viscosity: $\mu_\infty = 1.833 \cdot 10^{-5} \frac{\text{kg}}{\text{ms}}$
- Air density: $\rho_\infty = 1.203 \frac{\text{kg}}{\text{m}^3}$

These properties are valid for undisturbed flow – at the air inlet and far away from vehicle.

- **Reynolds number:**

Reynolds number is dimensionless coefficient that represents ratio of inertial and viscous forces in a fluid flow:

$$Re = \frac{\textit{inertial forces}}{\textit{viscous forces}}$$

In the case of the air flow investigated here, Reynolds number is:

$$Re = \frac{\rho_\infty \cdot u_\infty \cdot L_{ref}}{\mu_\infty} = \frac{1.203 \cdot 38.89 \cdot 1.8}{1.833 \cdot 10^{-5}}$$

$$\mathbf{Re = 4.6 \cdot 10^6}$$

$u_\infty = 38.89 \text{ m/s}$ – air inlet speed

$L_{ref} = 1.8 \text{ m}$ – referent length (vehicle width)

If the formula for Reynolds number is analyzed, it is obvious that air speed is only variable that can significantly change Reynolds number in the case of full-scale vehicle (ref. length, density and viscosity are constant). Later, in the Chapter 6, when wind tunnel scaled model will be introduced, this connection between air speed and Reynolds number will be significant for air inlet speed determination, required for scaled model tests.

Boundary conditions

Flow domain is surrounded by six planes, called wind tunnel boundaries (see chapter 4.1.2 – Importing “Wind Tunnel”). Each plane need to poses valid boundary condition. Figure 4.16 shows three planes of a virtual wind tunnel. Grey plane is defined as air inlet, blue plane as air outlet and the purple plane as a moving ground. Other three planes that are not showed here (two side planes and top plane) are defined as symmetry plane.

Except for the wind tunnel, boundary conditions also need to be defined for the car geometry. Wheels are defined as rotating wall, and all other parts of the car are simply defined as walls. The flow is defined as viscous flow, which implies boundary layer on all surfaces.

For details and settings explanations see [25].

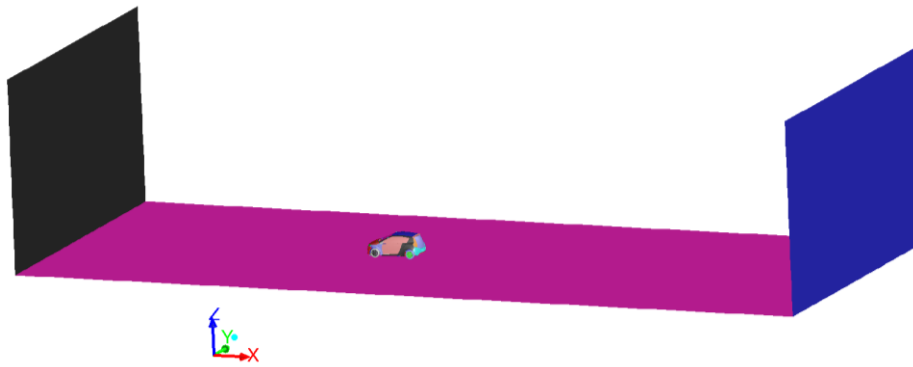


Figure 4.16 Virtual Wind Tunnel around car– boundary conditions. Purple plane is defined as a ground, grey plane as an air inlet and the blue plane as an air outlet.

Cooling package

Cooling package radiators in simulation are presented as cuboid volume cells - Figure 4.7 in Chapter 4.1.2. Adding adequate porosity level to the cells allows accurate simulation of pressure drop through the coolers. The only problem here is correct determination of porosity level, which requires experimental measurements.

Coordinate system

In the automotive standards, origin of coordinate system in CAD geometry is usually not same as in CFD simulation. Before simulation starts it is necessary to move origin to the position required for CFD simulation in order to correctly compute forces and moments acting on the car (see Chapter 1.2.2).

Settings overview – CULT simulation 01

Bellow the settings overview for basic simulation in this thesis (CULT simulation 01) is given. All other simulations are based on these settings.

Table 4.1 Grid settings overview for CULT simulation 01

Grid settings						
Tetrahedral settings	Value:	Unit:	Tetrah. refinement boxes		Max. cell vol. [mm ³]:	Local growth rate:
Number of tetrahedral el.	56.3	millions	Box	Location		
Global growth rate	1.4	-	Box10	Side mirrors	80	1.1
Max cell volume	7.0E+06	mm ³	Box15	Wheels	250	1.1
Prism settings			Box25	Engine compart.	500	1.1
Number of prism el.	5.7	millions	Box50	Close to vehicle surf.	3500	1.1
Number of prism layers	5	-	Box100	Vehicle and wake	35000	1.1
First layer height	0.3	mm	Box200	Far from vehicle	400000	1.15
Prism layer growth rate	1.2	-				
Prism layer total height	2.23	mm				
Number of surface el.	1.14	millions				
Edge size min/max	2/8	mm				
Tot. number of grid el.	62	millions				

Table 4.2 Numerical and physical settings overview for CULT simulation 01

Numerical settings		Physical settings		
Simulation type	Steady simulation		Value:	Unit:
Type of flow	Viscid flow	Fluid type	Air	-
Solver	Coupled (pressure based)	Reynolds number	4.6·10 ⁶	-
Turbulence model	k-ω SST	Max. Mach number	0.16	-
Number of iterations	1500	Air properties		
Boundary conditions		Temperature	20	°C
Vehicle		Density	1,203	kg/m ³
Vehicle's surface	Stationary wall - roughness 0	Dynamic viscosity	1.833·10 ⁽⁻⁵⁾	kg/ms
Wheels	Rotating wall - roughness 0	Air inlet speed	38.89	m/s
Wind tunnel		Referent values		
Ground	Moving wall - roughness 0.5m	Referent area	1.978	m ²
Air inlet	Yaw 0° - air speed 38.89m/s	Wheelbase	2.3	m
Air outlet	Pressure outlet	Vehicle width	1.8	m
Side walls	Symmetry plane			
Top wall	Symmetry plane			

5 POST-PROCESSING

Post processing is the most challenging phase of every CFD process and it needs to be carried out with great attention. After the simulation finishes, it needs to be inspected. If engineer conclude that simulation is valid, Post-processing needs to be carried out.

In a typical aerodynamics development project many simulations are performed and it is often necessary to compare results of various simulations. In practice, there is usually no time to post-process all simulations with the same standards (with the same procedure), but only the simulations which carry most important information for the project. However, later in the project engineer usually wants to compare simulations from different state of car development (new results against old results) and that often means doing the post-processing of old results again. That is one of the main reasons for introducing standards into Post-processing. If every simulation is post-processed in the same way, comparing simulation results is much easier and more efficient.

Deadlines in the project are one more reason for introducing standardization in the post processing. With standardization, a lot of time can be saved. This time can be used for improving accuracy of simulation results and/or simulating additional aerodynamics parts of the car in development.

In this Chapter standard post-processing phase in the CULT project will be overviewed and briefly explained. Results from the first simulation made for purpose of this thesis, CULT simulation Nr. 01, will be used for that purpose. For every simulation, a standardized set of pictures and data is stored in the simulation folder, allowing easier data manipulation and comparison of different simulations.

5.1 Simulation results

Simulation results from simulation folder are loaded into Excel file. It is very convenient to have all important simulation data in one place, sorted and visualized. Microsoft Excel is good and simple solution for that purpose. It has a possibility to be programmed to read Fluent output text files and create diagrams and tables. Table 5.1 and Table 5.2 shows data from CULT simulation 01 stored in Excel table.

Table 5.1 An example of simulation data stored in Microsoft Excel

Project and calculation data			
Date:	24.11.2012	Inlet velocity [m/s]	38,889999
Jobnumber:	358824	Density [kg/m ³]	1,20279
Data status:	CAS open, basic simulation	Projected area [m ²]	1,978
Job user name:	Puljic Damjan	Wheel base[m]	2,300
		Dyn. pressure q [Pa]	909,57
Temperature air [°C]	20	Number of iter.s for avg. Values	200
Dyn. viscosity [Pa*s]	1,8330767E-05	Standard deviation Cx in points	2,0
		Standard deviation Cz in points	6,0
		Standard deviation Cmy in points	1,0

Table 5.2 An example of simulation results in Microsoft Excel

Results with heat-exchanger(s)					
Name	[unit]		Coefficients		
Drag Force	Px [N]	609,2	Cx	0,339	$Cx=Px/(qx F)$
Side Force	Py [N]		Cy		$Cy=Py/(qx F)$
Lift Force	Pz [N]	-49,2	Cz	-0,027	$Cz=Pz/(qx F)$
Rolling moment	Mx [Nm]		Cmx		$Cmx=Mx/(qx Axt)$
Pitching moment	My [Nm]	-302,5	Cmy	-0,0730	$Cmy=My/(qx AxL)$
Yawing moment	Mz [Nm]		Cmz		$Cmz=Mz/(qx AxL)$
Front wheel lift force	Pzf [N]	-156,6	Czf	-0,087	$Czf=Cz/2+Cmy$
Rear wheel lift force	Pzr [N]	108,0	Czr	0,060	$Czr=Cz/2-Cmy$

The most important results are drag and lift coefficients (for definition of these coefficients see Chapter 1.1). Excel calculates these values from diagrams created during simulation. Final values, represented in Table 5.2, are average values of certain number of last iterations. Number of iterations that is averaged is defined in Table 5.1. It is very important to have properly converged results, which enable extraction of unambiguous mean values, otherwise results are not valid. Simplest way to estimate convergence is to look at aerodynamic coefficient diagrams.

Aerodynamic coefficient diagrams

For each iteration during simulation, Fluent is storing aerodynamic coefficients values into textual files that can be read into Excel. These data can be easily presented in a diagram (Figure 5.1).

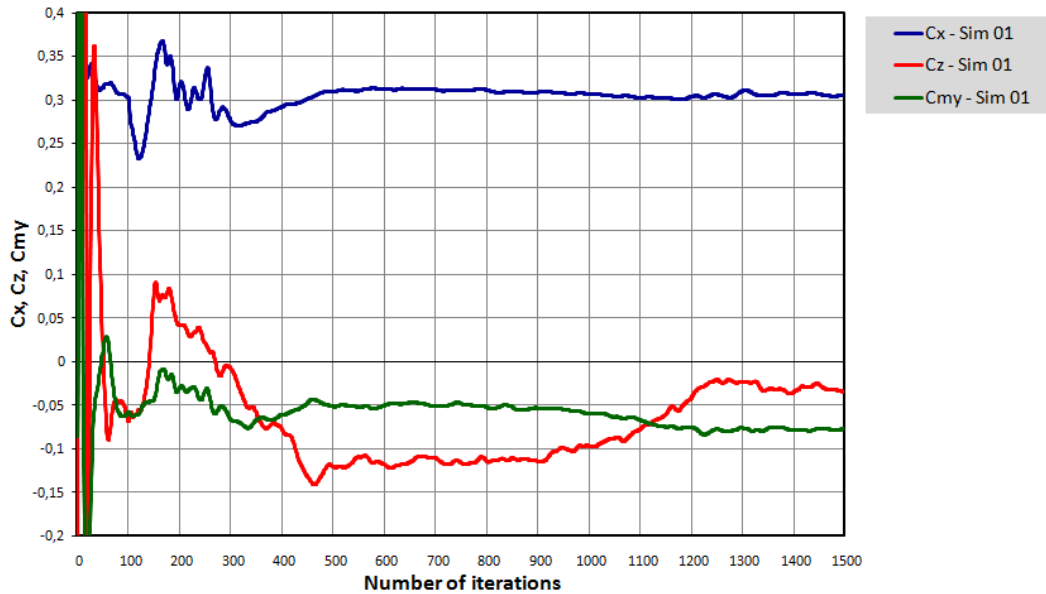


Figure 5.1 Aerodynamic coefficients diagram, monitored during simulation – CULT simulation 01

From this diagram engineer can evaluate convergence of the results. To be on the safe side it is always good to have stable mean value for at least 500 iterations. This is not case in the Figure 5.1, therefore this simulation was prolonged for additional number of iterations (more in Chapter 7).

In the diagram in Figure 5.1 calculated aerodynamic coefficients are not taking into account drag produced by the porous media (cooling package). This additional drag need to be calculated separately and added to the aerodynamic coefficients after the simulation. In the Chapter 7, all simulation results in the tables will contain both drag coefficients – partial values without cooling package (WCP) and total values with contribution of cooling package.

5.2 Geometry overview

Usually there are a lot of geometry variations in the vehicle development project, especially in the early phase, therefore it is necessary to inspect geometry regularly and keep track of geometrical changes. Aerodynamics engineer needs to be sure which geometry he is dealing with in all stages of the project. Geometry overview can be easily made in Fluent by visualizing all surfaces defined as “solid wall”. Usually, these surfaces represent vehicle and road. For better overview, road is excluded from figures, therefore only vehicle geometry is inspected (Figure 5.2).

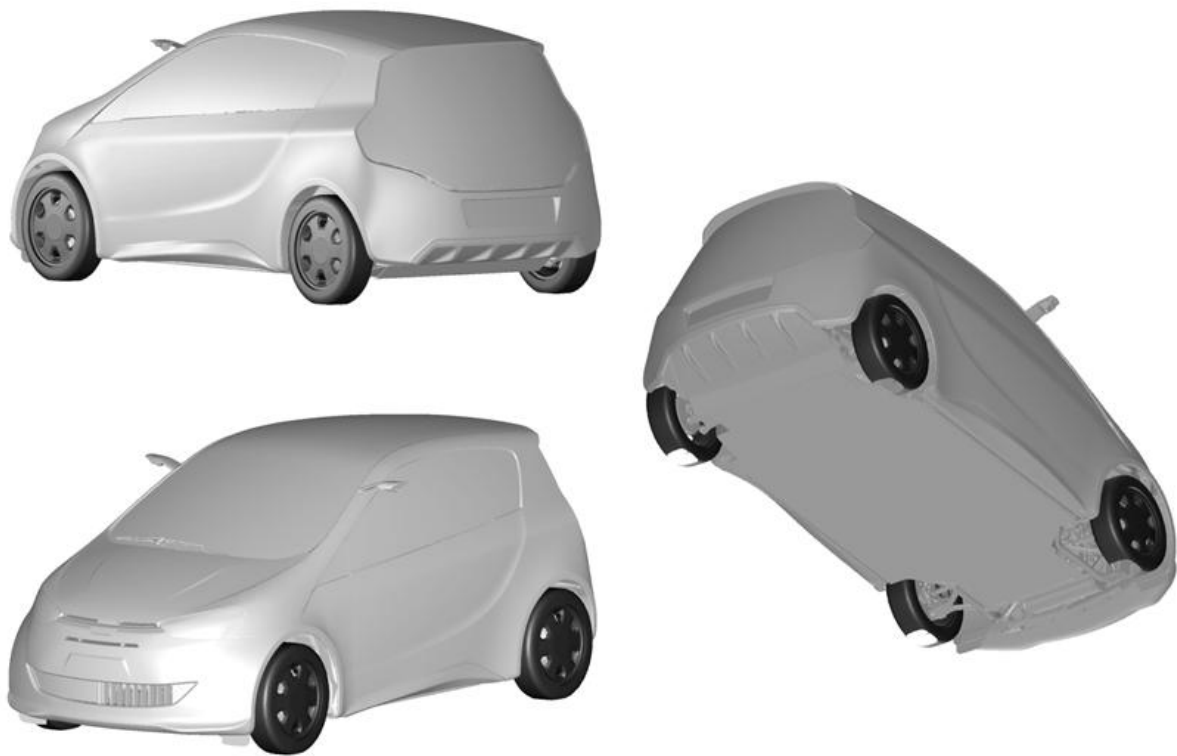


Figure 5.2 Geometry overview 3D visualization – CULT simulation 01

5.3 Flow visualization

Flow visualization is one great advantage of CFD when compared to wind tunnel tests. In order to understand flow visualization it is very important to understand physical values shown on pictures. This chapter will give overview, definition and short description of each physical value used for flow visualization in this thesis.

5.3.1 Cut planes flow visualization

All cut planes flow visualizations are made at the following locations - **Y0 plane**, **Z276 plane**, **Z815 plane** and **Z470 plane** (Figure 5.3). Number represents value of that coordinate (in millimeters).

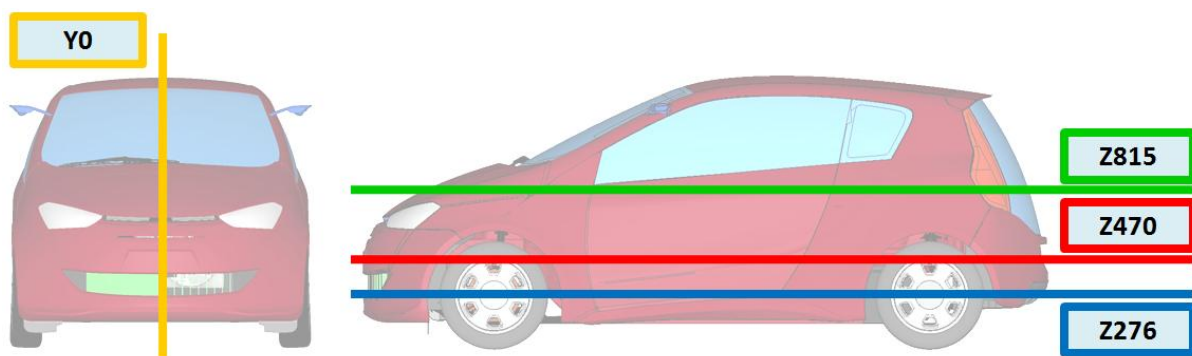


Figure 5.3 Cut planes definition

Velocity magnitude coefficient – C_v

Velocity magnitude coefficient is ratio between velocity magnitude at the observed point and velocity magnitude of undisturbed flow:

$$C_v = \frac{u}{u_\infty}$$

Similar flow visualization can be made observing velocity instead of velocity coefficient. However, by showing velocity coefficient simulations with different air speed can be easily compared. For the sake of standardization of post-processing it is always better is to use non-dimensional coefficients.

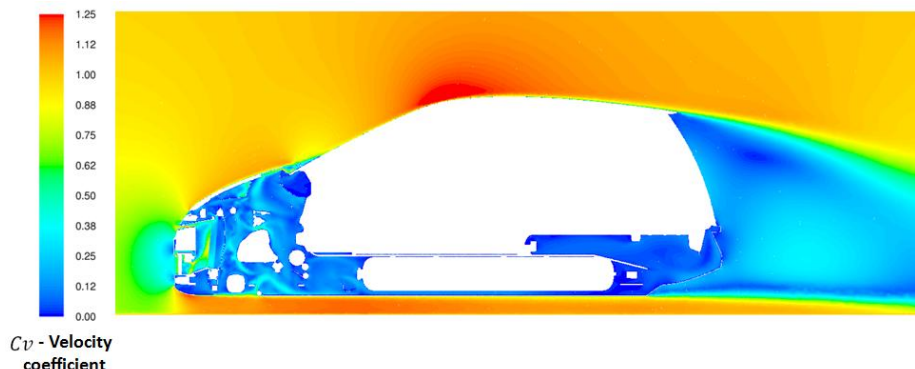


Figure 5.4 Velocity coefficient visualization in Y0 plane – CULT simulation 01

Velocity-X coefficient - Cv_x

Velocity-X coefficient is ratio between velocity in x direction at the observed point and the velocity magnitude of undisturbed flow:

$$Cv_x = \frac{u_x}{u_\infty}$$

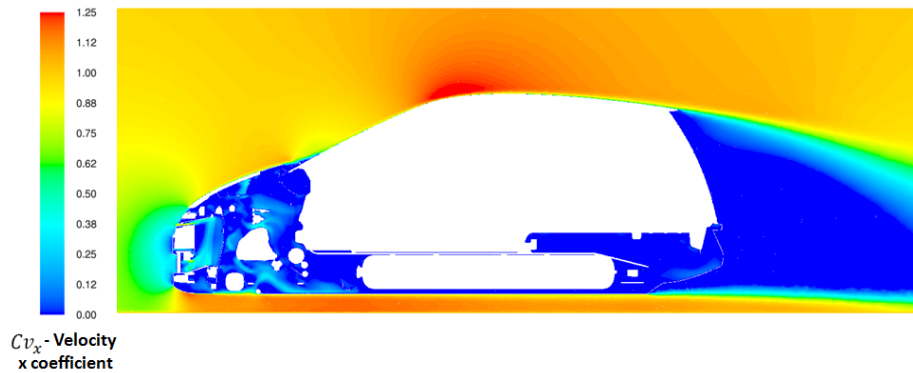


Figure 5.5 Velocity-X coefficient visualization in Y0 plane – CULT simulation 01

Velocity-X has the advantage of clearly showing the zones of boundary layer separation and flow recirculation. These zones of energy losses in the flow are mainly responsible for creation of aerodynamic drag.

Total pressure coefficient - $C_{p_{tot}}$

Total pressure coefficient is ratio between local total pressure and free stream total pressure (Chapter 1.3.2.):

$$C_{p_{tot}} = \frac{p_{tot}}{p_{tot\infty}} = \frac{p_{stat} + p_{dyn}}{p_{tot\infty}} = \frac{p + \frac{1}{2}\rho u^2}{\frac{1}{2}\rho_{\infty} u_{\infty}^2}$$

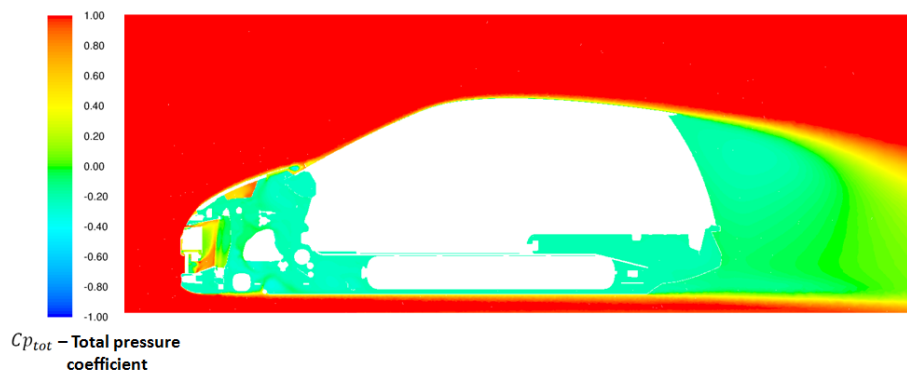


Figure 5.6 Total pressure coefficient visualization in Y0 plane – CULT simulation 01

Total pressure coefficient is very good at hinting where energy losses are observed in the flow. At the observed point, dynamic pressure can be observed as kinetic energy and static pressure as potential energy. Dynamic pressure can be transferred in static pressure and vice versa. When air is accelerating velocity is increasing and static pressure decreasing. That means kinetic energy is increasing and potential energy decreasing. The reverse is also true. Accordingly, if no losses are present total pressure doesn't change.

In viscous flow, when air particles are interacting mutually and with the body in flow, there are energy losses. Energy losses can be manifested as losses in dynamic pressure or losses in static pressure. Therefore, complete energy losses, independent from energy form, can be easily examined with total pressure coefficient visualization (if there are no energy losses sum of static and dynamic pressure is constant, therefore $C_{p_{tot}}$ does not change).

Figure 5.6 represents total pressure Y0 cut plane of CULT simulation 01. At the air inlet, average total pressure coefficient is equal to one. At the air outlet, at the end of the wind tunnel, average total pressure coefficient is smaller than one. These differences are energy losses caused by aerodynamic resistance.

Here is more precise explanation: At the air outlet, at the end of the wind tunnel, due to mass conservation law, amount of air that exits from the wind tunnel is same as the air mass that enters. Since areas of the air inlet and air outlet surfaces are same, average outlet velocity is same as average inlet velocity. Since average air speed is same at the inlet and outlet, also kinetic energy is the same. Due to energy conservation law, air flow energy that exits from the wind tunnel is smaller than energy that enters, for the size of energy losses in the fluid flow. Therefore, all energy losses are manifesting in average static pressure reduction at the air outlet.

Vorticity magnitude - $|\vec{\omega}|$, $\left[\frac{1}{s}\right]$

Vorticity magnitude is the magnitude of vorticity vector [25]. Vorticity vector is a measure of the rotation of the center point of a fluid element as it moves along the streamline in the flow field and is defined as the curl of velocity vector [27]:

$$\vec{\omega} = \nabla \times \vec{u} = \left(\frac{\partial}{\partial x}, \frac{\partial}{\partial y}, \frac{\partial}{\partial z} \right) \times (u_x, u_y, u_z)$$

$$\vec{\omega} = \left(\frac{\partial u_z}{\partial y} - \frac{\partial u}{\partial z}, \frac{\partial u_x}{\partial z} - \frac{\partial u_z}{\partial x}, \frac{\partial u}{\partial x} - \frac{\partial u}{\partial y} \right) = (\omega_x, \omega_y, \omega_z)$$

$\vec{\omega}$ – vorticity

\vec{u} – air speed

∇ – curl (vector operator) [26]

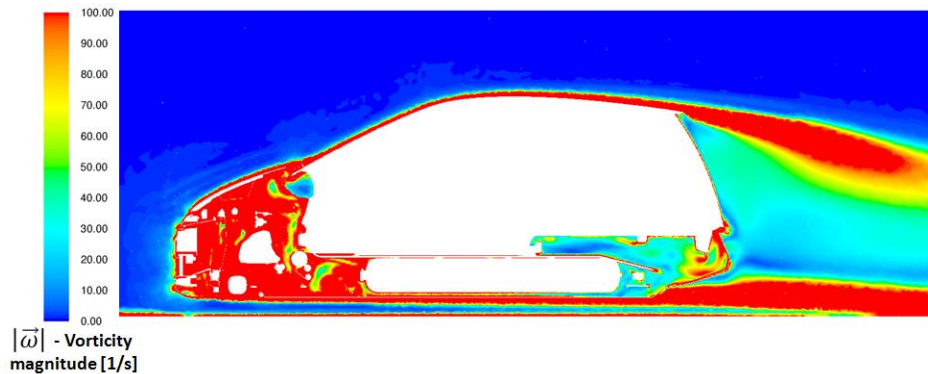


Figure 5.7 Vorticity magnitude visualization in Y0 plane – CULT simulation 01

In words, the vorticity tells how the velocity vector changes when one moves by an infinitesimal distance in a direction perpendicular to it. Stronger rotary movements are present in fluid flow, greater the vorticity magnitude is.

Turbulence kinetic energy – k , $\left[\frac{\text{J}}{\text{kg}}\right]$

Turbulence fluctuations, because of their nature, have to gain energy from the main flow. Turbulence kinetic energy is the kinetic energy per unit mass of the turbulent fluctuations in a turbulent flow [28]:

$$k = \frac{1}{2} \overline{u_i'^2 u_i'^2} = \frac{1}{2} (\overline{u_x'^2} + \overline{u_y'^2} + \overline{u_z'^2}) = \frac{3}{2} \overline{u'^2}$$

k – turbulence kinetic energy $\left[\frac{\text{J}}{\text{kg}}\right]$, or $\left[\frac{\text{m}^2}{\text{s}^2}\right]$

u_i' – turbulent fluctuations $\left[\frac{\text{m}}{\text{s}}\right]$

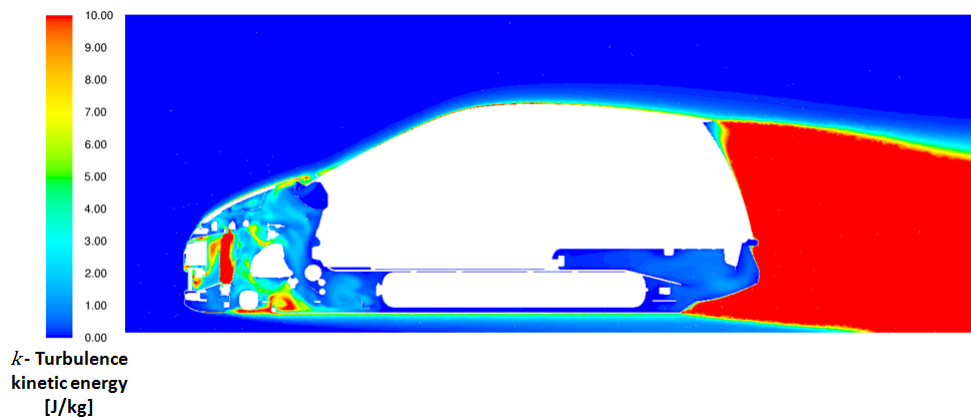


Figure 5.8 Turbulence kinetic energy visualization in Y0 plane – CULT simulation 01

Turbulence kinetic energy is also a way to represent energy losses. Turbulence kinetic energy is one part of total energy losses in the flow. With the help of this visualization, size of vehicle’s wake can be observed. Smaller wake is usually one of indicators for lower drag – if the wake is smaller that means flow is less disrupted. However, the above statement is not always correct, since vehicle drag depends largely from the negative pressure acting on the vehicle base. In general the base surface pressure depends on the location of recirculation zones (vortices) in the wake, as well as on the size of these vortices.

5.3.2 3D contours flow visualization

All 3D contours are made for three standardized views: View 1, View 2 and View 3 (Figure 5.9). 3D contours generally help to observe what is happening on the vehicle surface. This chapter will describe two types of 3D contours that are used in the thesis, both of them representing overall aerodynamic drag created on the vehicle.

Pressure coefficient - C_p

Pressure coefficient is the non-dimensional ratio between static pressure at the observed point and total pressure of undisturbed flow (Chapter 1.3.2):

$$C_p = \frac{p}{p_{tot\infty}} = \frac{p}{\frac{1}{2}\rho_{\infty}u_{\infty}^2}$$

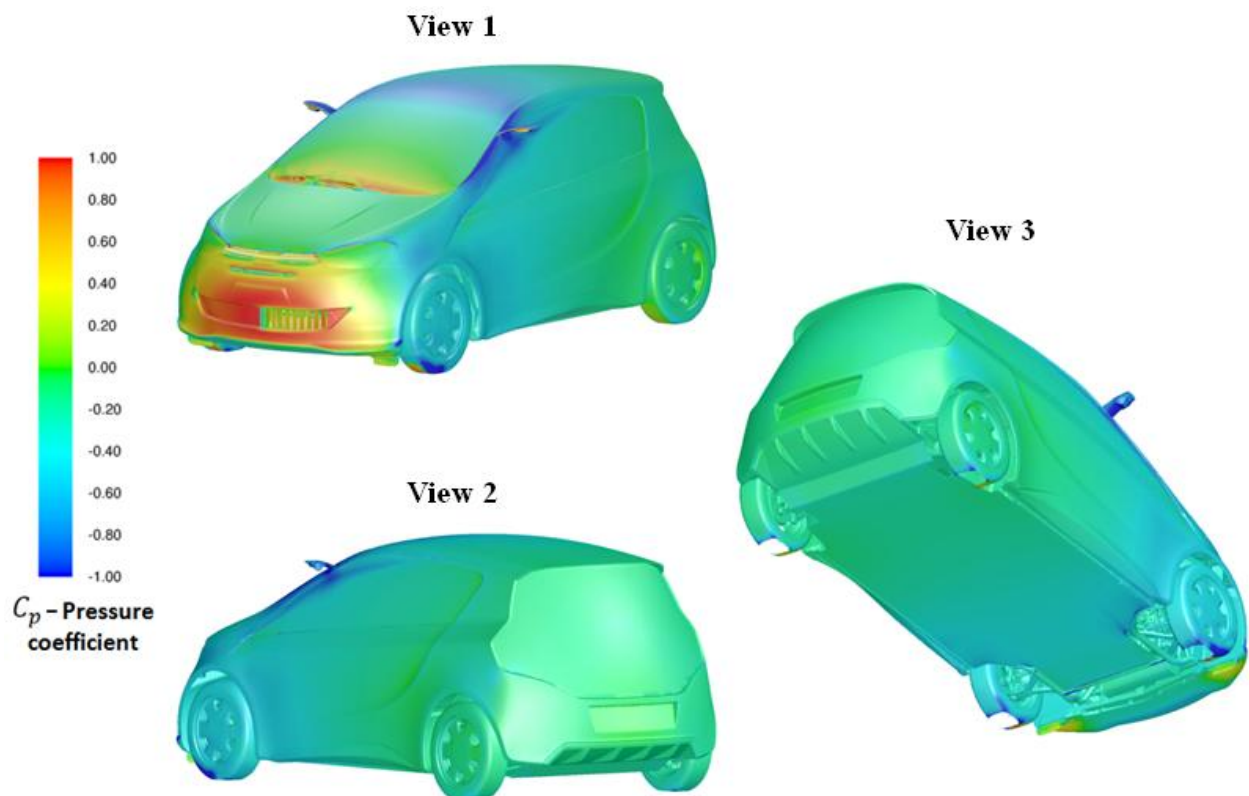


Figure 5.9 Pressure coefficient 3D visualization – three standard views: View 1, View 2, and View 3 – CULT simulation 01

In general, most of the drag on the vehicles is caused by pressure difference on vehicle surfaces facing the flow in upstream and downstream directions (Chapter 1.1). Pressure distribution on the vehicle surface can best be represented by pressure coefficient contours (Figure 5.9). From these pictures, it is easy to find areas responsible for pressure drag – gauge or stagnation pressure on the front and vacuum pressure or suction on the rear end of the vehicle.

Wall shear stress - τ_w , [Pa]

Wall shear stress is representing shear stress acting on solid walls. It is a result of friction between fluid flow and the wall. It is given by formula [29]:

$$\tau_w = \mu \left(\frac{\partial u}{\partial y} \right)_{y=0}$$

μ – dynamic viscosity

u – air speed

y – distance from the wall

As it can be seen from the formula, wall shear stress exists on the surface areas where boundary layer is present. Consequently, where boundary layer is detached there is either no wall shear stress or it is very low.

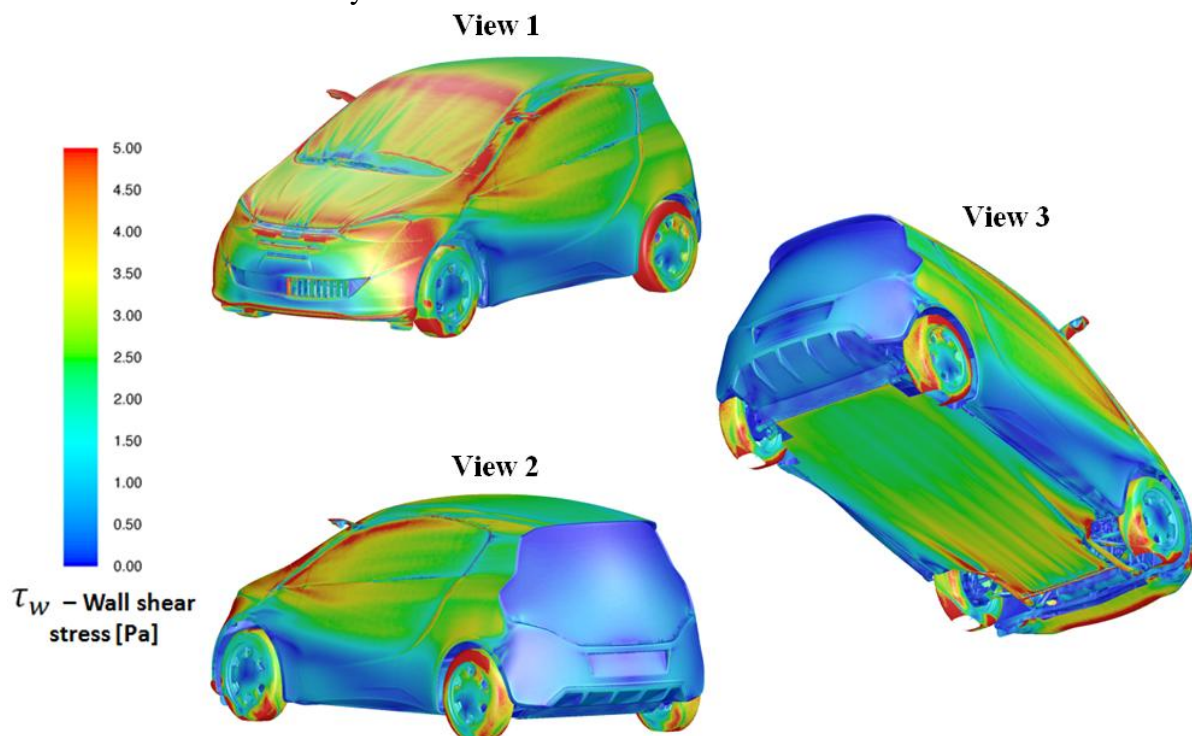


Figure 5.10 Wall shear stress 3D visualization – three standard views: View 1, View 2, and View 3 – CULT simulation 01

Wall shear stress is creating friction part of total aerodynamic drag (see Chapter 1.1). Since friction drag plays only secondary role in total drag for ground vehicles, wall shear stress contours are usually used to clearly see detachment and reattachment of fluid flow.

E.g. Figure 5.10 can be used to estimate efficiency of rear diffuser – more in Chapter 7.

To sum up, pressure coefficient contours and wall shear stress contours together give a good representation of overall aerodynamic drag acting on the vehicle.

5.4 C_p diagrams

C_p diagrams are very good for comparison of results between CFD simulation and wind tunnel measurement (details about wind tunnel measurements in Chapter 6.4). This chapter will shortly describe general procedure for creating pressure coefficient diagrams in CFD.

Y0 plane is used as a standard for exporting C_p values. First, car is intersected with the Y0 plane (Figure 5.3). On the intersection between car’s surface and Y0 plane a curve is created. C_p values are exported on that curve. For clear display in diagrams, that curve is divided into three parts – upper body line, under body line and rear base line (Figure 5.11). Division is made with three division points: one point is between roof and rear windscreen and other two are defined with the separation plane (Figure 5.11). Separation plane position is defined with z coordinate of the point on the end of the diffuser (separation plane defines diffuser as the part of under body).

In this way C_p values can be easily presented in three diagrams (Figure 5.12, Figure 5.13 and Figure 5.14).

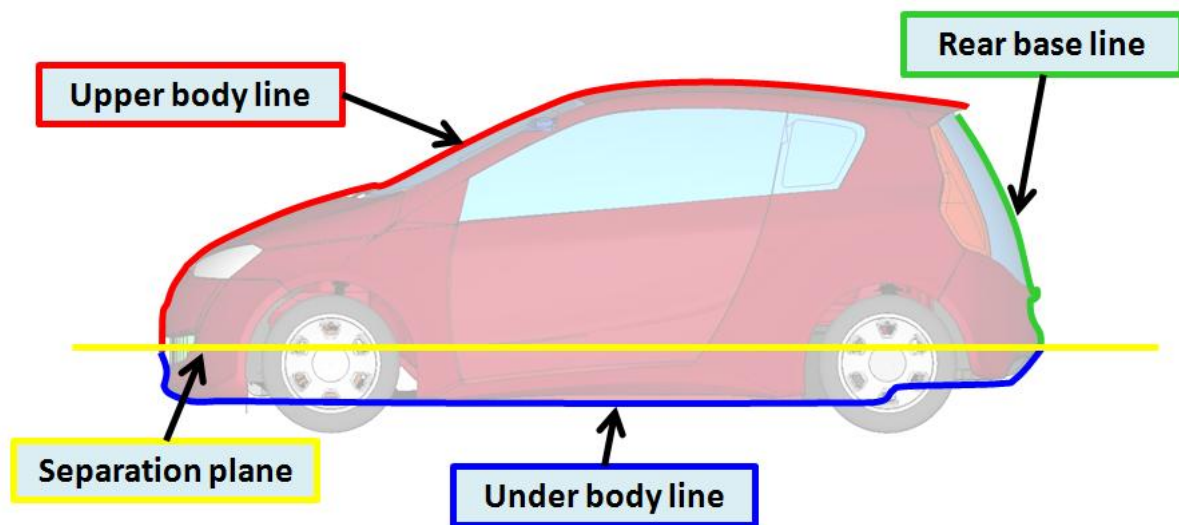


Figure 5.11 Three curves of CULT’s outer surface in Y0 plane used for visualization of C_p values

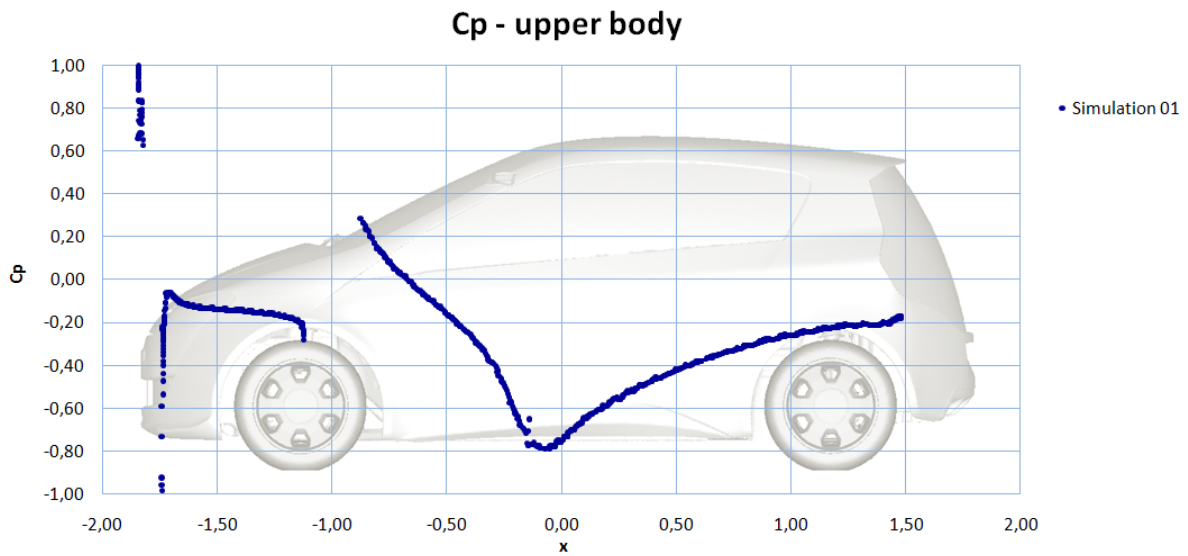


Figure 5.12 Pressure coefficient distribution on the upper body – CULT simulation 01

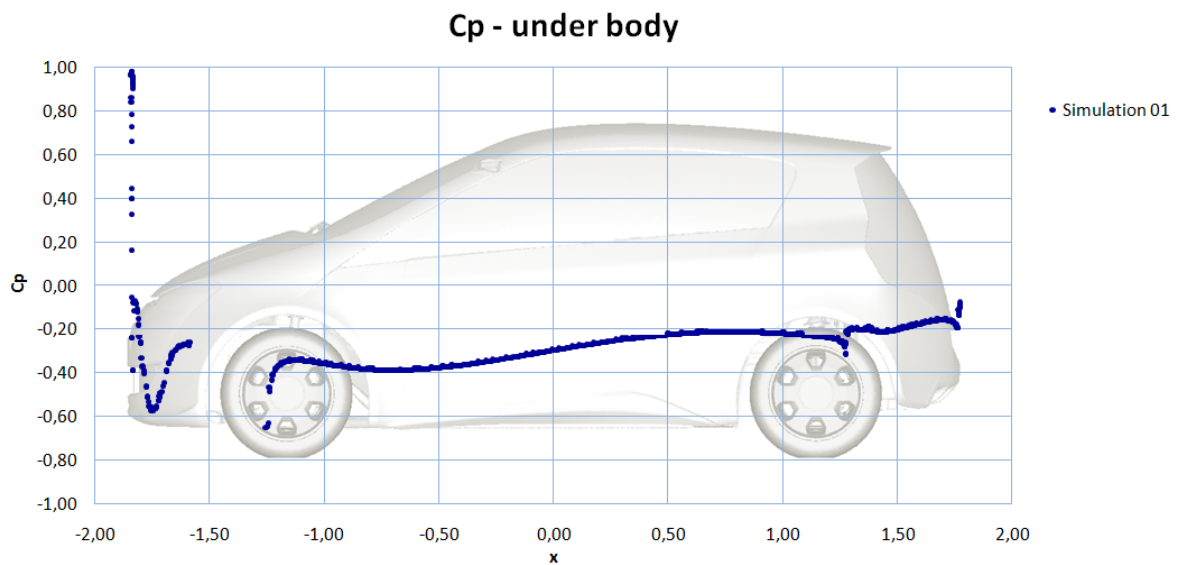


Figure 5.13 Pressure coefficient distribution on the under body – CULT simulation 01

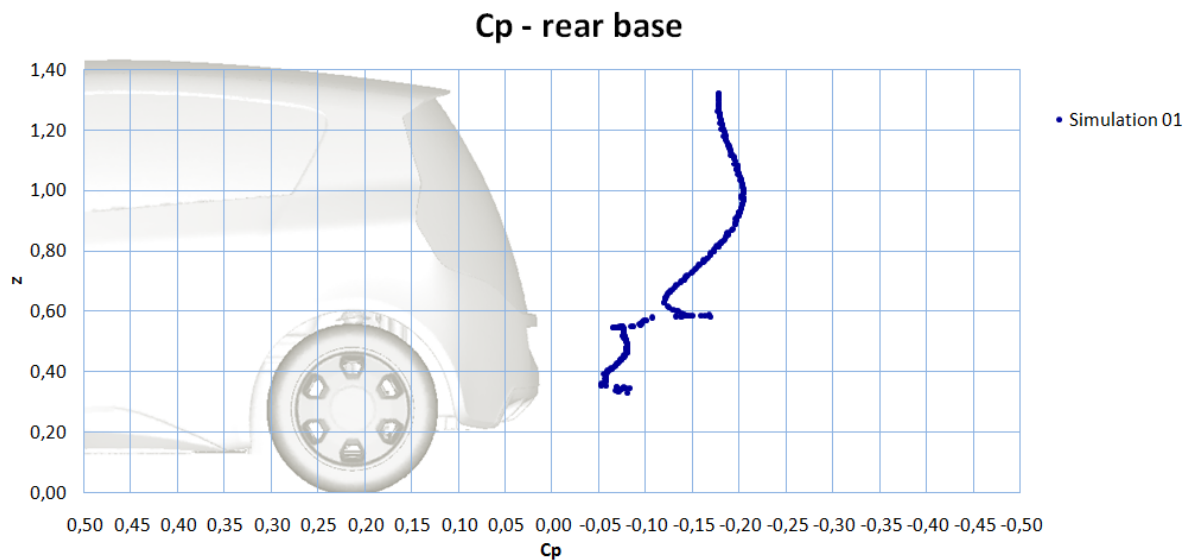


Figure 5.14 Pressure coefficient distribution on the rear base – CULT simulation 01

As it can be seen from figures above, there is also a picture of the car in the diagrams. Position of the picture matches coordinates of C_p values. This is useful for easier diagram reading.

Diagrams created at this step have proved to be suitable not only for comparing results with wind tunnel test, but also for mutual comparison of different CFD results. Reason is that diagram comparison is much clearer than comparison of 3D pictures (e.g. C_p 3D contours).

5.5 F_x and F_z accumulated diagrams

Accumulated aerodynamic forces can be presented in diagrams. One possible way to do this is to divide the vehicle in slices with a certain number of X planes (planes defined with $x = \text{const.}$ coordinate). Aerodynamic force, acting on each vehicle slice, need to be calculated. Then, moving from the front end of the car to the rear end, aerodynamic forces for each slice can be accumulated and values presented as diagrams. Final value is total aerodynamic force on the vehicle. For aerodynamic drag only force acting in X direction is important, therefore F_x accumulated diagram shows drag force accumulating from the front to the rear end of the car (Figure 5.15). Final value in F_x accumulated diagram is total aerodynamic drag.

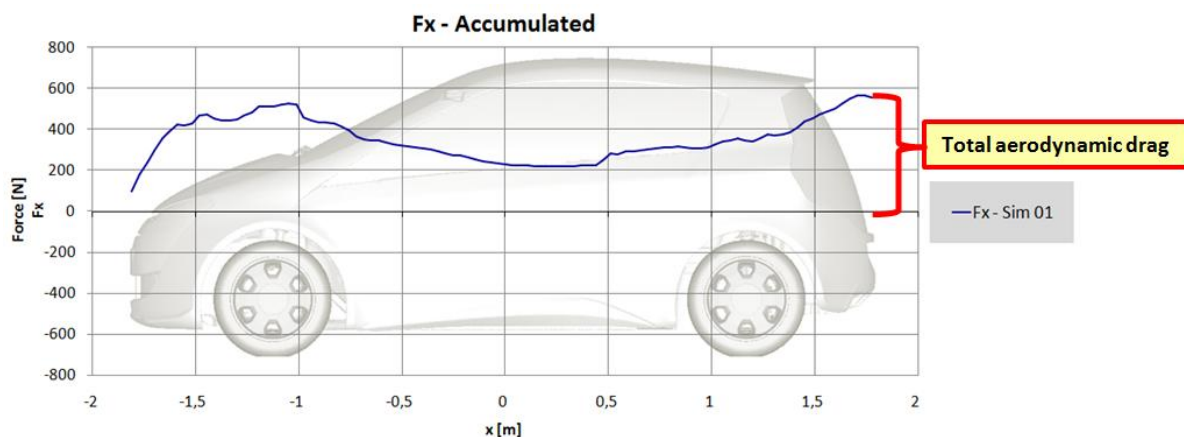


Figure 5.15 An example of diagram of accumulated force in X-direction (drag force - F_x)

Observing this F_x accumulated diagram, it can be seen on which part of the vehicle the most of the drag force is generated. In Figure 5.15 drag is increasing from the front end of the car due to high pressure on the front (stagnation point – air particles stop and maximum static pressure is reached). Then along the front windscreen flow is accelerating and there is a low pressure region. Low pressure in that area creates negative aerodynamic force (thrust force which actually reduces drag locally). This phenomenon is present until about half point of the roof. Then, drag starts to increase due to combined action of low pressure at the rear base of the car, flow losses along the floor and influence of rear wheels. More detailed investigation of different influences on total accumulated drag will be shown in Chapter 7.

In a similar manner also accumulated force in vertical direction (F_z) can be observed. Principles are same as with the F_x accumulated force. The F_z accumulated diagram shows lift force accumulating from the front end to the rear end of the car. Final value is the total lift (Figure 5.16).

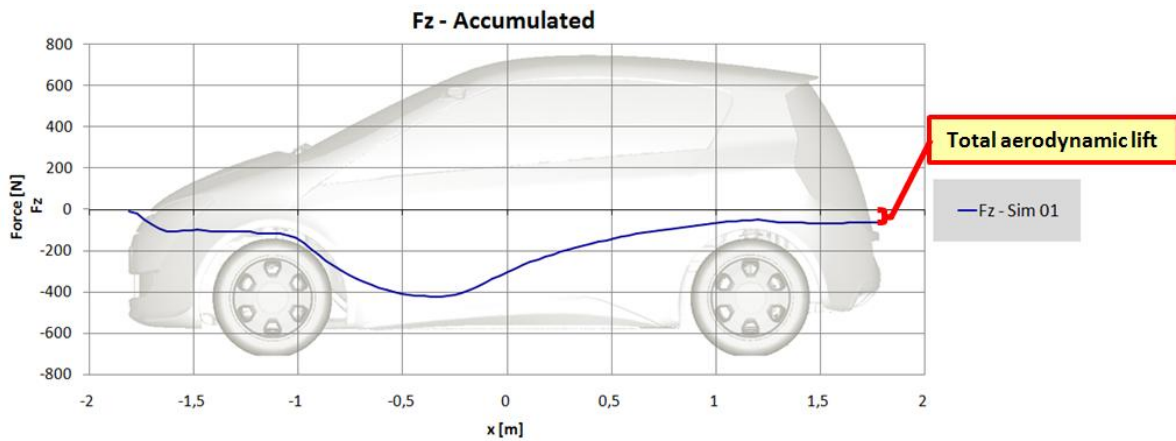


Figure 5.16 An example of diagram of accumulated force in Z-direction (lift force - F_z)

Simulation comparison

Accumulated force diagrams come to the fore when two or more simulations are compared. An example of simulation comparison is showed in Figure 5.17.

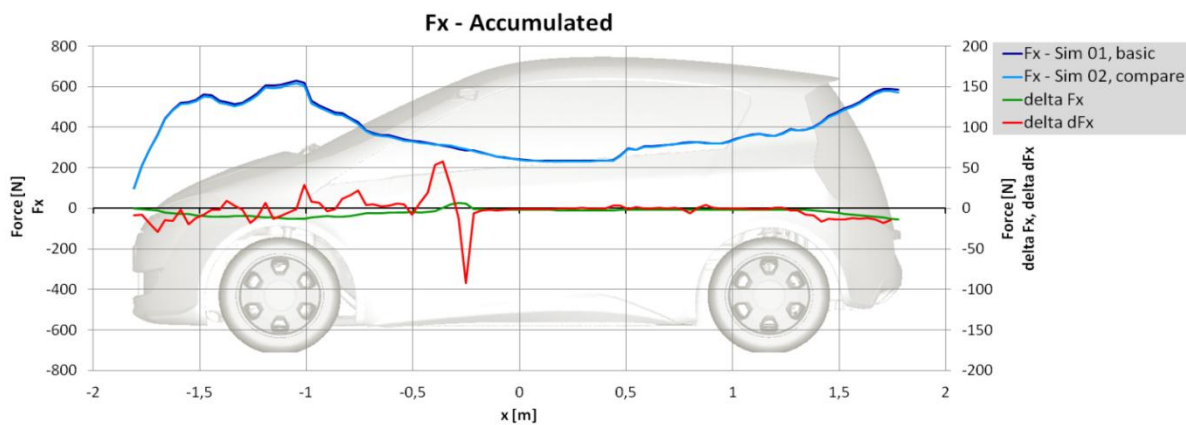


Figure 5.17 Example of simulation comparison in F_x accumulated diagrams.

Two blue lines (light blue and dark blue) represent accumulated force for each simulation. Because there is no big difference between forces, not too much can be seen.

Green line (ΔF_x) represents difference between accumulated forces (between blue lines), but in finer scale (local scale is defined on the right):

$$\Delta F_x = F_{x \text{ sim } 02} - F_{x \text{ sim } 01}$$

Now difference between simulations is better noticeable. Because accumulated force diagram is accumulating forces, differences created on one part of the vehicle (e.g. front end) stay visible until the end. That is not always suitable for analysis. In some cases it would be more suitable to have a diagram which will show only exact position where difference is created. That is the reason for introducing red line into the diagram.

Red line (ΔdF_x) represents gradient of the green line (or the difference between blue lines gradients):

$$\Delta dF_x = d(\Delta F_x) = dF_{x \text{ sim}02} - dF_{x \text{ sim}01}$$

For better understanding of ΔdF_x there is Figure 5.18 below. Green and blue lines are arbitrary F_x accumulated forces. On the left diagram value ΔF_x (Delta F_x) is defined. On the right diagram gradients of accumulated forces are defined ($dF_{x \text{ sim}01}$ and $dF_{x \text{ sim}02}$) – tangents of the α_1 and α_2 angles. Difference between tangents of these two angles is ΔdF_x . In the case on the Figure 5.18 α_2 angle is bigger than α_1 , therefore ΔdF_x value is positive.

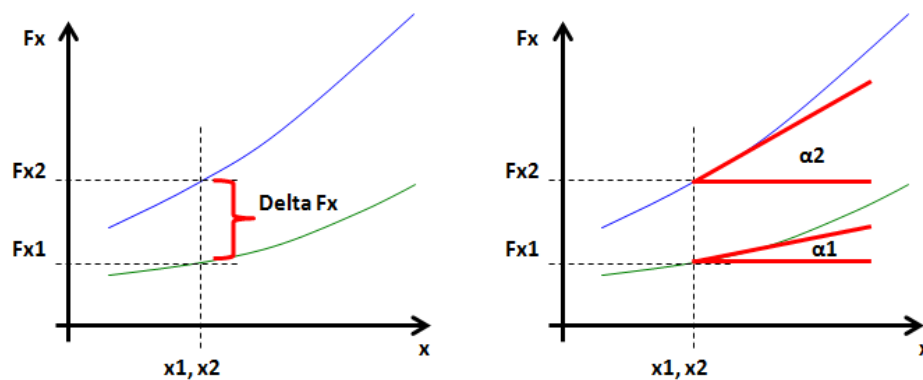


Figure 5.18 Red line (ΔdF_x) explanation

If accumulated forces for compared simulations are changing with the same intensity, red line has the value zero. When one of the simulations starts to behave differently, red line starts to move up or down from zero (positive or negative). After this local zone of different behavior, if simulations start to behave in the same way again (with same gradients), red line goes back to zero. That is what is necessary during vehicle optimization process. Red line shows exactly part of the vehicle where difference in drag force between simulations is created. This is often valuable information during vehicle optimization process.

Example in Figure 5.17 shows two simulations with different side mirrors configuration (all other parts of geometry and simulation settings are the same). Red line in the diagram clearly shows that there is different behavior of the aerodynamic drag, mostly at the side mirrors position – as expected.

6 WIND TUNNEL SCALED MODEL (1:4)

In a modern car development process CFD and the wind tunnel tests are used in parallel (Chapter 4). At the early stage of the project there is no real vehicle (prototype), therefore the only available option for aerodynamic testing is CFD. But there is also a possibility to create a simplified scaled model for aerodynamic tests in the wind tunnel. Purpose of that model is to validate CFD results and get some reference points for further development in early stage of the project. Usually, the size of scaled models is between 1:2 (50% model) and 1:4 (25% model).

Benefits of using the 1:4 scale model:

- Overall cost considerably less than with 1:1 testing
- Efficient method for the evaluation and optimization of different styling proposals in the early project phase
- Flexible platform – one frame for A/B-Segment vehicles, due to adjustable wheelbase and adjustable track width
- Modular constructions enable easy styling updates changes to new styling
- Quick optimization in the wind tunnel possible: approx. 50 variants per shift
- Possibility to use state-of-art wind tunnel technique approved by OEM's: moving center belt, rotating wheels

As it can be seen in Figure 6.1, scaled model experiment is done before the so-called Design Freeze Point, which opens more possibilities for shape and details change on the vehicle design surface. Other very important benefit is early validation of CFD results. Based on the scaled model results, CFD set-up can be upgraded for better accuracy in upcoming simulations.

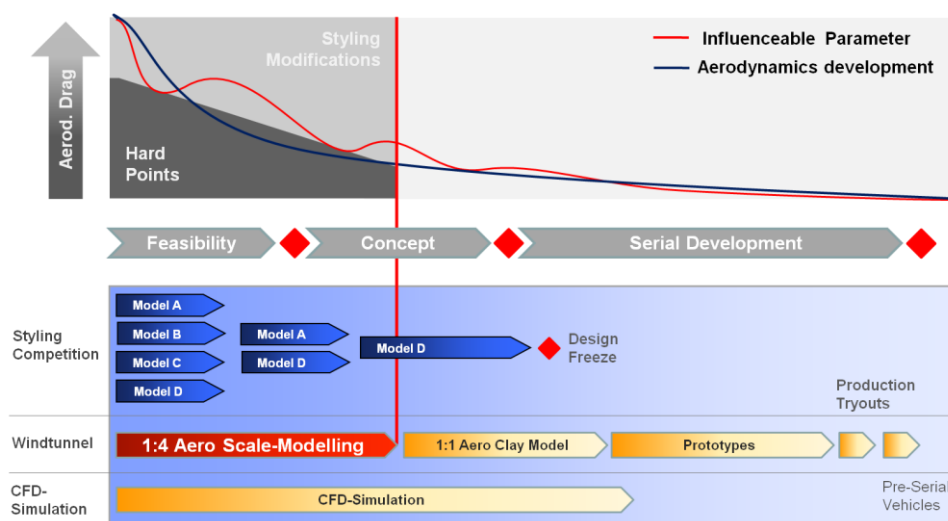


Figure 6.1 Aerodynamics in a design process of a car

Geometry overview

The CULT 1:4 wind tunnel model is also called ASM, short from Aero Scaled Model. The ASM model consists of parts showed in the Figure 6.2 and Figure 6.3. Main structure is a frame, which carry all other parts. With this universal frame and adjustable chassis it is possible to use same frame for more vehicles, which potentially decreases costs of models and testing.

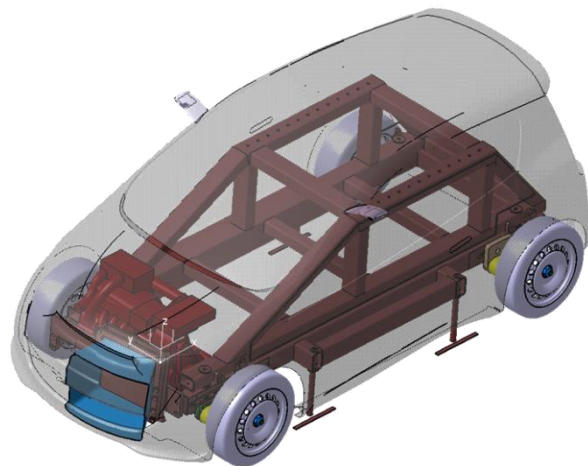


Figure 6.2 Aero Scaled Model (ASM) Geometry

With today’s technology it is possible to create very detailed body models, with realistic parts in engine compartment. That enables tests with air flow through the car and brings scaled model aerodynamics closer to aerodynamics of real vehicle.

Another benefit is possibility to use various removable parts (modular build), enabling fast geometry changes during experiment. This improves efficiency of wind tunnel tests and reduces overall costs. In ASM the rear end is modular and few different rear end parts are interchangeable (Figure 6.3). Also, side mirrors are separated and it is possible to change position (nine different positions for side mirrors were provided). Different positions of side mirrors and their aerodynamic effects are elaborated in Chapter 7.10.

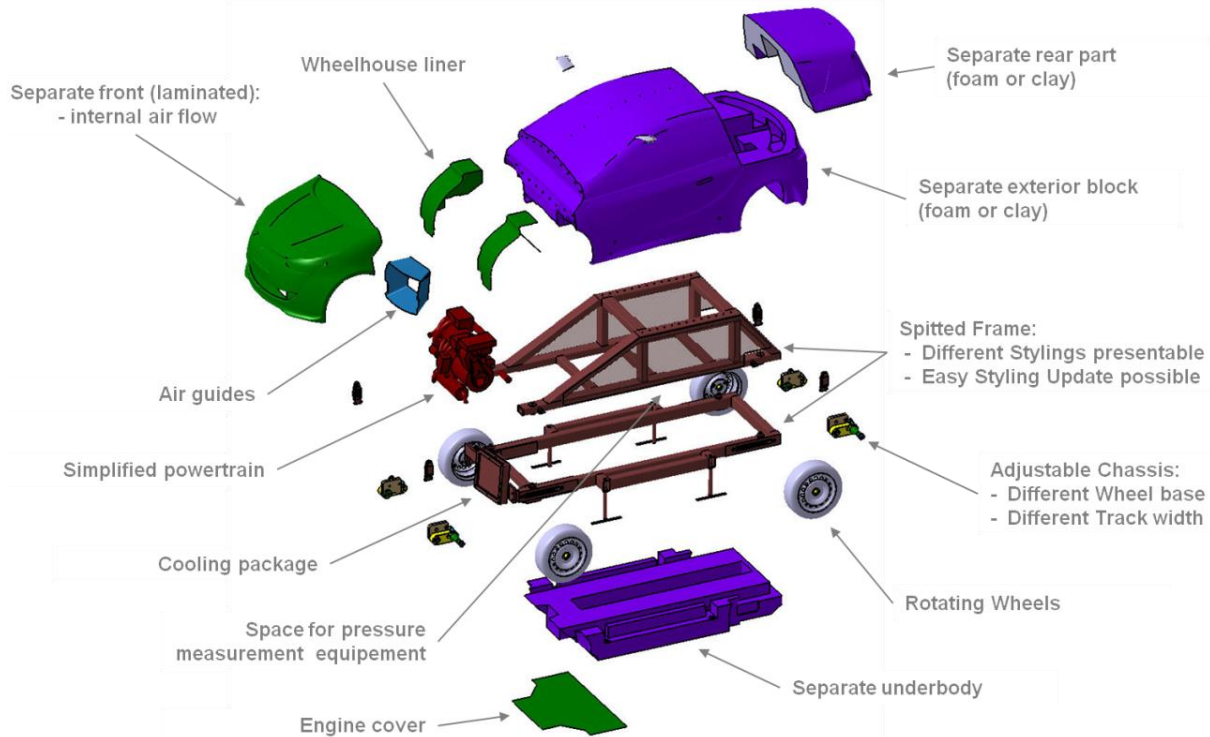


Figure 6.3 Aero Scaled Model (ASM) parts

Pressure probes

Alongside measurements of aerodynamic forces, pressure distribution around the car was also measured during CULT 1:4 wind tunnel tests. This is very important for evaluation of CFD results. Sometimes comparison of global aerodynamic forces between CFD simulation and the wind tunnel measurement can show only small differences, leading to the conclusion that results are matching. However, in reality the air flow can be completely different and matching of CFD and WT results can be a coincidence. Comparison of pressure contours is used to tell engineer if virtual and realistic flows really matching.

Figure 6.4 shows pressure probes holes on the ASM. Since Y0 cut plane is used as a standard for validation process between CFD and Wind tunnel experiment, pressure probes are positioned on this cut plane along the whole car (Figure 6.5). Also some additional probes are positioned on Z815 cut plane on the rear end of the model. In this thesis only pressure measurements in Y0 plane will be processed and compared to CFD (Chapter 7).

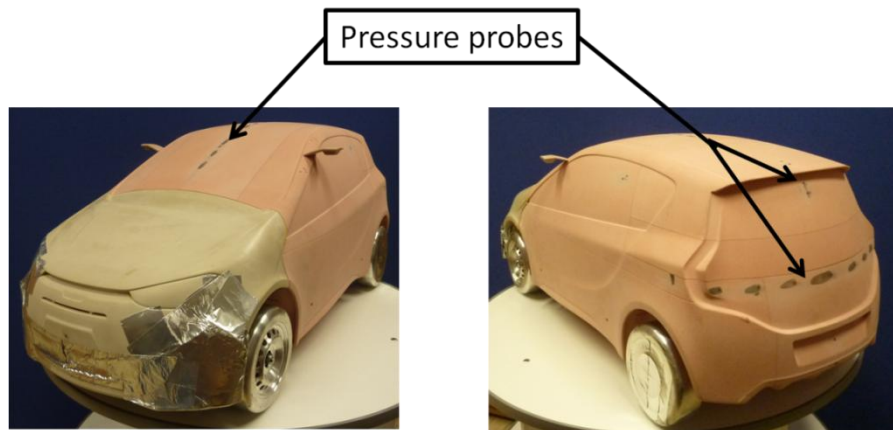


Figure 6.4 Pressure probes position on the ASM

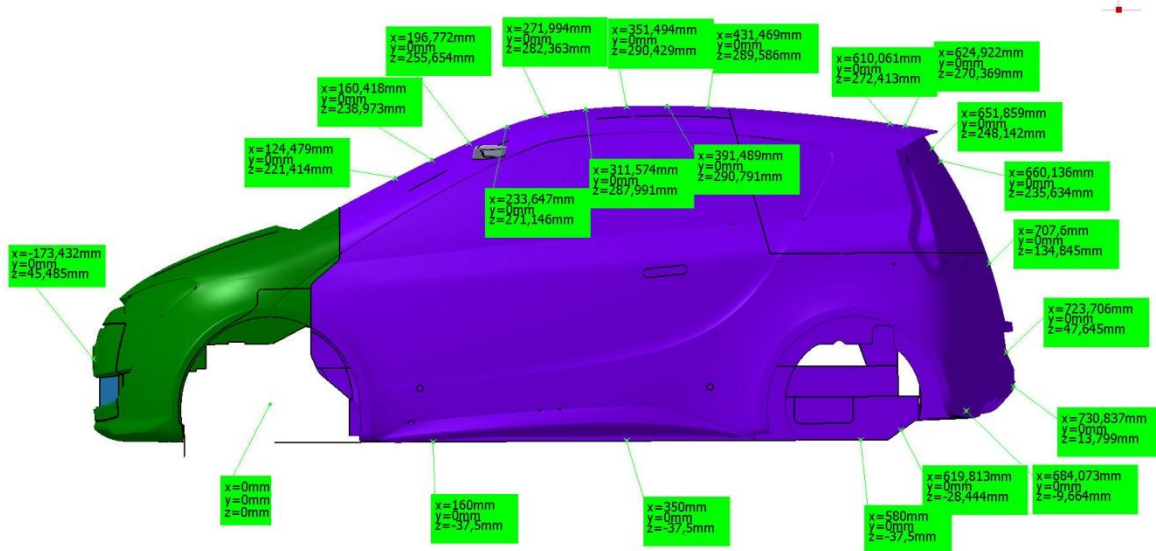


Figure 6.5 Pressure probes coordinates in Y0 section plane – CAD coordinate system

6.2 Wind Tunnel Test Set-up

Standard wind tunnel experiment procedure includes moving ground, enabled by moving center belt and rotating wheels on four small belts (so-called “five belt” system). This procedure is one of the standard wind tunnel techniques approved by OEM’s. Complete wind tunnel measurement procedure and details are not subject of this thesis. Therefore, only basic settings necessary for comparing results with CFD will be explained.

Since this measurement is carried out with the scaled model, it is not possible to get identical flow behavior as with the 1:1 scale model. However, for engineering purposes it is still possible to get very similar flow and sufficiently accurate results.

- Reynolds number and air speed:

Reynolds number was introduced in Chapter 4.2.2. This parameters needs to be same in both, CFD and the wind tunnel measurement. Since scaled model is four times smaller, also the referent length is four times smaller. To get same Reynolds number as in the 1:1 simulation it is necessary to increase speed four times (as it was already said in Chapter 4.2.2., air speed is only variable that can significantly change Reynolds number – L_{ref} , ρ_{∞} and μ_{∞} are constant):

$$Re = \frac{\rho_{\infty} \cdot u_{\infty} \cdot L_{ref}}{\mu_{\infty}}$$

In the current case, increasing air speed four times would push flow around the car into compressible flow regime: $4 \times 38 \text{ m/s} = \text{approx. } 150 \text{ m/s}$. Hence, air speed is increased only twice (that increased speed is on the edge between compressible and incompressible flow). Therefore, air inlet speed in the scaled model wind tunnel measurement is around 270 km/h (75 m/s). Reynolds number is then:

$$Re_{1:4} = \frac{\rho_{\infty} \cdot u_{\infty} \cdot L_{ref}}{\mu_{\infty}} = \frac{1.203 \cdot 77.78 \cdot 0.45}{1.833 \cdot 10^{-5}}$$

$$\mathbf{Re_{1:4} = 2.3 \cdot 10^6}$$

$$u_{\infty} = 38.89 \frac{\text{m}}{\text{s}} \quad \text{- air inlet speed}$$

$$L_{ref} = 0.45 \text{ m} \quad \text{- referent length (vehicle width)}$$

In addition to air inlet speed of 270 km/h , also measurements with slower air inlet speeds were made to investigate influence of Reynolds number in the experiment – more in Chapter 7.6.

Reynolds number calculated above does not match the Reynolds number in CFD simulations, but it is maximum Reynolds number allowed not to cross the line between incompressible and compressible flow. In order to have the same Re as in the WT, CFD simulations are simulated also with speed of 70 km/h (in addition to standard 140 km/h):

$$Re_{1:1} = \frac{\rho_{\infty} \cdot u_{\infty} \cdot L_{ref}}{\mu_{\infty}} = \frac{1.203 \cdot 19.4 \cdot 1.8}{1.833 \cdot 10^{-5}}$$

$$Re_{1:1} = 2.3 \cdot 10^6$$

$u_{\infty} = 19.4 \frac{m}{s}$ - air inlet speed (CFD reduced air speed to match 1:4 experiment)

$L_{ref} = 1.8 \text{ m}$ - referent length (vehicle width) for 1:1 geometry

Now, Reynolds numbers are matching and flow can be considered as similar.

- Mach number

Mach number was introduced in Chapter 4.2.2. In wind tunnel measurement it is:

$$M = \frac{v}{v_{sound}} = \frac{100}{340} \approx 0.29$$

$v \approx 100 \frac{m}{s}$ - assumed greatest air speed in simulation (at the leading edge of the roof)

$v_{sound} \approx 340 \frac{m}{s}$ - local speed of sound

Mach number is very close to 0.3, but it is still below. Therefore, flow can be considered as incompressible.

6.3 Wind Tunnel Test Results

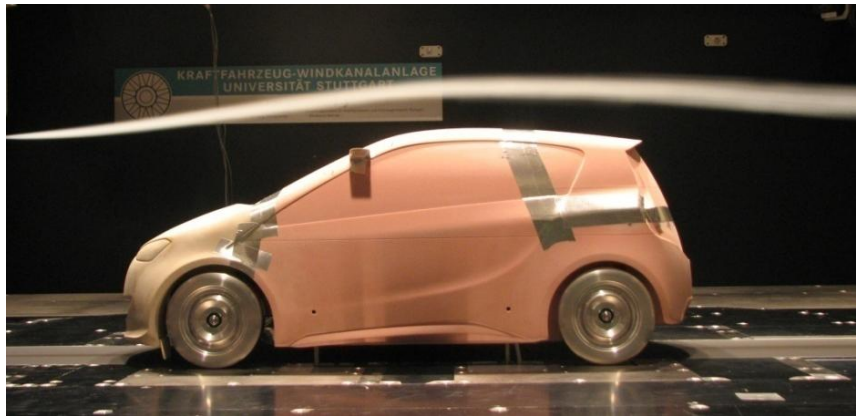


Figure 6.6 CULT ASM in wind tunnel during test

Wind tunnel allows tests of different geometry settings in a short time. On the scaled model like the current one, easy manipulation of parts makes an engineer’s job more productive.

Figure 6.7 shows diagram of the ASM wind tunnel test optimization progress. Experiment has been started with the default geometry (Cult ASM with cooling air shutter CAS open) and, in the end, it reached the best configuration with almost 50 drag counts improvement. This best-case geometry can be kept for scan and later integrated in the next iteration of geometry changes in the project.

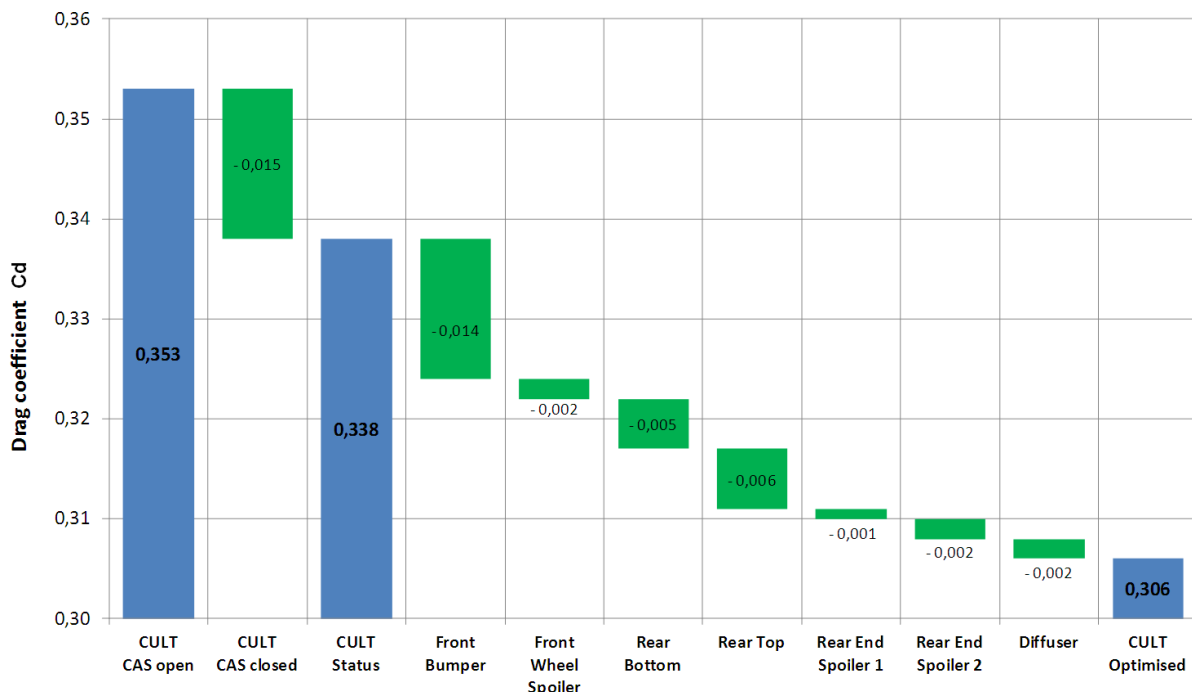


Figure 6.7 ASM wind tunnel test - aerodynamic optimization progress

Results and measurements from the wind tunnel test will be discussed parallel with CFD results in Chapter 7.

6.4 Wind tunnel data post-processing

Aerodynamic forces are directly measured in the wind tunnel, so it is not difficult to post-process these data. More demanding is to post-process data from pressure measurement.

As mentioned above, purpose of pressure measurements in the wind tunnel is to obtain more insight into the flow around the car and to validate results of CFD simulations. Data obtained from the wind tunnel are pressure values for each pressure probe on the vehicle. Pressure is measured during whole measurement cycle – Figure 6.8. As it can be concluded from the diagram below, in one cycle three different measurements, with three different air inlet speeds were carried out. These different air speeds can be used for investigation of different Reynolds number influence (Chapter 7.6).

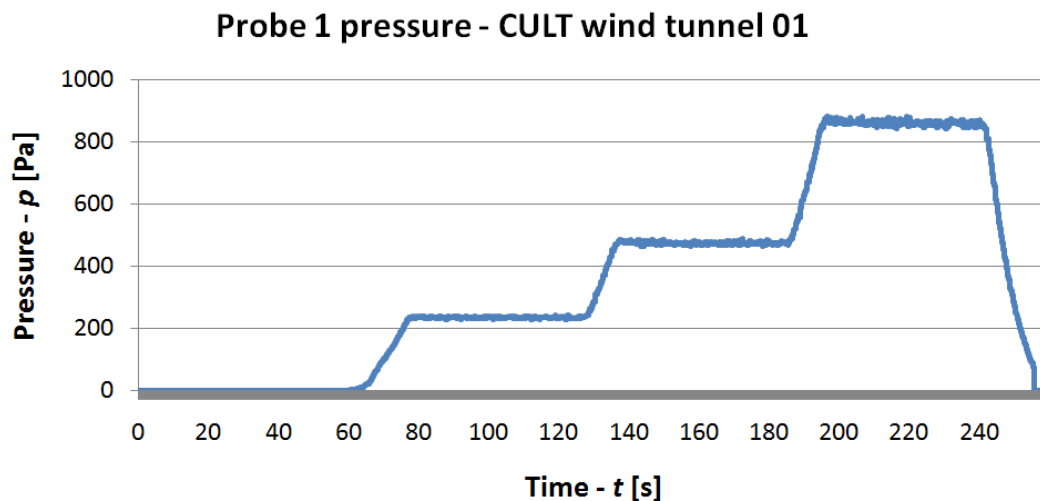


Figure 6.8 Example of pressure probe measurement – CULT wind tunnel 01

Next step is to pick up probe values for desired air inlet speed and calculate average value for each probe. When average pressure is calculated, it needs to be transferred into the pressure coefficient (C_p) using the following formula (Chapter 1.3.2):

$$C_p = \frac{p}{p_{tot\infty}} = \frac{p}{\frac{1}{2}\rho_{\infty}v_{\infty}^2}$$

It is necessary to emphasize that C_p values gained from the wind tunnel measurement usually need pressure correction. From the flow physics it is known that pressure coefficient value (C_p) on the stagnation point is equal to one. Since stagnation point is exactly on the license plate position, pressure probe positioned there is used as a reference point for pressure correction. Also, it is necessary to match vehicle coordinate system with the one in CFD. After these preparations, diagrams showed in the Figure 6.9, Figure 6.10. and Figure 6.11. can be created.

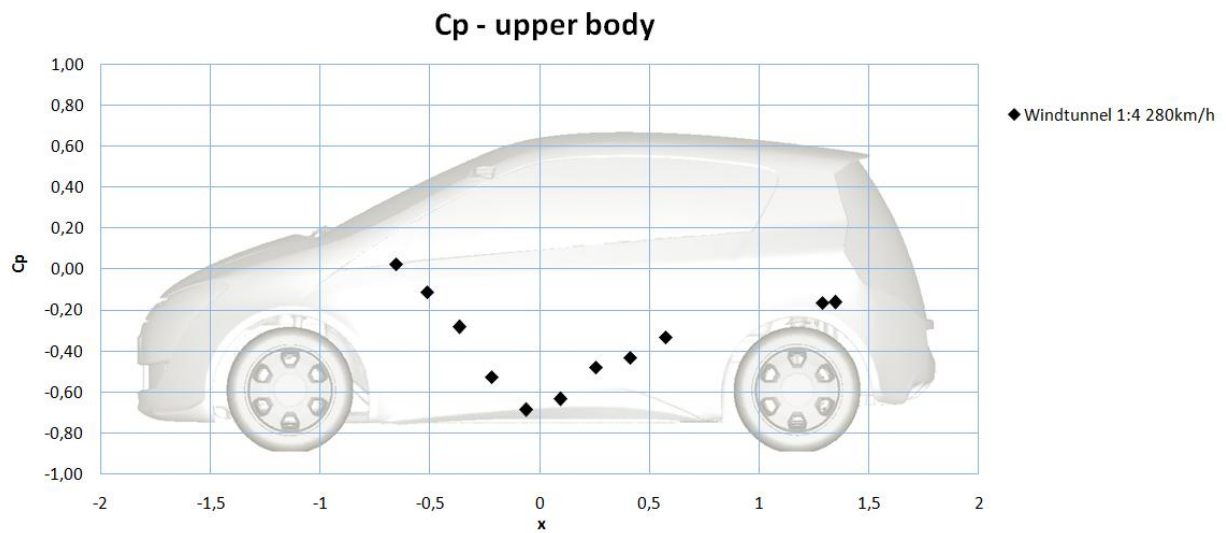


Figure 6.9 Pressure coeff. distribution on the upper body – WT measurement

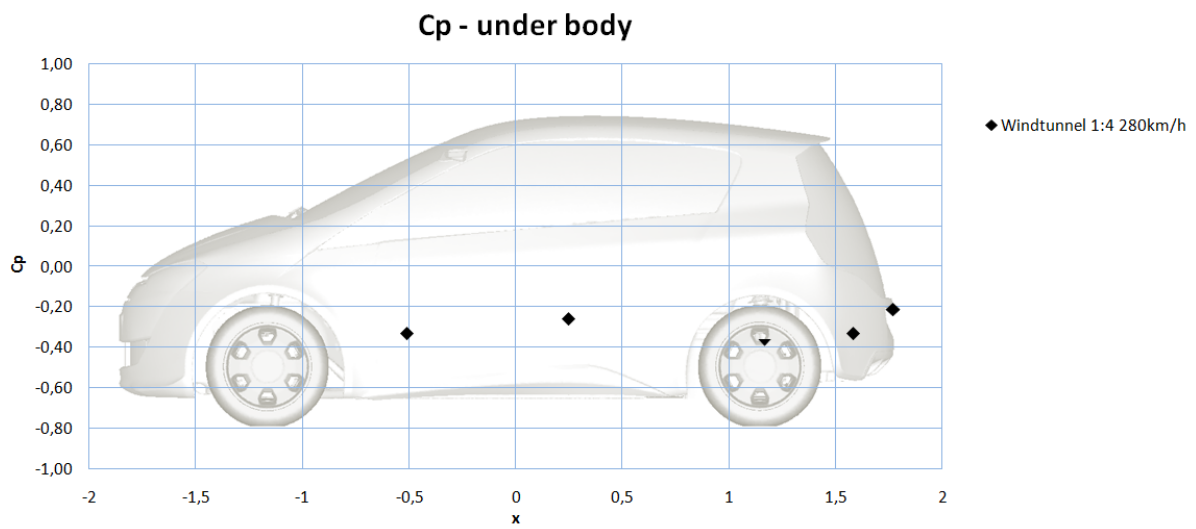


Figure 6.10 Pressure coeff. distribution on the under body – WT measurement

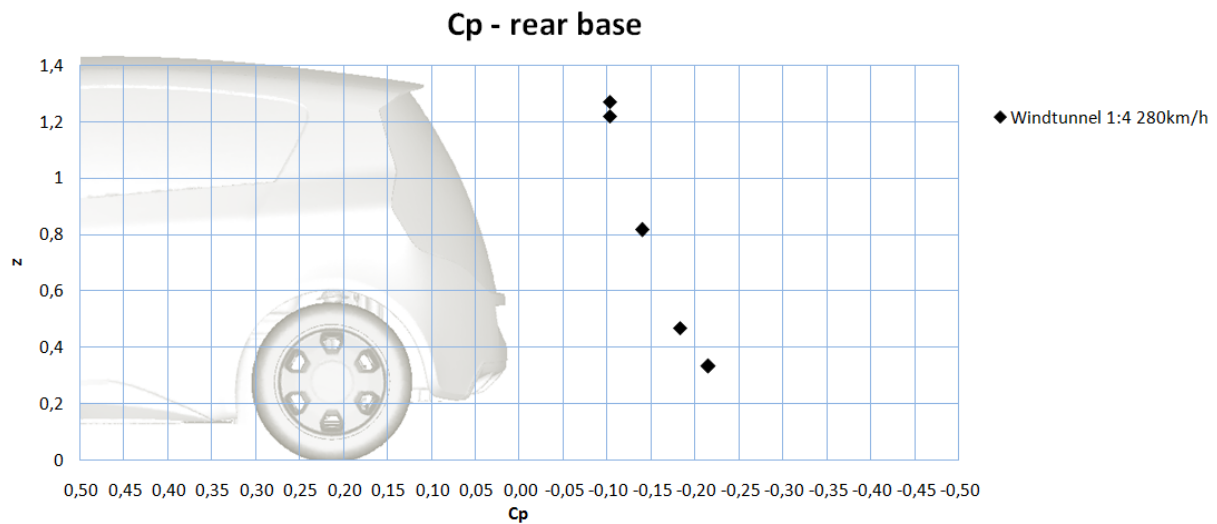


Figure 6.11 Pressure coeff. distribution on the rear base – WT measurement

Figure 6.9, Figure 6.10 and Figure 6.11 show wind tunnel measurement C_p values. Picture of the car is positioned correctly to match x or z coordinate, allowing better analysis of the results. These diagrams will be very useful in analysis and validation of results in Chapter 7.

7 ANALYSIS AND VALIDATION OF THE RESULTS

Total, 57 simulations were made. In the Table 7.1, 55 simulations are showed. Two additional simulations, with different basic geometry, are discussed separately in Chapter 7.7. Table 7.1 shows overview, short description and basic results for each of 55 simulations:

- First column shows simulation's number. During post processing simulation number is used for easier data manipulation
- Second column (“*Data status*”) describes geometry used in the simulation. Label “*basic simulation*” marks simulation with default geometry and default settings. There are two basic simulations – one with opened CAS mechanism (simulation 01) and one with closed (simulation 12). Also abbreviation “*bs*” is used in this column. It tells which simulation is used as a basic simulation for current simulation (e.g. if “*bs 01*” is noted that means simulation 01 is basis for current simulation). Also, it is noted what or where the difference is, compared with basic simulation (e.g. mock up, wheel spoilers, finer grid...)
- Third column (“*Extra information*”) contains important settings in the simulation. Usually, here is described what is different from basic simulation in more details. Also, some other interesting settings are noted here (e.g. number of prism layers).
- Last three columns represent basic simulation results – aerodynamic coefficients (average value of last 200 iterations).

On the end of the thesis, in the attachments, same table is printed and it can be taken out for easier reading and comparison during analysis and comparison of the results. Table alone can show only basic results, but it connects all simulations what gives an opportunity to mutually compare all simulations in the table. Thanks to standardization during all phases in CFD process – pre processing, processing and post processing, all post-processed data and visualizations are already prepared for comparison.

This whole chapter contains 10 subchapters. CFD settings, different geometry set up and comparison between CFD and Wind Tunnel measurement were investigated trough these chapters.

At this point, one more term need to be introduced – **COUNT**. Count is a thousandth part of the aerodynamic coefficient. If two C_d values are compared, e.g. $C_d = 0.322$ and $C_d = 0.318$, it can be sad that difference between these two values is 4 counts. That term is in common usage in automotive aerodynamics and it eases communication, what is very important during analysis of the results.

Table 7.1 CULT – all simulations overview

General information			Results		
Nr.	Data status	Extra information	Cd	Czf	Czr
1	CAS open, basic simulation	wheels sp. standard, 5 prisms	0,339	-0,087	0,060
2	CAS open, bs 01, without wh. sp.	no wheels sp., 5 prisms	0,333	-0,117	0,072
3	CAS open, bs 01, closed inlets	closed middle and upper inlets, 5 prisms	0,333	-0,106	0,062
4	CAS open, bs 01, wheels sp. opt.	wheels sp. middle in&out, 5 prisms	0,342	-0,074	0,059
5	CAS open, bs 01, wheels sp. opt.	wheels sp. middle in, 5 prisms	0,343	-0,078	0,056
6	CAS open, bs 01, wheels sp. opt.	wheels sp. middle out, 5 prisms	0,339	-0,084	0,058
7	CAS open, bs 02, wheels rot.	wheels rotation at angle, 5 prisms	0,333	-0,116	0,070
8	CAS open, bs 01, fine mesh	100 mio. tetra, 5 prisms	0,345	-0,109	-0,015
9	CAS open, bs 01, more iter.	1000 more iterations, 5 prisms	0,336	-0,090	0,060
10	CAS open, bs 01, 10 prism	10 prism layers	0,351	-0,084	-0,014
11	CAS open, bs 01, add. ref. zone	fine ref. zone around wheels sp., 5 prisms	0,339	-0,082	0,062
12	CAS closed, basic simulation	wheels sp. standard, 10 prism	0,324	-0,116	0,069
13	CAS closed, bs 12, without wh. sp.	no wheels sp., 10 prism	0,321	-0,147	0,076
14	CAS closed, bs 12, mock up	closed middle and upper inlets, 10 prism	0,320	-0,131	0,073
15	CAS closed, bs 12, road rough. 0	10 prism	0,292	-0,105	0,038
16	CAS closed, bs 12, no side mirrors	without side mirrors, 10 prism	0,321	-0,115	0,074
17	CAS open, bs 12	CAS closed deleted, open added, 10 prism	0,340	-0,094	0,055
18	CAS open, bs 17, 5 prism	compare with sim 01, 5 prism	0,342	-0,091	0,055
19	CAS closed, bs 12, 5 prism	5 prism	0,327	-0,115	0,068
20	CAS closed, bs 12, wheels sp. opt.	wheels sp. front, 10 prisms	0,321	-0,123	0,072
21	CAS closed, bs 12, wheels sp. opt.	wheels sp. front in, 10 prisms	0,322	-0,115	0,070
22	CAS closed, bs 12, wheels sp. opt.	wheels sp. front out, 10 prisms	0,327	-0,123	0,072
23	CAS closed, bs 12, wheels sp. opt.	wheels sp. front in&out, 10 prisms	0,326	-0,116	0,069
24	CAS closed, bs 12, wheels sp. opt.	wheels sp. rear, 10 prisms	0,328	-0,107	0,075
25	CAS closed, bs 12, wheels sp. opt.	wheels sp. rear in, 10 prisms	0,343	-0,118	-0,018
26	CAS closed, bs 12, wheels sp. opt.	wheels sp. rear out, 10 prisms	0,323	-0,112	0,085
27	CAS closed, bs 12, wheels sp. opt.	wheels sp. rear in&out, 10 prisms	0,325	-0,103	0,082
28	CAS closed, bs 12, side mirrors opt.	mirrors top 0°, 10 prisms	0,323	-0,110	0,073
29	CAS closed, bs 12, side mirrors opt.	mirrors bottom 0°, 10 prisms	0,322	-0,125	0,070
30	CAS closed, bs 12, side mirrors opt.	mirrors top +15°, 10 prisms	0,323	-0,100	0,080
31	CAS closed, bs 12, side mirrors opt.	mirrors middle +15°, 10 prisms	0,319	-0,094	0,084
32	CAS closed, bs 12, side mirrors opt.	mirrors bottom +15°, 10 prisms	0,318	-0,094	0,087
33	CAS closed, bs 12, side mirrors opt.	mirrors top -15°, 10 prisms	0,330	-0,124	0,054
34	CAS closed, bs 12, side mirrors opt.	mirrors middle -15°, 10 prisms	0,332	-0,129	0,052
35	CAS closed, bs 12, side mirrors opt.	mirrors bottom -15°, 10 prisms	0,332	-0,133	0,052
36	CAS open, bs 10	diff. ref. Zon. (ver. after sim. 12), 10 prism	0,341	-0,092	0,057
37	CAS closed, bs 14, diff. speed	70km/h, mid. & up. air inl. closed, 10 prism	0,321	-0,130	0,076
38	CAS closed, bs 14, diff. speed	280km/h, mid. & up. air inl. closed, 10 prism	0,320	-0,137	0,070
39	CAS open, bs 17, diff. speed	140km/h, mid. & up. air inl. closed, 10 prism	0,337	-0,112	0,059
40	CAS open, bs 17, diff. speed	70km/h, mid. & up. air inl. closed, 10 prism	0,337	-0,104	0,062
41	CAS open, bs 17, diff. speed	280km/h, mid. & up. air inl. closed, 10 prism	0,333	-0,112	0,059
42	CAS open, bs 17, ref. z. UBV opt.	10 prism	0,339	-0,097	0,051
43	CAS open, bs 18, ref. z. UBV opt.	5 prism	0,343	-0,097	0,052
44	CAS open, bs 18, ref. z. UBV opt.	diffusor ref. zone, 5 prism	0,343	-0,095	0,057
45	CAS open, bs 18, ref. z. UBV opt.	fine mesh, 130 mio. el., 5 prism	0,348	-0,108	-0,016
46	CAS open, bs 18, ref. z. UBV opt. 2	sharp UBV, 5 prism	0,342	-0,097	0,060
47	CAS open, bs 18, ref. z. UBV opt. 2	5 prism,	0,343	-0,098	0,052
48	CAS open, bs 18, ref. z. UBV opt.	sharp UBV, wake refinement, 5 prism	0,340	-0,099	0,059
49	CAS open, bs 18, ref. z. UBV opt.	sharp UBV, "box 25", 5 prism	0,346	-0,114	-0,012
50	CAS open, bs 18, ref. z. UBV opt.	sharp UBV, "box front", 5 prism	0,343	-0,094	0,060
51	CAS open, bs 01, restart 3500 iter.	simulation 01 restart, 5 prism	0,332	-0,094	0,058
52	CAS open, bs 46, cell based	sharp UBV, 5 prism	0,324	-0,084	0,064
53	CAS open, bs 49, "box 25"	sharp UBV, 5 prism	0,330	-0,099	-0,003
54	CAS closed, bs 12, cell based	10 prism	0,307	-0,117	0,032
55	CAS open, bs 01, new ref. zones	5 prism	0,342	-0,106	-0,008

7.1 CFD Grid Influence

This chapter deals with CFD grid influence. Idea of this chapter is to prove that default grid settings are good. Therefore, additional simulations with finer grids are compared against simulations with basic settings. If finer grid simulations do not show big differences, compared with standard simulations, default settings are good.

Since CFD grid consists of prism and tetrahedral grid, this chapter is divided into two subchapters. Chapter 7.1.1 deals with tetrahedral part of the grid and chapter 7.1.2 deals with prism layer part.

7.1.1 Tetrahedral Elements Refinement Influence

There are two different grid settings which will be investigated. One refers to the default settings and other to the fine grid settings. Difference between these grid settings lays in the refinement areas around car. Two refinement boxes define refinement areas around car – one box in the area of engine compartment and another around rest of the car (Figure 7.1). In these boxes, maximum tetrahedral cell volume is limited, as it is showed in the Figure 7.1. Fine grid settings are defined with decreased maximum cell volume in the box around rest of the car to 400mm^3 . This volume reduction increased tetrahedral cell number from 62 to 82 million elements.

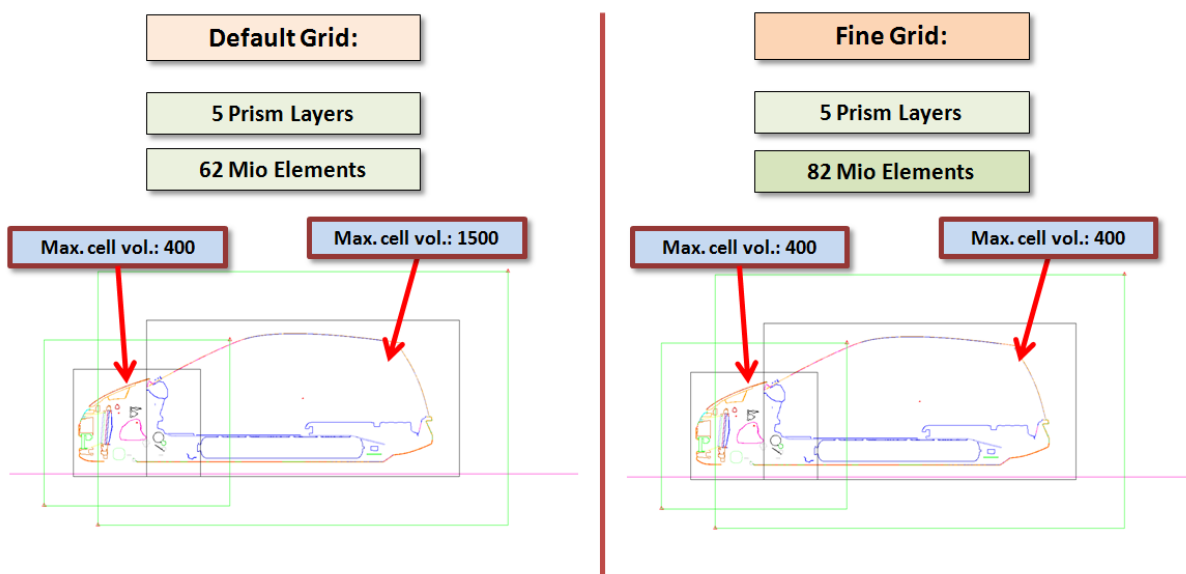


Figure 7.1 Default and fine grid settings comparison

Reduction of tetrahedral elements size was carried out close to the car’s surface because biggest gradients in the air flow are present exactly in that area. To prove that default settings are good, following results for compared simulations should be very similar.

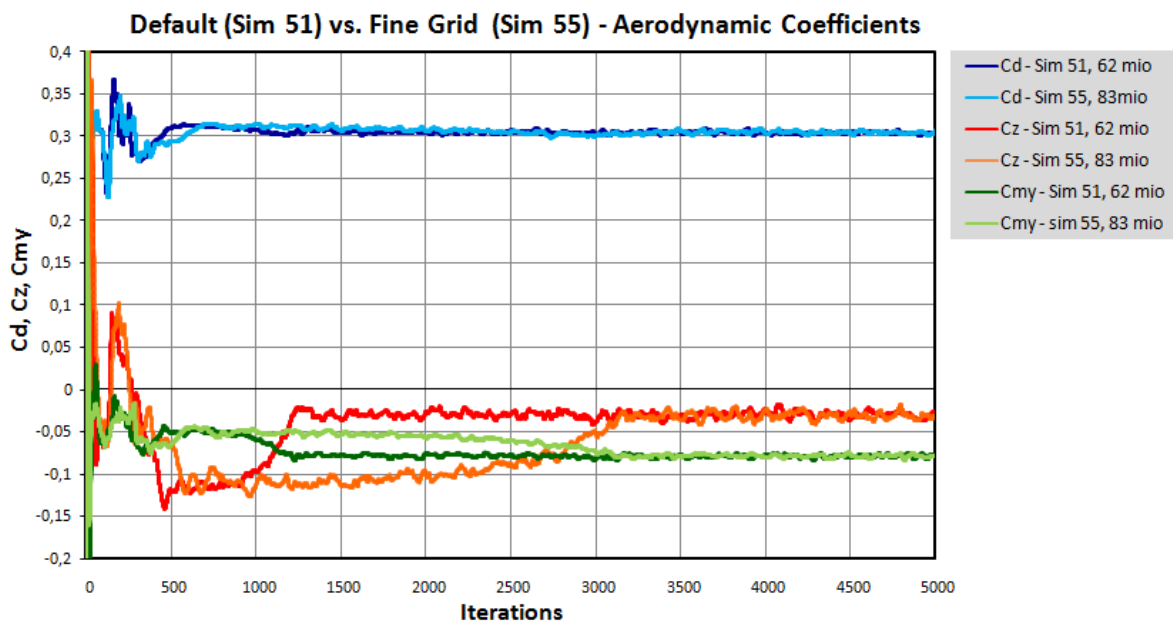


Figure 7.2 Aerodynamic coefficients diagram – Default grid vs. Fine grid

Table 7.2 Aerodynamic coeff. – simulations 51 and 55 (avg. values for last 200 iter.)

Cult Basic – Sim. 51			Fine Grid – Sim. 55		
Cd (WCP)		0,303	Cd (WCP)		0,303
Cz		-0,031	Cz		-0,032
Cmy		-0,079	Cmy		-0,079
	Czf	-0,095		Czf	-0,095
	Czr	0,064		Czr	0,063
	Cd	0,332		Cd	0,333

Figure 7.2 and Table 7.2 show results for default grid and fine grid simulations. Both simulations converged. Results are very close and it is clear that default grid has same precision as fine grid. Therefore, default refinement settings are fine enough to “catch” air flow gradients around vehicle and there is no need for increasing grid refinement in that area.

Another very interesting phenomenon is minimum number of iterations required for simulation to converge. From the diagram in Figure 7.2 it is clear that simulation with default grid settings converged long before compared with fine grid simulation (approx. 1200 iterations vs. 3100 iterations). Explanation for that can lay in a fact that disturbances in finer grid leave flow domain much later. Because of decreased element size, with each iteration disturbances move shorter way in finer grid. Therefore disturbances need much more iterations to leave flow domain.

Accordingly, fine grid computing time is increased not only because of larger number of elements, but also because it needs much more iterations to converge.

In order to confirm statements above and utilize CFD benefits, such as flow visualization, these two simulations are additionally compared below.

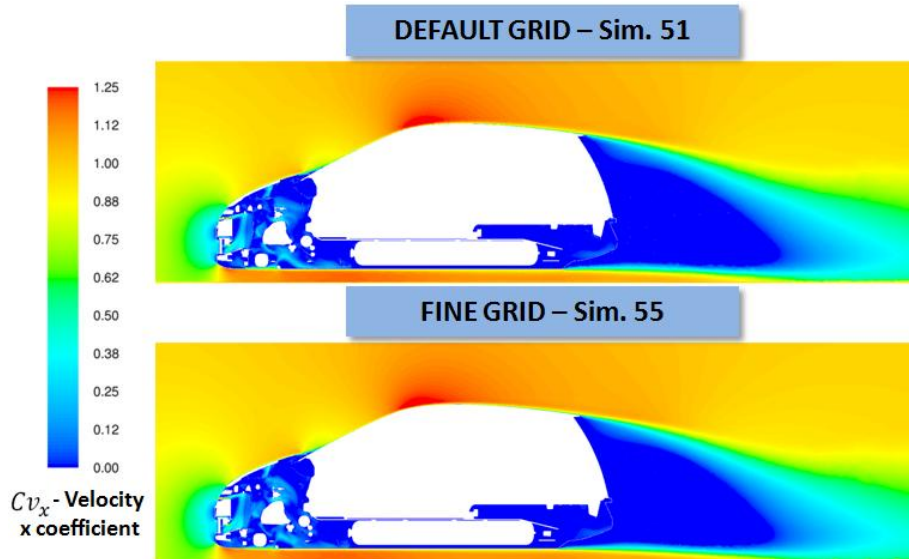


Figure 7.3 Velocity-X coefficient visualization in Y0 plane – CULT simulations 51 and 55

Figure 7.3 shows Velocity-X coefficient visualization in Y0 plane. There are no notable differences between simulations.

Also, if distribution of pressure coefficient on the car’s surface in Y0 plane is observed below, no significant differences can be found.

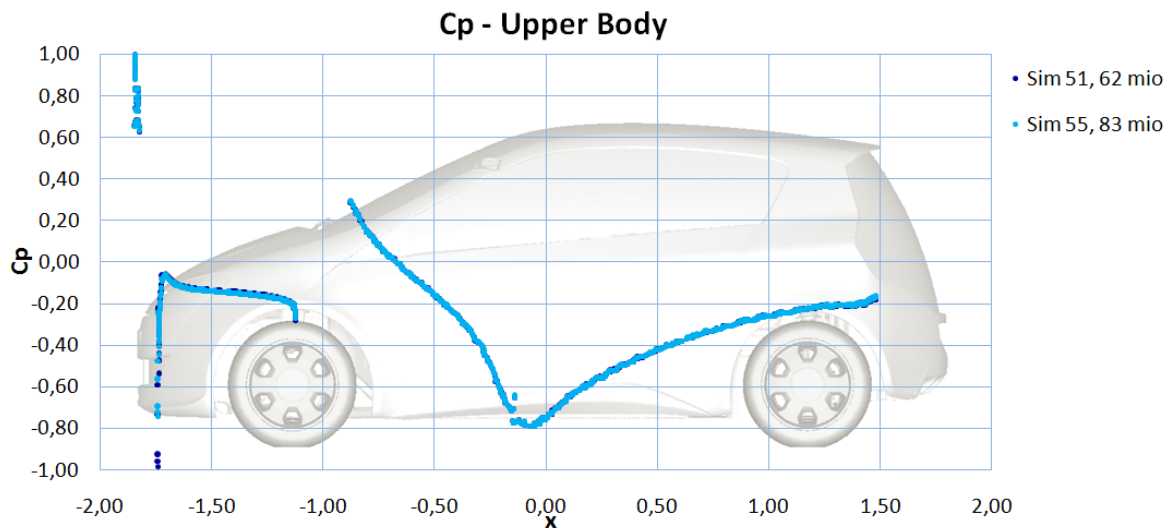


Figure 7.4 Pressure coeff. distribution on the upper body – CULT simulation 51 and 55

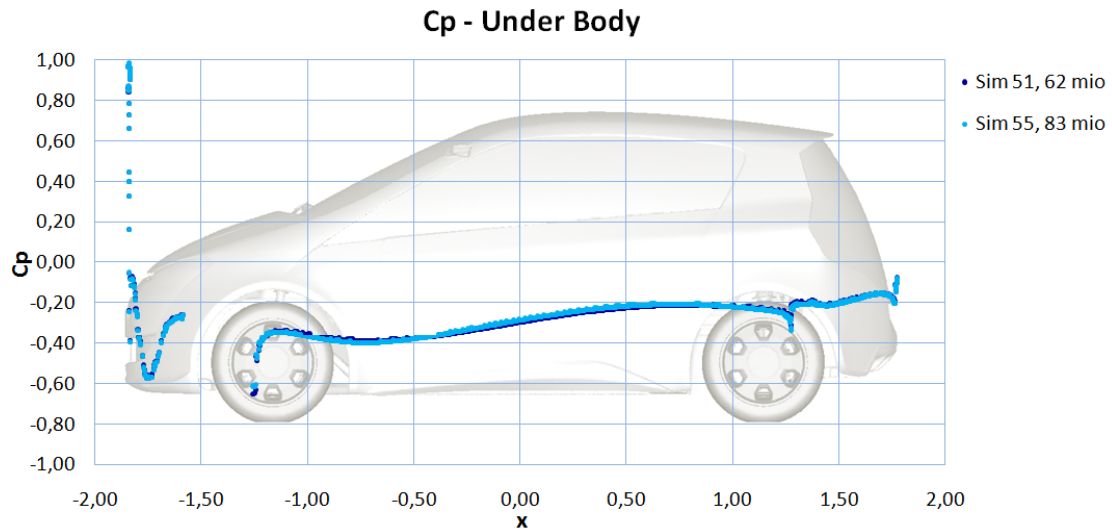


Figure 7.5 Pressure coeff. distribution on the under body – CULT simulation 51 and 55

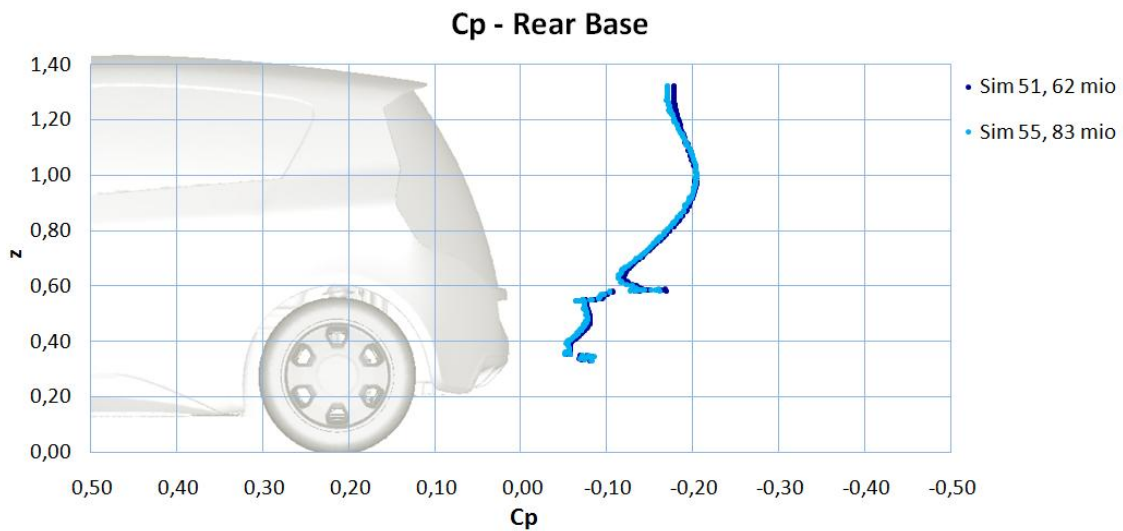


Figure 7.6 Pressure coeff. distribution on the rear base – CULT simulation 51 and 55

Conclusion

With fine grid a lot more computing time was spent without any benefit in the accuracy of the final results. This example shows that decreasing element size should be carried out very carefully, without unnecessary and expensive exaggeration. Also, this comparison leads to conclusion that default settings, defined by standards, are good enough.

7.1.2 Influence of Different Prismatic Layers

Default prism layer settings imply 5 prism layers with total height of 2.23mm. To investigate prism layer thickness influence, additional 5 prism layers were added. With same growth rate, new prism layer has 10 layers with total height of 7.79mm (Table 7.3).

Table 7.3 Prism layer settings for 5 and 10 prism layers grid

	5 Prism Layers Grid	10 Prism Layers Grid
Number of layers	5	10
Growth rate	1.2	1.2
First layer height [mm]	0.3	0.3
Total height [mm]	2.23	7.79

Boundary layer thickness (δ) can be calculated from Blasius solution [1] for turbulent flow (see Chapter 4.1.3):

$$\delta = \frac{0.37x}{Re^{\frac{1}{5}}} = \frac{0.37 \cdot 2}{(4.6 \cdot 10^6)^{\frac{1}{5}}} \approx 0.034\text{m} = 34\text{mm}$$

$x \approx 2\text{m}$ – referent length, approximately length of the vehicle roof

$Re = 4.6 \cdot 10^6$ – Reynolds number

Meaning of this calculation is not to get perfectly correct results, but to get numbered value which is good enough to compare it with CFD prism layer height. Referent length (x) was chosen approximately. Guidance for choosing referent length value was length of car’s roof and upper part of front windscreen. On the trailing edge of the roof (on the rear end) thickest boundary layer is expected, and exactly that value is approx. calculated here.

Everywhere else boundary layer is expected to be thinner. Therefore, total height of CFD prism layers need to be in a range that will suit most of the car’s surfaces and doesn’t need to be thick as boundary layer on the trailing edge of the roof. That is one of the simplifications used here.

10 prism layers grid is much closer to boundary layer thickness calculated from Blasius solution. Bellow, it will be investigated if and how this differences in prism layer thickness manifests on the simulation results.

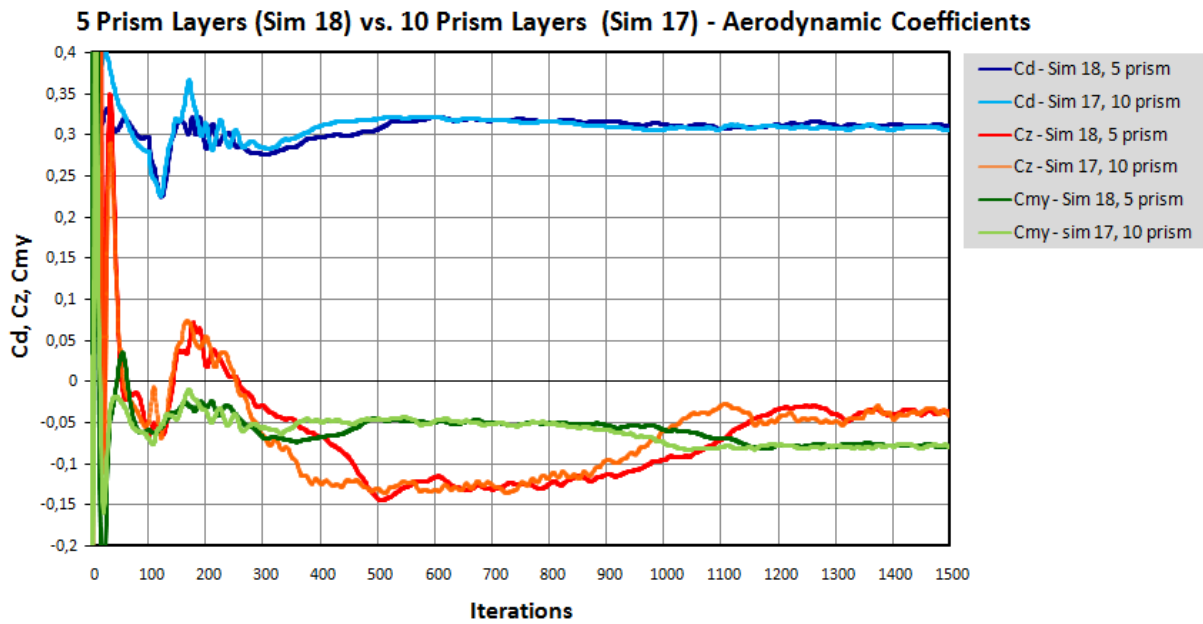


Figure 7.7 Aerodynamic coefficients diagram – 5 prism layers vs. 10 prism layers

Table 7.4 Aerodynamic coeff. – simulations 18 and 17 (avg. values for last 200 iter.)

5 Prism Layers – Sim. 18			10 Prism Layers – Sim. 17		
	Cd (WCP)	0,311		Cd (WCP)	0,308
	Cz	-0,039		Cz	-0,042
	Cmy	-0,078		Cmy	-0,079
	Czf	-0,098		Czf	-0,100
	Czr	0,059		Czr	0,058
	Cd	0,342		Cd	0,340

Figure 7.7 and Table 7.4 shows compared simulations results. There is a difference of two counts between results (better total drag value for simulation with 10 prism layers). If it is taken into account that 10 prism layers requires much more time at the pre processing phase, accuracy/time consumption ratio is much lower compared with 5 prism layers grid. Therefore, it seems that effort to create additional 5 prism layers is not justified.

Regardless to the results above, to confirm results, three figures below show pressure coefficient distribution on the car’s surface in Y0 plane. No significant differences are present.

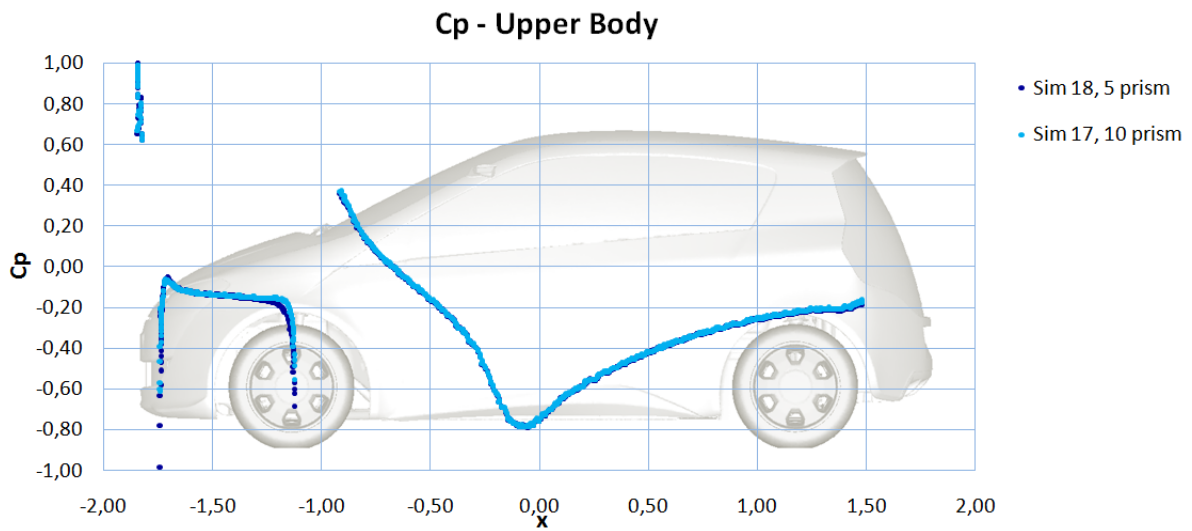


Figure 7.8 Pressure coeff. distribution on the upper body – CULT simulation 18 and 17

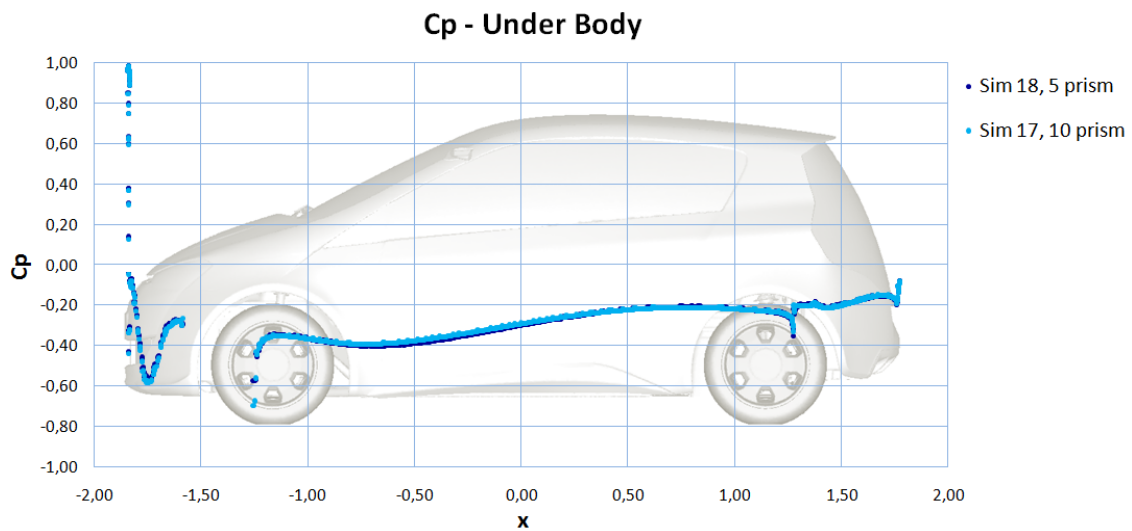


Figure 7.9 Pressure coeff. distribution on the under body – CULT simulation 18 and 17

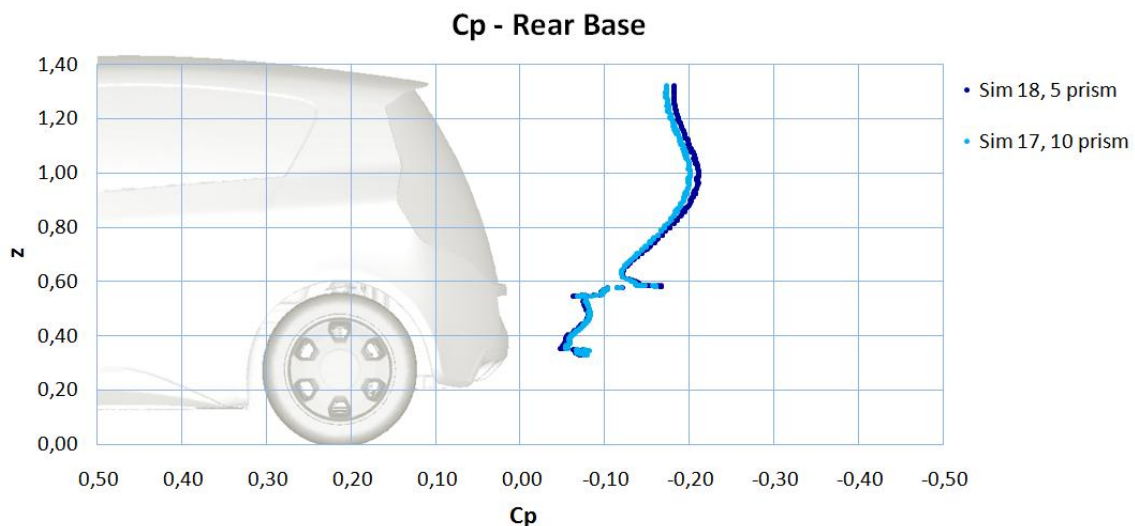


Figure 7.10 Pressure coeff. distribution on the rear base – CULT simulation 18 and 17

The biggest differences in the diagrams above are on the rear base of the vehicle (Figure 7.10). 10 prism layers grid has slightly higher pressure – that is the main reason for better drag values.

Conclusion

5 prism layers grid has better accuracy/time consumption ratio. Pre-processing is much faster when creating only 5 prism layers because it is not necessary to have surface mesh quality as it is case with 10 prism layers. Despite large effort to create 10 prism layers, results are very similar, what leads to conclusion that 5 prism layer grid, defined with standards is good enough.

7.2 Solver Influence – Cell-Based vs. Node-Based Reconstruction of Gradients

Gradients are needed not only for constructing values of a scalar at the cell faces, but also for computing secondary diffusion terms and velocity derivatives. The gradient $\nabla\phi$ of a given variable ϕ is used to discretize the convection and diffusion terms in the flow conservation equations [25]. Here, two types of the gradients evaluation methods, used in Fluent, are investigated:

- Green-Gauss Cell-Based Gradient Evaluation
- Green-Gauss Node-Based Gradient Evaluation

Green-Gauss theorem is used to compute the gradient of the scalar ϕ at the cell center c_0 , using the formula [25]:

$$(\nabla\phi)_{c_0} = \frac{1}{V} \sum_f \bar{\phi}_f \vec{A}_f$$

ϕ_f – ϕ value at the cell centroid

Green-Gauss Cell-Based Gradient Evaluation

By default, the face value $\bar{\phi}_f$ in Green-Gauss theorem Equation is taken from the arithmetic average of the values at the neighboring cell centers, i.e.:

$$\bar{\phi}_f = \frac{\phi_{c_0} + \phi_{c_1}}{2}$$

Green-Gauss Node-Based Gradient Evaluation

Alternatively, $\bar{\phi}_f$ can be computed by the arithmetic average of the nodal values on the face:

$$\bar{\phi}_f = \frac{1}{N_f} \sum_n^{N_f} \bar{\phi}_n$$

N_f – number of nodes on the face

The nodal values, $\bar{\phi}_n$ in equation above, are constructed from the weighted average of the cell values surrounding the nodes. This scheme reconstructs exact values of a linear function at a node from surrounding cell-centered values on arbitrary unstructured grids by solving a constrained minimization problem, preserving a second-order spatial accuracy [25].

The node-based averaging scheme is known to be more accurate than the default cell-based scheme for unstructured grids, most notably for triangular and tetrahedral grids. This claim will be investigated below.

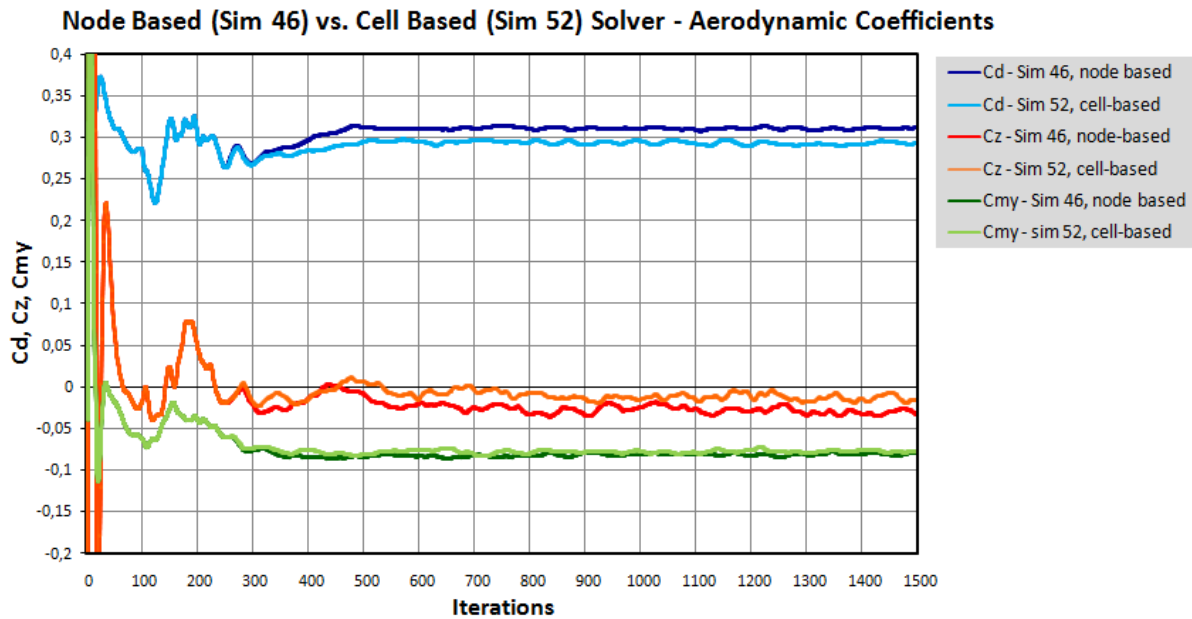


Figure 7.11 Aerodynamic coefficients diagram – Node Based vs. Cell Based Solver

Table 7.5 Aerodynamic coeff. – simulations 46 and 52 (avg. values for last 200 iter.)

Node Based – Sim. 46			Cell Based – Sim. 52		
Cd (WCP)		0,311	Cd (WCP)		0,293
Cz		-0,031	Cz		-0,014
Cmy		-0,081	Cmy		-0,077
		Czf			-0,084
		Czr			0,070
		Cd			Cd
		0,342			0,324

Figure 7.11 and Table 7.5 show simulation results. In one simulation Node-based solver was used (Sim. 46) and in another Cell-based solver (Sim. 52). Simulation which used Cell-based solver showed lower drag – difference between simulations is 18 drag counts. That difference is significant. Therefore, it can be concluded that solver has significant influence on the results with this type of the CFD grid.

Below are flow visualizations extracted from standard post processing material. Only visualizations which show visible differences between simulations are showed.

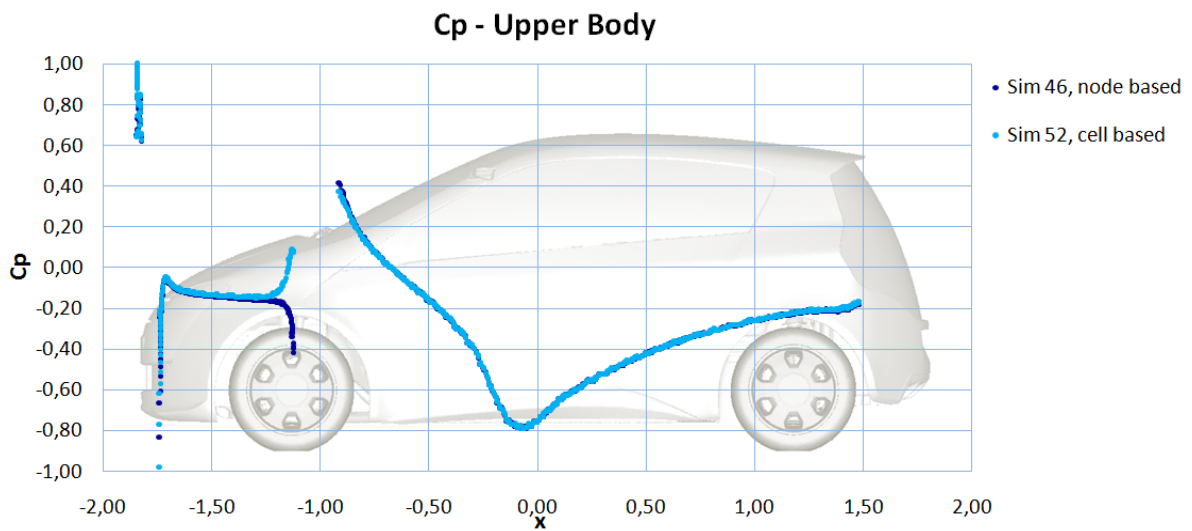


Figure 7.12 Pressure coeff. distribution on the upper body – CULT simulation 46 and 52

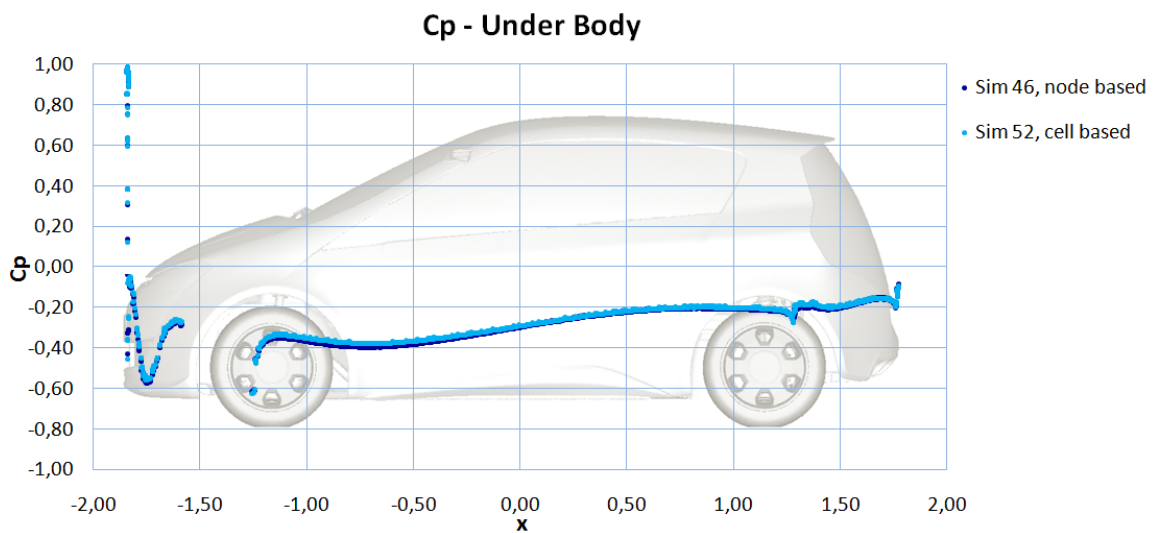


Figure 7.13 Pressure coeff. distribution on the under body – CULT simulation 46 and 52

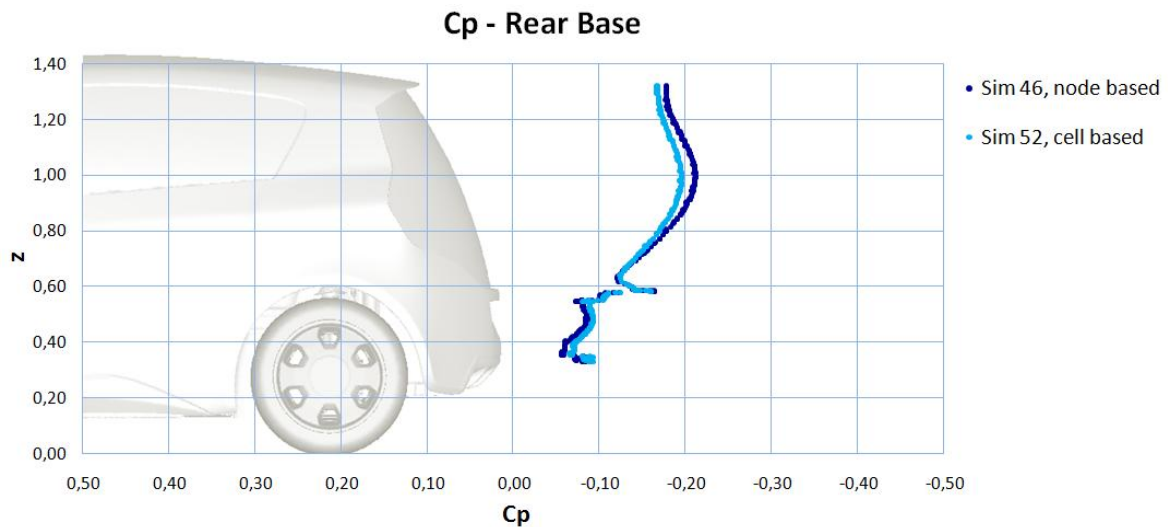


Figure 7.14 Pressure coeff. distribution on the rear base – CULT simulation 46 and 52

Set of pressure coefficient distribution on the car’s surface in Y0 plane above shows higher pressure on the car’s rear base for Cell-based simulation. That is one of the reasons for lower drag when using Cell-based solver.

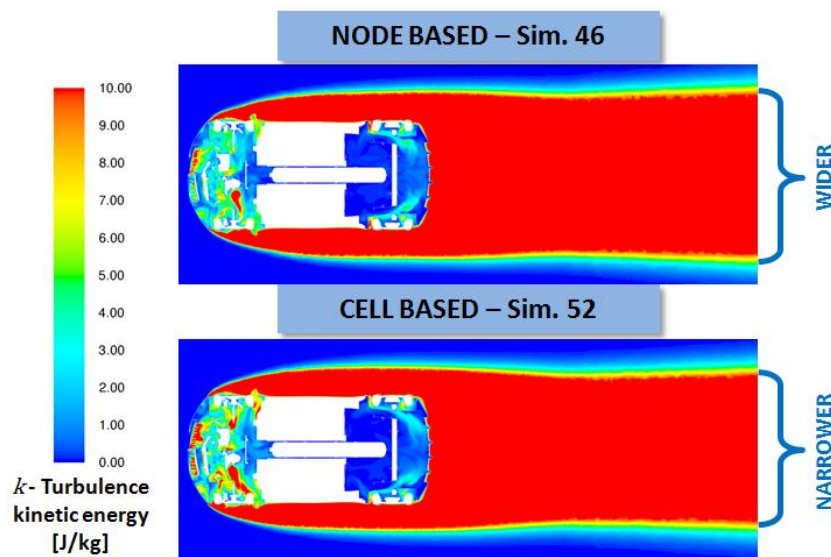


Figure 7.15 Turbulence kinetic energy in Z276 plane – CULT simulations 46 and 52

Wake, which is visible observing turbulence kinetic energy in the Figure 7.15 above is narrower when Cell-based solver is used. Narrower wake is one of the lower drag indicators (see Chapter 5.3.1).

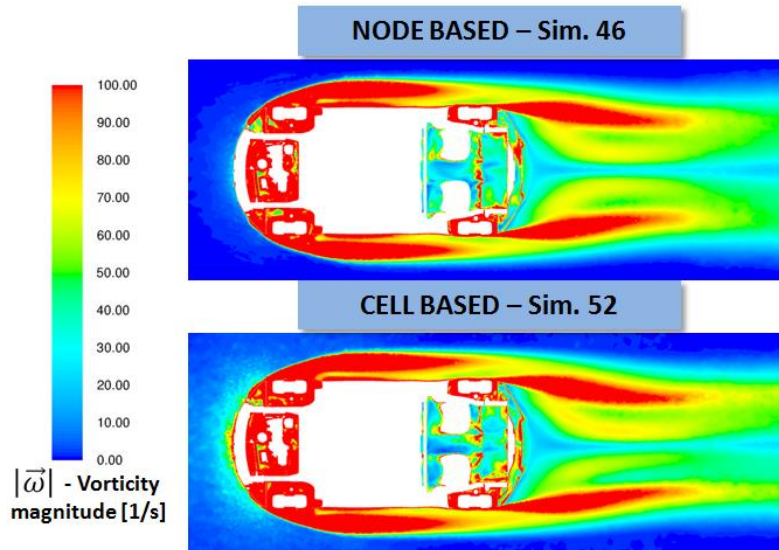


Figure 7.16 Vorticity magnitude in Z470 plane – CULT simulations 46 and 52

Vorticity magnitude in the Figure 7.16 shows interesting difference between Node-based and Cell-based solver. That difference is located on the front end of the car, in the area of high pressure, close to the stagnation point. While Node-based solver shows barely noticeable vorticity magnitude in that area, Cell-based solver shows significant vorticity presence. Answer for that phenomenon probably lies in gradient evaluation difference between these two methods mentioned at the beginning of this chapter. More precise answers and details are out of scope for this thesis.

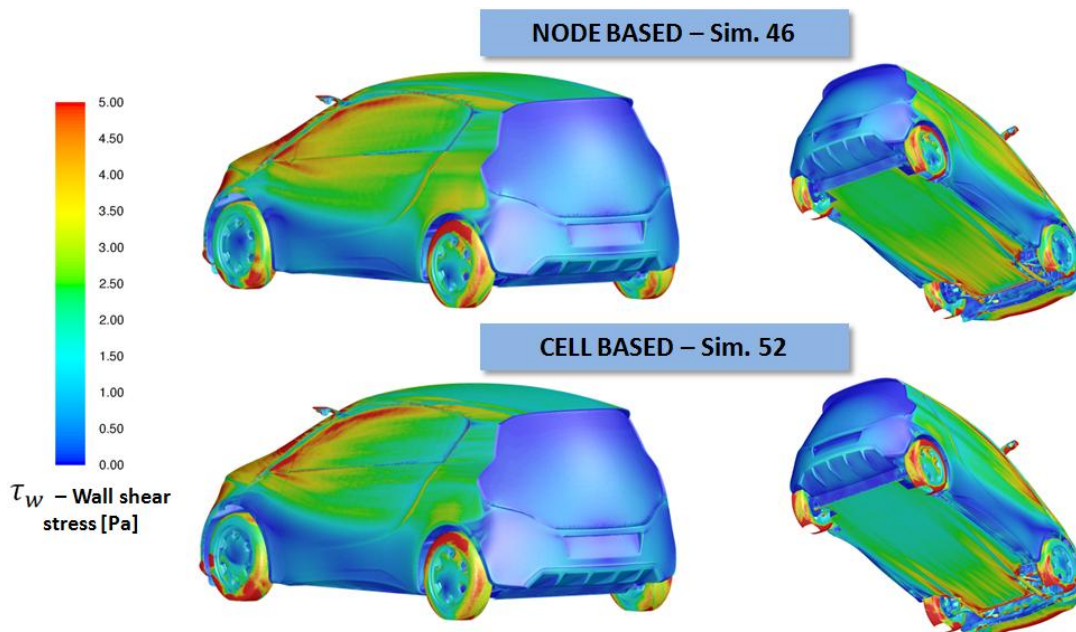


Figure 7.17 Wall shear stress 3D visualization – CULT simulations 46 and 52

Wall shears stress contours in the Figure 7.17 above show that Cell-based solver calculated less intense wall shear stress on the car’s outer surface. That is visible on the rear end of the roof, on the side of the car and on the under body. Less intensive wall shear stress is another reason for lower drag when using Cell-based solver.

Conclusion

Claim that the Node-based averaging scheme is known to be more accurate than the Cell-based scheme for unstructured grids, such is case here, proved to be correct. Differences between results are significant. But, how is it doubtless that exactly Node-based averaging scheme is correct? Answer lies in flow physics. Node-based results are closer to the real flow physics as it was showed in the flow visualization examples above. Cell-based simulation showed some physically unexplainable phenomenon – Vorticity magnitude in the Figure 7.16 shows vortices where they should not exist.

7.3 Road Roughness Influence

In the automotive aerodynamics ground has very important role, because it has a strong influence on the overall air flow around vehicle. Therefore, road roughness in simulation properties should be carefully determined. In project CULT default road roughness is set up to 0.5 m. That number was determined in earlier projects by comparing CFD and wind tunnel results. Physically, 0.5 m is enormously high. But, with that value CFD simulations showed best congruence with wind tunnel tests.

In this chapter, goal is to show importance of road roughness value. Hence, two simulations are compared – one with standard road roughness (0.5m) and one with road roughness set to 0.0 m. These two simulations can be called simulations with rough (0.5m) and smooth ground (0.0m).

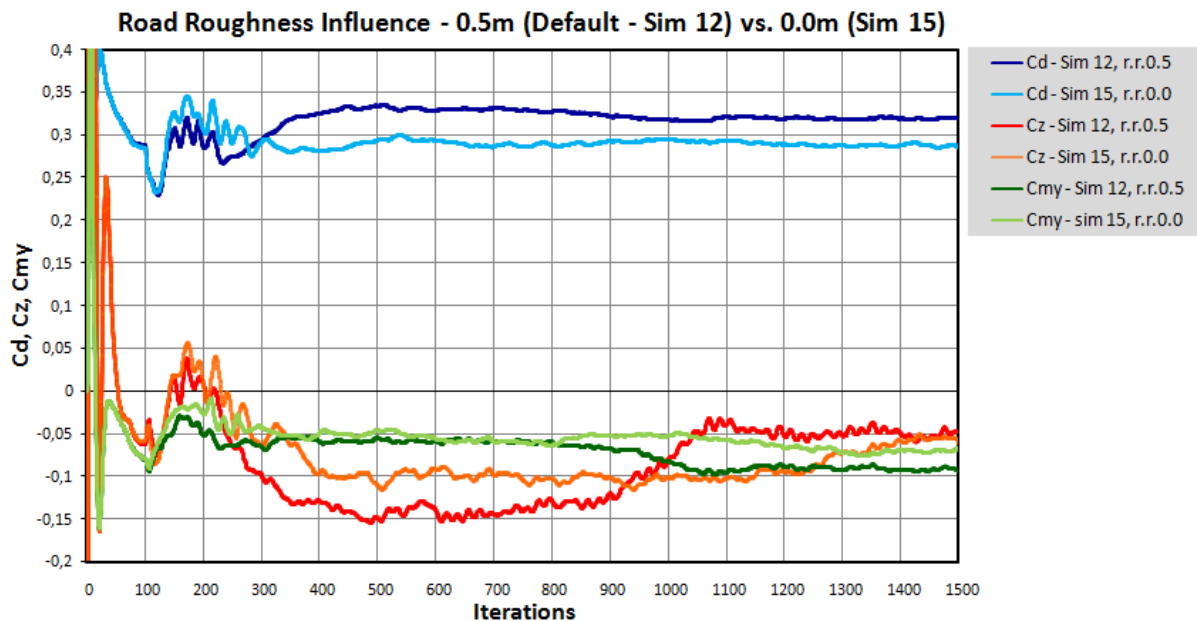


Figure 7.18 Aerodynamic coefficients diagram – Road roughness influence

Table 7.6 Aerodynamic coeff. – simulations 12 and 15 (avg. values for last 200 iter.)

Road Roughness 0.5m – Sim. 12			Road Roughness 0.0m – Sim. 15		
	Cd (WCP)	0,320		Cd (WCP)	0,288
	Cz	-0,050		Cz	-0,060
	Cmy	-0,091		Cmy	-0,070
	Czf	-0,116		Czf	-0,100
	Czr	0,066		Czr	0,040
	Cd (CP)	0,324		Cd	0,292

Results in Figure 7.18 and Table 7.6 show that smooth ground has much lower drag – difference between simulations is 32 drag counts. Also, it is important to emphasize that simulation with smooth ground did not totally converged – lift coefficient (C_z) did not reached necessary convergence. It means that smooth ground needs more iterations to converge. Nevertheless, these two simulations will be compared below.

First, set of pressure coefficient distribution on the vehicle surface in the Y0 plane figures are showed. The biggest difference is on the rear base. Close to the roof’s trailing edge (Figure 7.19) pressure coefficient for smooth ground simulation starts to grow. Last point on the roof’s trailing edge is starting point on the rear end top (Figure 7.21). Because pressure at this point is much higher for smooth ground simulation, on the whole rear end smooth ground has much higher pressure. That higher pressure on the rear base is the main reason for lower drag in a case of the smooth ground.

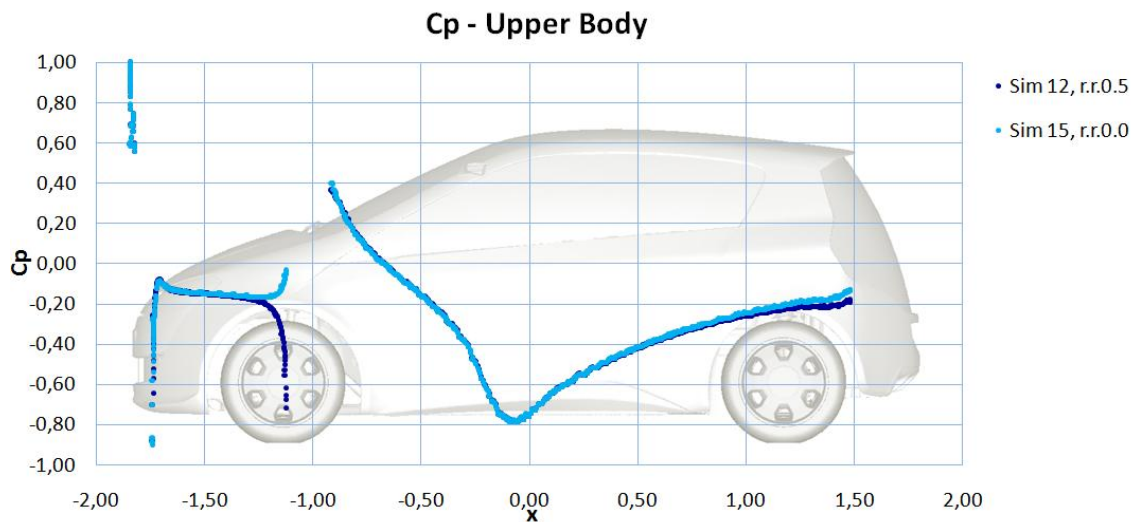


Figure 7.19 Pressure coeff. distribution on the upper body – CULT simulation 12 and 15

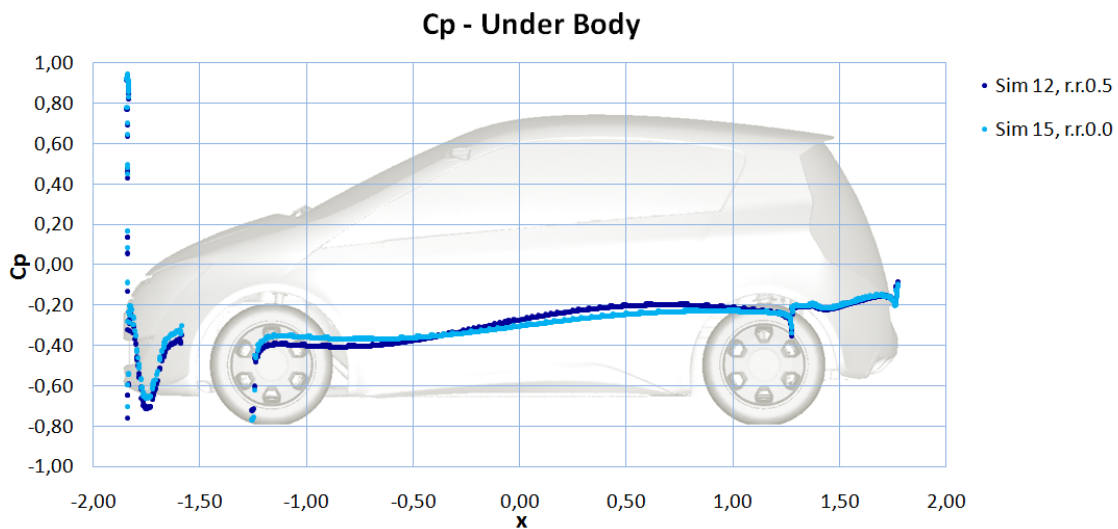


Figure 7.20 Pressure coeff. distribution on the under body – CULT simulation 12 and 15

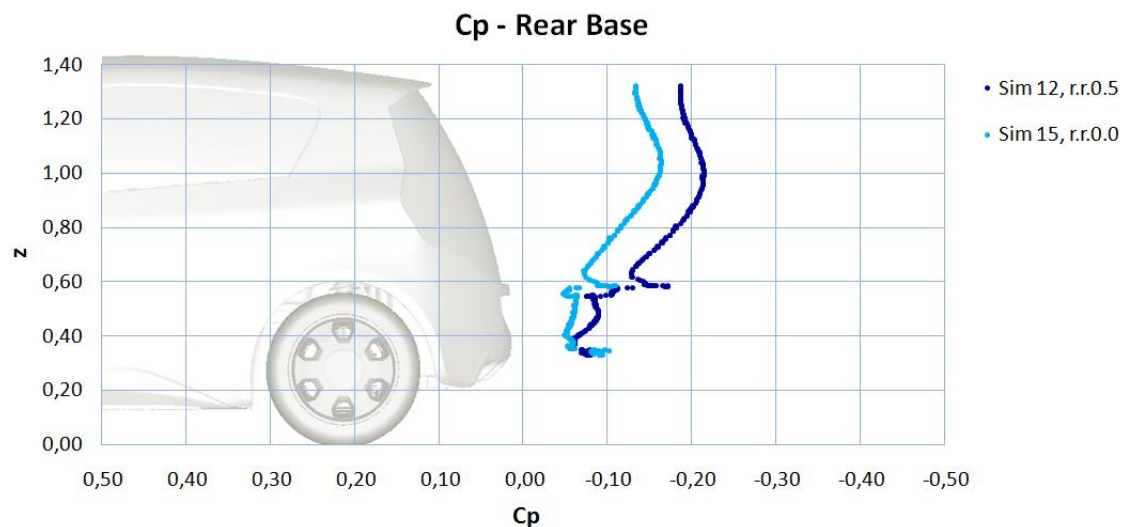


Figure 7.21 Pressure coeff. distribution on the rear base – CULT simulation 12 and 15

Furthermore, in the Figure 7.22 total pressure coefficient in Y0 cut plane is showed. It is obvious that there is a higher pressure on the rear end for smooth ground simulation – same as above, but now it is visualized in the whole Y0 cut plane.

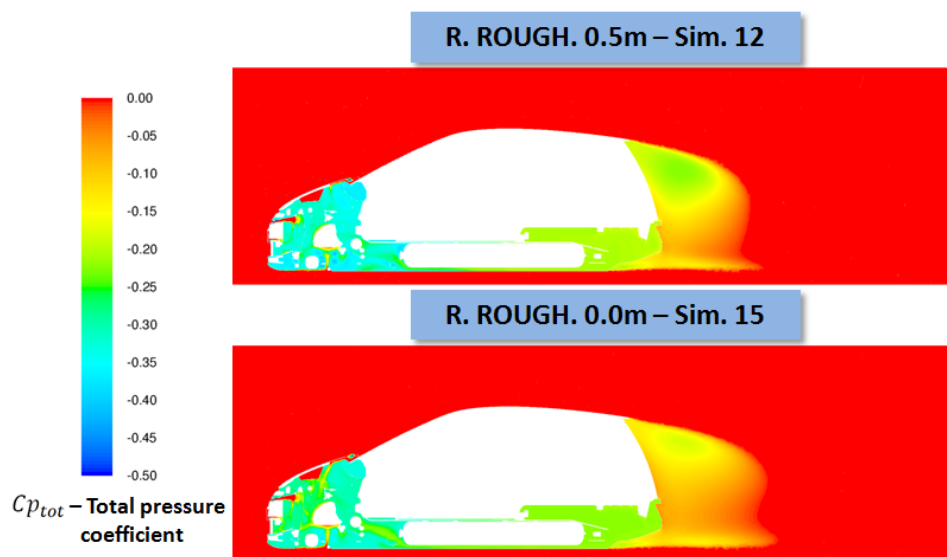


Figure 7.22 Total pressure coefficient in Y0 plane – CULT simulations 12 and 15

In the Figure 7.23 total pressure coefficient in the Z470 cut plane is showed. That figure is presented to show that simulation with smooth ground has much smaller and differently shaped side wakes. Accordingly, road roughness has strong influence, not only on the air flow on the rear end of the car, but also on the side flow – especially on the side wake along front wheels.

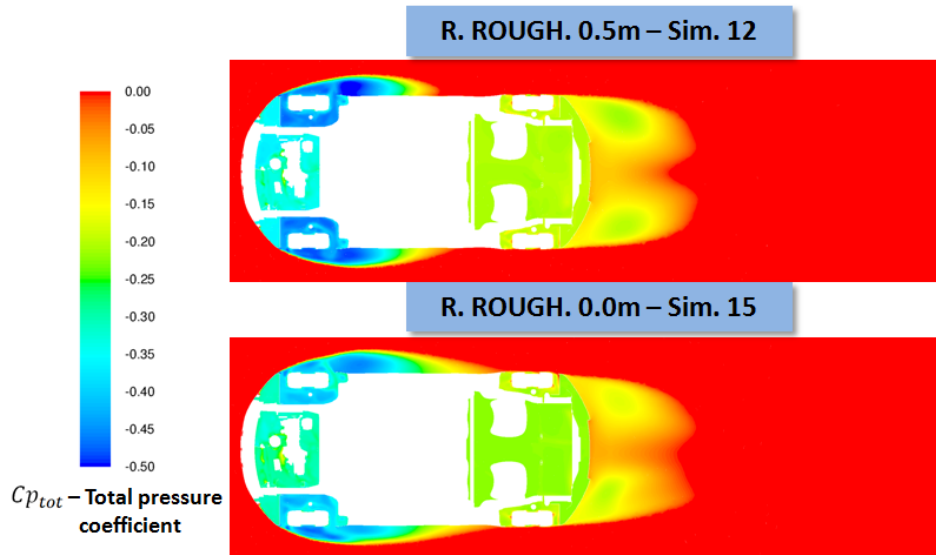


Figure 7.23 Total pressure coefficient in Z470 plane – CULT simulations 12 and 15

On the end, in the figure bellow, turbulence kinetic energy in the Z276 cut plane is showed. Wake, visible in the figure, is narrower for the smooth ground simulation. Narrower wake is indicator of lower drag (see Chapter 5.3.1).

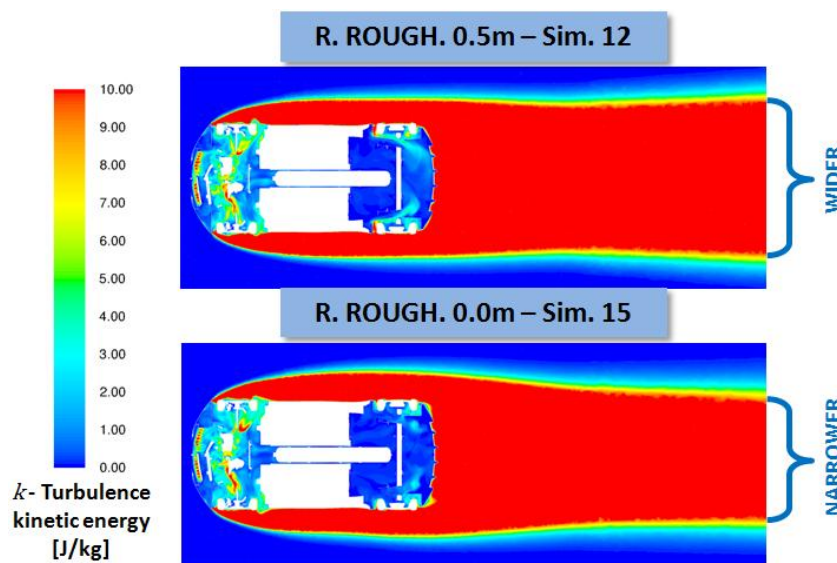


Figure 7.24 Turbulence kinetic energy in Z276 plane – CULT simulations 12 and 15

Conclusion

Simulations comparison, showed in this chapter, clearly indicates importance of correct road roughness set up. Road roughness greatly affects whole air flow around vehicle. In this particular case, rough ground decreases pressure on the rear end and increases total aerodynamic drag.

7.4 Geometry Discretization - Blunt vs. Sharp Edge

This chapter deals with edges on the vehicle geometry. During simulation pre processing, when wrapper surface is being created, there are two approaches for sharp edges. Either, they can be kept as a sharp, or they can be blunted.

It is important to explain how TGrid is dealing with sharp edges when wrapping surface. TGrid has an option to keep region boundaries during wrapping – hence, if vehicle surface is divided on the regions on that way that boundaries between regions are exactly on the sharp edge, sharp edges will be kept. It is important to remember that dividing surface on the regions is also important to create different mesh element size (each region can have its own element size). Therefore, when dividing surfaces in TGrid two guiding taught should be followed:

- Different element sizes – explained in Chapter 4.1.2
- Keeping sharp edges – investigated in this chapter

Consequently, keeping sharp edges requires additional effort in wrapping preparation. This chapter will investigate is it profitable to keep sharp edges on the vehicle geometry. To investigate this, edge showed in the Figure 7.25 was chosen. Observed edge is close to the rear diffuser. Rear diffuser on the CULT vehicle is specific because of step geometry transition on the under body – this step was created because of design requirements. It has a strong influence on the diffuser air flow and, consequently, on the whole rear end of the vehicle. Reason for that is flow separation which occurs exactly at the observed edge.

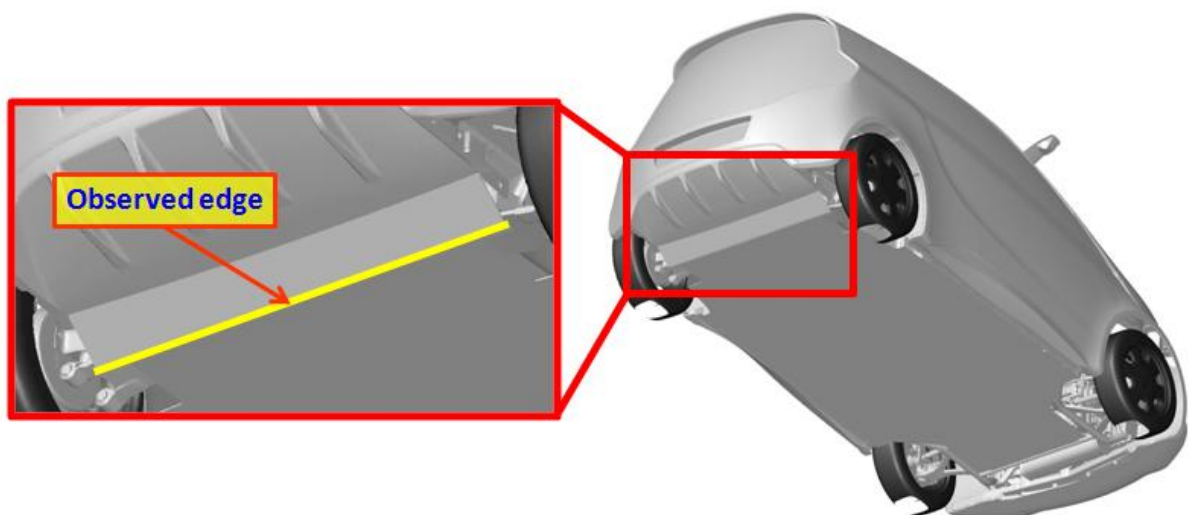


Figure 7.25 Observed edge – trailing edge of the under body (beginning of rear diffuser)

To investigate influence of this particular edge sharpness to the flow separation, two simulations were made and will be compared bellow. On the one simulation, under body was not divided on the regions before wrapping, hence wrapper surface make observed edge blunt. On the other simulation under body was divided on the regions, with the observed edge exactly at the regions boundary and edge remained sharp. It is important to emphasize that this one edge is the only difference between simulations.

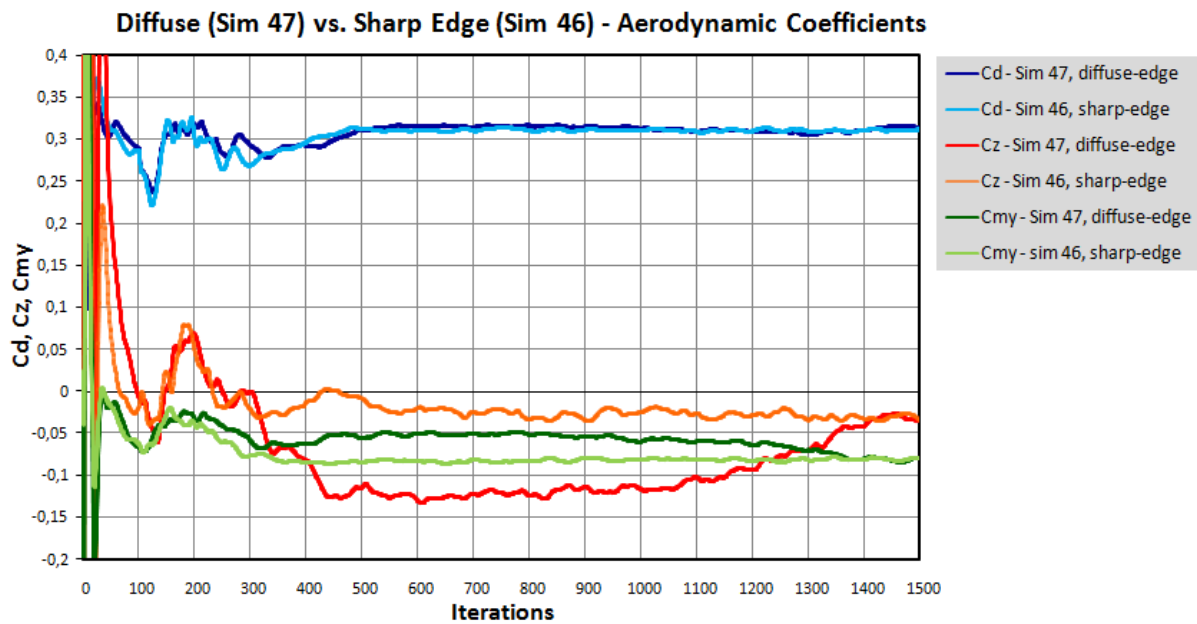


Figure 7.26 Aerodynamic coefficients diagram – Blunt edge vs. Sharp edge

Table 7.7 Aerodynamic coeff. – simulations 47 and 46 (avg. values for last 200 iter.)

Diffuse Edge – Sim 47			Sharp Edge – Sim 46		
Cd (WCP)		0,312	Cd (WCP)		0,311
Cz		?	Cz		-0,031
Cmy		-0,078	Cmy		-0,081
	Czf	?		Czf	-0,097
	Czr	?		Czr	0,066
	Cd	0,343		Cd	0,342

Figure 7.26 and Table 7.7 show results of two compared simulations. From the diagram in the Figure 7.26 it is obvious that simulation with blunt edge need much more iterations to converge. Therefore, standard set up with 1500 iterations was not enough for simulation to converge.

All simulations made in this thesis, except simulations 46, 48, 49, 50, 52 and 53 are made with blunt edge between under body and diffuser (observed edge). It is very interesting if the diagram in the Figure 7.26 is compared with the diagram in the Figure 7.2 and Figure 7.11. Figure 7.2 contains two simulations with blunted observed edge, and the Figure 7.11 contains two simulations with sharp observed edge. From those three diagrams it can be concluded that descend and ascent of C_z value is caused by the observed edge. That is a proof that only slight blunting of one edge can have strong influence on the CFD calculation. Of course, that is because of specific position of this edge, where it has a strong influence on the flow behind the car.

That conclusion leads to the idea to divide edges on the vehicle outer surface to important and not important edges. Goal is to invest time to keep important edges sharp, without losing time on not important edges. Observed edge in this investigation certainly belongs to the important edges.

Figure 7.27 and Figure 7.28 show flow visualization in the Y0 cut plane. After interaction with the sharp edge, flow remained smooth. On the contrary, blunt edge created diffused air flow after separation. That phenomenon is in small scale and therefore it has no big influence on the final result.

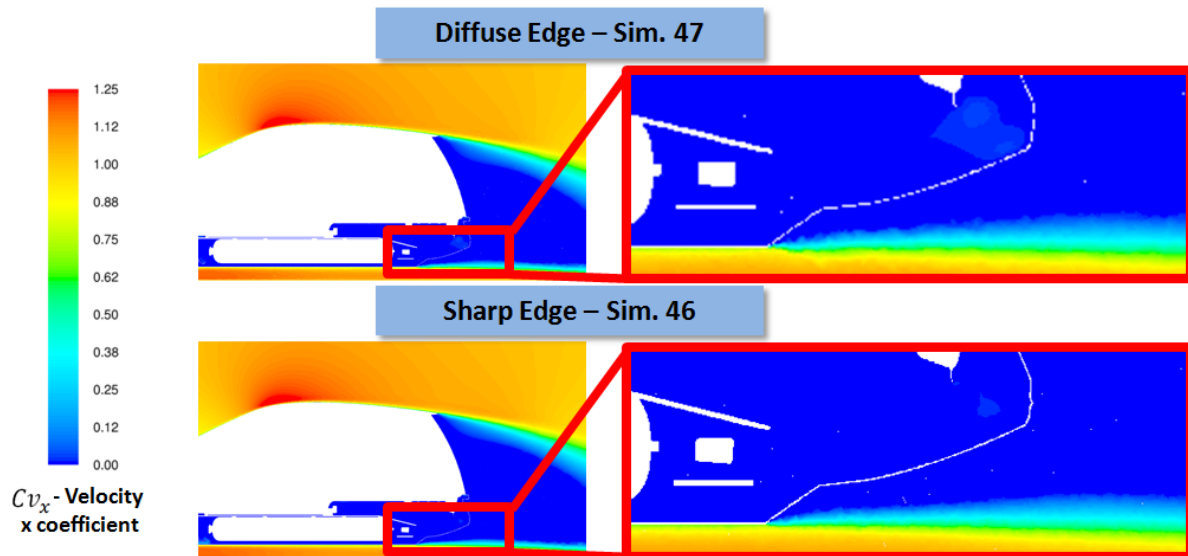


Figure 7.27 Velocity-X coefficient in Y0 plane – CULT simulations 47 and 46

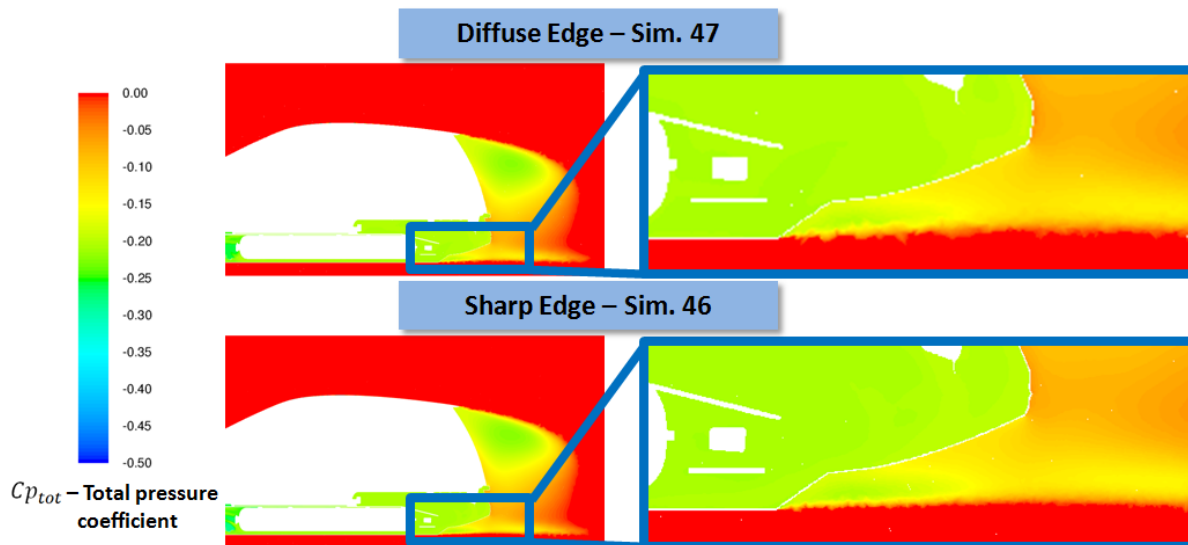


Figure 7.28 Total pressure coefficient in Y0 plane – CULT simulations 47 and 46

Conclusion

Blunt edges increase minimum number of iterations required for simulation to converge. On the end there is no big influence on the final results. Sometimes, when fine grids are used (Chapter 7.1.1), blunt edge can give false signal that simulation converged – if the only first 1500 iterations are observed on the diagram in the Figure 7.2.

Most of the simulations in this thesis were made with the observed edge left blunt. It can be seen that each aerodynamic coefficient diagram of these simulations have small false convergence at the beginning of the simulation. On the coarse grids this false convergence disappear fast (a lot before standard 1500 iterations). On the fine grids, this false convergence can lead to totally wrong conclusion if only first 1500 iterations are used for post-processing. Therefore, a lot of energy was spent during creation of this thesis before it was concluded that 1500 iterations are not enough in a case of finer grid. Advice, learned after this, is to always prolong basic simulations and simulations with finer grids to be sure that simulation converged correctly.

Other very important conclusion is that, if this edge was recognized as an important edge when first simulation was created, it would be created and kept sharp in all simulations. A lot of time would be saved. Therefore, invest time to create sharp edges is profitable. Also, it is very good to divide edges on important and not important in order to avoid losing time not important edges during simulation Pre-Processing.

Also, it can be concluded that rear diffuser on the CULT is probably on the edge of working ability. Reason for that is inconvenient geometry step on the underbody. That claim will be proved in Chapter 7.7.

7.5 CFD and Wind Tunnel (1:4) Comparison

This section compares CFD results with the wind tunnel measurement results. Default geometry settings with open CAS are used. In the wind tunnel, two physical values are measured:

- aerodynamic force – used for aerodynamic coefficients calculation
- pressure – measured on the model’s surface in Y0 cut plane

These values can be compared with the CFD simulation. Figure 7.29 and Table 7.8 show CFD simulation results and Table 7.9 compare these results with the wind tunnel measurement.

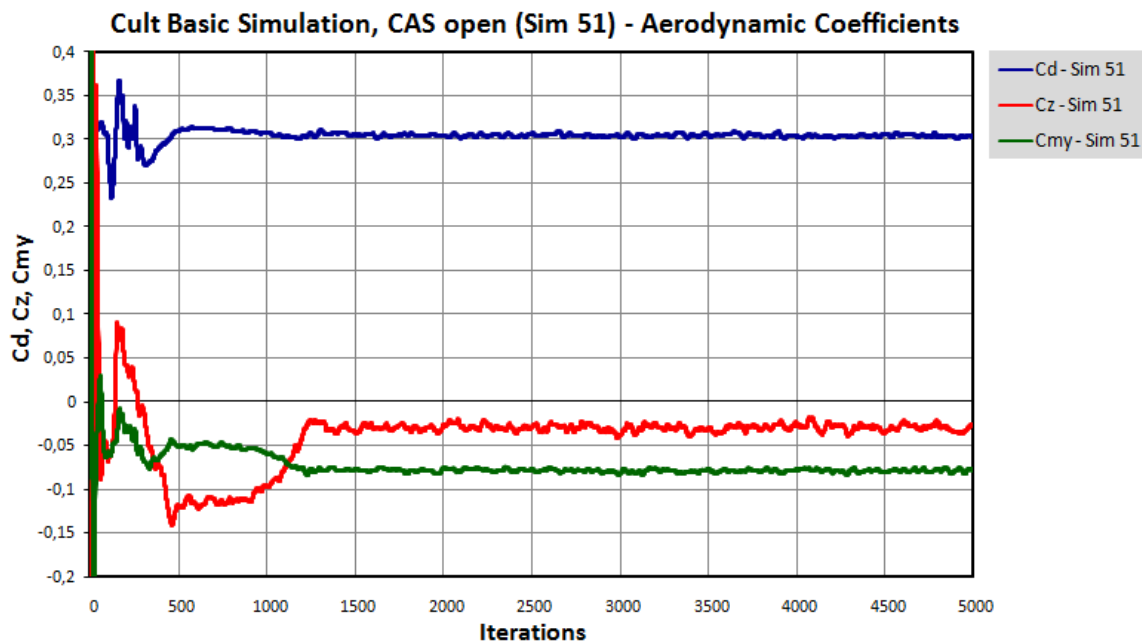


Figure 7.29 Aerodynamic coefficients diagram – CULT basic simulation, CAS open

Table 7.8 Aerodynamic coefficients – sim. 51 (avg. values for last 200 iter.)

Cult Basic – Sim. 51		
Cd (WCP)		0,303
Cz		-0,031
Cmy		-0,079
	Czf	-0,095
	Czr	0,064
	Cd	0,332

Table 7.9 Aerodynamic coefficients – CFD basic and WT basic (CAS open)

	Cult Basic – Sim. 51	Wind Tunnel Basic	Δ
Cd	0,332	0,353	0,021
Czf	-0,095	-0,057	0,038
Czr	0,064	-0,023	0,087

Differences between compared results are significant. CFD has better (lower) aerodynamic drag for 21 counts. There is also big difference in lift coefficients. All that indicates that air flow in the CFD simulation is not same as in the wind tunnel (or vice versa).

At this point importance of the pressure measurements in the wind tunnel come to the fore. Numbers in the Table 7.9 can only tell that there are differences, but pressure measurements can tell exactly where the differences are (where is the flow in the wind tunnel different from

the flow in the CFD). In the Figure 7.30, Figure 7.31 and Figure 7.32 pressure coefficients on the vehicle surface in the Y0 cut plane are compared. Black marks show pressure coefficient values measured from the probes during wind tunnel test.

Values on the upper body (Figure 7.30) are satisfactorily close. Hence, it can be sad that flow on the upper body matches.

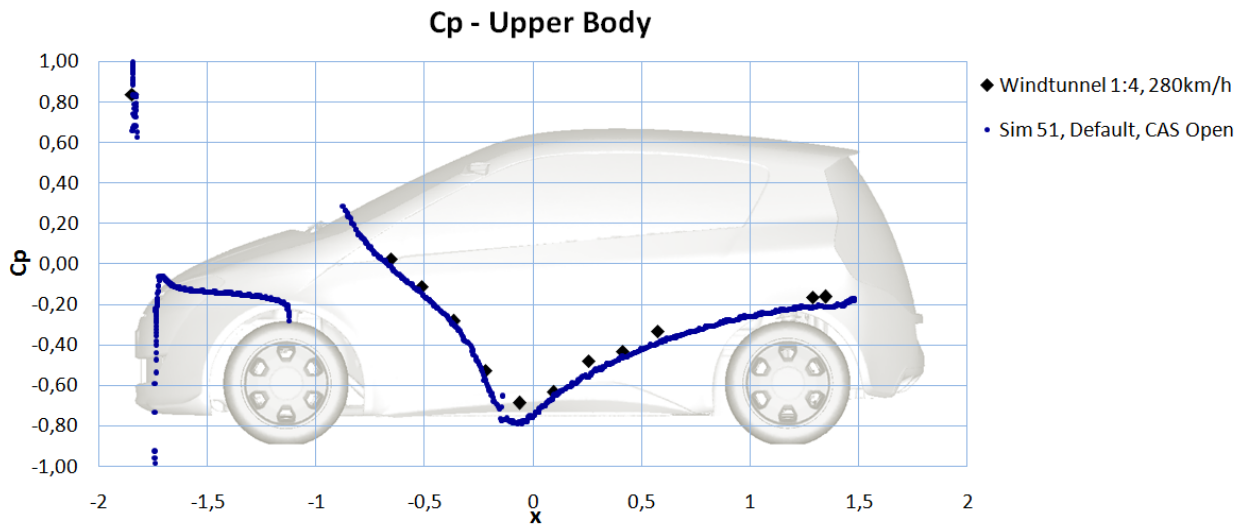


Figure 7.30 Pressure coeff. distribution on the upper body – WT and CFD sim. 51

Values on the under body are matching satisfactorily until rear end, where the values significantly diverge.

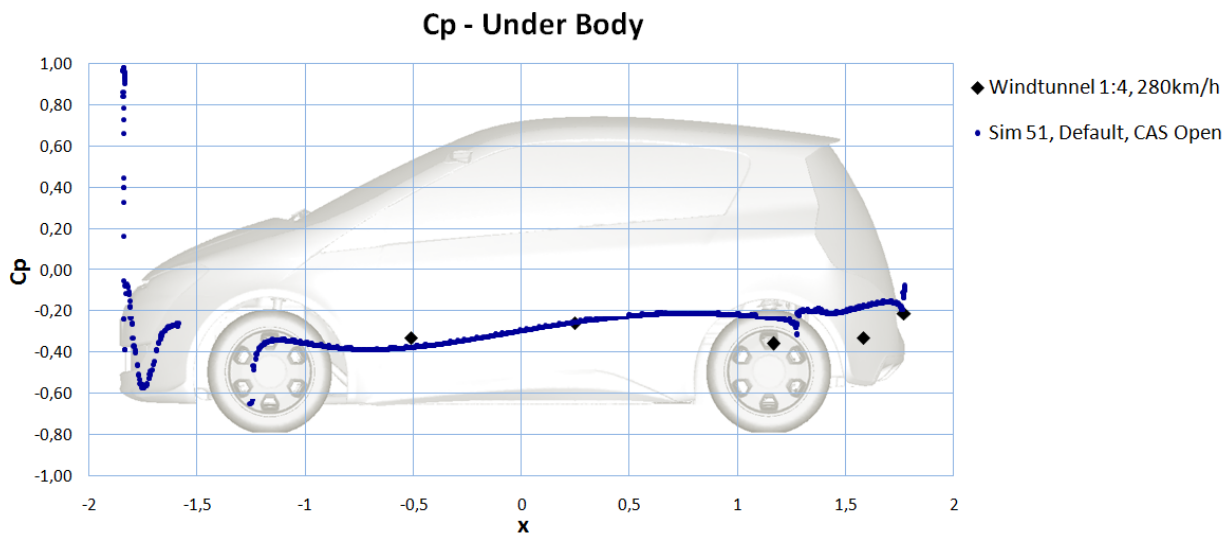


Figure 7.31 Pressure coeff. distribution on the under body – WT and CFD sim. 51

Further, if the rear base is observed (Figure 7.32), flow is totally different – it does not match at all. Now, differences showed in the Table 7.9 have sense.

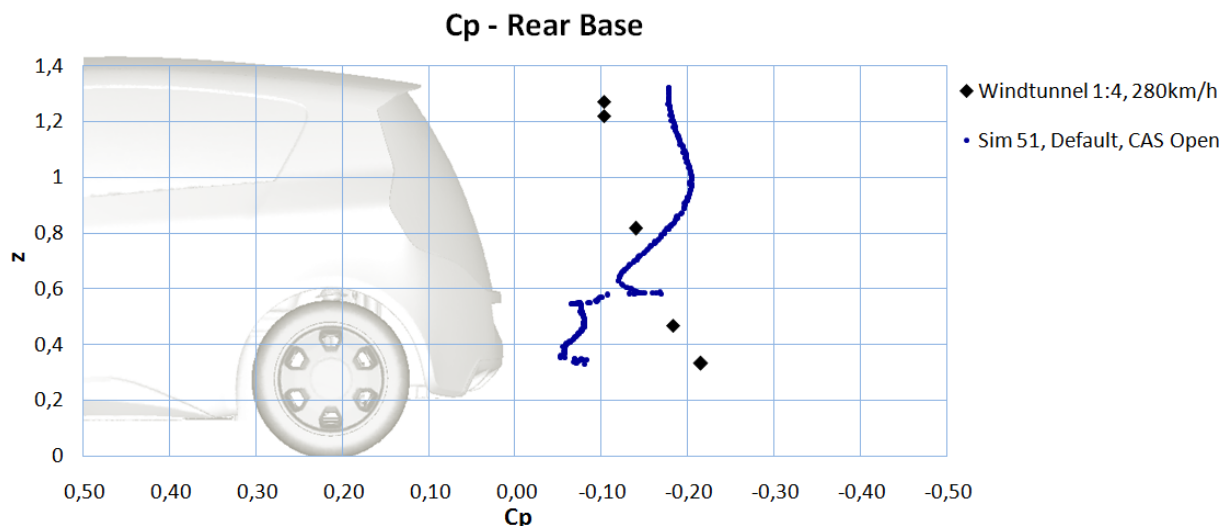


Figure 7.32 Pressure coeff. distribution on the rear base – WT and CFD sim. 51

If Figure 7.32 is observed more, it can be seen that there is higher pressure in the wind tunnel on the top of the rear base and opposed on the bottom of the rear base.

Theoretically, it can happen (for example) that differences in aerodynamic drag between CFD and the wind tunnel are imperceptible. That can happen if the pressure differences from the upper part of the rear base cancel differences on the lower part. On the end, average pressure can be very similar and aerodynamic drag values can be very close. But, despite that fact, air flow can be totally different. Therefore, it is always necessary to compare pressure values from wind tunnel measurements with CFD results, at least in Y_0 plane as it is done here.

Next step is to figure out “why is the flow totally different?” That was a very difficult task, but on the end answer was simple. Next two chapters deal with that task.

Because in this cases two geometries are compare, one geometry is in scale 1:1 (CFD) and other in scale 1:4 (WT), first assumption is that Reynolds number influence can be reason for such differences in flow behavior. Hence, Reynolds number influence will be investigated in next chapter.

Other reasonable assumption is that differences between the wheels are responsible for different flow behavior. Wheels used in the wind tunnel measurement are different compared with the wheels which are used is CFD simulation. Therefore, after Reynolds number influence investigation, influence of different wheels geometry will be carried out.

These next two chapters will give conclusion to this chapter.

7.6 Reynolds Number Influence

Flow behavior is closely related to the Reynolds number. Reynolds number depends (among other variables) on the air speed. In this chapter, CFD simulations and wind tunnel measurements with different air inlet speeds (Reynolds numbers) will be investigated. Goal is to see how much type of the flow investigated here depends from the air inlet speed (or Reynolds number). Basic geometry in this investigation is Mock up geometry.

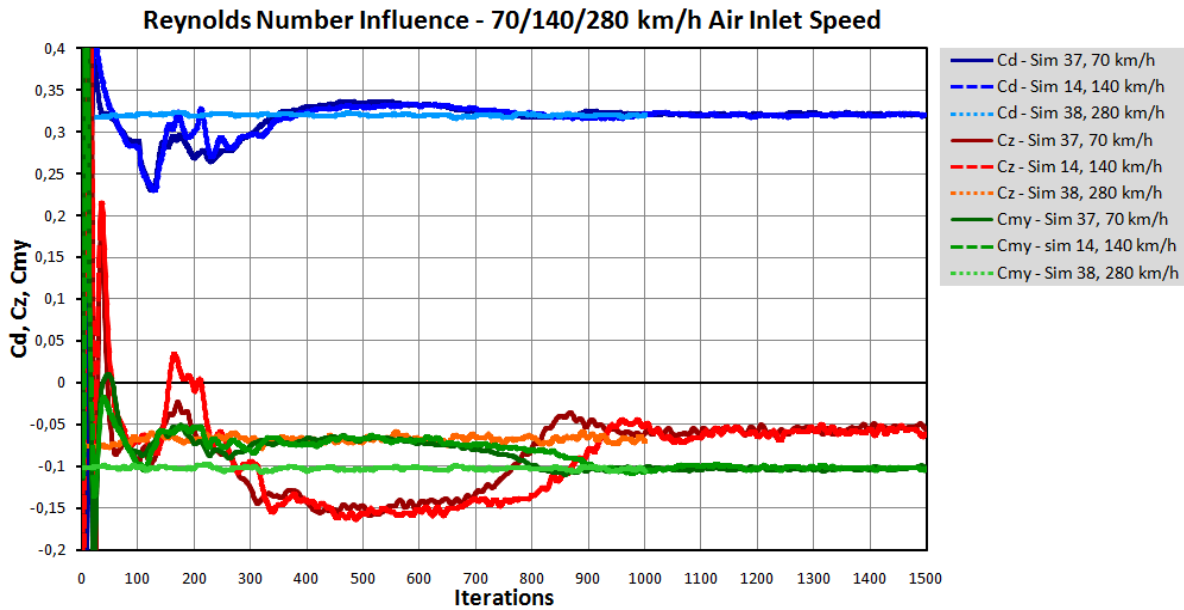


Figure 7.33 Aerodynamic coefficients diagram – Different air inlet speeds, MOCK UP

Table 7.10 Aerodynamic coefficients – CULT CFD simulations (MOCK UP)

		70 km/h	140 km/h	280 km/h
Cd	Cd (WCP)	0,321	0,320	0,320
Cz	Cz	-0,054	-0,058	-0,067
Cmy	Cmy	-0,103	-0,102	-0,103
	Czf	-0,130	-0,131	-0,137
	Czr	0,076	0,073	0,070
	Cd	0,321	0,320	0,320

Table 7.11 Aerodynamic coefficients – ASM WT measurement (MOCK UP)

	140 km/h	200 km/h	270 km/h
Cd	0,346	0,343	0,339
Czf	-0,090	-0,091	-0,094
Czr	-0,011	-0,010	-0,008

Figure 7.33 shows CFD simulation results from three different air inlet speeds. In the Table 7.10 average values from these three simulations are showed. It can be concluded that, in CFD simulation, different Reynolds number has no significant influence on the final results (at the observed air inlet speed values).

In the Table 7.11, wind tunnel results, with the same geometry settings as CFD (mock up), show Reynolds number influence. Difference in drag between 140km/h and 270km/h air inlet speeds is 7 counts.

Figure 7.34, Figure 7.35 and Figure 7.36 shows pressure coefficient values on the car’s surface in the Y0 cut plane. Both, CFD simulations and wind tunnel measurements results are showed on each figure. Pressure coefficient values for different air inlet speeds are compared. There is no significant Reynolds number influence on the pressure. Hence, Reynolds number does not changes air flow appearance.

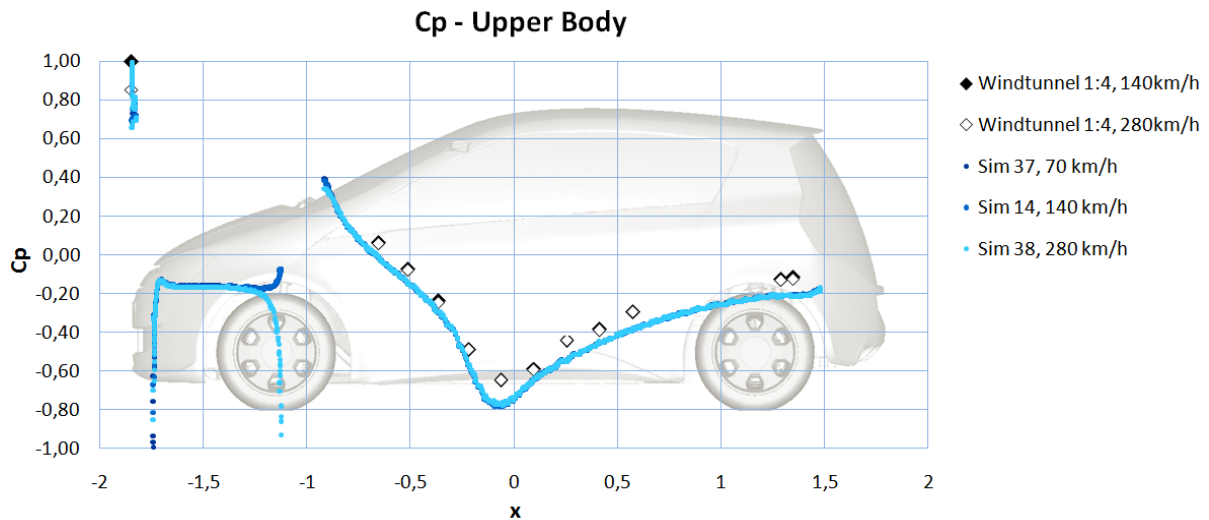


Figure 7.34 Pressure coeff. distribution on the upper body – WT and CFD (different air speeds)

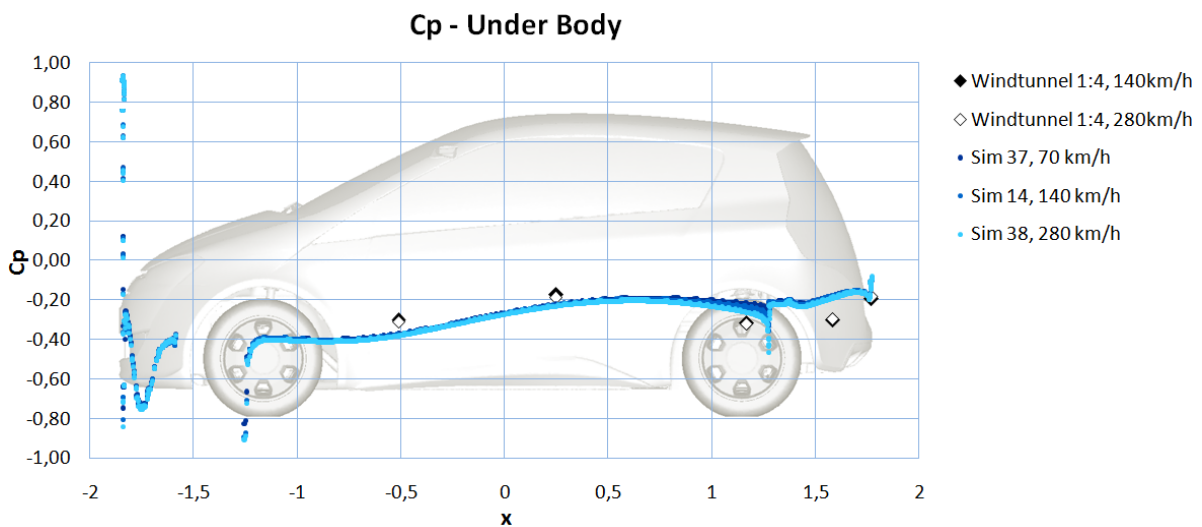


Figure 7.35 Pressure coeff. distribution on the under body – WT and CFD (different air speeds)

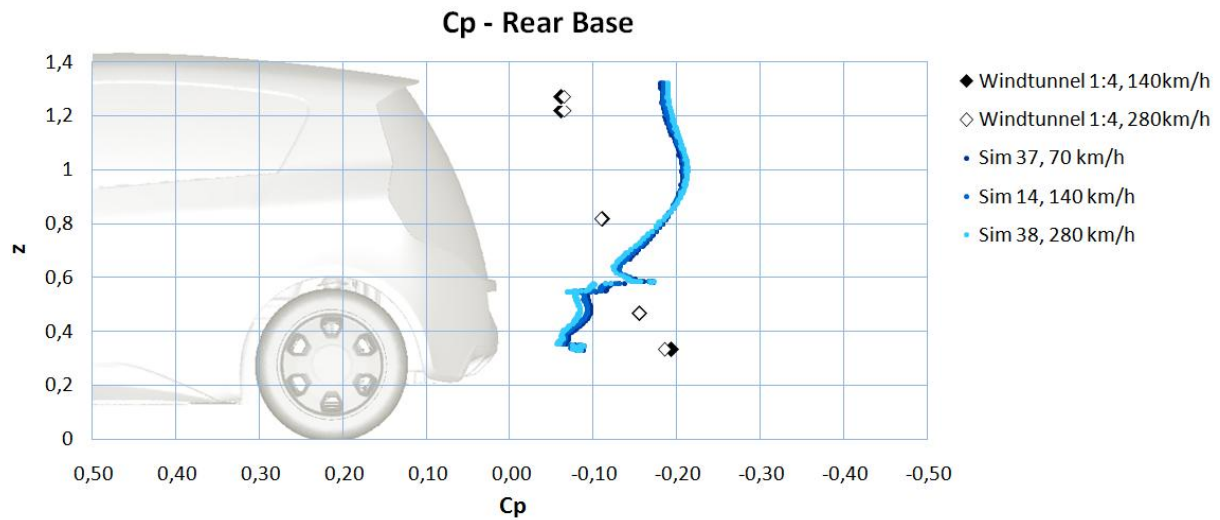


Figure 7.36 Pressure coeff. distribution on the rear base – WT and CFD (different air speeds)

However, there are still big differences between CFD simulations and wind tunnel measurements.

Conclusion

In CFD, Reynolds number influence is not significant, neither on the aerodynamic coefficient values, neither on the flow appearance. In the wind tunnel measurement, Reynolds number influence is measurable on the aerodynamic coefficients, but differences are in small scale. Differences in the flow appearance are negligible.

After this investigation it is clear that Reynolds number influence is not cause for differences between CFD and wind tunnel measurement air flow.

7.7 Wheel Geometry Influence

Wheels have very important role in automotive aerodynamics. They are vehicle’s only connection to the ground. They are rotating and, therefore, they are rotating air close to them. Rims (especially designed alloy rims) can act like a fan – they can suck air from side to the under body, or vice versa. Accordingly, size and shape of the wheels are not negligible. On the contrary, just small differences in the wheels size and shape can totally change whole air flow.

In the CULT project two wheel types were used. One type is called CULT type, and other type ASM type. Figure 7.37 shows CULT type wheels. They are default wheels for project CULT and they are used in all CFD simulations in the Table 7.1.

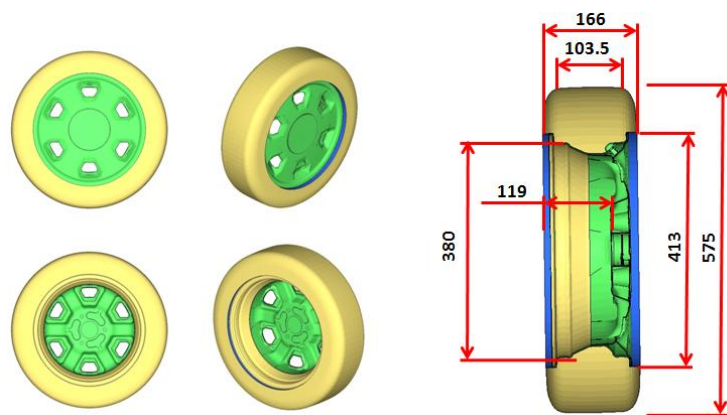


Figure 7.37 CULT type wheels

Figure 7.38 shows ASM type wheels. They are used during scaled model wind tunnel tests.

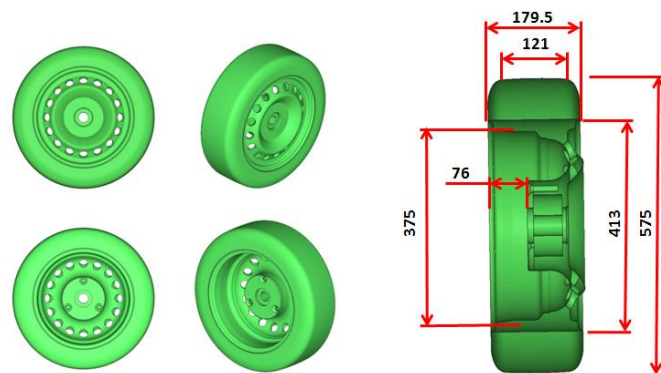


Figure 7.38 ASM type wheels

If these two types of wheels are compared, it is clear that both, design and size are different. ASM wheels are wider and their rim’s design is “steel” type. On the contrary, CULT wheels are narrower and their rim’s design is “alloy” type.

Purpose of wheels influence investigation here is to find explanation for differences between CFD and wind tunnel results (Chapter 7.5). Accordingly, beside simulations in Table 7.1, two additional simulations were made:

1. ASM geometry - ASM wheels
2. ASM geometry - CULT wheels

Geometry used in the wind tunnel scaled model tests is now basic geometry. It is called ASM geometry (Aero Scaled Model) - Figure 7.39. One simulation was made with ASM type wheels, same as in the wind tunnel, and other simulation was made with CULT type wheels (ASM geometry with CULT type wheels).

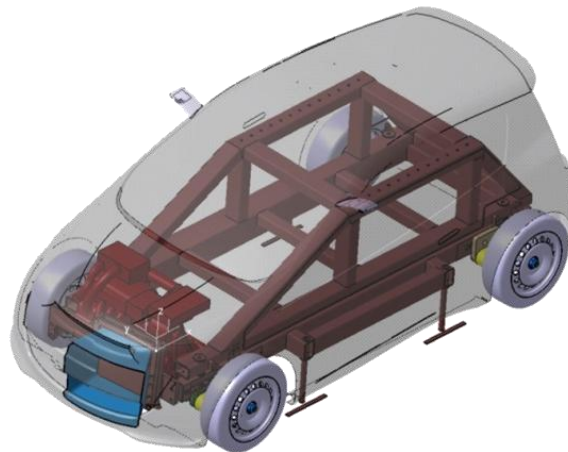


Figure 7.39 CULT Aero Scaled Model (ASM) geometry

In this chapter, goal is not to investigate phenomena that occur when model is scaled. That is subject for separate research. Here, focus was only on the wheels influence. Therefore, scale 1:1 was used – ASM geometry was in scale same as other CFD simulations (real size). To get the simulation closer to the wind tunnel test, moving ground in the simulation was simulated as five belt system – same as in the wind tunnel tests.

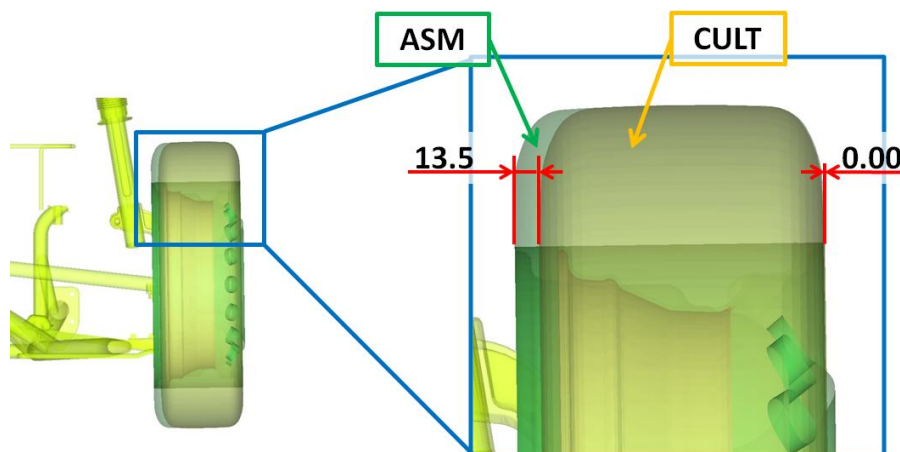


Figure 7.40 ASM vs. CULT wheels – position comparison

Figure 7.41 and Table 7.12 show results from these new simulations. Results fairly deviate one from other. Accordingly, in this case, wheels have very important role in the air flow.

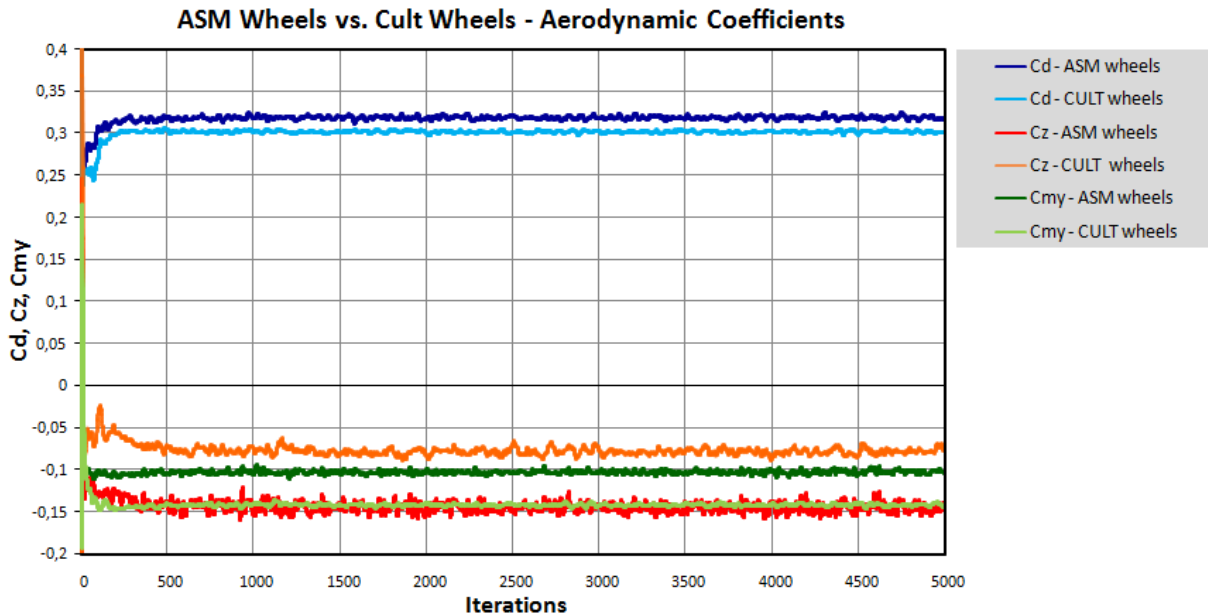


Figure 7.41 Aerodynamic coefficients diagram – ASM wheels vs. CULT wheels

Table 7.12 Aerodynamic coefficients – ASM wheels vs. CULT wheels (avg. val. for last 200 iter.)

ASM Wheels			CULT Wheels		
Cd (WCP)		0,319	Cd (WCP)		0,302
Cz		-0,145	Cz		-0,077
Cmy		-0,102	Cmy		-0,142
	Czf	-0,175		Czf	-0,181
	Czr	0,030		Czr	0,104
	Cd	0,319		Cd	0,302

Difference in aerodynamic drag is around 17 counts. Lift on the rear wheel is around 70 counts higher in the simulation with CULT wheels. That suggests that air flow have different behavior in that area.

To examine results more closely, set of diagrams and flow visualizations is presented bellow.

Figure 7.42, Figure 7.43 and Figure 7.44 show pressure coefficient values on the car’s surface in the Y0 cut plane. Except these two CFD simulations, also results from the wind tunnel measurements are in the diagram.

In the upper body region all results matches (Figure 7.42).

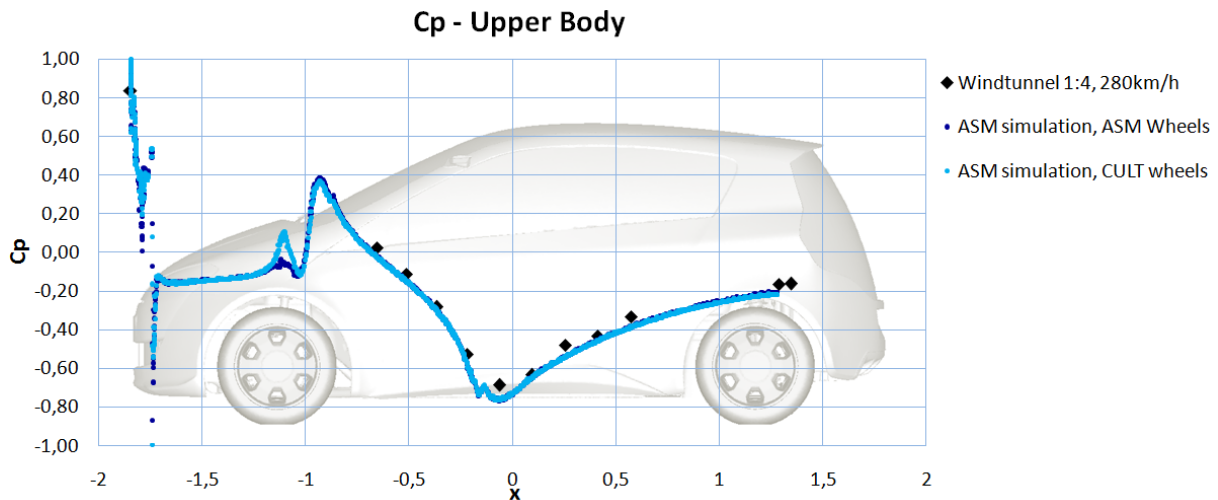


Figure 7.42 Pressure coeff. distribution on the upper body – ASM vs. CULT wheels

In the under body region (Figure 7.43) simulation results are different on the rear end. Simulation with ASM wheels has more under pressure than simulation with CULT wheels. As it was expected, simulation with ASM wheels corresponds with wind tunnel measurements.

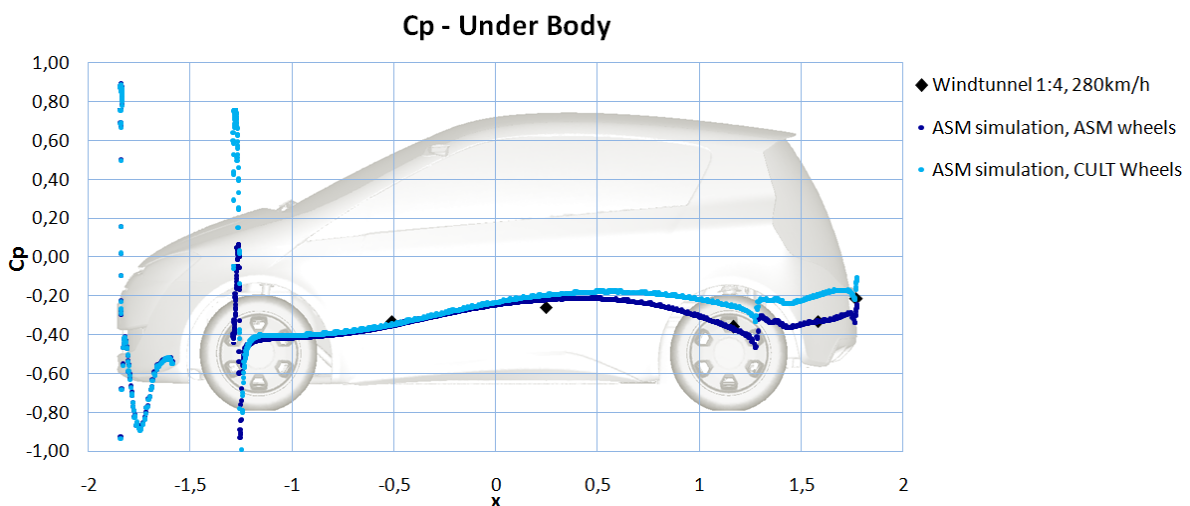


Figure 7.43 Pressure coeff. distribution on the under body – ASM vs. CULT wheels

On the rear base (Figure 7.44), situation is similar. Simulations mismatches totally. Simulation with ASM wheels correspond to the wind tunnel measurements and simulation with CULT wheels have different shape. If this diagram is compared with the diagram in the Figure 7.32 (in the Chapter 7.5.) it is obvious that ASM simulation with CULT wheels is very similar to default CULT simulation.

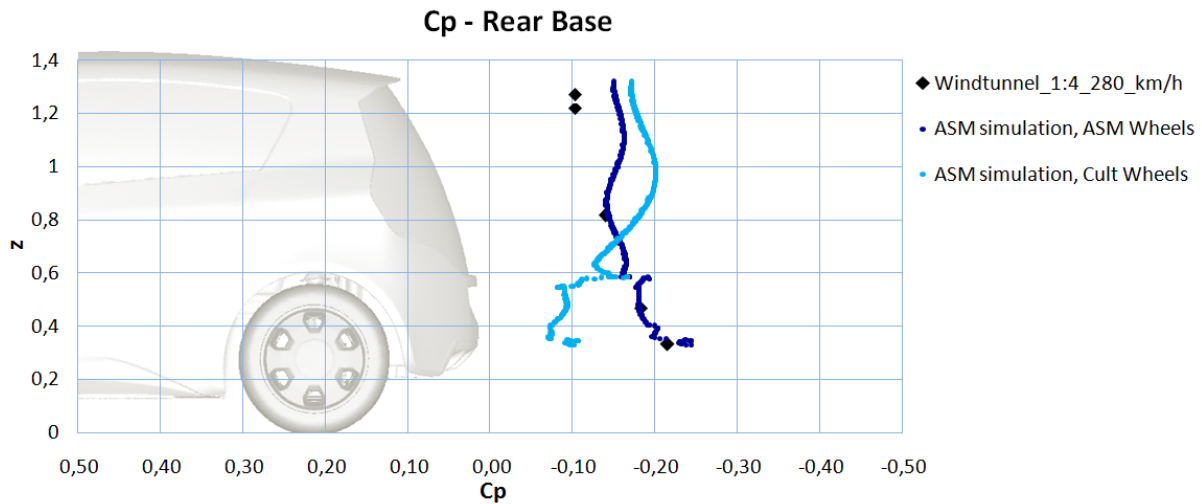


Figure 7.44 Pressure coeff. distribution on the rear base – ASM vs. CULT wheels

Now some conclusions can be made:

- Figure 7.44 proves that simulation with ASM geometry and ASM wheels is close to the wind tunnel test (CFD validation)
- Figure 7.44 and Figure 7.32 together proves that ASM simulation with CULT wheels is close to the CULT default simulation (ASM geometry validation)

It is very interesting to observe flow visualizations in Y0 plane to get better feeling how small differences on the wheels can change whole air flow. Figure 7.45 shows Velocity-X coefficient value. With ASM Wheels rear diffuser is working a bit, while with CULT wheels rear diffuser is not working at all. When rear diffuser is working it brings lower pressure on the rear, increasing aerodynamic drag. That is the reason of lower pressure on the rear end when ASM wheels are used.

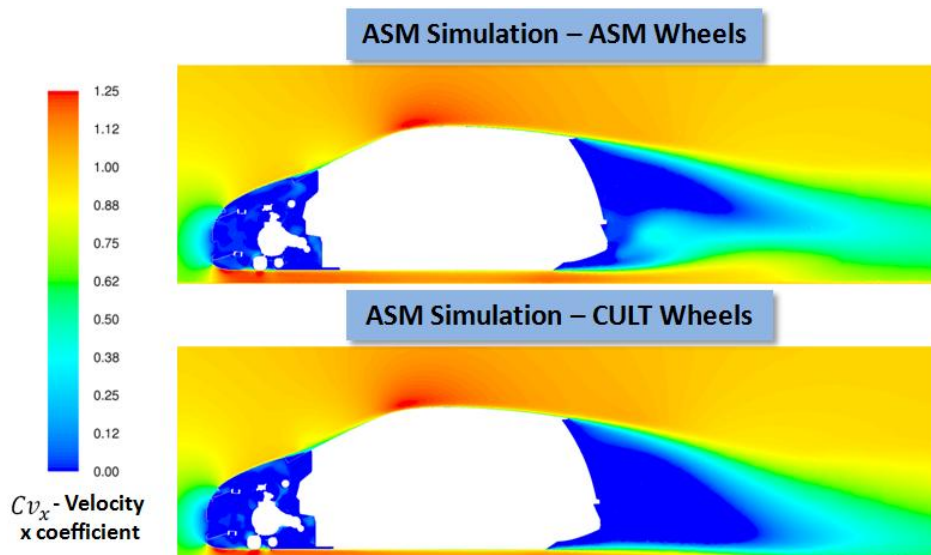


Figure 7.45 Velocity-X coefficient in Y0 plane – ASM wheels vs. CULT wheels

Figure 7.46 shows total pressure coefficient comparison. Figure also shows how rear diffuser does not work with CULT wheels and works with ASM wheels.

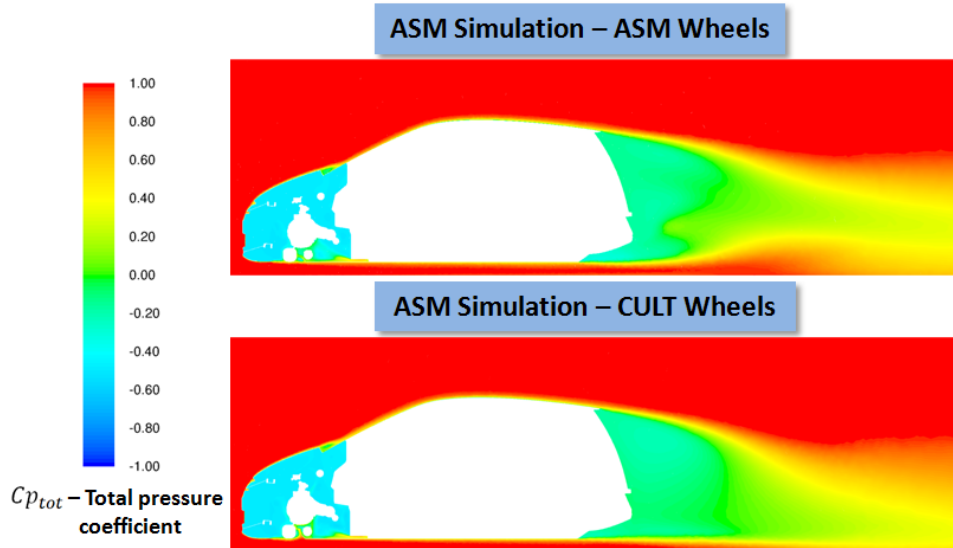


Figure 7.46 Total pressure coefficient in Y0 plane – ASM wheels vs. CULT wheels

Figure 7.47 shows Vorticity magnitude. This figure is very interesting, because operation of the diffuser is showed very good and clear.

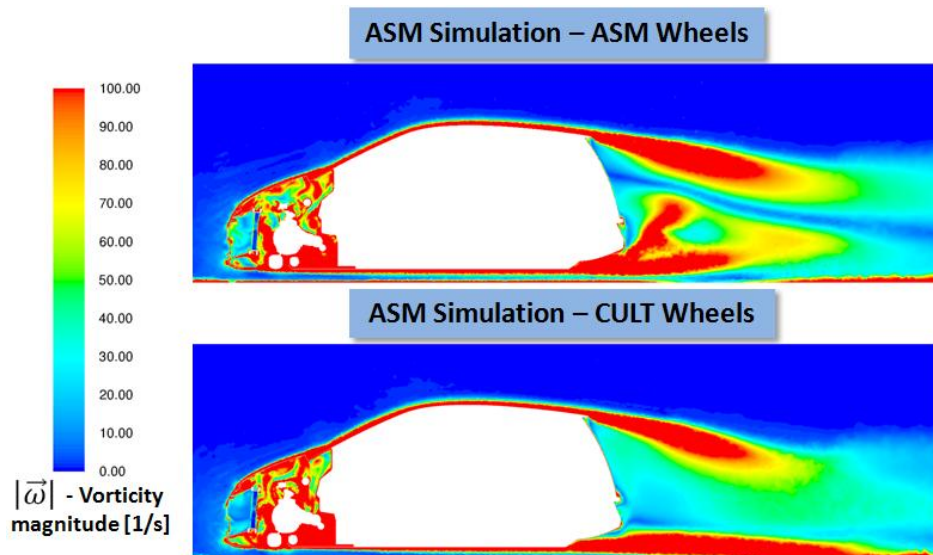


Figure 7.47 Vorticity magnitude in Y0 plane – ASM wheels vs. CULT wheels

Figure 7.48 shows wall shear stress 3D contours on the vehicle surface. Here it can be seen which parts of diffuser are working. Where flow is attached to the surface there is a boundary layer and friction. Friction causes wall shear stress. Consequently, if there is a presence of the wall shear stress on the diffuser, diffuser is working. In this case, on the simulation with ASM wheels, only two of five diffuser channels are working.

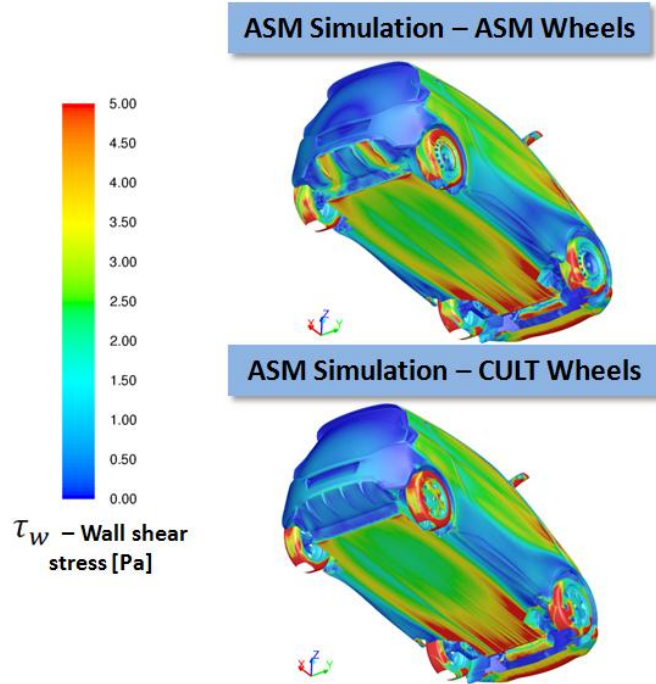


Figure 7.48 Wall shear stress 3D visualization – ASM wheels vs. CULT wheels

On the end, Figure 7.49 shows pressure distribution on the rear base of the vehicle. If region around license plate position is observed, it can be seen that ASM wheels cause lower pressure in that region. That is caused by the working diffuser, which transfers high velocity flow from the under body to the rear base.

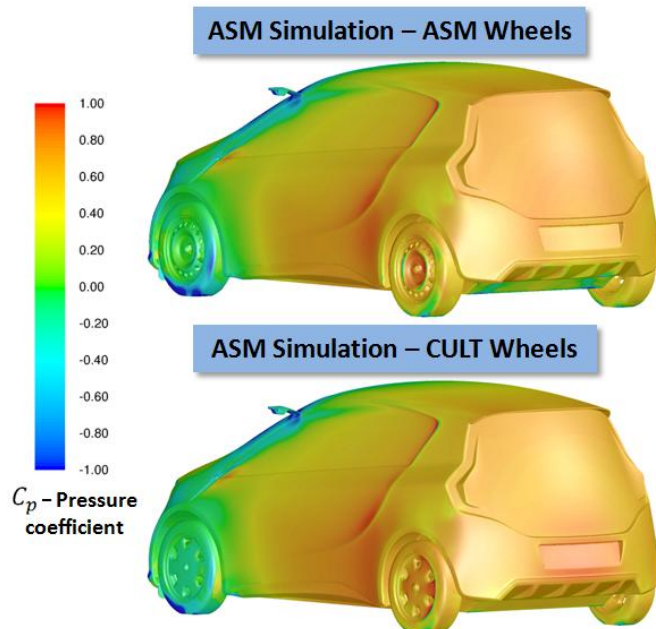


Figure 7.49 Pressure coefficient 3D visualization – ASM wheels vs. CULT wheels

Conclusion

In this case influence of the wheels is very high. After this investigation it can be concluded that wheels are the answer for differences between CFD simulations and wind tunnel tests, investigated in Chapter 7.5. These small differences in wheels size and shape caused that big differences in the air flow, especially on the under body and on the rear base of the vehicle. If situation is observed deeper, probably wheels are not the only reason for air flow differences. More precise explanation would be that reason for different air flow behavior is the combination of wheels differences and specific and sensitive geometry in the region where under body connects to the rear diffuser (sensitive separation edge was investigated in Chapter 7.4).

Also, based on investigation in this chapter, very interesting conclusion for rear diffuser can be made. With ASM wheels rear diffuser is partially working and causes higher drag and lower pressure on the rear end of the under body, compared with the diffuser in the case with the CULT wheels, which is not working at all. Lower pressure on the rear end of the under body is very good for racing purposes and sacrificing drag is reasonable in that case. But, CULT is a city car with the goal of minimum fuel consumption. Therefore, this diffuser has no sense from aerodynamic point of view – in this case, it is a drag increasing device. Actually, the fact that diffuser on the basic CULT geometry (with CULT basic wheels) is not working is very good for low aerodynamic drag.

7.8 Cooling Inlets Influence

Cooling inlets definition and their purpose is explained in Chapter 3.1. In this chapter their influence on the overall aerodynamic drag will be investigated. Chapter is divided into two subchapters. First subchapter deals with CAS mechanism and second subchapter deals with other two air inlets (CAC air inlet and upper cooling inlet)

7.8.1 Cooling Air Shutter (CAS) Mechanism Influence

Purpose of Cooling Air Shutter (CAS) mechanism is to reduce aerodynamic drag when there is no need for engine cooling – therefore, CAS mechanism is aerodynamic reduction device. In order to investigate influence of the CAS mechanism on the CULT, two simulations are compared in this chapter. One simulation with CAS open and another with CAS closed.

CAS open simulation simulates CAS partially open – only left side open. Reason for that is position of radiator, which is on the left side (Figure 7.50). If whole CAS is open it would not increase air flow through radiator compared with only partially open. With whole CAS open a lot of unnecessary air would go through the engine compartment, increasing aerodynamic drag. Therefore, for best aerodynamic properties only half of the CAS air inlet is opened.



Figure 7.50 CAS closed and CAS open definition

Except CFD simulation, also wind tunnel results are included here. In the wind tunnel measurement also only left side of the CAS was investigated (right side was closed during all of the measurements).

Results presented in the Figure 7.51 and Table 7.13 show that CAS influence is around 15 counts. Except aerodynamic drag, CAS has no other influences – influence on the vehicle lift is negligible.

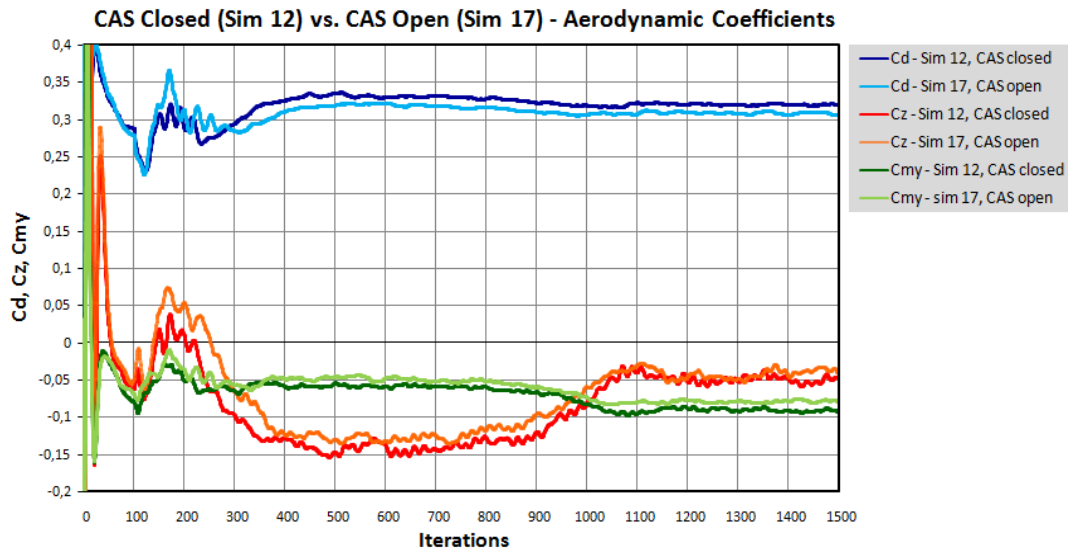


Figure 7.51 Aerodynamic coefficients diagram – CAS closed vs. CAS open

Table 7.13 Aerodynamic coeff. – simulations 12 and 17 (avg. values for last 200 iter.)

CAS Closed – Sim 12			CAS Open – Sim 17		
	Cd (WCP)	0,320		Cd (WCP)	0,308
	Cz	-0,050		Cz	-0,042
	Cmy	-0,091		Cmy	-0,079
	Czf	-0,116		Czf	-0,100
	Czr	0,066		Czr	0,058
	Cd	0,324		Cd	0,340

In the Table 7.14 results from wind tunnel measurements are showed. Last column, containing delta values (differences), is included. For easier comparison there is also Table 7.15 which contains CFD results presented on the same way as the wind tunnel results in the Table 7.14. CAS influence on the aerodynamic drag is very similar between wind tunnel and CFD (around 15 counts).

Table 7.14 CAS influence – wind tunnel measurement

	WT CAS Open	WT CAS Closed	Δ
Cd	0,353	0,338	0,015
Czf	-0,057	-0,093	0,036
Czr	-0,023	-0,009	0,014

Table 7.15 CAS influence – CFD simulation

	CFD CAS Open	CFD CAS Closed	Δ
Cd	0,340	0,324	0,016
Czf	-0,100	-0,116	0,016
Czr	0,058	0,066	0,08

To confirm that CAS has no big influence on the overall air flow, three figures with pressure coefficient distribution on the car’s surface in Y0 cut plane are showed bellow.

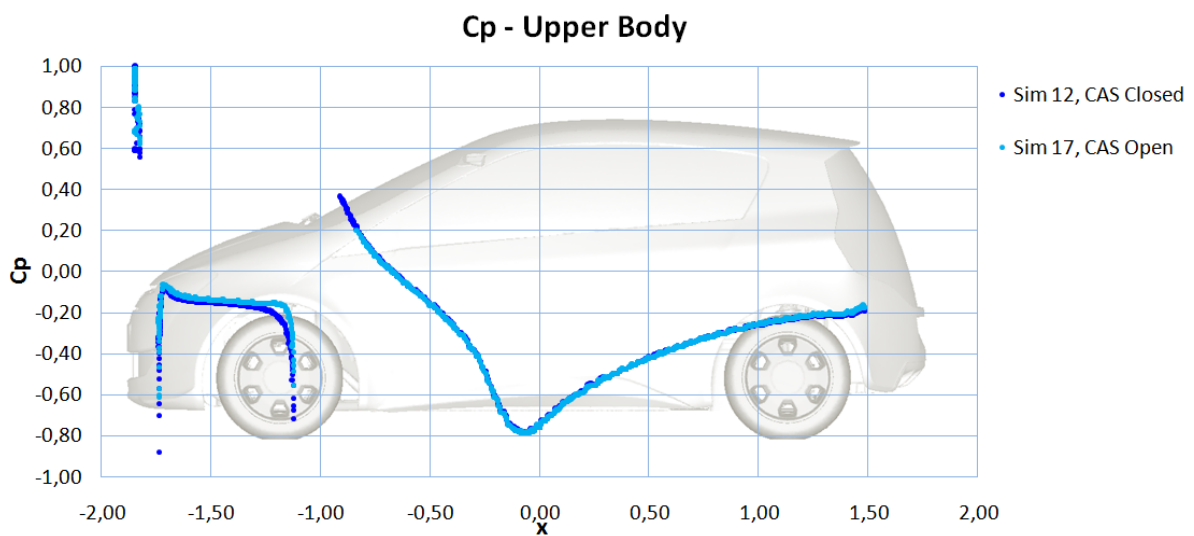


Figure 7.52 Pressure coeff. distribution on the upper body – CAS closed vs. CAS open

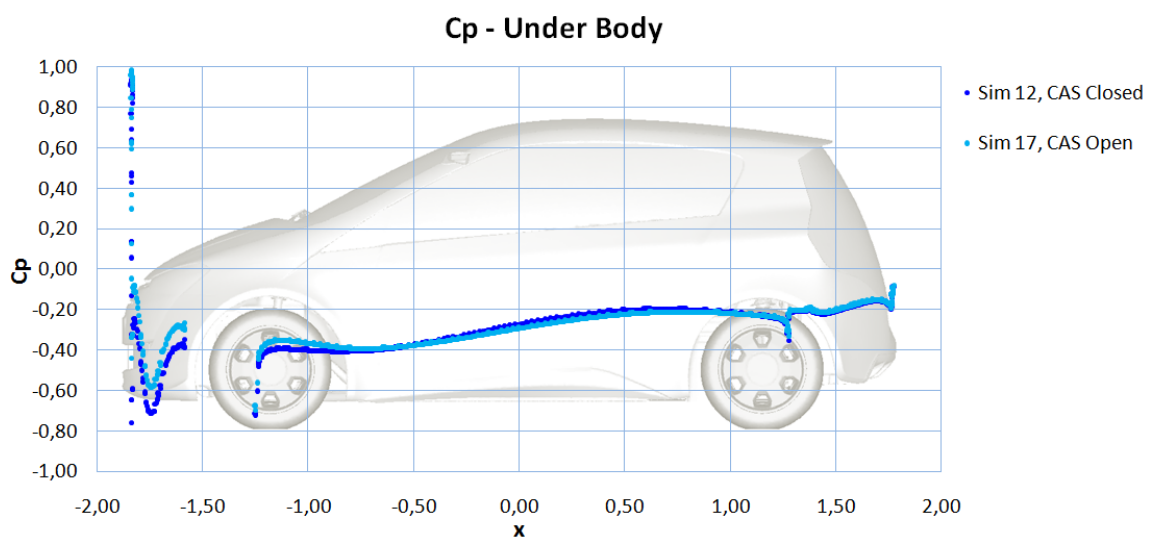


Figure 7.53 Pressure coeff. distribution on the under body – CAS closed vs. CAS open

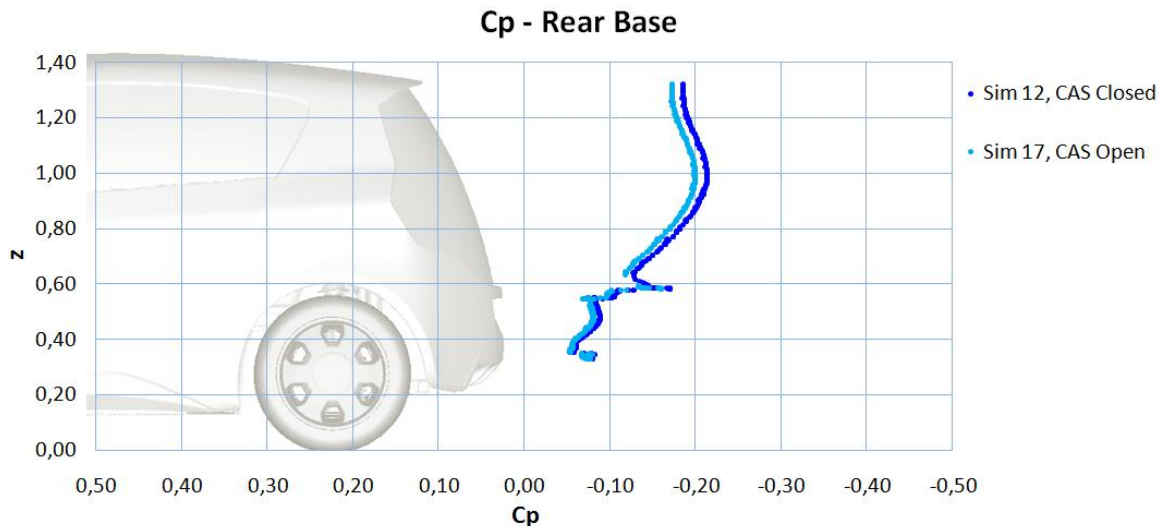


Figure 7.54 Pressure coeff. distribution on the rear base – CAS closed vs. CAS open

The only differences are in the on the rear base (Figure 7.54) Simulation with CAS closed has lower pressure and therefore higher aerodynamic drag on the rear end. If the drag produced by the cooling package is not taken into account, bigger drag is on the simulation with CAS closed (Table 7.13 – C_d (WCP) value). Because 12 counts difference in C_d (WCP) is smaller than 28 drag counts of the cooling package, total aerodynamic drag is higher on the simulation with CAS open – 16 counts higher drag (cooling package drag for the CAS closed simulation is zero).

Conclusion

When CAS mechanism is closed, CULT has 16 counts better drag value. Measurements in the wind tunnel gave similar results. Efficiency of CAS mechanism in the wind tunnel is 15 counts (Figure 6.7).

These results show that, when designing a low drag vehicle, CAS mechanism can serve as a very good aerodynamic drag reduction device.

7.8.2 Influence of Other Cooling Air Inlets

Except CAS, there are two more air inlets (Chapter 3.1) – CAC air inlet and Cooling inlet upper (Figure 7.55). Influence on the aerodynamic drag from these two inlets will be investigated below. Two simulations are compared – one simulation has opened investigated air inlets and another simulation closed. CAS mechanism is closed in both simulations.

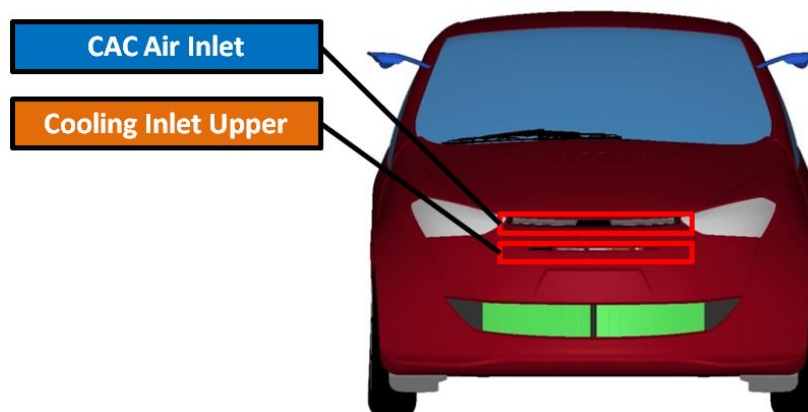


Figure 7.55 Position of the CAC air inlet and Cooling inlet upper

Simulation with all inlets closed is so-called Full Mock-up simulation. Results are showed in the Figure 7.56 and Table 7.16.

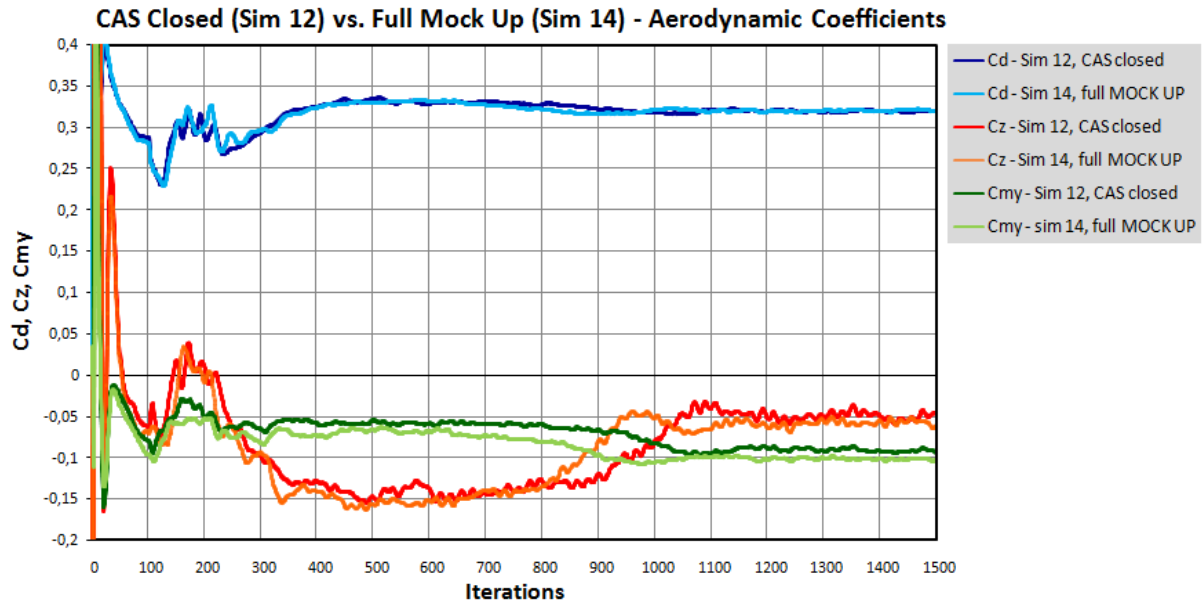


Figure 7.56 Aerodynamic coefficients diagram – CAS closed vs. Full MOCK UP

Table 7.16 Aerodynamic coeff. – simulations 12 and 14 (avg. values for last 200 iter.)

CAS Closed – Sim 12			Full Mock Up – Sim 14		
	Cd (WCP)	0,320		Cd (WCP)	0,320
	Cz	-0,050		Cz	-0,058
	Cmy	-0,091		Cmy	-0,102
	Czf	-0,116		Czf	-0,131
	Czr	0,066		Czr	0,073
	Cd	0,324		Cd	0,320

Conclusion

Influence of these two air inlets is around 4 drag counts. Therefore, investigated air inlets have very low influence on the air flow around car.

7.9 Front-Wheel Spoilers Optimization

CULT posses front-wheel spoilers, introduced in Chapter 3.3. It is known that front-wheel spoilers are good for aerodynamics because of two reasons:

- Reducing aerodynamic drag (drag reduction device) – they are redirecting air, which commonly encounters with wheels, to bypass them.
- Aerodynamic lift control – on the front and on the rear axle.

In this chapter, three different positions of wheel spoilers will be investigated (Figure 7.57).

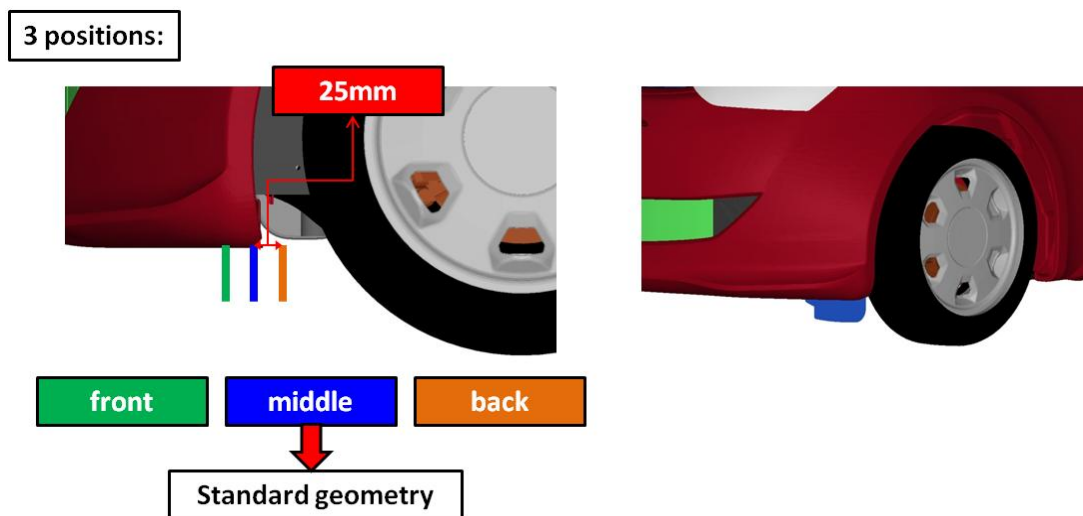


Figure 7.57 Front-wheel spoilers – three investigated positions

Middle position is default position, used in all simulations (except simulations where wheel spoilers have been investigated). From that middle position, two additional positions were derivate by moving spoilers 25mm to the front and to the back.

Results from all three simulations (default, front and back position) are shown in the Figure 7.58 and Table 7.17.

As it was expected, simulations showed that different positions have influence on the both, aerodynamic drag and lift. Here, focus will be on the aerodynamic drag. If front and back positions are compared, difference is 7 drag counts. Accordingly, if the spoilers position change for only 50mm, drag value changes for 7 drag counts.

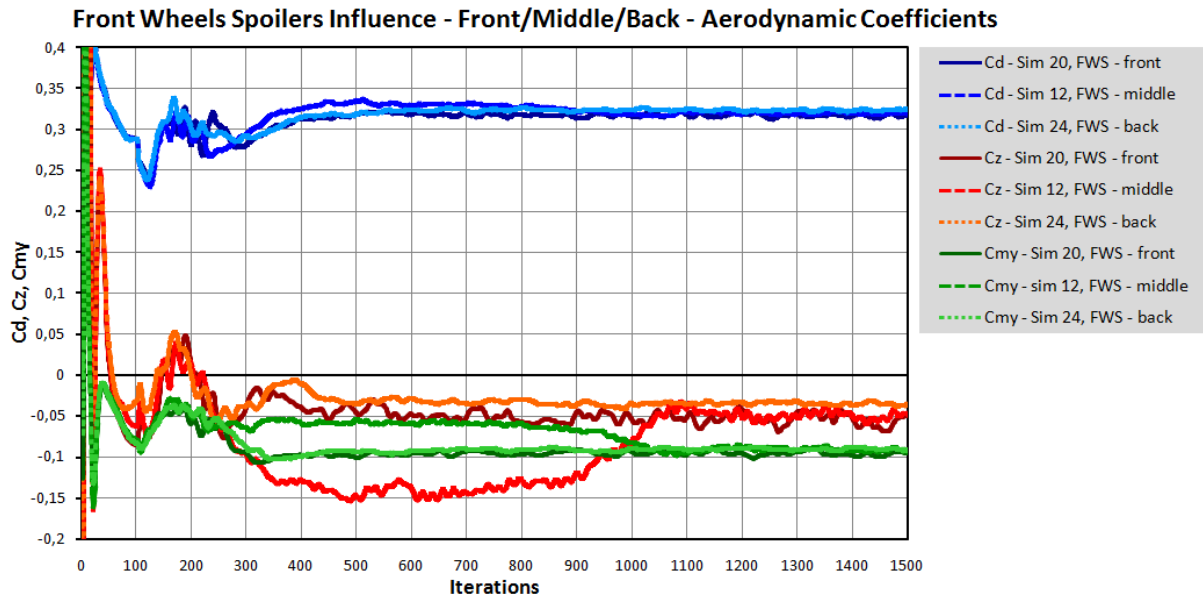


Figure 7.58 Aerodynamic coefficients diagram – front-wheel spoilers position influence

Table 7.17 Aerodynamic coefficients – FWS-s influence (avg. values for last 200 iter.)

		Front	Middle	Back
	Cd (WCP)	0,317	0,320	0,324
	Cz	-0,054	-0,050	-0,035
	Cmy	-0,096	-0,091	-0,090
	Czf	-0,123	-0,116	-0,108
	Czr	0,069	0,066	0,073
	Cd	0,321	0,324	0,328

If values are placed into the diagram, it is clear that as wheel spoiler is moving forward, drag value drops (Figure 7.59).

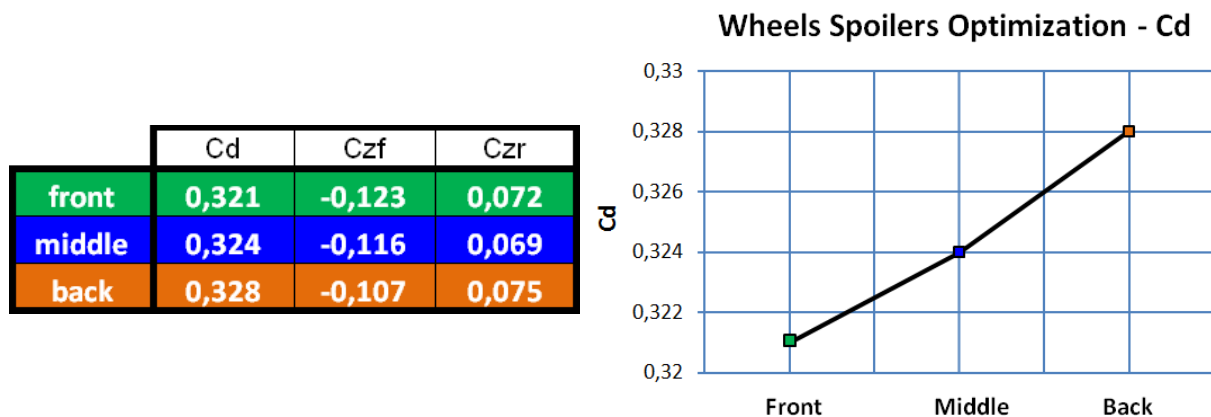


Figure 7.59 Front-wheel spoilers influence - aerodynamic drag

That phenomenon can be explained on the following way (Figure 7.60). Because of its shape, front-wheel spoiler creates small wake behind. As wake is going further from the spoiler it is becoming bigger. Therefore, the bigger distance between spoiler and the wheel is, more of the wheel’s surface is covered by the wake. On the end, if the wheel is covered more, it produces less drag.

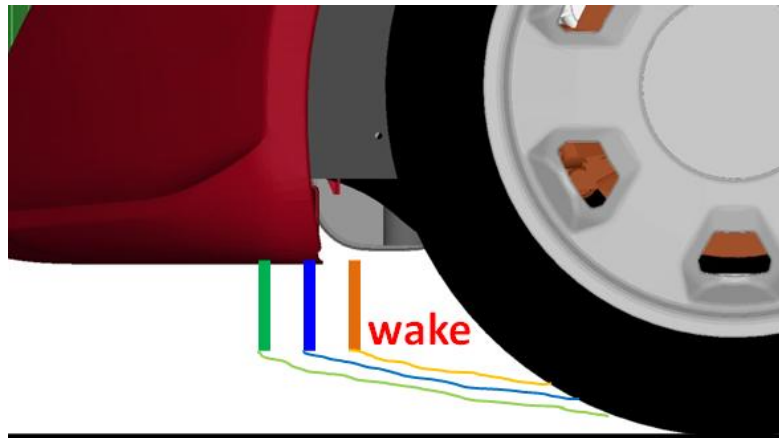


Figure 7.60 Front-wheel spoiler wake sketch

Conclusion

Moving wheel spoiler to the front reduces amount of drag created on the wheels and, at the same time, it does not increase aerodynamic drag on the rest of the vehicle. As a result, total drag on the vehicle is lower. For further investigation it would be interesting to see how far wheel spoilers can be moved to reduce drag even more.

7.10 Side Mirrors Influence and Optimization

Conventional side mirrors generally increase aerodynamic drag. Idea here is to investigate is it possible to do opposite - to reduce aerodynamic drag with the side mirrors. On that way, side mirrors would be aerodynamic drag reduction devices.

That possibility will be investigated by moving side mirrors to the different position and use side mirrors special design (see Chapter 3.2).

Two variables here are related to the side mirrors position:

- **Position** of side mirrors – **top**, **middle** and **bottom** position (Figure 7.61)
- **Incidence angle** (angle of attack) – 0° , $+15^\circ$ and -15° (Figure 7.62)

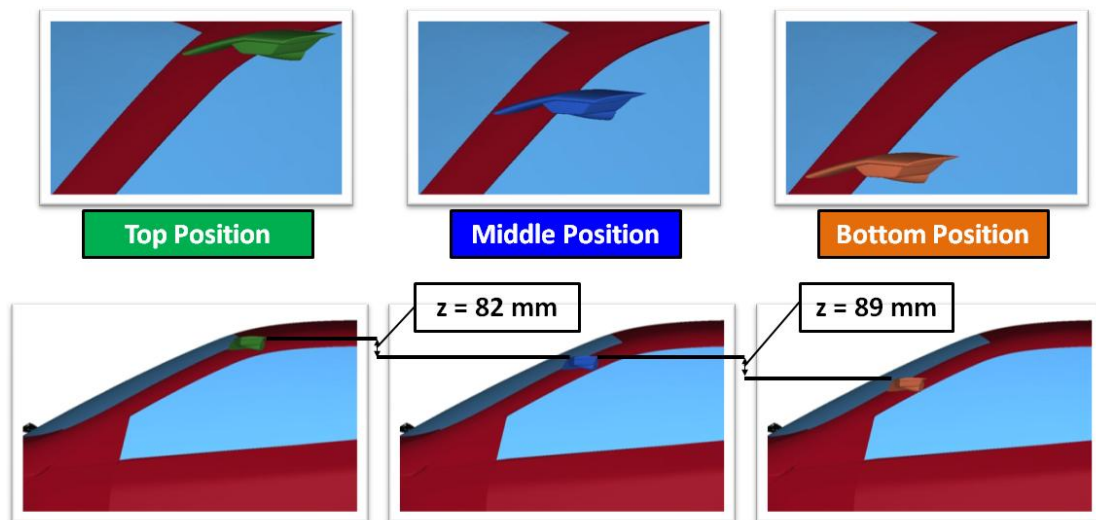


Figure 7.61 Three different side mirror’s positions

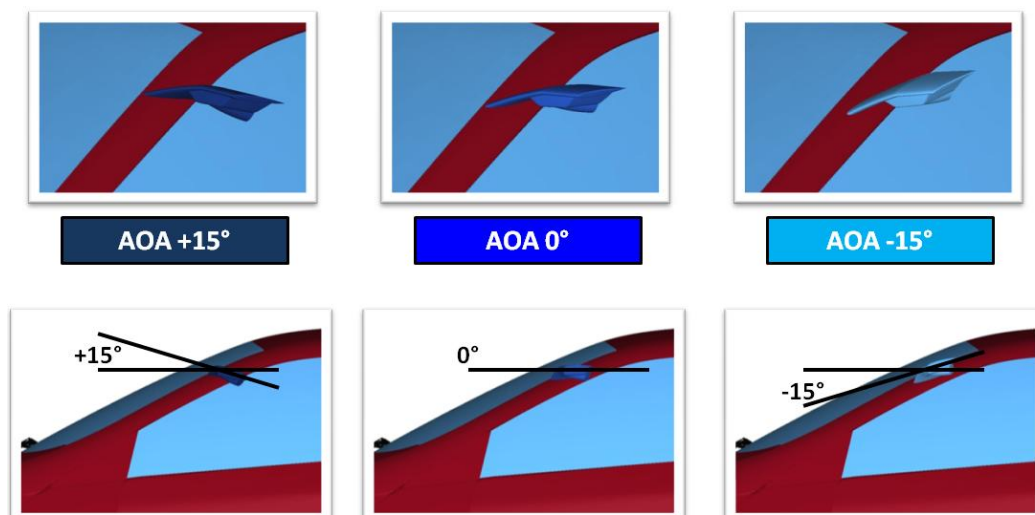


Figure 7.62 Three different side mirror’s incidence angles (angles of attack)

With all combinations of these two variables, nine different geometry configurations were formed. In order to investigate is it possible to use side mirrors as drag reduction devices, also one geometry case without side mirrors was added.

Simulations results with these 10 different geometry configurations are showed in following table.

Table 7.18 Side mirrors position influence – results

Side Mirrors Position	Sim. Nr.	Cd	Czf	Czr	ΔC_d
Without Side Mirrors	Sim. 16	0,321	-0,115	0,074	0,000
Side Mirrors top +15°	Sim. 30	0,323	-0,100	0,080	0,002
Side Mirrors middle +15°	Sim. 31	0,319	-0,094	0,084	-0,002
Side Mirrors botttom +15°	Sim. 32	0,318	-0,094	0,087	-0,003
Side Mirrors top 0°	Sim. 28	0,323	-0,110	0,073	0,002
Side Mirrors middle 0°	Sim. 12	0,324	-0,116	0,069	0,003
Side Mirrors bottom 0°	Sim. 29	0,322	-0,125	0,070	0,001
Side Mirrors top -15°	Sim. 33	0,330	-0,124	0,054	0,009
Side Mirrors middle -15°	Sim. 34	0,332	-0,129	0,052	0,011
Side Mirrors bottom -15°	Sim. 35	0,332	-0,133	0,052	0,011

Last column in the Table 7.18 shows delta values of drag coefficients compared with basic simulation. Basic simulation here is simulation without side mirrors (first row in the table). In the following text, for the purpose of easier understanding, simulations names will be based on the side mirrors position (e.g. “Simulation 31” will be called “Simulation Middle +15°”)

From the results in the Table 7.18 it is clear that side mirrors have influence on the overall aerodynamics on the vehicle. First, if the basic position (Simulation Middle 0°) is compared with the simulation without side mirrors, it is clear that design of the mirrors is very effective. Side mirrors in basic position add only 3 drag counts compared with the geometry case without side mirrors. Compared with the convectional side mirrors design, these side mirrors produce very low drag.

Second, it can be seen that configurations with negative incidence angle (-15°) have the worst results – hence, these results are not interesting here.

Further, it can be concluded that incidence angle have more influence than position of the mirrors.

Eventually, the best geometry case is Simulation Bottom +15°. This geometry case is interesting because it has the lowest drag coefficient value (even lower than configuration without side mirrors). In the following subchapters this best case will be compared, first with the basic side mirrors position, and then with the configuration without side mirrors.

7.10.1 Side Mirrors Influence – Middle 0° vs. Bottom +15°

This chapter compares basic side mirrors position (Simulation Middle 0°) with the best case position (Simulation Bottom +15°). Simulations results are shown on the Figure 7.64 and Table 7.19.

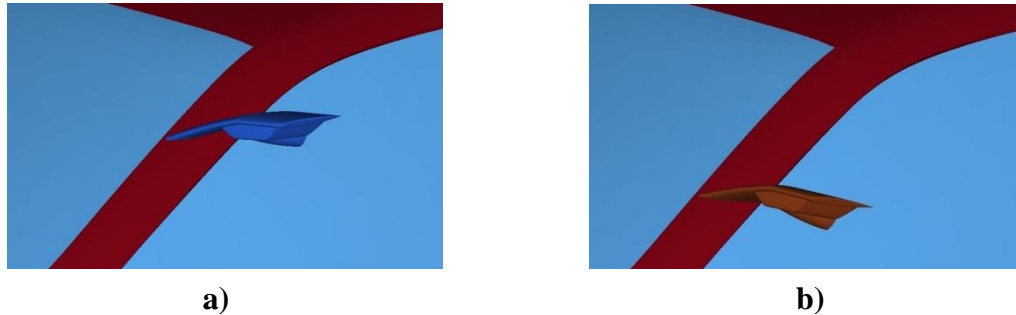


Figure 7.63 a) Basic position – Middle 0°, b) Best case position – Bottom +15°

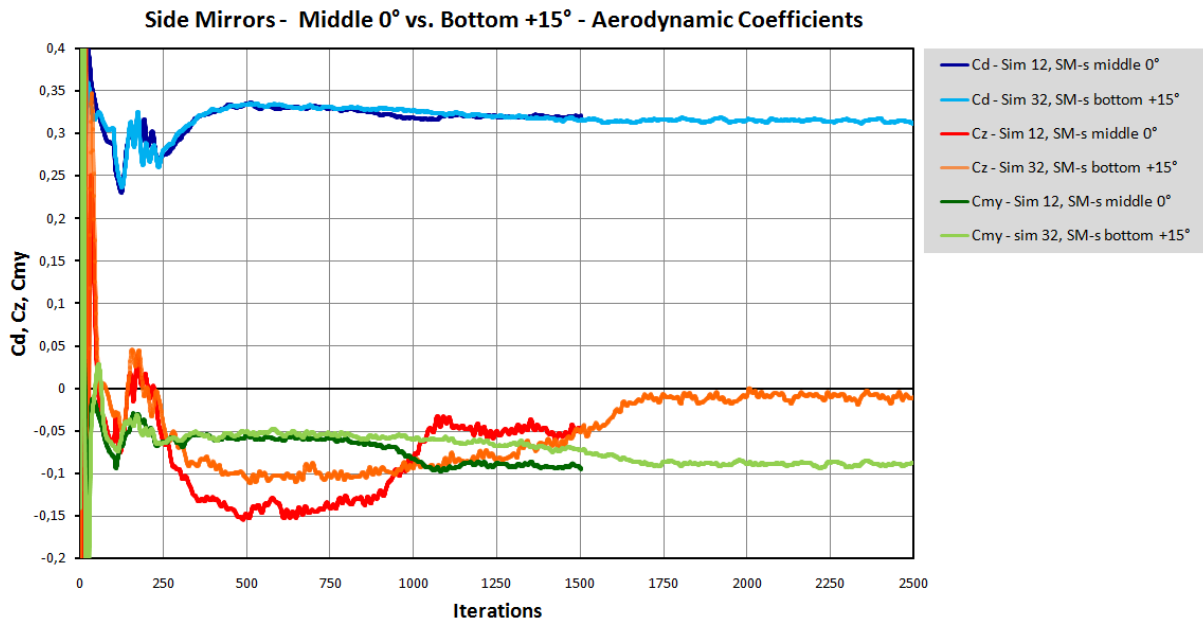


Figure 7.64 Aerodynamic coefficients diagram – Side Mirrors Middle 0° vs. Bottom +15°

Table 7.19 Aerodynamic coeff. – simulations 12 and 32 (avg. values for last 200 iter.)

SM-s Middle 0° - Sim 12			SM-s Bottom +15° - Sim 32		
Cd (WCP)		0,320	Cd (WCP)		0,314
Cz		-0,050	Cz		-0,010
Cmy		-0,091	Cmy		-0,089
	Czf	-0,116		Czf	-0,094
	Czr	0,066		Czr	0,084
	Cd	0,324		Cd	0,318

Simulation Bottom +15° need much more iterations to converge, therefore it has 2500 iterations. Results show 6 drag counts lower drag for Simulation Bottom +15°. If it is taken into account that, in general, these side mirrors do not have great impact on the overall aerodynamics (due to special “low drag” design) these 6 drag counts are certainly significant.

To compare these two simulations more closely, extensive set of flow visualizations and diagrams is showed bellow. First, total pressure coefficient values in Y0 plane are showed on the Figure 7.65. There is a smaller low pressure zone on the rear base (middle region of the rear base) for the Simulation Bottom +15°. This smaller zone indicates lower drag.

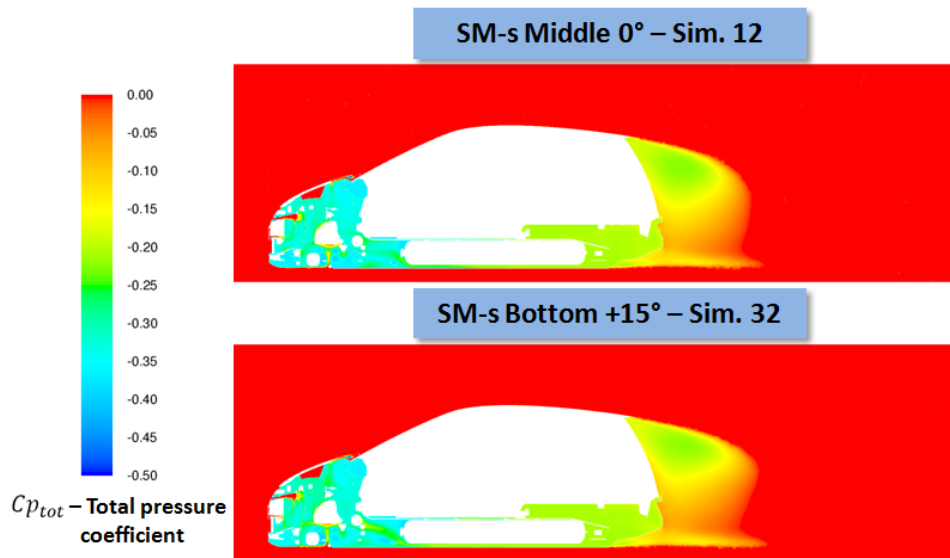


Figure 7.65 Total pressure coefficient in Y0 plane – SM-s Middle 0° vs. Bottom +15°

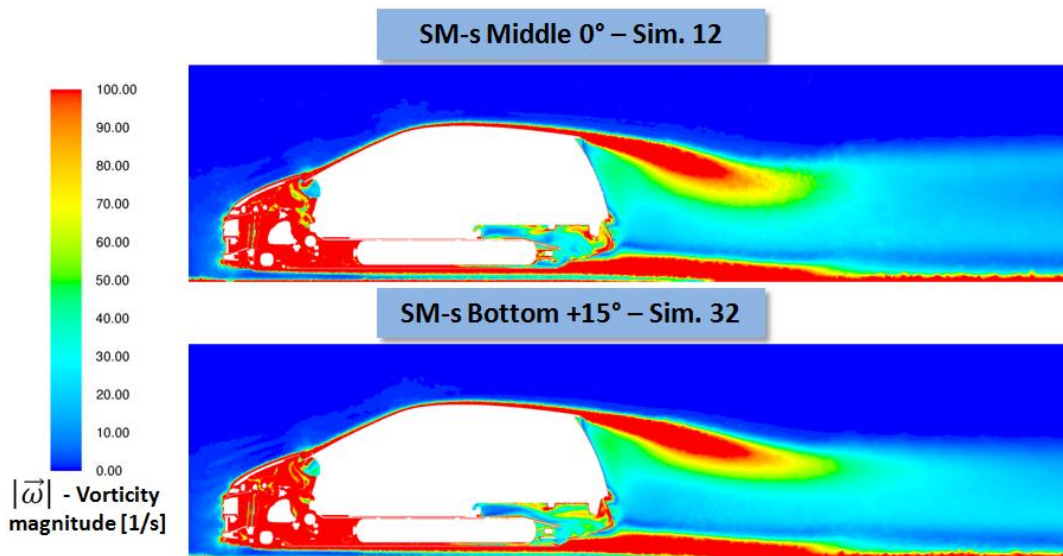


Figure 7.66 Vorticity magnitude in Y0 plane – SM-s Middle 0° vs. Bottom +15°

Figure 7.66 shows vorticity magnitude in the Y0 plane. Simulation Bottom +15° has smaller amount of vortices and hence smaller wake – indications of lower drag.

The biggest differences in the wake are in the region around plane Z815. Therefore, vorticity magnitude in that plane is showed on the Figure 7.67.

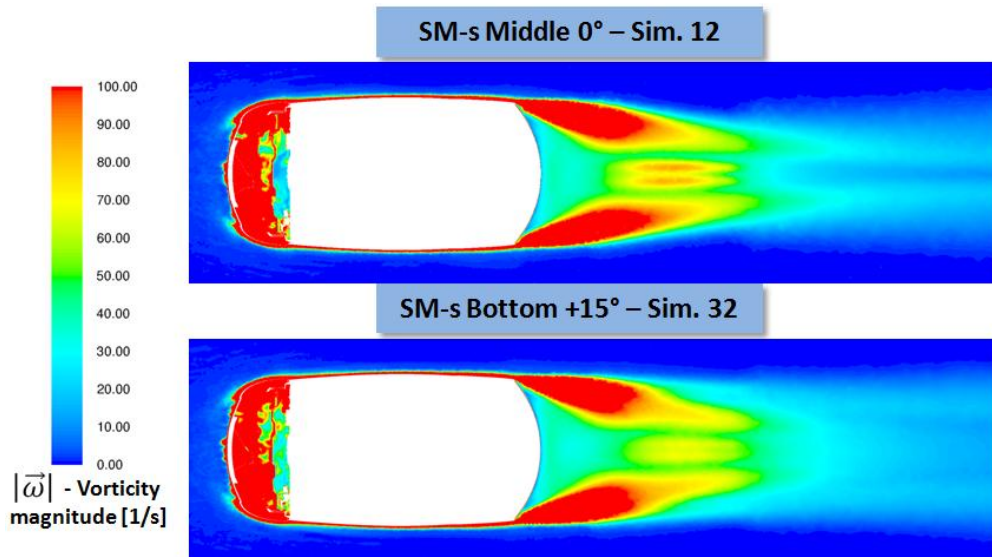


Figure 7.67 Vorticity magnitude in Z815 plane – SM-s Middle 0° vs. Bottom +15°

Figure 7.68 shows turbulence kinetic energy, also in the Z815 plane. Simulation Bottom +15° certainly has less turbulences and lower wake intensity – indications of lower drag.

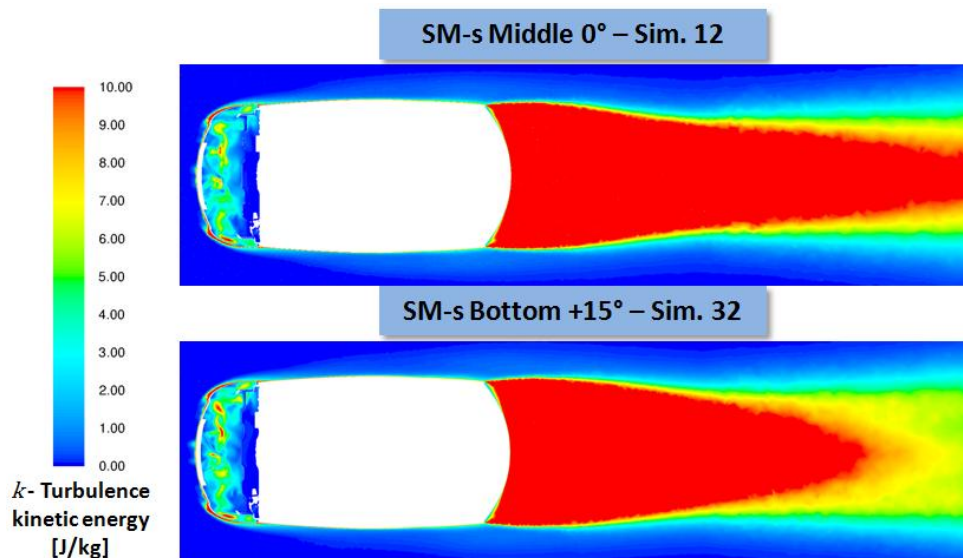


Figure 7.68 Turbulence kinetic energy in Z815 plane – SM-s Middle 0° vs. Bottom +15°

To see where air detaches from the surface it is good to observe 3D wall shear stress contours. Because side mirrors are in the spotlight, in the Figure 7.69 wall shear stress in the region downstream of the side mirrors is showed. It can be seen how side mirrors affect flow detachment.

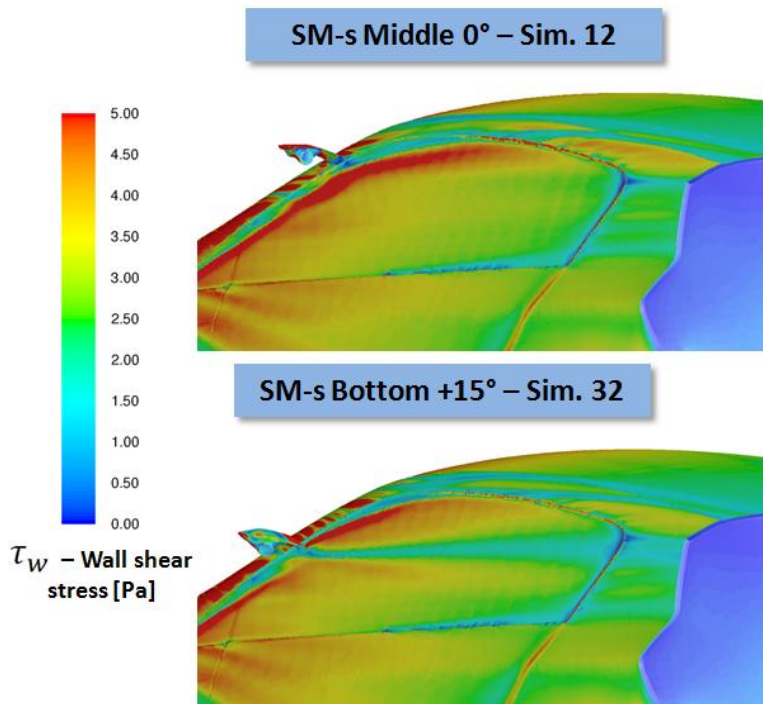


Figure 7.69 Wall shear stress 3D visualization - SM-s Middle 0° vs. Bottom +15°

To better understand flow detachment also 3D streamlines around side mirrors are showed in the Figure 7.70 and Figure 7.71. It is the best to study all three figures together (wall shear stress with streamlines).

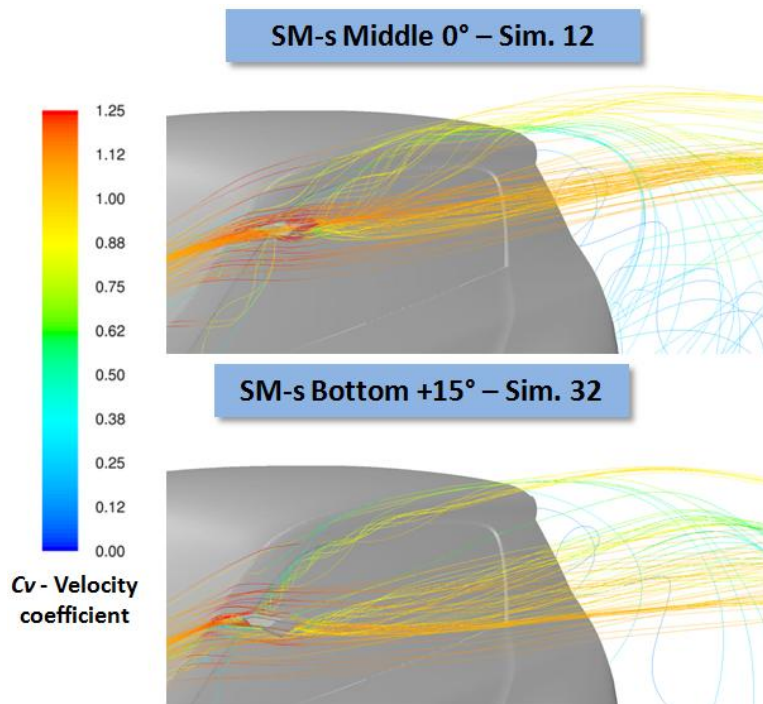


Figure 7.70 Veloc. coeff. streamlines in isometric view – SM-s Middle 0° vs. Bottom +15°

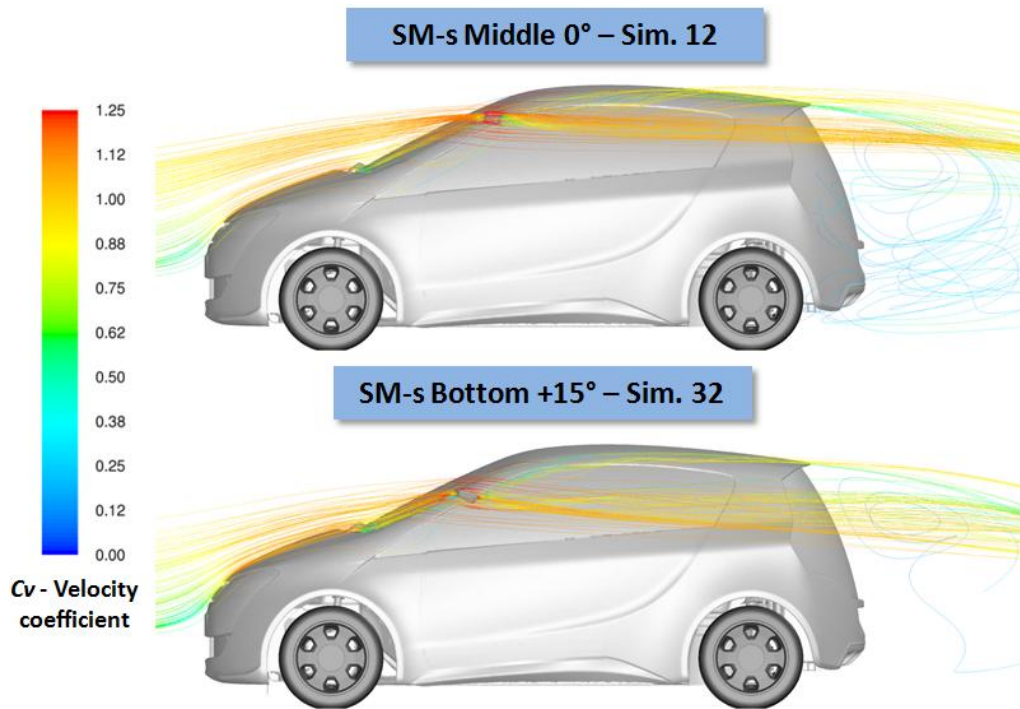


Figure 7.71 Veloc. coeff. streamlines in side view – SM-s Middle 0° vs. Bottom +15°

Streamlines indicates that side mirrors in the position Bottom +15° move turbulences, which are created on the A-pillar. These turbulences go to the side of the vehicle, instead over the roof to the back of the vehicle, as is the case with the position middle 0°. These differences between streamlines are cause of pressure differences on the rear base of the vehicle.

Figure 7.72, Figure 7.73 and Figure 7.74 show pressure coefficient distribution on the car’s surface in the Y0 cut plane:

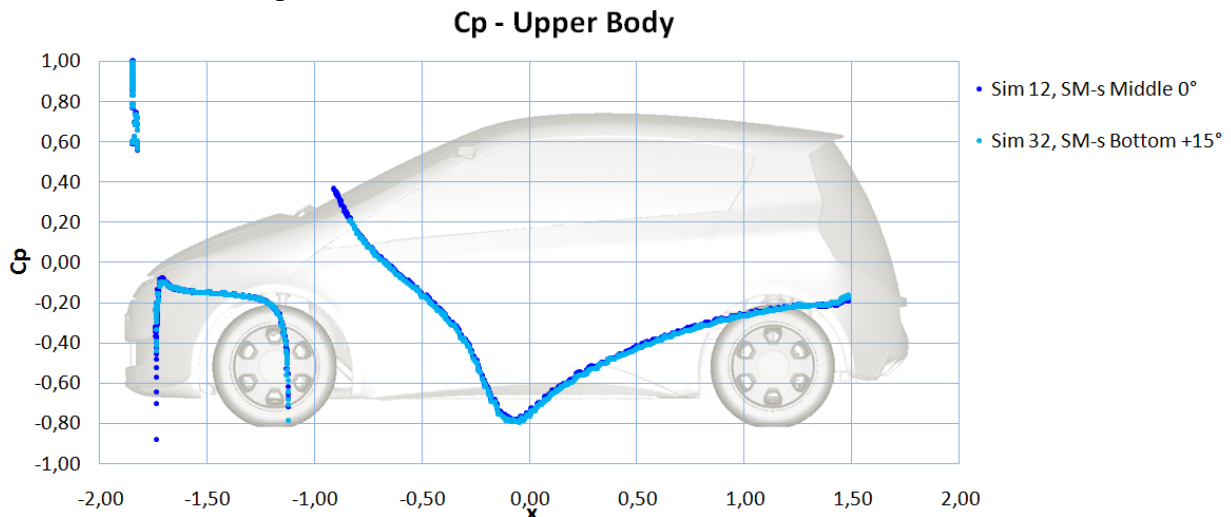


Figure 7.72 Pressure coeff. distribution on the upper body – SM-s Middle 0° vs. Bottom +15°

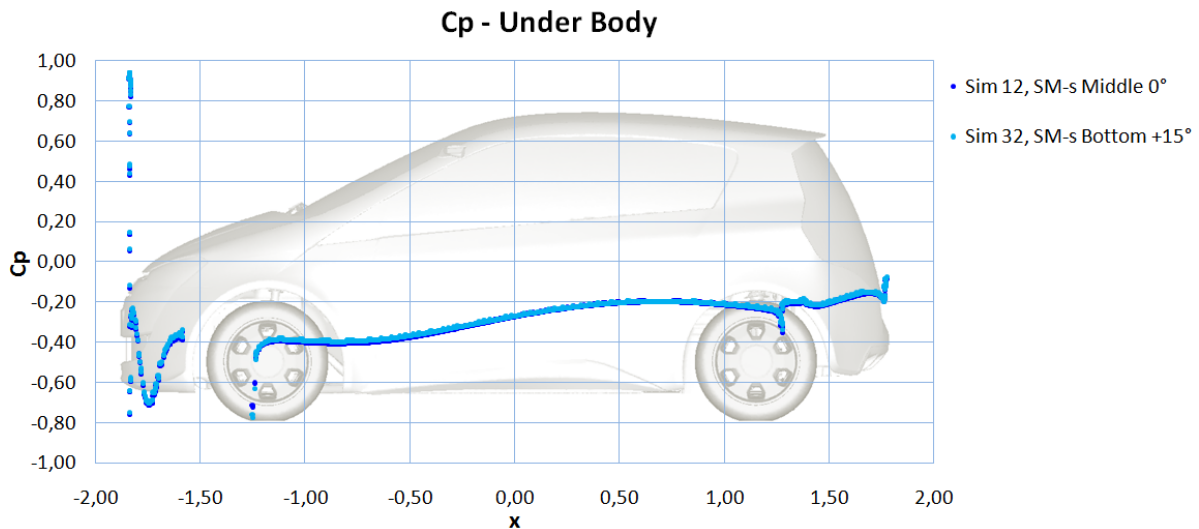


Figure 7.73 Pressure coeff. distribution on the under body – SM-s Middle 0° vs. Bottom +15°

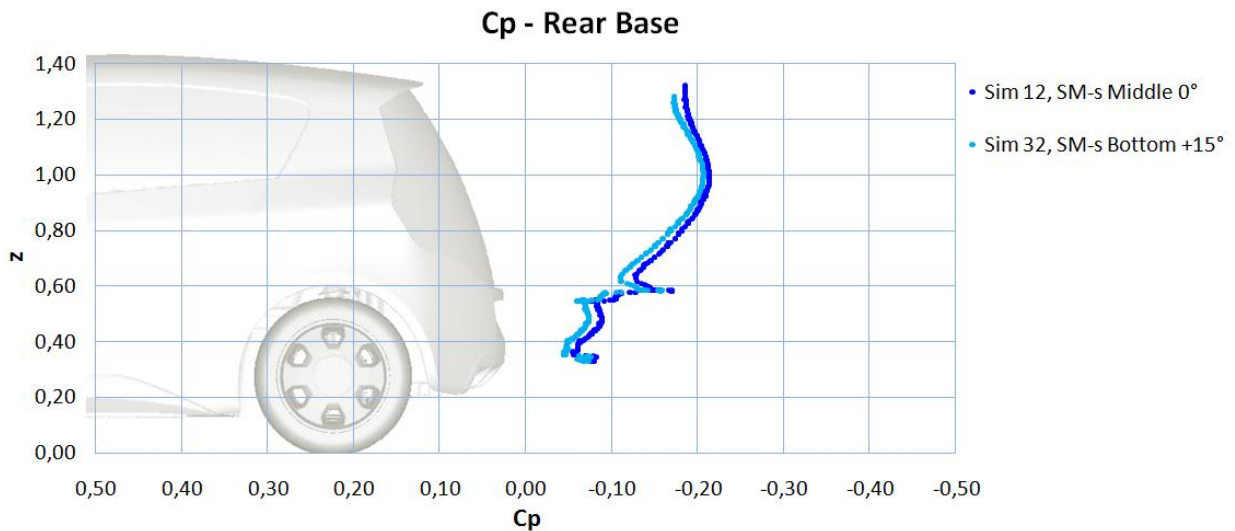


Figure 7.74 Pressure coeff. distribution on the rear base – SM-s Middle 0° vs. Bottom +15°

As it can be seen from the diagrams above, pressure coefficient distribution differences in the Y0 plane are on the rear base of the vehicle. As it was already concluded before, Simulation Bottom +15° has higher pressure on the back of the vehicle – indications of lower drag.

Now, accumulated force diagrams, created during post processing, will be used for the first time in this thesis. This case, with only one geometry change on the vehicle, is suitable for comparison with the accumulated force diagrams. In the Figure 7.75, F_x accumulated diagram is showed and in the Figure 7.76, F_z accumulated diagram (for explanation how to read these diagrams see Chapter 5.5).

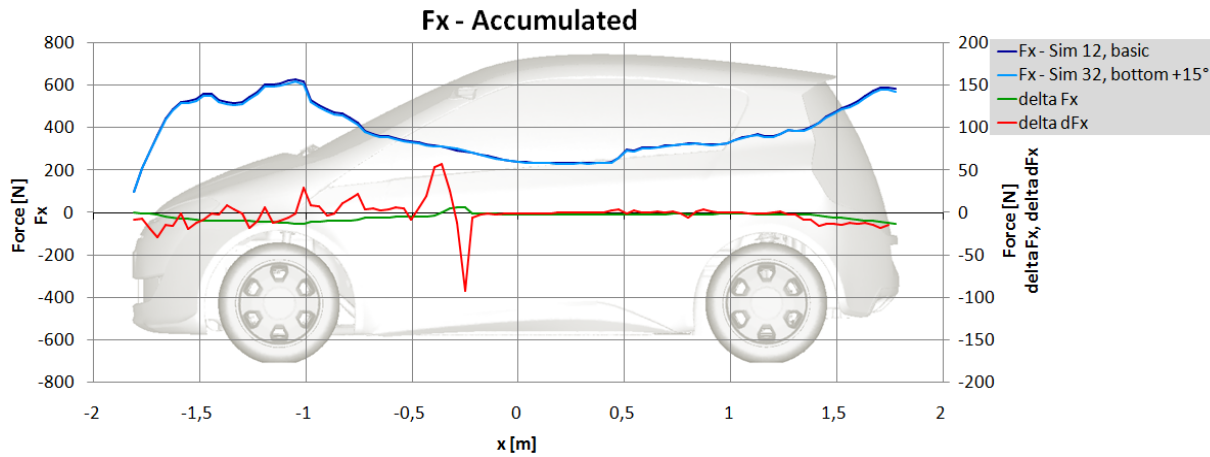


Figure 7.75 F_x accumulated diagram – SM-s Middle 0° vs. Bottom $+15^\circ$

Diagrams are observed from the front end to the rear end of the vehicle. First, F_x accumulated diagram in the Figure 7.75 will be explained. Delta dF_x (red line) is the most important – it represents changes between simulations. First significant changes of delta dF_x are in the position of the side mirrors. After side mirrors, from approximately middle of the vehicle, both, delta F_x and delta dF_x are equal to zero. That tells that until this point (around $x = 0$) total drag difference between simulations is zero. But, if it is continued to the rear end, it can be seen that, on the end, delta F_x drops. That means lower drag force for Simulation bottom $+15^\circ$. Therefore, side mirrors locally did not change aerodynamic drag, but they affected flow on the rear end of the vehicle and changed drag force in that area.

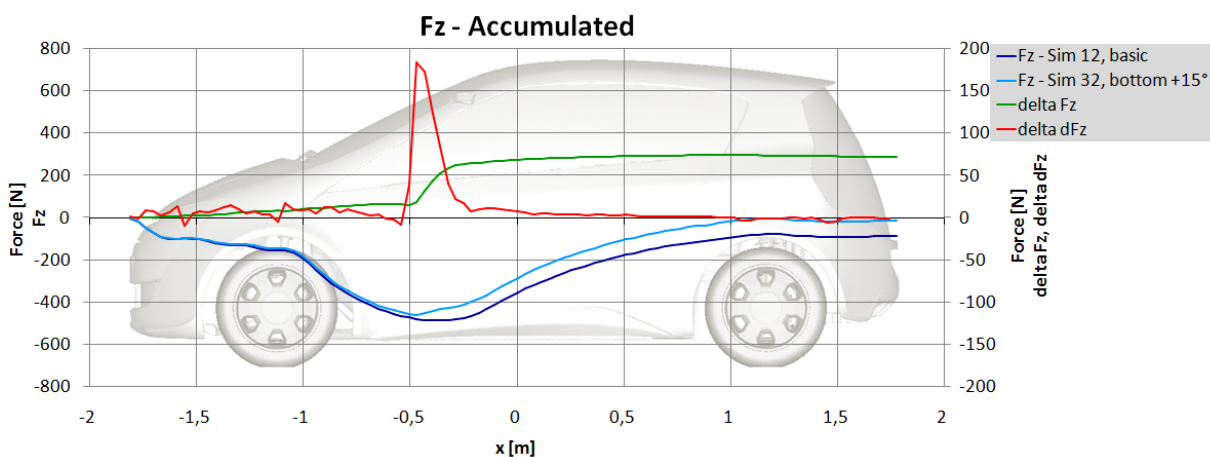


Figure 7.76 F_z accumulated diagram – SM-s Middle 0° vs. Bottom $+15^\circ$

F_z accumulated diagram is much easier to explain. Because of positive incidence angle, Simulation bottom $+15^\circ$ has lift increase in the region around side mirrors. After that region there are no significant differences in lift forces between simulations.

Conclusion

If the side mirrors are moved from the position Middle 0° to the position Bottom +15° they change air flow around vehicle. Turbulences created on the A-pillar are moved to the side of the vehicle, instead on the roof and further on the rear base. This change affects flow, reducing aerodynamic losses in the wake behind the car. That phenomenon affects the vehicle by increasing pressure on the rear base. As a result, there is 6 drag counts lower drag for Simulation Bottom +15°.

7.10.2 Side Mirrors Influence – Without SM-s vs. Bottom +15°

This chapter compares geometry case without side mirrors with the best case geometry (Simulation Bottom +15°). Purpose of this comparison is to prove that side mirrors can serve as drag reduction devices.

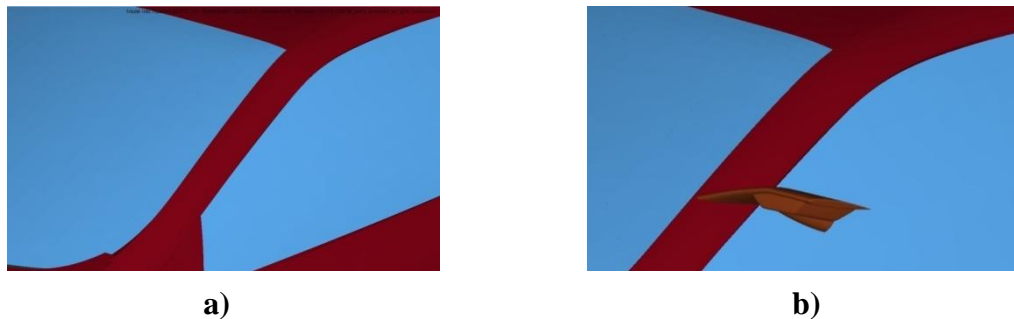


Figure 7.77 a) Geometry case without side mirrors, b) Best case position – Bottom +15°

Simulations results are shown in the Figure 7.78 and Table 7.20:

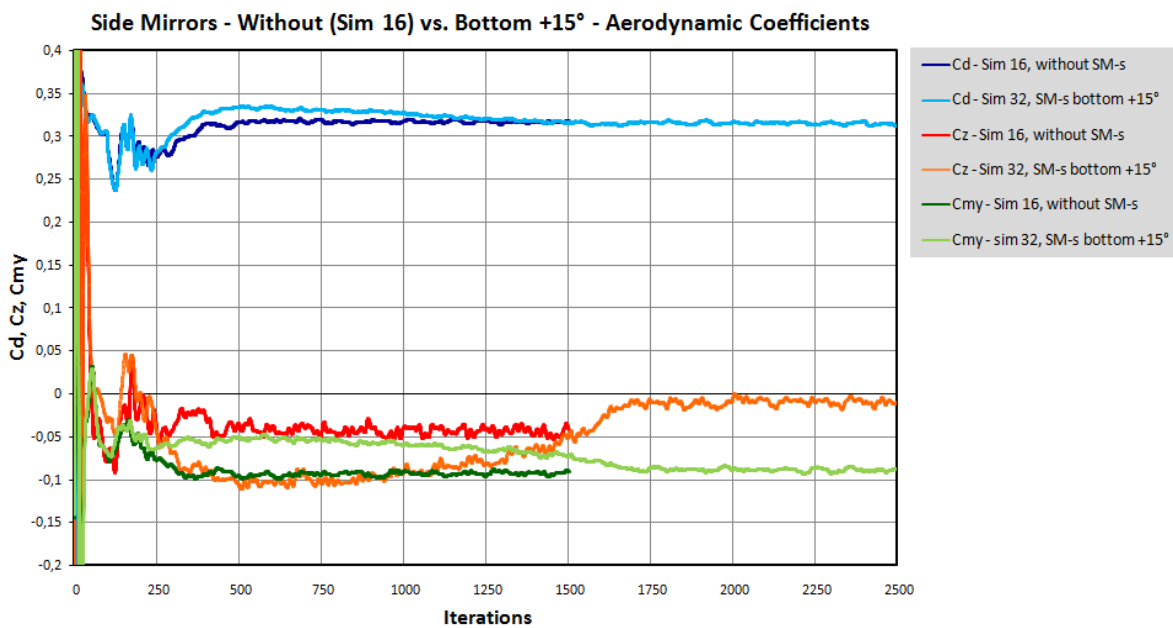


Figure 7.78 Aerodynamic coefficients diagram – without SM-s vs. Bottom +15°

Table 7.20 Aerodynamic coeff. – simulations 16 and 32 (avg. values for last 200 iter.)

Without SM-s - Sim 16			SM-s Bottom +15° - Sim 32		
Cd (WCP)		0,317	Cd (WCP)		0,314
Cz		-0,044	Cz		-0,010
Cmy		-0,093	Cmy		-0,089
	Czf	-0,115		Czf	-0,094
	Czr	0,071		Czr	0,084
	Cd (CP)	0,321		Cd (CP)	0,318

Simulation without side mirrors converged very fast, compared with the 2500 iterations required for Simulation Bottom +15°. Simulation Bottom +15° has 3 drag counts lower drag coefficient. Because the only geometry difference between these two simulations is side mirrors presence, side mirrors can be called “**Drag reduction devices**”.

To compare these two simulations more closely, as in the chapter above, an extensive set of flow visualizations and diagrams is showed bellow. First, total pressure coefficient value in Y0 plane is showed in the Figure 7.79. Again, there is a smaller low pressure zone on the rear base (middle region of the rear base) for the Simulation Bottom +15°. This smaller zone indicates lower drag.

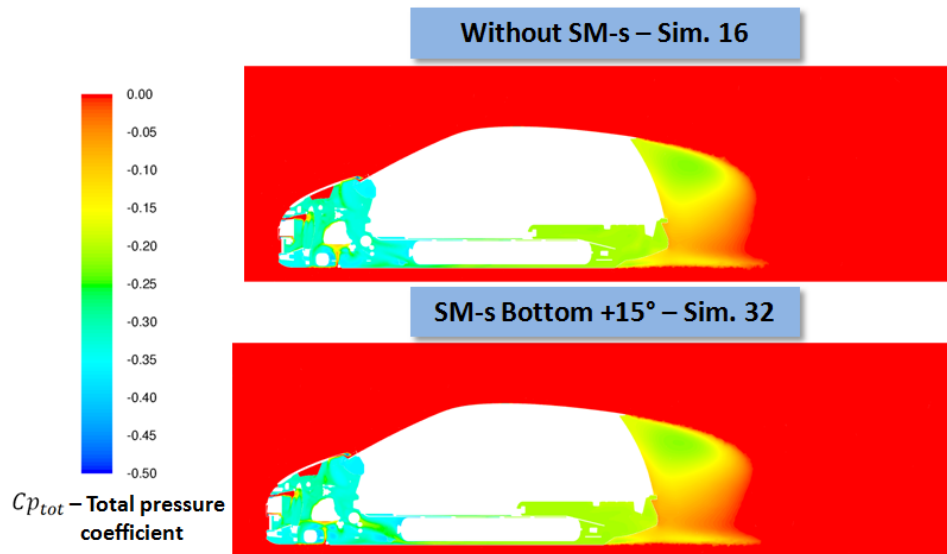


Figure 7.79 Total pressure coefficient in Y0 plane – without SM-s vs. Bottom +15°

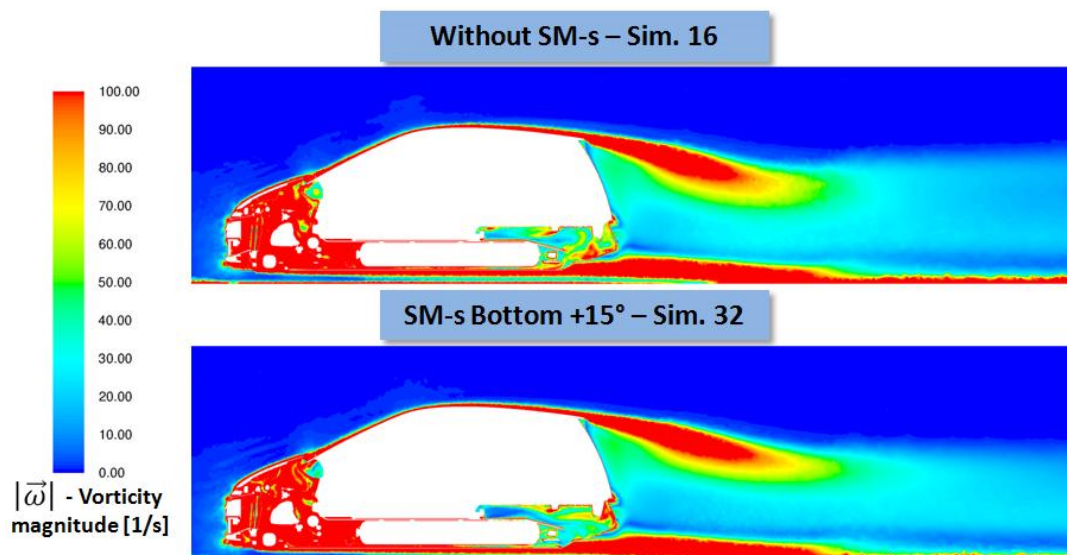


Figure 7.80 Vorticity magnitude in Y0 plane – without SM-s vs. Bottom +15°

Figure 7.80 shows vorticity magnitude in the Y0 plane. Simulation Bottom +15° has smaller amount of vortices and smaller wake – indications of lower drag.

The biggest differences in the wake are in the region around plane Z815. Therefore, vorticity magnitude in that plane is showed in the Figure 7.81.

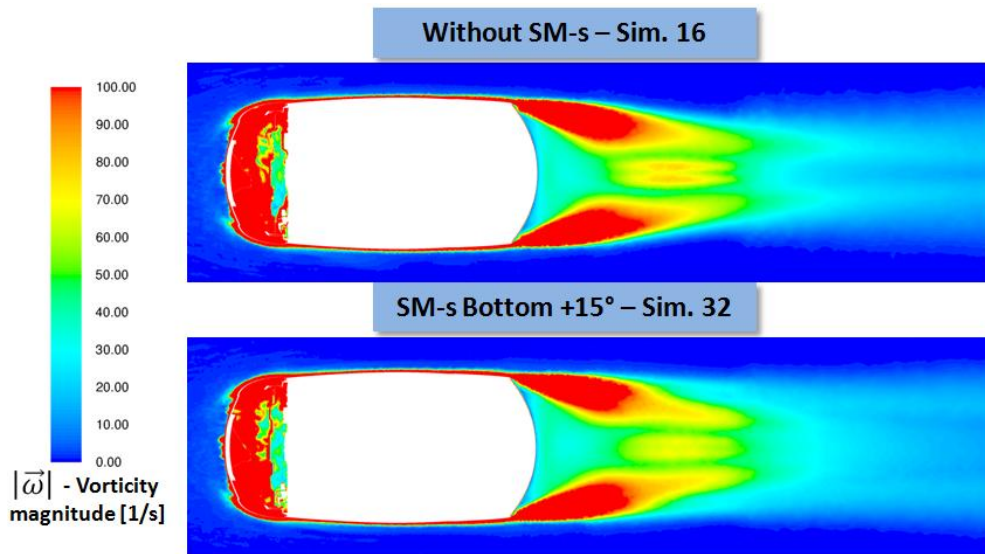


Figure 7.81 Vorticity magnitude in Z815 plane – without SM-s vs. Bottom +15°

Figure 7.82 shows turbulence kinetic energy, in the Z815 plane. Simulation Bottom +15° certainly has less turbulences and lower wake intensity – indications of lower drag.

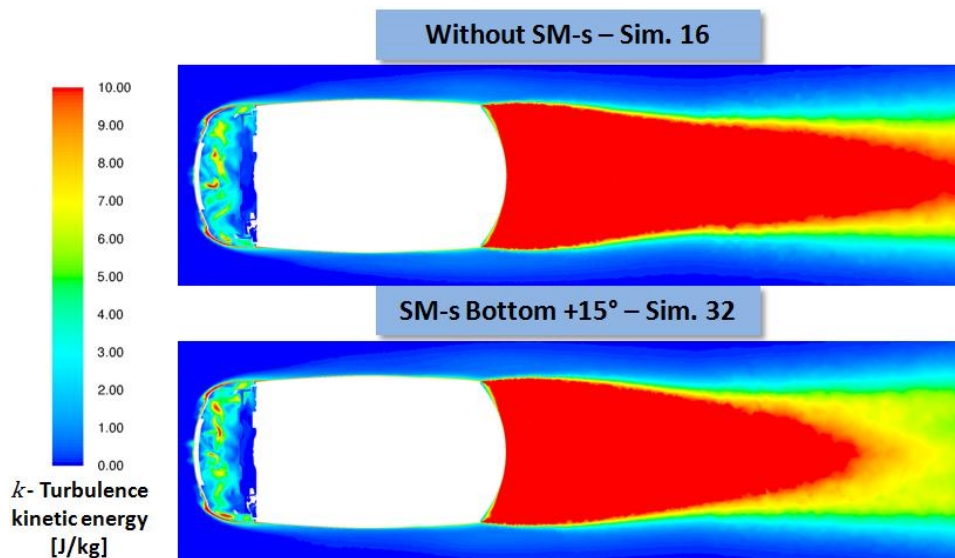


Figure 7.82 Turbulence kinetic energy in Z815 plane – without SM-s vs. Bottom +15°

The last visualizations are 3D wall shear stress and 3D streamlines around side mirrors position. As it the case in chapter above, it is good to compare these visualizations together, in order to better understand flow. Figure 7.83 shows wall shear stress downstream the side mirrors. Figure 7.84 and Figure 7.85 show streamlines around side mirrors area.

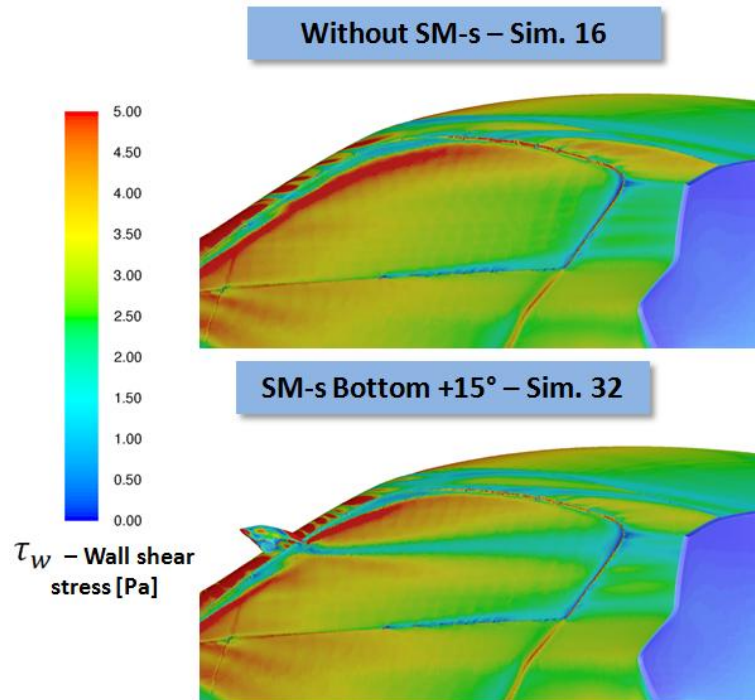


Figure 7.83 Wall shear stress 3D visualization – without SM-s vs. Bottom +15°

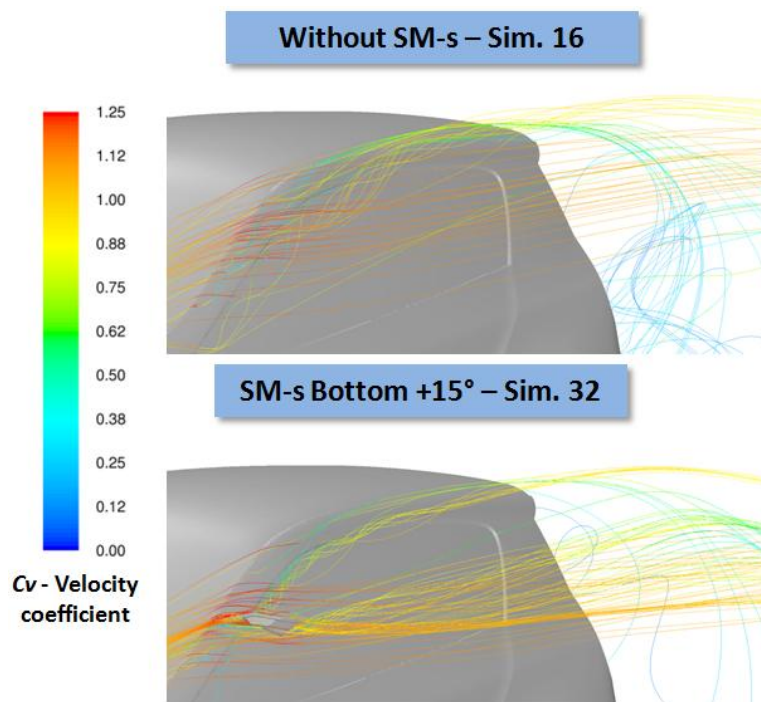


Figure 7.84 Veloc. coeff. streamlines in isometric view – without SM-s vs. Bottom +15°

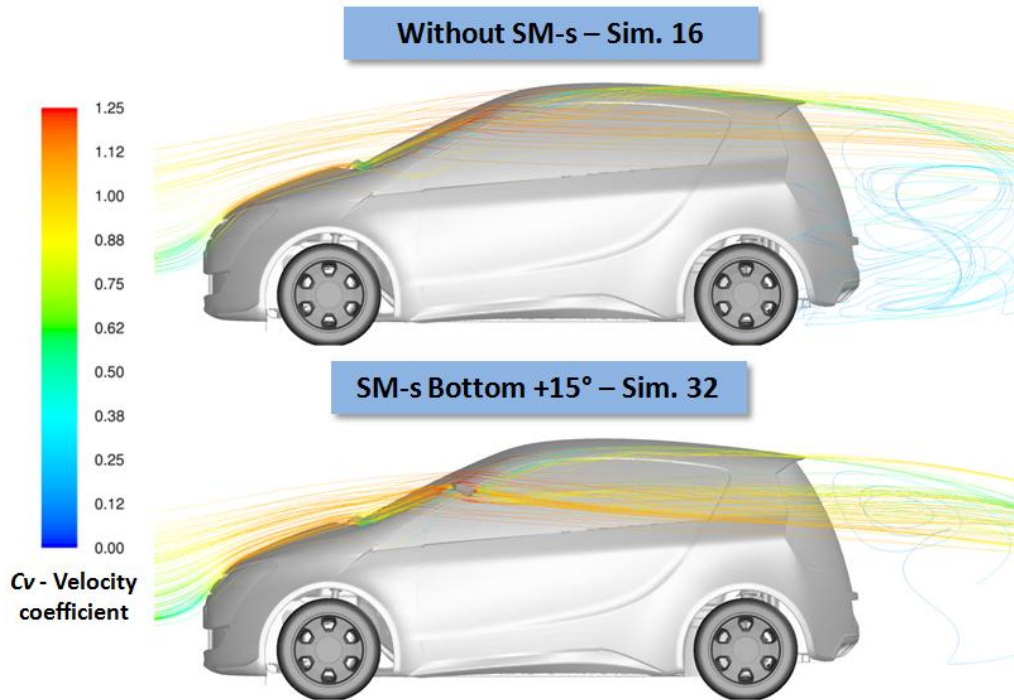


Figure 7.85 Veloc. coeff. streamlines in side view – without SM-s vs. Bottom +15°

Simulation without side mirrors has similar behavior as Simulation middle 0° (basic position). They both have A-pillar turbulences going to the roof and to the back of the vehicle. Simulation Bottom +15° moves most of these turbulences to the side of the vehicle. It seems that whole comparison of flow visualization is practically same as in the case in the chapter above. Accordingly, these differences between streamlines are cause of pressure differences on the rear base of the vehicle.

Figure 7.86, Figure 7.87 and Figure 7.88 show pressure coefficient distribution on the car’s surface in the Y0 cut plane:

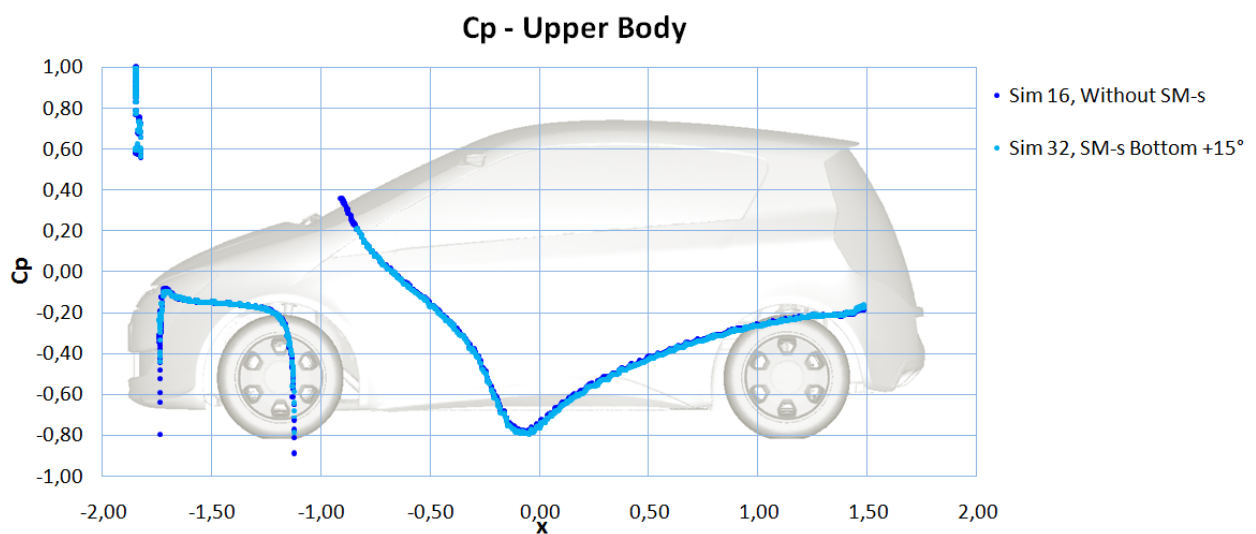


Figure 7.86 Pressure coeff. distribution on the upper body – without SM-s vs. Bottom +15°

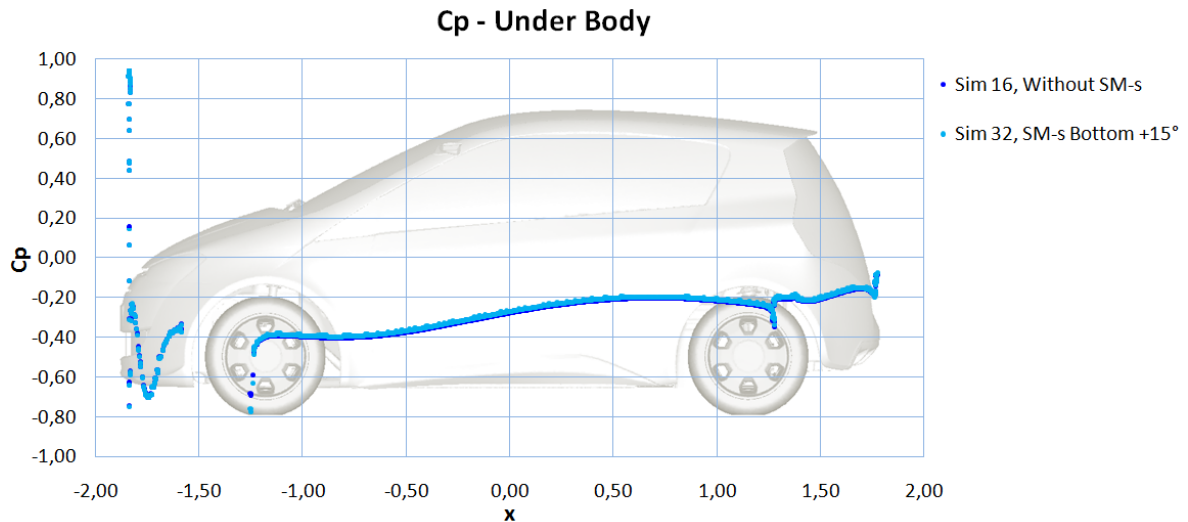


Figure 7.87 Pressure coeff. distribution on the under body – without SM-s vs. Bottom +15°

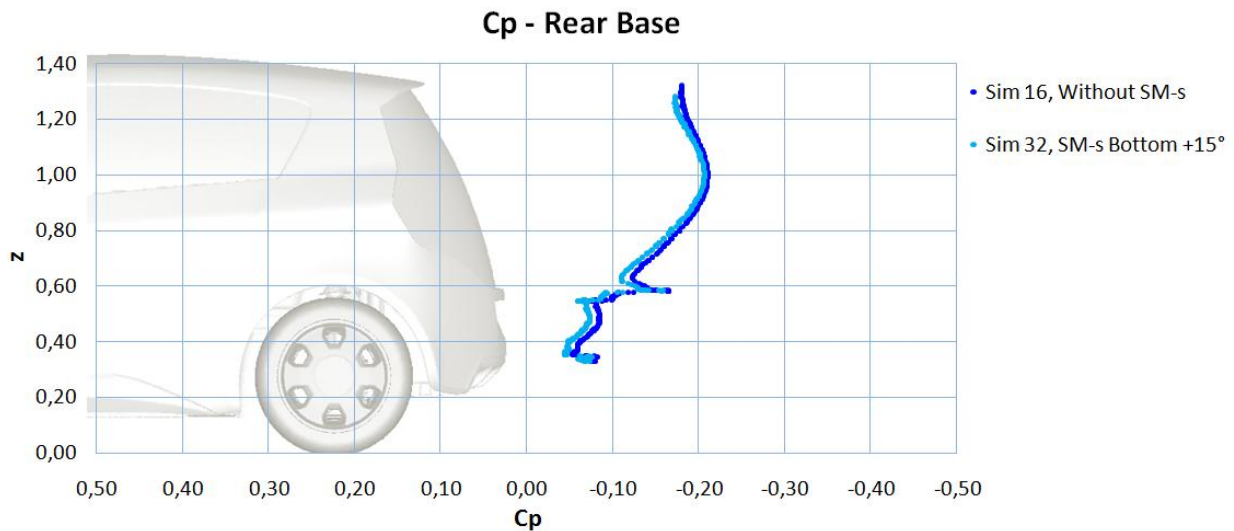


Figure 7.88 Pressure coeff. distribution on the rear base – without SM-s vs. Bottom +15°

As it can be seen from the diagrams above, there are pressure coefficient distribution differences in the Y0 plane on the back of the vehicle. Higher pressure is for the simulation Bottom +15°, what is indication of lower drag. If it is compared with the previous chapter (Figure 7.74), these differences between compared simulations are smaller. It makes sense because a difference in aerodynamic drag is 3 against 6 drag counts.

In the Figure 7.89 F_x accumulated diagram is showed (for explanation how to read accumulated force diagrams see Chapter 5.5). First significant changes of delta dF_x value are in the position around side mirrors. After side mirrors, from approximately middle of the vehicle (around $x = 0$), delta dF_x is around zero. Going to the rear end, delta dF_x drops a little for three more times.

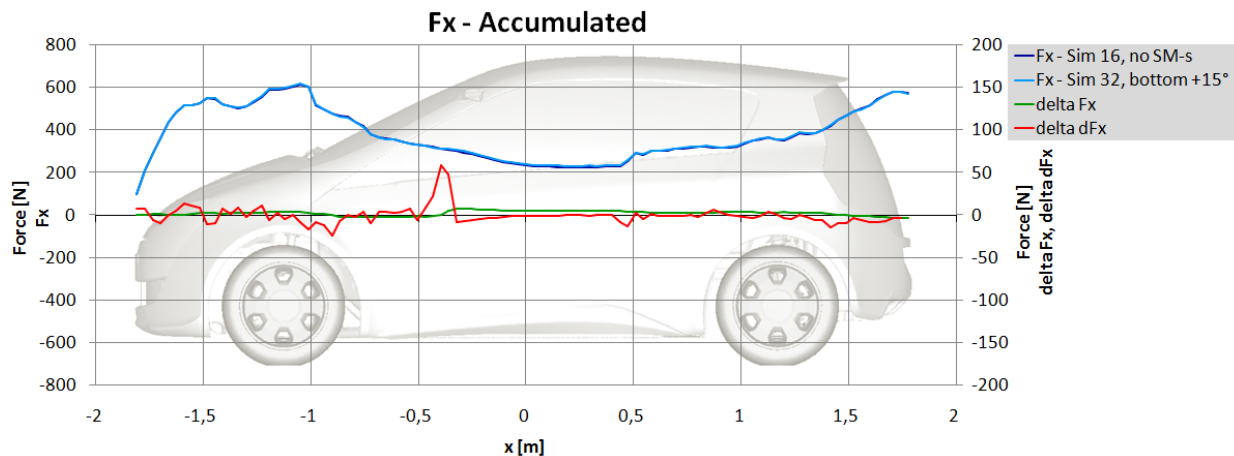


Figure 7.89 F_x accumulated diagram – without SM-s vs. Bottom +15°

If the delta F_x value is observed, it can be seen that it increases after position of the side mirrors. That means simulation without side mirrors has lower drag force observed at the point after position of side mirrors (around $x = 0$). But, if it is continued to the rear end, it can be seen that on the end delta F_x drops slightly below zero (each time delta dF_x drops, delta F_x decrease its value). Biggest drop is on the rear end of the vehicle. On the end, total drag force is slightly lower for the Simulation Bottom +15°.

Also, it is important to separate drag force and drag coefficient. Because Simulation Bottom +15° has side mirrors, reference area is slightly bigger. Therefore, there is a bigger difference in aerodynamic drag coefficient between simulations, compared with the drag force. Simulation Bottom +15° has barely noticeable lower drag force, but because of bigger reference area it has noticeably lower drag coefficient value.

It can be concluded that, compared with the geometry without side mirrors, side mirrors locally increased aerodynamic drag, but they affected the flow downstream, especially on the rear end and globally decreased aerodynamic drag force.

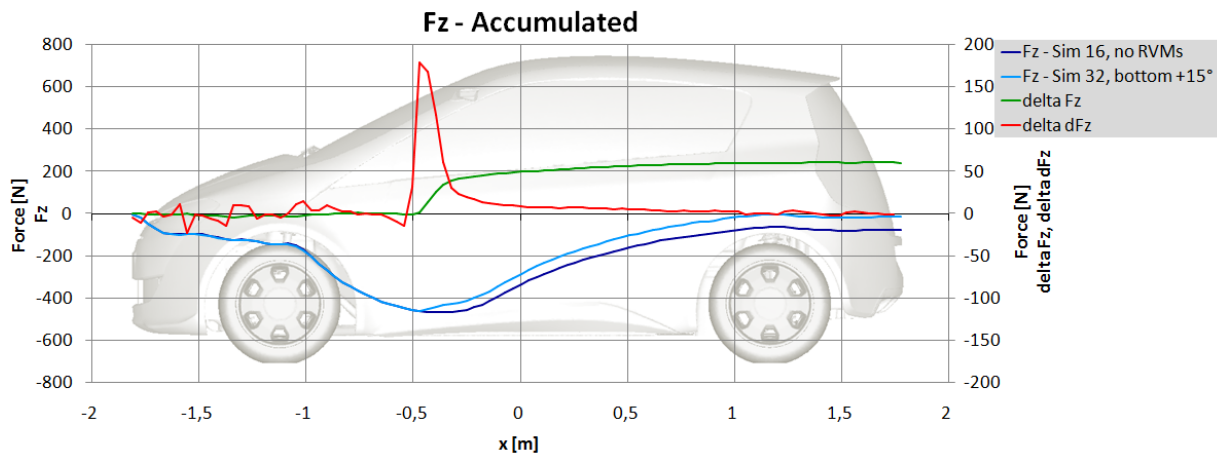


Figure 7.90 F_z accumulated diagram – without SM-s vs. Bottom +15°

In the Figure 7.90, F_z accumulated diagram is showed. Because of the side mirror’s positive incidence angle, Simulation Bottom +15° has lift increase in the region around side mirrors. After that region there are no significant differences between lift forces of these two simulations.

Conclusion

It can be sad that flow differences between compared simulations have similar behavior as in the chapter above (Chapter 7.10.1). In this case, side mirrors locally increased drag value, but they also reduced drag force downstream and on the rear end and, globally, decreased aerodynamic drag force. Therefore, total drag force is slightly lower for the Simulation Bottom +15°. In that case, side mirrors can be called **drag reduction devices**.

Because of different reference area between simulations compared here, it is important to emphasize once more that Simulation Bottom +15° has both, aerodynamic drag force and aerodynamic drag coefficient better (lower) than simulation without side mirrors.

8 RECOMMENDATIONS FOR CFD METHOD IMPROVEMENTS

It is known that in engineering practice is not necessary (and also not possible) to get perfect results, instead it is necessary to design a good product in a given time. Deadlines are always at the first place. That is the reason why a lot of simplifications are in usage. Sometimes it is very hard to put a line between “wrong” and “correct”.

However, some simplifications are not good and they can give incorrect results, what can lead to totally different (and wrong) conclusions. Some simplifications, used in this project, will be highlighted in this chapter. Opinion is that these simplifications are improvement worthy. With good standardization of the whole process, these simplifications can be avoided without spending additional time. Even if the little more time is spent, benefits from more accurate results would be more valuable.

8.1 Averaging of the Results

Figure 8.1 shows drag coefficient monitored during CFD simulation. It is obvious that C_D value is fluctuating all the time during simulation process. That is the reason for averaging the values. In this thesis all aerodynamic coefficients results represents average value of certain number of iterations (usually last 200 iterations).

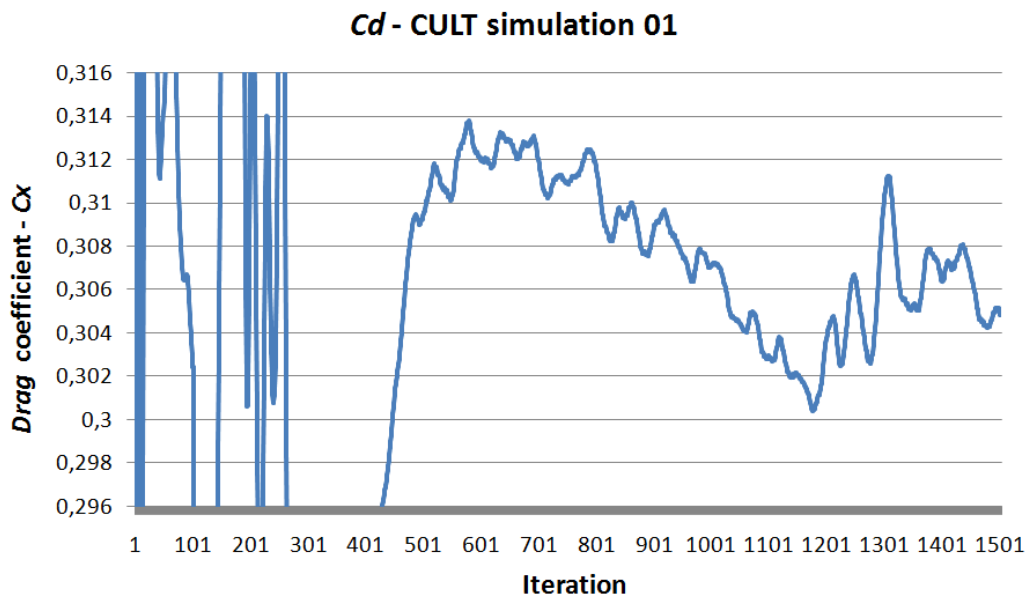


Figure 8.1 Drag coefficient (C_D) data from CFD simulation – CULT simulation 01

However, during creation of accumulated force diagrams, pressure coefficient diagrams and flow visualizations creation, averaging was not used. Instead, results after last iteration were in use. Recommendation for future projects is to use average values, as is the case with the aerodynamic forces. Then, engineer can be sure that differences noticed during visual comparison of two simulations are not consequence of the lack of averaging process.

8.2 Dimensionless Wall Distance (y^+)

To properly simulate boundary layer flow it is important to understand flow physics in that area. Even more important is to adjust solver and grid properly in order to calculate flow sufficiently accurate. Therefore, solver settings need to be taken into account during grid creation. Attention in this chapter is on good approximation on boundary layer fluid flow.

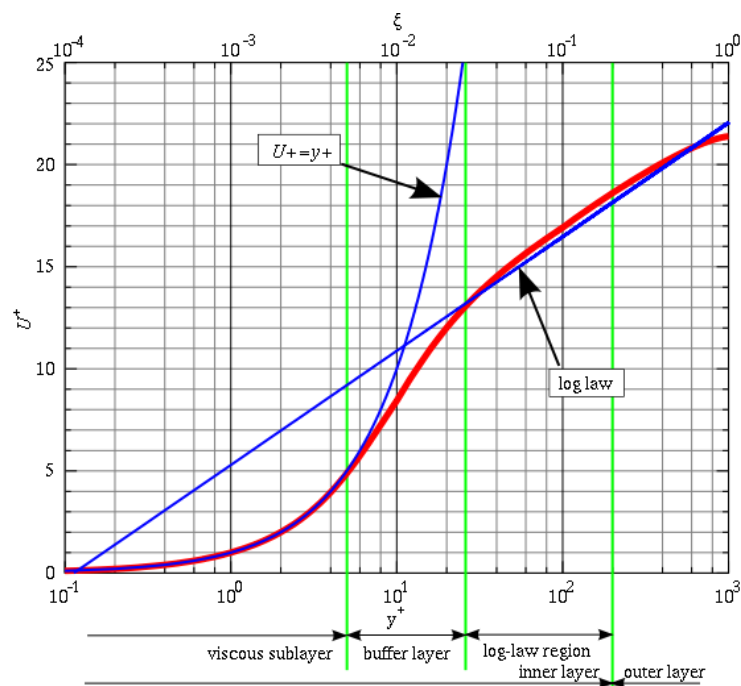


Figure 8.2 Dimensionless velocity (u^+) in a function of dimensionless distance (y^+) [30]

Boundary layer and boundary layer velocity profile is defined in Chapter 1.1 (Figure 1.3). Diagram in Figure 8.2 also shows velocity profile of the boundary layer, but in different way. On the ordinate is dimensionless velocity (u^+) and on abscissa is dimensionless distance from the wall (y^+) - dimensionless distance is in logarithmic scale. They are defined with following formulas:

$$u^+ = \frac{u}{u_\tau}$$

u – velocity
 u_τ – friction or shear velocity

$$y^+ = \frac{yu_\tau}{\nu}$$

y – velocity
 ν – kinematic viscosity

Red line in the Figure 8.2 represents velocity profile of the boundary layer and two blue lines represent two approximations of velocity profile. In a viscous sub-layer approximation $u^+ = y^+$ is adequate. In buffer layer, no one from two approximations is valid. After buffer layer comes log-law region, where other approximation is close to reality - $u^+ = \log y^+$

If the height of the first cell is big enough to skip over viscous sub-layer and buffer layer, only log-law can be used to calculate boundary layer flow. This method is very economical and gives satisfying results. To use only log-law region, y^+ values should be between 30 and 500 (upper limit depends from flow).

This here is only basic explanation, probably enough good to draw attention to importance of y^+ in the CFD simulation.

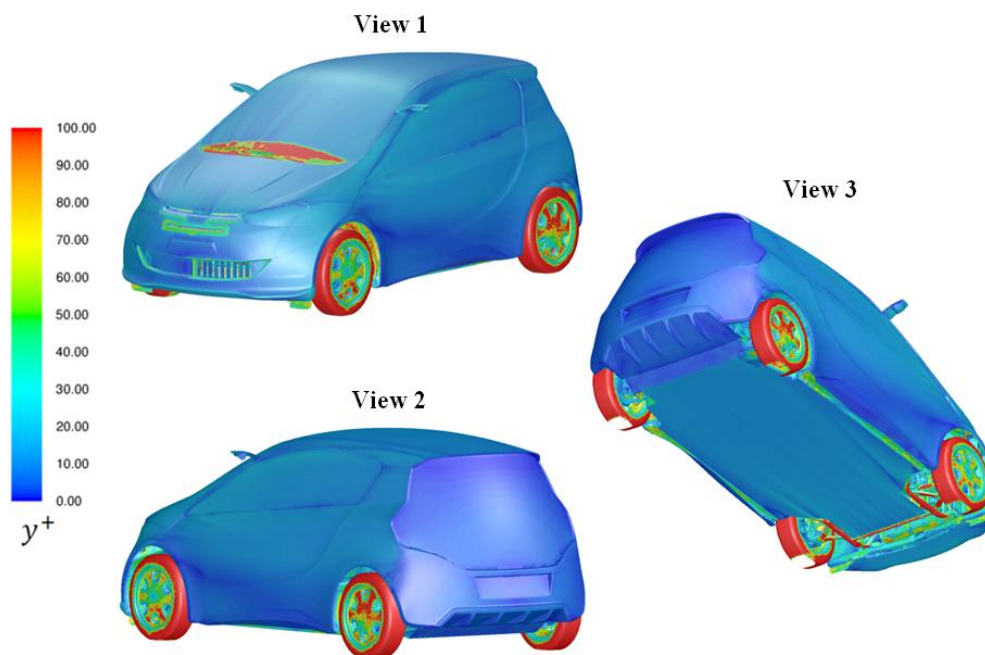


Figure 8.3 Wall y^+ 3D visualization – three standard views: View 1, View 2, and View 3 – CULT simulation 01

In the Figure 8.3 wall y^+ values from CULT simulation 01 are showed. y^+ is important on surfaces where boundary layer is present. On these surfaces values between 30 and 100 are expected. As it can be seen from the figure, values are barely thirty. Therefore, to be on the safe side, a little higher first layer of prism elements would probably give better and more stable results.

9 CONCLUSION

This thesis showed that aerodynamic drag can be reduced with the help of aerodynamic drag reduction devices. Three of these devices were investigated and proved to be very useful – front-wheel spoilers, Cooling Air Shutter (CAS) mechanism and side mirrors. Compared with the aerodynamic benefits from these devices, their production costs are not great.

Except that, this thesis investigated several basic CFD procedure related settings and phenomena. These investigations showed that CFD and aerodynamics in general, are fields that require a lot of knowledge and engineering skills.

Also, CFD comparison with the wind tunnel measurement showed that, on first sight, small differences between geometries can lead to totally different results and conclusions.

All together, this thesis has 13 different analyses which were carried out. Each of them has its own conclusion at the end of its chapter.

Aerodynamics has a lot of potential on the vehicles as the CULT is. There is a lot of space for investigation in that area. Environmental awareness and today's transportation difficulties will, for sure, bring more money for projects like CULT is and, also, to the aerodynamic investigations in general.

REFERENCES

- [1] Hucho, W. H.: Aerodynamik der stumpfen Körper , Germany, 2002.
- [2] Hucho, W. H.: Aerodynamics of Road Vehicles, Fourth Edition, Society of Automotive Engineers, 1998.
- [3] Ortel, H.: Introduction to Fluid Mechanics, University of Karlsruhe, Germany, 2005.
- [4] Šoda A., Ormuž K., Motorna Vozila (eng. *Motor Vehicles*), Lecture Notes - Faculty of Mechanical Engineering and Naval Architecture, 2011/2012.
- [5] Katz, J.: Race Car aerodynamics, Bentley Publishers, Cambridge, USA 1995.
- [6] Buresti, G.: Bluff Body Aerodynamics Lecture Notes, Department of Aerospace Engineering, University of Pisa, Italy 2000.
- [7] Jiyuan, T., Guan., H. Y., Chaoquin, L.: Computational Fluid Dynamics, USA 2008.
- [8] Šoda A., Mannini, C., Sjerić, M.: Investigation of Unsteady air Flow Around Two-Dimensional Rectangular Cylinders, Transactions of FAMENA XXXV-2 (2011), Faculty of Mechanical Engineering and Naval Architecture, University of Zagreb, ISSN 1333-1124, pages 11 – 34
- [9] http://en.wikipedia.org/wiki/Computational_fluid_dynamics, 2. March 2013.
- [10] International Association of Public Transport – Public Transport and CO2 Emissions, http://www.uitp.org/news/pics/pdf/MB_CO23.pdf , 2. March 2013.
- [11] http://en.wikipedia.org/wiki/City_car, 3. March 2013.
- [12] http://en.wikipedia.org/wiki/Fiat_500, 3. March 2013.
- [13] http://en.wikipedia.org/wiki/Puch_500, 5. May 2013.
- [14] http://www.auto-motor-und-sport.de/bilder/aerodynamik-report-spritsparmodelle-aus-dem-windkanal-4022658.html?fotoshow_item=20, 3. March 2013.
- [15] http://en.wikipedia.org/wiki/Ford_Model_T, 3. March 2013.
- [16] http://en.wikipedia.org/wiki/Volkswagen_Beetle, 3. March 2013.

-
- [17] <http://www.magnasteyr.com>, 4. March 2013.
- [18] <http://www.bmw.com>, 5. March 2013.
- [19] <http://www.altairhyperworks.com>. 5. March 2013.
- [20] <http://www.ansys.com/Products/Other+Products/ANSYS+TGrid>, 6. March 2013.
- [21] <http://www.ansys.com/Products/Simulation+Technology/Fluid+Dynamics/Fluid+Dynamics+Products/ANSYS+Fluent>, 6. March 2013.
- [22] http://en.wikipedia.org/wiki/New_European_Driving_Cycle, 18. May 2013.
- [23] <http://kurier.at/lebensart/motor/erdgasauto-cult-oesterreichs-preisguenstige-alternative-zum-elektroauto/11.279.136>, 18. May 2013.
- [24] http://ec.europa.eu/clima/policies/transport/vehicles/cars/index_en.htm, 18. May 2013.
- [25] Fluent 13.0 Help
- [26] [http://en.wikipedia.org/wiki/Curl_\(mathematics\)](http://en.wikipedia.org/wiki/Curl_(mathematics)), 6. March 2014.
- [27] <http://en.wikipedia.org/wiki/Vorticity>, 6. March 2014.
- [28] http://www.cfd-online.com/Wiki/Turbulence_kinetic_energy, 6. March 2014.
- [29] http://www.cfd-online.com/Wiki/Wall_shear_stress, 6. March 2014.
- [30] http://en.wikipedia.org/wiki/Law_of_the_wall, 6. March 2014.
- [31] http://en.wikipedia.org/wiki/Johann_Puch, 8. November 2014.
- [32] http://en.wikipedia.org/wiki/Frank_Stronach, 8. November 2014.
- [33] <http://www.amazon.com/The-Magna-Man-Economic-Freedom>

APPENDIX

1. Table with simulations results – one A3 sheet
2. DVD disc with all simulations data – 1 copy

APPENDIX 1 – TABLE WITH SIMULATIONS RESULTS

General information			Results		
Nr.	Data status	Extra information	Cd	Czf	Czr
1	CAS open, basic simulation	wheels sp. standard, 5 prisms	0,339	-0,087	0,060
2	CAS open, bs 01, without wh. sp.	no wheels sp., 5 prisms	0,333	-0,117	0,072
3	CAS open, bs 01, closed inlets	closed middle and upper inlets, 5 prisms	0,333	-0,106	0,062
4	CAS open, bs 01, wheels sp. opt.	wheels sp. middle in&out, 5 prisms	0,342	-0,074	0,059
5	CAS open, bs 01, wheels sp. opt.	wheels sp. middle in, 5 prisms	0,343	-0,078	0,056
6	CAS open, bs 01, wheels sp. opt.	wheels sp. middle out, 5 prisms	0,339	-0,084	0,058
7	CAS open, bs 02, wheels rot.	wheels rotation at angle, 5 prisms	0,333	-0,116	0,070
8	CAS open, bs 01, fine mesh	100 mio. tetra, 5 prisms	0,345	-0,109	-0,015
9	CAS open, bs 01, more iter.	1000 more iterations, 5 prisms	0,336	-0,090	0,060
10	CAS open, bs 01, 10 prism	10 prism layers	0,351	-0,084	-0,014
11	CAS open, bs 01, add. ref. zone	fine ref. zone around wheels sp., 5 prisms	0,339	-0,082	0,062
12	CAS closed, basic simulation	wheels sp. standard, 10 prism	0,324	-0,116	0,069
13	CAS closed, bs 12, without wh. sp.	no wheels sp., 10 prism	0,321	-0,147	0,076
14	CAS closed, bs 12, mock up	closed middle and upper inlets, 10 prism	0,320	-0,131	0,073
15	CAS closed, bs 12, road rough. 0	10 prism	0,292	-0,105	0,038
16	CAS closed, bs 12, no side mirrors	without side mirrors, 10 prism	0,321	-0,115	0,074
17	CAS open, bs 12	CAS closed deleted, open added, 10 prism	0,340	-0,094	0,055
18	CAS open, bs 17, 5 prism	compare with sim 01, 5 prism	0,342	-0,091	0,055
19	CAS closed, bs 12, 5 prism	5 prism	0,327	-0,115	0,068
20	CAS closed, bs 12, wheels sp. opt.	wheels sp. front, 10 prisms	0,321	-0,123	0,072
21	CAS closed, bs 12, wheels sp. opt.	wheels sp. front in, 10 prisms	0,322	-0,115	0,070
22	CAS closed, bs 12, wheels sp. opt.	wheels sp. front out, 10 prisms	0,327	-0,123	0,072
23	CAS closed, bs 12, wheels sp. opt.	wheels sp. front in&out, 10 prisms	0,326	-0,116	0,069
24	CAS closed, bs 12, wheels sp. opt.	wheels sp. rear, 10 prisms	0,328	-0,107	0,075
25	CAS closed, bs 12, wheels sp. opt.	wheels sp. rear in, 10 prisms	0,343	-0,118	-0,018
26	CAS closed, bs 12, wheels sp. opt.	wheels sp. rear out, 10 prisms	0,323	-0,112	0,085
27	CAS closed, bs 12, wheels sp. opt.	wheels sp. rear in&out, 10 prisms	0,325	-0,103	0,082
28	CAS closed, bs 12, side mirrors opt.	mirrors top 0°, 10 prisms	0,323	-0,110	0,073
29	CAS closed, bs 12, side mirrors opt.	mirrors bottom 0°, 10 prisms	0,322	-0,125	0,070
30	CAS closed, bs 12, side mirrors opt.	mirrors top +15°, 10 prisms	0,323	-0,100	0,080
31	CAS closed, bs 12, side mirrors opt.	mirrors middle +15°, 10 prisms	0,319	-0,094	0,084
32	CAS closed, bs 12, side mirrors opt.	mirrors bottom +15°, 10 prisms	0,318	-0,094	0,087
33	CAS closed, bs 12, side mirrors opt.	mirrors top -15°, 10 prisms	0,330	-0,124	0,054
34	CAS closed, bs 12, side mirrors opt.	mirrors middle -15°, 10 prisms	0,332	-0,129	0,052
35	CAS closed, bs 12, side mirrors opt.	mirrors bottom -15°, 10 prisms	0,332	-0,133	0,052
36	CAS open, bs 10	diff. ref. Zon. (ver. after sim. 12), 10 prism	0,341	-0,092	0,057
37	CAS closed, bs 14, diff. speed	70km/h, mid. & up. air inl. closed, 10 prism	0,321	-0,130	0,076
38	CAS closed, bs 14, diff. speed	280km/h, mid. & up. air inl. closed, 10 prism	0,320	-0,137	0,070
39	CAS open, bs 17, diff. speed	140km/h, mid. & up. air inl. closed, 10 prism	0,337	-0,112	0,059
40	CAS open, bs 17, diff. speed	70km/h, mid. & up. air inl. closed, 10 prism	0,337	-0,104	0,062
41	CAS open, bs 17, diff. speed	280km/h, mid. & up. air inl. closed, 10 prism	0,333	-0,112	0,059
42	CAS open, bs 17, ref. z. UBV opt.	10 prism	0,339	-0,097	0,051
43	CAS open, bs 18, ref. z. UBV opt.	5 prism	0,343	-0,097	0,052
44	CAS open, bs 18, ref. z. UBV opt.	diffusor ref. zone, 5 prism	0,343	-0,095	0,057
45	CAS open, bs 18, ref. z. UBV opt.	fine mesh, 130 mio. el., 5 prism	0,348	-0,108	-0,016
46	CAS open, bs 18, ref. z. UBV opt. 2	sharp UBV, 5 prism	0,342	-0,097	0,060
47	CAS open, bs 18, ref. z. UBV opt. 2	5 prism,	0,343	-0,098	0,052
48	CAS open, bs 18, ref. z. UBV opt.	sharp UBV, wake refinement, 5 prism	0,340	-0,099	0,059
49	CAS open, bs 18, ref. z. UBV opt.	sharp UBV, "box 25", 5 prism	0,346	-0,114	-0,012
50	CAS open, bs 18, ref. z. UBV opt.	sharp UBV, "box front", 5 prism	0,343	-0,094	0,060
51	CAS open, bs 01, restart 3500 iter.	simulation 01 restart, 5 prism	0,332	-0,094	0,058
52	CAS open, bs 46, cell based	sharp UBV, 5 prism	0,324	-0,084	0,064
53	CAS open, bs 49, "box 25"	sharp UBV, 5 prism	0,330	-0,099	-0,003
54	CAS closed, bs 12, cell based	10 prism	0,307	-0,117	0,032
55	CAS open, bs 01, new ref. zones	5 prism	0,342	-0,106	-0,008